Vortex-Induced Vibration of a Circular Cylinder with Combined In-line and Cross-flow Motion

by

Jason Dahl

Bachelor of Science in Naval Architecture and Marine Engineering (2002)
Webb Institute, Glen Cove, NY, USA

Submitted to the Center for Ocean Engineering, Department of Mechanical Engineering
in partial fulfillment of the requirements for the degree of

Doctor of Philosophy

at the

MASSACHUSETTS INSTITUTE OF TECHNOLOGY

June 2008

Author .....
Center for Ocean Engineering, Department of Mechanical Engineering
April 1, 2008

Certified by .....
Michael S. Triantafyllou
Professor of Mechanical and Ocean Engineering
Thesis Supervisor

Accepted by .....
Lallit Anand, Professor of Mechanical Engineering
Chairman, Departmental Committee on Graduate Students

Vortex-Induced Vibration of a Circular Cylinder with Combined In-line and Cross-flow Motion

by

Jason M. Dahl

Submitted to the Center for Ocean Engineering, Department of Mechanical Engineering
on April 1, 2008, in partial fulfillment of the
requirements for the degree of
Doctor of Philosophy

Abstract

Deep water, string-like, marine risers subject to strong ocean currents, suffer from vortex-induced vibrations (VIV), where vortex shedding interacts with the structural properties of the riser, resulting in large amplitude vibrations in both in-line and cross-flow directions. This thesis presents an experimental approach to model and quantify the motions and hydrodynamic forces associated with the excitation of a deep water marine riser by considering the combined cross-flow and in-line excitation of a rigid cylinder.

For deep water risers, the excitation of the structure through vortex shedding can lead to a condition of dual resonance, where the vortex shedding frequency locks in to the effective natural frequency (adjusted for added mass effects) in both in-line and cross-flow directions. Large motion amplitudes are observed in this condition along with large magnitude third harmonic forces in lift. Flow visualization of the wake behind the cylinder in combined in-line and cross-flow motion, shows that third harmonic forces are caused by the relative motion of the cylinder with respect to a '2P' (two pairs of vortices) or '2T' (two triplets of vortices) shedding pattern, since vortices shed in these modes remain in close proximity to the cylinder over one cycle of motion.

Forced motions of a cylinder with combined in-line and cross-flow motions are performed, generating a database of force coefficients to be used in riser VIV prediction. The assumption of dual resonance is used to predict the motions of an elastically mounted rigid cylinder using measurements from forced cylinder motions. Two passive vortex suppression methods are studied for eliminating combined cross-flow and in-line cylinder motions and suppressing large third harmonic forces.

Thesis Supervisor: Michael S. Triantafyllou
Title: Professor of Mechanical and Ocean Engineering

Acknowledgments

First of all, I would like to acknowledge my wife Rachel for supporting me through this research, spending long hours with me at the tank on weekends. I would like to acknowledge my advisors Prof. Michael Triantafyllou and Prof. Franz Hover for their support and insight on this project. I would like to acknowledge Prof. Suchuan Dong from Purdue University and Prof. Karniadakis from Brown University for allowing the use of their direct numerical simulation data. I would like to thank Prof. Vandiver and his research group for their shared research which has helped to refine the scope of this thesis. I must also acknowledge the Norwegian Deepwater Programme for allowing the use of the flexible cylinder experimental data described in Chapter 5. Finally, I would like to acknowledge the various towing tank undergraduate and graduate students, post-docs, and research staff that were involved with either helping in experimental work or lending moral support: Matthias Bloennigen, Stephen Licht, Yahya Modarres-Sadeghi, Harish Mukundan, Pradya Prempraneerach, Sam Roberts, Kjetil Skaugset, Dan Walker, Gabe Weymouth.

Contents

List of Figures

List of Tables

Chapter 1

Introduction

Steady fluid flow across a circular cylinder is one of the canonical problems of fluid dynamics based on the simplicity of the problem formulation and the ubiquitous presence of cylinders in engineering applications [3, 4]. Vortex induced vibrations are a modern day problem resulting from vortex shedding in the wake of bluff bodies. Vibrations experienced due to vortex shedding can occur in a large variety of structures. Ocean structures affected by vortex shedding from ocean currents include drilling risers, spar buoys, tension-leg platforms, mooring lines, cables, and undersea piping. Buildings and bridges experience vibrational problems due to wind induced vibrations. The humming of telephone wires in the wind is even attributed to vortex shedding.

1.1 Research Motivation

The primary goal of this research is to analyze vortex induced vibrations in the context of ocean structures. With an increasing demand for energy in the United States, the search for energy resources is partially focused on the ocean. Recent discoveries of oil and natural gas fields in the deep water of the Gulf of Mexico has prompted the engineering problem of retrieving natural resources at extreme ocean depths. Ocean structures operating at extreme depths will undoubtedly be plagued with vibrational problems as extremely long risers and cables have very high mode numbers, becoming

susceptible to excitations over a broad range of frequencies.

Researchers in the past have focused primarily on cross-flow (transverse) oscillations of circular cylinders when determining the force and motion responses due to vortex induced vibrations since the cross-flow oscillation of elastically mounted cylinders, excited through vortex shedding, is very large compared to in-line oscillations. Limiting motions to the cross-flow direction alters the wake behind the cylinder and the resulting motion response. Very long cylinders in deep water suffer from vibrational problems that affect both in-line and cross-flow resonance.

As ocean structures move to deeper and deeper water, the necessity for an accurate understanding of the physics of two degree of freedom VIV becomes apparent. Ocean structures such as risers and cables typically have mass ratios on the order of 1-2. In addition to low mass ratio, these long flexible structures exhibit structural characteristics similar to long beams or strings depending on the application. If one considers a long cylindrical structure to be similar to a beam under tension, it possesses a countable set of natural frequencies and modes in the in-line and transverse directions. In each direction, depending on the ratio of the tension to bending stiffness, the natural frequency of the n-th mode lies between $n \times f_1$ (string) and $n^2 \times f_1$ (beam), where f_1 is the fundamental natural frequency of the structure. The in-line excitation force from vortex shedding has a period equal to half the period of the transverse force since vortex shedding always occurs downstream of the cylinder. Consequently, dual resonance requires the transverse natural frequency to be equal, or at least close to the frequency of vortex shedding, f_s, and the in-line natural frequency to be equal to twice f_s, i.e. $f_{ny} \approx f_s$ and $f_{nx}/f_{ny} = 2$. This is possible in a string, for example, when the third natural frequency is excited in the transverse direction and the sixth natural frequency is excited in the in-line direction. In a beam, the ratio f_{nx}/f_{ny} can rarely reach a value close to 2; therefore, the transverse motion resonates with the fluid excitation, while the in-line motion is non-resonant. Since most shallow water structures bear characteristics closer to a beam than a string, the perfect resonance condition is rarely achieved and the prevalent condition is that of $f_{nx}/f_{ny} \approx 1$. In deep water however, perfect resonance of very long structures is nearly inevitable as

the number of modes increase and the structure appears string-like. This necessitates the parametric investigation for a range of f_{nx}/f_{ny} values. A simple apparatus that can be used in these experiments may consist of a rigid cylinder tuned with a single, adjustable natural frequency in each direction.

This thesis begins with a study of the free vibrations of an elastically mounted, rigid cylinder in a uniform flow , where the cylinder is allowed to move in the in-line and cross-flow directions. The ratio of natural frequencies in each direction can be tuned independently, allowing for adjustment of the frequency ratio, f_{nx}/f_{ny}, and the mass ratio is designed to be low, comparable to the mass ratio of ocean structures. Analysis of the forces measured from these free vibrations indicate that under dual resonance, the assumptions made for simplifying vortex induced vibrations to cross-flow motions only are no longer valid. Strong, third harmonic components of lift appear in the lift force under resonance in two degrees of freedom, overwhelming the fundamental frequency components of lift under certain conditions. Previously, common design practices have assumed that the primary component of lift occurred at or near the fundamental frequency of vortex shedding as defined by the Strouhal number. These experiments show that this assumption is not always valid.

The observation of large amplitude third harmonic forces in lift under perfect resonance prompts further analysis of the cause of these forces. Digital particle image velocimetry (DPIV) techniques were used to visualize the wake of a cylinder undergoing forced vibrations in two degrees of freedom. Forced vibrations were kinematically matched to the free vibrations in an attempt to visualize the wake of the free vibrations. Various patterns of vortex shedding were observed to explain the presence of high harmonic forces in lift. Some patterns differ slightly from the traditional wake modes observed with purely cross-flow motions.

Since the traditional single degree of freedom force model does not apply when the cylinder resonates in two degrees of freedom, it is necessary to identify the force coefficients associated with higher harmonic forces and forcing changes caused by in-line motions. This is done by measuring forces on a cylinder forced with combined in-line and cross-flow motions. With both in-line and cross-flow motion, it

is necessary to vary in-line amplitude, cross-flow amplitude, phase between in-line and cross-flow motions, and reduced velocity to cover the motion parameter space. These additional parameters drastically increase the number of tests essential for determining force coefficients. The forced vibration database described in this thesis is a sparse database, constructed with the intention of identifying higher harmonic lift coefficients and generating force coefficients that can be used to predict the motions and forces associated with two degree of freedom cylinder vibrations.

Vortex induced vibrations can either be dealt with by monitoring the damage caused by the vibrations or by suppressing the vibration. Both methods are addressed in this thesis by estimating force coefficients on a flexible riser and testing a few method of VIV suppression. Since combined in-line and cross-flow motions are shown to enhance vortex-induced vibrations, causing large third harmonic forces, VIV suppression devices are tested to show their effectiveness with handling cross-flow motions and third harmonic forces.

1.2 Chapter Preview

Chapter 2 gives much of the background information on vortex shedding, vortex induced vibrations, and nomenclature used throughout the thesis. This chapter gives a detailed description of the problem of vortex shedding and mentions a number of studies involving free and forced vibrations in single degree of freedom and two degree of freedom vibrations of a circular cylinder.

Chapter 3 explains the two degree of freedom free vibration experiments. A description of the apparatus and methods is given, along with the results of the experiment. A discussion of the results emphasizes the effects of in-line motion and dual resonance on lift force, drag force, and cylinder response.

In Chapter 4, flow visualizations behind a rigid cylinder in forced two degree of freedom motion is shown along with visualizations behind two flexible cylinders. A description of the digital particle image velocimetry method and forced vibration apparatus are given. Selected cylinder motions from free vibrations are kinematically

reproduced to estimate the wake of the freely vibrating cylinder. Additionally, small perturbations of the parameters around a free vibration are shown to see how the wake and subsequent forces will vary based on changes in amplitude, phase, and reduced velocity.

Chapter 5 discusses the forces associated with forced motion of a rigid cylinder in cross-flow and in-line motions. A sparse database of measured force coefficients is obtained and rigid cylinder free vibrations are predicted using this coefficient database. The distribution of forces along the length of a flexible riser are inferred from the database as well.

Chapter 6 deals with the topic of vortex suppression. A description of two tested vortex suppression devices is given along with a description of various vortex suppression devices that exist in practice. A discussion of the effectiveness of the two vortex suppression devices is given with particular emphasis on their effect on mean drag reduction, suppression of vibration, and suppression of third harmonic lift forces.

Chapter 7 is the conclusion of this thesis. The contributions of this thesis to science are outlined along with recommendations for future work.

Chapter 2

Vortex Induced Vibrations - Background and Nomenclature

In this chapter, the basic concept of vortex shedding and vortex induced vibrations are explained and previous research is examined to illustrate the relevant parameters associated with vortex induced vibrations in the context of the ocean environment. Past simplifications in analyzing vortex induced vibrations are shown and the relevant non-dimensional parameters for properly modeling and scaling the forces associated with vortex induced vibrations are defined. The problem of combined in-line and cross-flow vibration of an elastically mounted circular cylinder is introduced with an explanation of previous studies on the topic.

2.1 Bluff body vortex shedding

When a bluff body, such as a circular cylinder, is placed in a uniform free stream of fluid, such that the flow is essentially two dimensional, the fluid is forced to deviate from its uniform straight path, moving around the cylinder. At very low Reynolds number ($Re < 5$), the streamlines of the flow around a circular cylinder resemble those of the potential flow solution and the flow remains unseparated. In this case, stagnation points exist both fore and aft of the cylinder [4]. As Reynolds number increases slightly ($5 < Re < 40$), two vortices form in the wake of the cylinder,

yet remain attached to the cylinder. The wake is still steady in this case. Beyond $Re = 40$, the wake becomes unstable and small perturbations in the flow or on the surface of the cylinder will cause vortices to break off from the cylinder and shed periodically downstream.

The problem of vortex shedding is not limited to circular cylinders, but can exist for any bluff body cross-section, i.e. square, rectangle, oval. Bluff bodies, defined as cross sectional shapes that have a span-to-chord ratio near one, suffer from having an adverse or positive pressure gradient on the downstream side of the body. A negative pressure gradient on the upstream side of the body effectively forces the fluid to adhere to the body. On the back side of the body, the pressure gradient switches signs and fluid is effectively forced to peel off from the body, resulting in separation. As the separated fluid curls into the deficit formed in the wake of the cylinder, vortices are formed. In the case of the circular cylinder, a regular pattern of vortex shedding will begin to form given sufficient time.

2.1.1 Kármán street and Strouhal Number

The pattern of periodically shed vortices behind a stationary cylinder in a free stream is called the Kármán vortex street. Fig. 2-1 shows an example of the Kármán vortex street. The street is characterized by the alternate shedding of vortices with opposite rotation. The characteristic non-dimensional parameter for this type of fluid flow is called the Strouhal number (St) and is defined below, where f_s is the frequency of vortex shedding in the wake (Strouhal frequency), D is the cylinder diameter, and U is the free stream velocity.

$$St = \frac{f_s D}{U} \tag{2.1}$$

Strouhal number has been experimentally shown to be a function of Reynolds number based on the cylinder diameter. For a large region of subcritical Reynolds numbers, however, the Strouhal number remains relatively constant, with a value of 0.2 for a circular cylinder [4].

Figure 2-1: Kármán vortex street. Image modified from picture by S. Taneda in Van Dyke [14].

2.1.2 Vortex Induced Vibrations

When a cylinder is flexible or elastically mounted, the natural frequency of the cylinder can be excited by vortex shedding. When the frequency of vortex shedding is near the natural frequency of the cylinder, large amplitude motions of the cylinder may occur. These motions are called vortex-induced vibrations (VIV) and are caused by the interaction of the cylinder structure with vortices shed in the cylinder wake. Vortex shedding behind an oscillating cylinder is similar to that behind a stationary cylinder, where vortices or groups of vortices will shed at or near the Strouhal frequency.

Vortex-induced vibrations are a subset of fluid mechanics instabilities called flow-induced vibrations. The term vortex-induced vibrations generally refers to vibrations that are stable and self-limiting, resulting from large scale vortex shedding. The self-limiting nature of vortex-induced vibrations is caused by a balance between excitation forces and fluid damping [67]. Vortex-induced vibrations differ from unstable oscillations, such as torsional galloping, which can be caused by geometrical asymmetry of

structures.

Unstable oscillations typically result in extreme loading on a structure that can cause failure from exceeding the yield strength properties of the material. In contrast, vortex-induced vibrations are typically moderate in amplitude, resulting in structural oscillations that are not large enough to cause catastrophic failure initially, but may result in material fatigue over a large number of oscillation cycles. The main concern of structures suffering from vortex-induced vibrations becomes failure by fatigue. Since material fatigue is related to the stresses on a given material and stress is directly related to the forces exerted on a structure, it is desirable to accurately predict the forces that a structure may encounter due to vortex-induced vibrations. Ocean structures are typically built to last in excess of 20 years and the fatigue life of these structures becomes very important in defining the design criteria.

The problem of vortex-induced vibrations is typically associated with long, slender structures that are characterized by a large number of natural frequencies. In ocean engineering applications, a floating structure such as an oil rig or ship may be connected to the ocean floor via long cylindrical structures in the form of a drilling riser, mooring line, tether, etc. Naval and research vessels typically tow vibration sensitive equipment in the wake of the vessel, such as SONAR arrays or remotely operated vehicles. The tethering lines can be very long and slender, making them susceptible to vortex-induced vibrations as well. In addition to ocean surface structures, sub-sea structures can be affected by vortex-induced vibrations. Thousands of miles of piping, conduit, and cabling exist on the ocean floor for carrying natural resources, housing wiring, and transmitting data across the ocean floor. Suspended portions of these long structures are susceptible to vibrations caused by ocean currents.

All of these applications share in common the long and slender, bluff circular cylinder cross sectional shape (high aspect ratio). Vibrations of these structures in the field can be very complex due to the high number of structural natural modes and sheared ocean currents. To better understand the problem and causes of vortex-induced vibrations, it is desirable to simplify the problem at hand.

One simplification for studying fluid flow around a long, slender body is to analyze

the flow over a small section of the body as illustrated in Fig. 2-2. By looking at only a small portion of a long cylinder, the cylinder appears as an elastically mounted, rigid cylinder and any sheared current will appear as a free stream of fluid with constant velocity. This simplification allows us to analyze the fluid mechanics as though the flow is nearly two dimensional. Although this is a gross simplification in the context of a marine riser, it allows one to understand the basic mechanisms that lead to the observed forces on the actual riser.

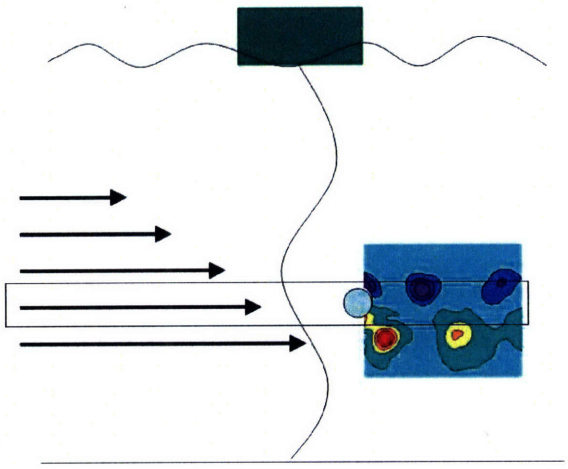

Figure 2-2: Schematic of marine riser. Riser motions are modeled by considering a small slice of the riser with cylindrical cross-section.

When vortices shed in the wake of a circular cylinder, the forcing frequency in the lift direction occurs at the frequency of vortex shedding. This is expected since one vortex or group of vortices sheds to one side of the cylinder once per cycle and one vortex or group of vortices sheds to the other side of the cylinder once per cycle. In the drag direction, however, all vortices are shed downstream. Therefore, the drag force associated with vortex shedding occurs at twice the frequency of the lift force since both vortices are shed to the same side of the cylinder in the drag direction. When the vortex shedding frequency is near the natural frequency of the elastically

mounted cylinder, the response motions resulting from these fluctuating forces result in relatively large cross-flow (perpendicular to the direction of fluid flow) motion on the order of one cylinder diameter. In-line vibrations (in the direction of the fluid flow) are not as large as cross-flow motions and are typically less than 0.5 diameters. For this reason, many experimental studies have simplified experiments by only considering cross-flow vibrations of the structure. Many of these studies have been documented in the comprehensive reviews of [54] and [74] and the premise of this simplification is described in the next section.

2.2 One Degree of Freedom Vibrations

In the one degree of freedom vortex induced vibration problem, an elastically mounted circular cylinder is situated in a free stream of fluid as in Fig. 2-3. The cylinder has mass m, the elastic mount has a spring constant k and a damping constant b. The fluid force on the cylinder in the cross-flow direction is denoted by L. This representation is a simple spring-mass-dashpot system as in equation 2.2. The natural frequency of the structure in a vacuum is determined according to equation 2.3.

$$m\ddot{y} + b\dot{y} + ky = L \tag{2.2}$$

$$\omega_n = \sqrt{\frac{k}{m}} \tag{2.3}$$

In the case of a cylinder vibrating in a free stream of fluid, the cylinder must accelerate through the fluid, resulting in an acceleration of displaced fluid around the body. The acceleration of surrounding fluid results in a force on the cylinder that is in phase with the inertial force on the left hand side of equation 2.2 and this force is referred to as the ideal added mass force. Vortex shedding in the wake of the cylinder can also result in fluid forces in phase with the structural inertia force, resulting in another portion of the fluid force that appears as an inertial force. Since these forces cannot be distinguished individually in a measurement of hydrodynamic forces, the

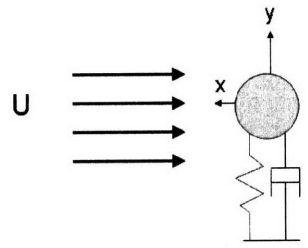

Figure 2-3: One degree of freedom spring-mass-dashpot cylinder in a uniform free stream.

total fluid forces on the right hand side of equation 2.2 that are in phase with the left hand side inertia are called the effective added mass force [35], with effective added mass denoted by m_a.

2.2.1 Relevant non-dimensional parameters

Table 2.2.1 shows the relevant non-dimensional parameters associated with vortex induced vibrations in one degree of freedom.

The true reduced velocity, V_r is similar to an inverse Strouhal number, except that the frequency of cylinder motion is used to normalize the fluid velocity. In this sense, the true reduced velocity is a comparison of the free stream velocity with respect to the cylinder's transverse velocity. Moe and Wu [42] showed that the true reduced velocity must be matched in order to compare the free vibration of a cylinder with forced vibrations. Many non-dimensional parameters are non-unique when compared against true reduced velocity in a free vibration since the ratio of velocity over frequency may remain constant in a free vibration depending on the interaction between the

Amplitude Ratio	$\frac{A_y}{D}$	$\frac{Motion\ Amplitude}{Cylinder\ Diameter}$
Frequency Ratio	$\frac{f_y}{f_{ny}}$	$\frac{Excitation\ Frequency}{Natural\ Frequency}$
True Reduced Velocity	$V_r = \frac{U}{fD}$	$\frac{Free\ Stream\ Velocity}{Transverse\ Cylinder\ Velocity}$
Nominal Reduced Velocity	$V_{rn} = \frac{U}{f_{ny}D}$	$\frac{Free\ Stream\ Velocity}{(Natural\ Frequency)(Cylinder\ Diameter)}$
Mass Ratio	$m^* = \frac{m}{\rho\pi\frac{D^2}{4}S}$	$\frac{Cylinder\ Mass}{Displaced\ Fluid\ Mass}$
Damping Ratio	$\zeta = \frac{b}{4\pi m f_{ny}}$	$\frac{System\ Damping}{Critical\ Damping}$
Added Mass Ratio	$C_m = \frac{m_a}{\rho\pi\frac{D^2}{4}S}$	$\frac{Effective\ Added\ Mass}{Displaced\ Fluid\ Mass}$
Drag Coefficient	$C_D = \frac{F_x}{\frac{1}{2}\rho U^2 DS}$	$\frac{Drag\ Force}{(Stagnation\ Pressure)(Projected\ Area)}$
Lift Coefficient	$C_L = \frac{F_y}{\frac{1}{2}\rho U^2 DS}$	$\frac{Lift\ Force}{(Stagnation\ Pressure)(Projected\ Area)}$
Reynolds Number	$Re = \frac{UD}{\nu}$	$\frac{Inertial\ Force}{Viscous\mathsf{Force}}$

structure and the fluid. This results in the cylinder undergoing different motions for equivalent true reduced velocities. In order to obtain a unique representation of measured non-dimensional parameters, it is common to instead use the nominal reduced velocity, V_{rn}, as defined in Table 2.2.1. Since the natural frequency of the structure is constant, this non-dimensional parameter will provide a unique mapping of measured parameters for a given flow velocity.

Amplitude ratio, frequency ratio, added mass ratio, drag coefficient, and lift coefficient are measured functions of the reduced velocity (nominal or true). These parameters normalize the cylinder response and forces exerted on the cylinder.

Mass ratio, or specific gravity, is a relative measure of the structural moving mass with respect to the displaced mass of fluid. In air, the mass ratio is typically very large since the density of the fluid is very small. In water, the fluid density is of the same order of magnitude as the density of the cylinder, hence ocean structures typically have mass ratios less than 3. The damping ratio is another property of the structure. It is a measure of the structural damping with respect to the critical damping. Ocean structures are typically lightly damped, with very low structural damping ($\zeta < 0.05$). The structural damping must be corrected for added mass effects when undergoing vibration in a dense fluid since the damping ratio is a function of mass and added mass. In this case, the mass and natural frequencies in the damping ratio must reflect the inertial changes from fluid forces [18]. The mass-damping ($m^*\zeta$) is a commonly cited parameter for vortex induced vibrations since this parameter directly affects the amplitude response of the cylinder. Govardhan and Williamson [20] showed that for a decreasing mass-damping, the cylinder will oscillate with larger peak amplitudes.

Reynolds number is defined based on the cylinder diameter. The recent studies of Govardhan and Williamson [20] have shown that the amplitudes and forces associated with vortex induced vibrations have a dependence on Reynolds number as well. In general, for the Reynolds numbers observed in the experiments, peak motion amplitudes were shown to increase with increasing Reynolds number.

2.2.2 Lock-in

When a cylinder is excited by vortex shedding, it undergoes a forced vibration. The fluid forces acting on the body, however, are influenced by the resulting motion of the cylinder. Through this feedback mechanism, the flow-structure interaction reaches a final dynamic equilibrium through matching of the flow and structure "impedances". The formation of the vortices is caused by an instability of the wake flow behind the cylinder (self-excited oscillations of the flow). As a result, vortex shedding is triggered by the slightest flow perturbations and excitation of the structure is unavoidable. The flow-structure interaction mechanism is strongest when the frequency of vortex shedding is relatively close to a natural frequency of the structure; the vortex-induced forces can cause a change in the effective added mass and bring the natural frequency even closer to the wake frequency. Furthermore, the frequency of vortex shedding can be entrained to exactly match the effective natural frequency of the structure. As a result, resonance in VIV can extend over a much wider parametric range than is usual for mechanical systems.

For an elastically mounted cylinder, it is possible for the wake to synchronize with the motion of the cylinder. The natural instability of the flow occurs at the Strouhal frequency. Once the structure moves, the frequency of vortex shedding may become entrained to the frequency of structure oscillation, within a frequency band around the Strouhal frequency. The frequency band increases with increasing amplitude of motion, and this property of VIV is called the wake capture phenomenon. This ability of the wake to follow the oscillation frequency of the structure results in substantial alterations of added mass forces, which can drive the effective natural frequency of the system to different values than the nominal natural frequency. A dynamic equilibrium is reached, dictated by frequency resonance and flow-structure energy balance. This phenomenon is called lock-in.

Under lock-in, the excitation frequency of the structure is equal to the natural frequency of the structure adjusted by the added mass effects of the fluid [54]. This is shown in equation 2.4, where m_a is the effective added mass of the fluid.

$$\omega_{ex} = \sqrt{\frac{k}{m + m_a}} \tag{2.4}$$

If one divides ω_{ex} by the natural frequency, and non-dimensionalizes the mass, one obtains equation 2.5.

$$\omega_{ex} = \omega_n \sqrt{\frac{m^*}{m^* + C_m}} \tag{2.5}$$

Equation 2.5 shows how the condition of lock-in is largely affected by the mass ratio and the added mass coefficient. In air, the system will have a large mass ratio and relatively small added mass coefficient. In this case, the right hand side of equation 2.5 will be nearly equal to ω_n, meaning the excitation frequency will be roughly equal to the true natural frequency of the structure. This was shown to occur in the experiments of Feng [15]. In a more recent study on the effects of mass ratio, Khalak and Williamson [35] showed that for low mass ratios, the excitation frequency will deviate away from the structural natural frequency. The relative difference between mass ratio and added mass coefficient are important for low mass ratio systems since the added mass will significantly alter the excitation frequency of the structure. The condition of lock-in in this case, occurs where the wake frequency is locking in to an effective natural frequency of the system as adjusted by added inertial forces from vortex shedding and fluid acceleration.

2.2.3 Forces on the cylinder

Experimental studies of a cylinder oscillating in one degree of freedom show that the forcing function L can be represented as a sinusoid of the same form as the motion y [52]. Once transients have died out, the particular solution of equation 2.2 will be sinusoidal, giving expressions for cylinder motion and lift force, y and L, where A_y is the amplitude of motion, F_y is the lift force amplitude, and ϕ is the phase between the motion and force.

$$y = A_y sin(\omega t) \tag{2.6}$$

$$L = F_y sin(\omega t + \phi) \tag{2.7}$$

Equation 2.7 can be expanded in terms of sines and cosines to yield equation 2.8.

$$L = F_y sin(\phi) cos(\omega t) + F_y cos(\phi) sin(\omega t) \tag{2.8}$$

In non-dimensional form, the lift force magnitude F_y is given in terms of the lift coefficient, C_L, as in Table 2.2.1. The lift coefficient in phase with velocity, C_{Lv}, and lift coefficient in phase with acceleration, C_{La}, are defined in equations 2.9 and 2.10.

$$C_{Lv} = C_L sin(\phi) \tag{2.9}$$

$$C_{La} = C_L cos(\phi) \tag{2.10}$$

Plugging equations 2.6 and 2.7 into equation 2.2 and non-dimensionalizing will yield relations between the amplitude of motion and the fluid forces on the cylinder. Sarpkaya [51], Bearman [3], and Khalak and Williamson [34] give this derivation in detail, although the form of this solution can be given in a number of different ways. Keeping with the formulation of the equations above and the standard methods of the MIT Towing Tank used by Gopalkrishnan [18] and Smogeli [57], the solutions to these equations are given in terms of non-dimensional amplitude and added mass coefficient.

$$\frac{A_y}{D} = \frac{V_{rn}^2 C_{Lv}}{4\pi^3 \frac{f_{ex}}{f_{ny}} m^* \zeta} \tag{2.11}$$

$$C_m = \frac{-C_{La}}{\frac{1}{4}\pi \rho D^2 S A_y \omega_{ex}^2} \tag{2.12}$$

The important non-dimensional parameters governing this physical system are the nominal reduced velocity, V_{rn}, frequency ratio, f/f_n, amplitude ratio, A_y/D, and mass ratio, m^*. The effective added mass coefficient, C_m, which is related to the force

in phase with acceleration, is actually a function of the amplitude and frequency. One can see that the amplitude of motion is affected by the reduced velocity, frequency ratio, mass ratio, damping ratio, and lift in phase with velocity.

2.2.4 Literature on vortex shedding and one degree of freedom VIV

A large number of experimental studies exist for characterizing vortex induced vibrations due to the large number of engineering applications that suffer from such vibrations. Many studies have been performed through both experimental model testing and numerical simulation. Experiments have focused on self-excited or free vibrations, where the cylinder is allowed to oscillate purely due to fluid excitation, and forced vibrations, where cylinder motions are mechanically forced and the resulting fluid forces are observed. This section will focus primarily on identifying those studies that are fundamental to the problem of vortex induced vibrations as applied to ocean structures.

The comprehensive reviews of Sarpkaya [52, 54], Bearman [3], and Williamson and Govardhan [74] refer to many forced vibrations experiments and the resulting measured force coefficients as well as the observed responses and forces from many free vibration experiments.

2.2.5 Vortex Shedding and Stationary Cylinders

The flow around a stationary cylinder has been studied by a large number of researchers with concern focused on the phenomenon of vortex shedding. General descriptions of the problems associated with fluid flow across circular cylinders and properties of this fundamental problem are discussed in the books by Sumer and Fredsoe [60] and Zdravkovich [78, 79] as well as in the comprehensive review of Norberg [47]. The instability of the wake behind a stationary cylinder is addressed by Huerre and Monkewitz [27] and Triantafyllou et al [64, 65].

Forced Cylinder Motions

Sarpkaya [51] presented a method for using force coefficients obtained through forced cylinder motions to predict the amplitude of a freely vibrating cylinder. In this study, a collection of forced vibrations were used to determine the measured force coefficients and these force coefficients were in turn used to predict the amplitude response of the cylinder through an iterative method. This method resulted in good agreement with free vibration measurements from Griffin and Koopman [22], although the aspect ratio was very low for the Griffin and Koopman experiments, ($L/D \approx 3$). Building on the approach of Sarpkaya [51], Staubli [59] generated a set of data based on the force coefficients derived above, defining the lift coefficient magnitude and phase between lift and motion as a function of reduced velocity. His procedure for predicting the free vibration response compared well with the free vibration measurements of Feng [15]. It is important to note that the experiments of Feng [15] were performed in a wind tunnel, where the mass ratio was very large ($m^* > 60$).

As mentioned above, when the mass ratio is high, wake dynamics are dominated by the structural natural frequency of the cylinder and the wake tends to 'lock-in' to the natural frequency of the cylinder. In this case, vortex shedding will occur at the natural frequency of the cylinder, rather than the frequency predicted by the Strouhal number. Large mass ratios and large damping can have a large effect on the observed response of the cylinder, as seen by the appearance of these values in equations 2.5, 2.11, and 2.12.

Building on the work of Staubli [59], Gopalkrishnan [18] constructed a large database of C_{Lv} and C_m coefficients with the purpose of extending motion predictions beyond a reconstruction of elastically mounted rigid cylinder motions, and instead applying these force coefficients to the reconstruction of long cable motions in a sheared flow using a quasi-steady flow (strip theory) assumption. These experiments were very successful and still serve as base measurements used in prediction programs at MIT. More recent forced vibrations of a cylinder in one degree of freedom were performed by Vikestad [71] and Vikestad et al [70] in order garner a more complete

understanding of effective added mass at higher Reynolds numbers. A very detailed set of forced oscillations with the purpose of clearly mapping forced oscillations for the prediction of free vibrations using quasi-steady flow assumptions has been performed by Morse and Williamson [43].

Free vibrations of cylinder

The free vibration of a cylinder in one degree of freedom has been shown to take on very different amplitudes of oscillation due to various experimental conditions, since mass ratio and damping can largely affect cylinder motions. Peak amplitude motions of a cylinder oscillating transverse to the oncoming free stream typically peak on the order of one diameter of motion near a reduced velocity of 6. The study of Khalak and Williamson [35] indicates a lower and upper branch of amplitudes that form dependent on the mass and damping associated with the structural characteristics of the dynamic system. These branches become more well defined for lower values of mass and damping as peak amplitudes of vibration increase.

The branches observed by Khalak and Williamson do not always occur in other experimental conditions, possibly due to Reynolds number differences or simple differences in the experimental conditions. Free vibration experiments by Smogeli [57] indicated a smooth transition from high amplitude motions to low amplitude motions as opposed to the hysteretic jump seen by Khalak and Williamsom [35].

Oscillating cylinder wake

The forces acting on a cylinder are primarily a function of the vortex structures in the wake of the cylinder. Understanding the fluid forces associated with vortex-induced vibrations requires an understanding of the wake structure behind the cylinder.

A large comprehensive study of the wake behind a cylinder forced to move with cross-flow oscillations was performed by Williamson and Roshko [76]. This study produced a map of the wake behind the circular cylinder over a wide variety of oscillation amplitudes and reduced velocities. The formation of different modes in the wake of the cylinder is apparent. The map of Williamson and Roshko [76] defines

the '2S' and '2P' modes. The '2S' mode is similar to the vortex street seen behind a stationary cylinder in a uniform flow, where 2 counter-rotating vortices shed per cycle. In the '2P' mode, two pairs of counter-rotating vortices shed each cycle of transverse motion. In free vibrations, the '2S' mode typically exists at lower reduced velocities and the '2P' mode is shown to exist where the phase between lift force and transverse motions shifts 180 degrees out of phase [19].

Additional wake modes exist in the Williamson and Roshko map, however these combinations of single and paired vortices only exist for forced motions of the cylinder. Many visualization studies have focused on learning more about the method of mode formations [8, 7, 9].

2.3 Two Degree of Freedom Vibrations

Limiting motions of the cylinder to only cross-flow motions ignores the possible effects of in-line motions on wake formation and forces exerted on the cylinder. Free vibration studies on flexible cylinders such as Vandiver and Jong [68], Brika and Laneville [6], Vandiver et al [69], and Swithenbank [61] are useful in determining effects of in-line motions on observed forces, however the flexible cylinder introduces added complexity to the problem of vortex-induced vibrations and simplification of the problem is necessary for understanding the fluid mechanisms leading to vortex-induced vibrations. Additionally, studies focusing primarily on in-line oscillation of the cylinder only, do not take into account the coupled effect of both in-line and transverse motions. A limited number of studies exist where an elastically mounted, rigid cylinder is allowed to vibrate in both the in-line and transverse directions. Some of the more relevant studies to this thesis are discussed in this section.

2.3.1 Nomenclature for two degree of freedom motions

In the two degree of freedom oscillation of a cylinder, the motions of the cylinder in the in-line and transverse directions are primarily sinusoidal and the system is treated as a spring-mass-dashpot in two degrees of freedom (see Fig. 2-4). The equations

of motion for the two degree of freedom rigid cylinder system are given in equations 2.13 and 2.14. In this case, the two equations are coupled through the fluctuating fluid forces, L and D_f. The transverse and in-line motions are typically represented as phase shifted sinusoids, as in equations 2.15 and 2.16.

$$m_y\ddot{y} + b_y\dot{y} + k_y y = L \tag{2.13}$$

$$m_x\ddot{x} + b_x\dot{x} + k_x y = D_f \tag{2.14}$$

$$y = A_y sin(\omega t) \tag{2.15}$$

$$x = A_x sin(2\omega t + \theta) \tag{2.16}$$

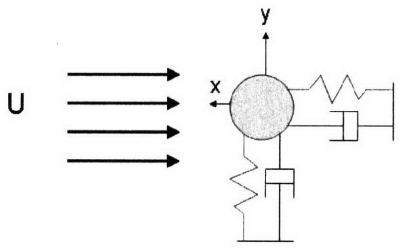

Figure 2-4: Two degree of freedom spring-mass-dashpot cylinder in a uniform free stream.

In these equations, the value θ is the phase between in-line and cross-flow motion

in accordance with the definitions of Jauvtis and Williamson [30]. The same value for Aronsen [2] is 180 degrees out of phase due to subtraction of the phase in equation 2.16 as opposed to addition. The amplitudes and phase between motions are integral non-dimensional parameters for two degree of freedom oscillations. Force parameters for in-line motion are calculated in the exact same fashion as transverse motion except the in-line motion frequencies are used, which are typically twice the transverse frequency. The cylinder directions and orbit shapes resulting from different phase, θ, are shown in Fig. 2-5

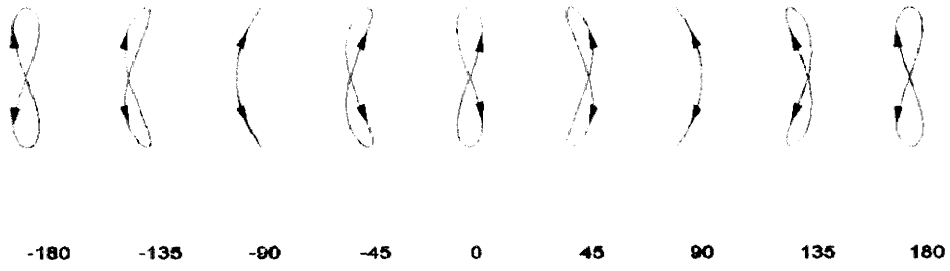

Figure 2-5: Cylinder motions in reference frame fixed to carriage for various phase angles, θ in degrees.

2.3.2 Literature on two degree of freedom rigid cylinder vibrations

An early study by Moe and Wu [42] discusses the forced and free motions of a cylinder in two degrees of freedom, however few results on the topic are reported. The

main observation of this study showed that true reduced velocity must be used as a comparison parameter when comparing free vibrations of the cylinder with forced oscillations of the cylinder.

Sarpkaya [53] discussed possible problems associated with having a cylinder with a natural frequency of in-line motion twice that of the natural frequency in the transverse direction. In this case, resonance of the structure would occur in both directions. In Sarpkaya's [53] study, a variety of in-line to transverse natural frequency ratios were analyzed between values of 1 and 2, however only results from frequency ratios 1 and 2 are reported. In this study, Sarpkaya [53] noted that the transverse oscillation amplitudes were largely different from the free vibrations of a cylinder in one degree of freedom. A natural frequency ratio of 1 resulted in much larger amplitude oscillations of the cylinder, where transverse oscillations of the cylinder were near $A_y/D = 1.2$. When the frequency ratio was increased to 2, the amplitude response displayed two peaks in transverse amplitudes at different reduced velocities. This study is used as model for the formulation of the study in Chapter 3.

In the experiment of Sarpkaya [53], the in-line mass of the system was not equal to the transverse mass of the system and springs were used to tune the natural frequencies to the proper ratio. Jauvtis and Williamson [29, 30] developed a system with equal mass ratios in each direction to study the vortex induced vibration of a cylinder in two degree of freedom motion with a natural frequency ratio of one. For high mass ratios in both in-line and transverse directions, Jauvtis and Williamson [29] found that the transverse motions of the cylinder were not largely different from the motions of a cylinder oscillating with cross-flow motion only. When the mass ratio was reduced to values comparable with ocean structures, Jauvtis and Williamson [30] observed very large amplitudes of transverse cylinder oscillations. The largest amplitude oscillations were associated with a 'super upper' branch of motions, where motions were as large as $A_y/D = 1.5$. Additionally, Jauvtis and Williamson [30] noted a significant third harmonic portion of force in lift that they attributed to a specific triplet vortex shedding mode in the wake of the cylinder.

Additional recent studies of free and forced vibrations in two degrees of freedom

have been performed by Aronsen [2]. Aronsen [2] found that the free vibration of a cylinder in combined in-line and cross-flow motion resembles motions observed for vibrating flexible cantilevered beams. Additionally, it is shown that using a strip theory assumption, the two degree of freedom free vibration of a flexible riser may be predicted using coefficients obtained from forced oscillations of the cylinder. Chapter 5 of this thesis describes a similar study. Aronsen [2] also noted third harmonic forces existing in the direction of lift.

2.3.3 Wake behind cylinder in two degree of freedom oscillation

Jeon and Gharib [31] studied visualizations of the wake behind a cylinder oscillating in two degrees of freedom by forcing the cylinder with particular motions and observing the wake formations behind the cylinder. Phases between in-line and transverse motions were varied between -45 degrees and 45 degrees based on observations of free vibrations. Transverse amplitudes were limited to 0.5 diameters. Jeon and Gharib [31] found that the phase between in-line and transverse motions can effectively delay the onset of a '2P' pattern in the wake of the cylinder as reduced velocity increases. The relatively small amplitudes of motion in this study resulted in the observation of wakes very similar to those observed for one degree of freedom oscillations.

For the large transverse motions observed by Jauvtis and Williamson [30], a '2T' pattern of two triplets of vortices forming per cycle of motion was noted [75, 30]. The observed third harmonic forces were attributed to the presence of vortex triplets in the wake of the cylinder, as illustrated through an energy transfer argument. Fluid forces calculated from the wake were used to establish how energy transfer from the wake resulted in cylinder excitation. The triplet wake was only observed for very large transverse motions of the cylinder. The large accelerations of the cylinder in its extreme cross-flow motion caused an additional vortex to shed during half of a typical '2P' shedding cycle.

Aronsen [2] shows visualizations of a cylinder forced with extremely different

phased motions at phases of 0 degrees and 180 degrees. The observed wake behind the cylinder indicates a narrower wake or different numbers of vortices shed depending on the direction of cylinder motion.

Chapter 3

Free Vibration with Combined Cross-flow and In-line Motion

The free vibration of a rigid cylinder in a uniform flow acts as a fundamental experiment for understanding the forces and motions associated with bluff-body, fluid-structure interactions. A free vibration experiment allows for observations of the physical vibrations of a system undergoing VIV, where observed measurements of motion response and forces can be taken while the fluid flow remains virtually two dimensional with respect to the cross-sectional shape the cylinder. The oscillation of the cylinder in these experiments is not a true free vibration in the sense that it oscillates in the absence of an external forcing function. Free vibration refers to the self-excited oscillation of a cylinder in free stream due to instability of the flow, as opposed to forced oscillations, where the path of the cylinder through the fluid is a prescribed motion, independent of fluid forces. The term 'free vibration' is commonly accepted nomenclature and will be used throughout this text.

In the experiments described in this chapter, the experimental focus was on seeing the effects of combined in-line and transverse motions on the response and forces of an elastically mounted circular cylinder in a free stream. The condition of dual resonance, where excitation of the structural natural frequencies in both in-line and transverse directions is addressed. Experiments are performed with similarities to ocean structures in mind, hence mass ratio and structural damping are low. The

experiments were performed with the following particular questions in mind:

1. How do in-line motions affect the amplitude of cross-flow response and measured lift and drag forces?

2. How does the in-line to transverse natural frequency ratio, f_{nx}/f_{ny}, affect the response of the cylinder and measured lift and drag forces?

3. How does excitation at the in-line and transverse effective natural frequencies affect cylinder response and forces?

3.1 Experiment Motivation

Long marine risers can be modeled as a long beam under tension. Equation 3.1, shows the equation for the natural frequencies of a simply supported beam under tension, where n is the mode, E is the modulus of elasticity of the beam, I is the area moment of inertia of the beam cross section, L is the beam length, T is the tension force in the beam, and M is the mass per unit length of the beam.

$$f_{tensioned-beam} = \sqrt{\frac{n^4\pi^2 EI}{4L^4M} + \frac{Tn^2}{4L^2M}} \tag{3.1}$$

The tension experienced by marine risers is primarily due to the weight of riser material, hence in shallow water, tension forces in the riser will be smaller compared with tension forces for a deep water riser of comparable geometric and material characteristics. In either shallow or deep water, bending stiffness will be comparable for equivalent geometric and material characteristics. Short risers typically display dynamic behavior similar to a beam. In shallow water, the restoring forces due to bending are large compared with the restoring force due to tension in the beam. In the extreme case, if we drive $T = 0$ from equation 3.1, we see that we are left with the natural frequencies of a simply supported beam (see equation 3.2).

$$f_{beam} = \frac{n^2\pi}{2}\sqrt{\frac{EI}{L^4M}} \tag{3.2}$$

Since vortex shedding causes an excitation force at one times the fundamental frequency to occur in the lift direction and two times the fundamental frequency to occur in the drag direction, one may be concerned with a situation where the beam has an in-line to transverse natural frequency ratio of 2:1. In the case of a bending dominated system with rotationally symmetric geometry (circular cylinder), this ratio of natural frequencies would be difficult to achieve because of the n^2 relationship between modal frequencies. The beam tends to respond with a natural frequency ratio of 1:1 in this case.

In the case of a very long riser, restoring forces due to tension are much larger compared with restoring forces due to bending stiffness. In the extreme case, the bending stiffness becomes negligible and equation 3.1 reduces to equation 3.3, the equation for the natural frequencies of a string under tension.

$$f_{string} = \frac{n}{2L}\sqrt{\frac{T}{M}} \tag{3.3}$$

In the case of the string, the natural frequencies are no longer a function of the beam geometry, but merely the tension, length, and mass properties of the string. If one considers a string of infinite length, then there are an infinite number of natural frequencies for the string, meaning that any given point along the string will have an in-line to transverse natural frequency ratio of 2:1 due to the factor n modal relationship of natural frequencies. In fact, any given point along the infinite string will have any natural frequency ratio, even intermediate values between 1 and 2. For a very long string, such as a long riser, there is a high probability that any given point will have a natural frequency ratio of 2 and vortex shedding may excite the natural frequency of the structure in both in-line and transverse directions. Fig. 3-1 shows a schematic of a beam under tension with 2:1 in-line to transverse natural frequency ratio along the length, where the beam under tension is excited in the first mode transverse to the flow and in the second mode in-line with the flow.

For a real riser, the natural frequencies will lie somewhere between the beam and string natural frequency as in equation 3.1. It is therefore relevant to know how the

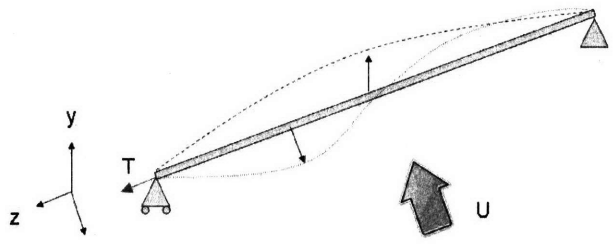

Figure 3-1: Schematic of beam under tension in a uniform flow, with excitation of the first mode transverse to the flow and the second mode in-line with the flow. The natural frequency ratio in this case will be 2.

riser will behave under conditions where the ratio of in-line to transverse natural frequencies takes on values between 1 (beam) and 2 (string). This is accomplished by constructing a rigid cylinder test apparatus where the cylinder is allowed to move in two degrees of freedom (in-line and transverse to the flow) and the natural frequency in each direction can be tuned independently.

3.2 Free Vibration Experimental Apparatus

The free vibration experimental apparatus is referred to as the Spring Cylinder Rig (SCR) and mounts to the main carriage in the MIT Towing Tank. The Towing Tank is 2.4 m wide, 1.2 m deep, and has a testing length of 22.5 m. The testing rig was designed to have lightweight parts in order to minimize the moving mass of the vibrating system (minimize mass ratio) and to ease in assembly. The original design of the SCR was made by Justin Harper and many components have since been modified

to make a working apparatus. The apparatus as it exists now, is constructed of five sections: support structure, guide railing assembly, test cylinder assembly, spring bank, linear motors. Figure 3-2 shows a picture of the complete SCR assembly in the towing tank.

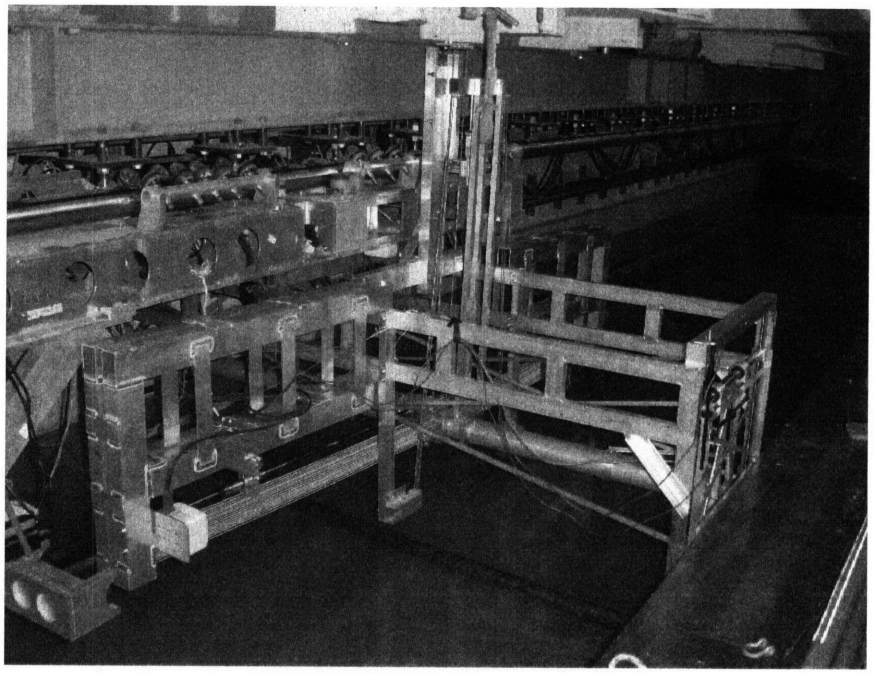

Figure 3-2: Free Vibration Experimental Apparatus - Spring Cylinder Rig

3.2.1 Support Structure

The support structure of the SCR consists of two aluminum clamps, two longitudinal beams, and two transverse beams. The aluminum clamps mount to the box beam on the towing tank carriage. Two longitudinal beams running along the length of the tank connect to the clamps, providing supports for the rest of the SCR. The two transverse beams connect below the longitudinal beams, creating an H-shape. The transverse beams act as the main structural components for supporting the spring

banks and guide railing assemblies. The support structure can be seem mounted to the carriage in Figure 3-2.

3.2.2 Guide Railing Assembly

The guide railing assembly consists of eight linear roller bearings, shafting for the roller bearings and structural supports. There is one guide bearing assembly on each side of towing tank width. The guide bearing assemblies connect to the transverse structural beams to form a rectangular box that spans the width of the tank. An individual guide bearing assembly has four vertical linear roller bearings that ride on two vertical shafts. An outer framework connects the vertical roller bearings so they can move as a unit. This framework must be accurately aligned and tightened to minimize friction in the system due to misalignment of the bearings. A small framework consisting of four horizontal roller bearings rides on the vertical bearing framework. The resulting assembly allows motion in the vertical (cross-flow) and horizontal (in-line) directions. Once an individual guide railing assembly has been aligned properly and installed, the assemblies on each side of the tank must be connected to ensure that both sides of the test apparatus move as a unit. Small, angled cross bracing is used to connect the vertical bearings on opposite sides of the tank. This allows both guide railing assemblies to move in unison. Figure 3-3 shows an individual guide railing assembly.

Since the horizontal bearings of the guide railing assembly ride on the vertical bearings, the moving masses in the vertical and horizontal directions are slightly different. This causes the mass ratios in the cross-flow and in-line directions to be slightly different. This differs from the experiments of Jauvtis and Williamson [30], where the in-line and transverse masses and damping were exactly the same. The consequences of unequal mass ratios will be addressed in Chapter 5.

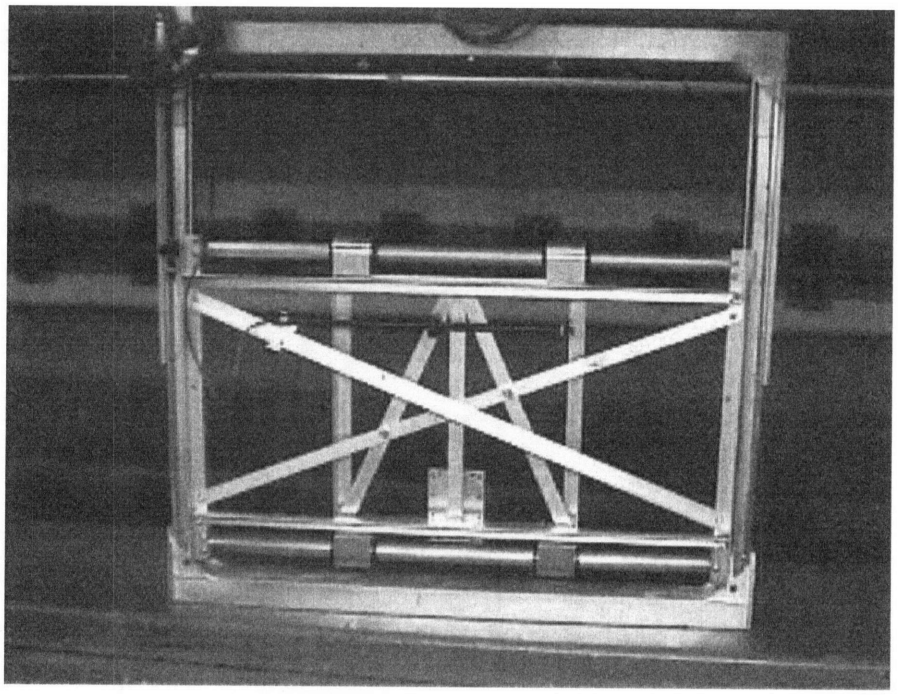

Figure 3-3: Individual guide railing assembly. In-line (horizontal) bearing assembly rides on the cross-flow (vertical) bearing assembly.

3.2.3 Test Cylinder Assembly

The test cylinder used in free vibration experiments had a diameter of 76.2 mm (3 in) resulting in a blockage ratio of 4.5 percent when installed in the tank. The cylinder is smooth aluminum tubing with end caps to prevent flooding of the cylinder. The test cylinder connects to two vertical spars that pierce the surface of the water. The vertical spars connect to the guide bearing assembly and are supported by a structural aluminum tube that spans the width of the tank. A schematic of the test cylinder assembly is shown in Figure 3-4. Pieces of aluminum bracing connect the guide bearing assembly to the structural tubing of the test cylinder assembly in order to help the test cylinder move as a unit along the guide bearings for in-line motion.

Hard plastic endplates are attached to the ends of the test cylinder in order to keep

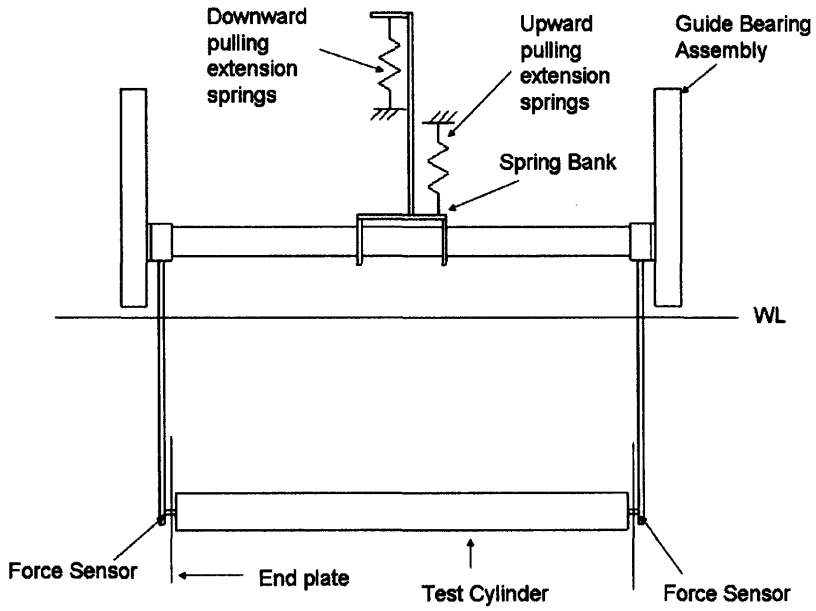

Figure 3-4: Test cylinder assembly.

the flow across the test cylinder two dimensional [58]. The endplates are attached to the vertical spars so that forces on the endplates are not measured. In order to reach high natural frequency ratios with the test apparatus, buoyancy plates are necessary to offset the weight of the test structure. These foam buoyancy plates connect to the outside of the endplates. The buoyancy plates are made of smooth, streamlined, shaped foam in order to minimize fluid damping effects from the buoyancy plates. The buoyancy plates were only used for frequency ratios of 1.67 and 1.9.

Two piezoelectric Kistler force sensors were located at the ends of the cylinder between the vertical spars and the test cylinder. The endplates were mounted to the vertical spar, such that forces on the end plates would not be measured with forces on the cylinder. The force sensors were aligned for measuring lift and drag on the cylinder.

Kistler Calibration

Calibration in lift was performed by directly hanging weights on the test cylinder at the location of each force sensor on each side of the cylinder. Calibration coefficients

were obtained by linearly fitting the measured voltage versus the applied force. In the drag direction, a pulley system located 5 m downstream of the cylinder was used to apply a force in the drag direction. Again, forces were applied individually to each side of the cylinder to obtain an accurate calibration of each sensor. Calibration of the force sensors was performed before and after every set of tests each day that testing was performed to ensure regularity in the sensor measurements. Figure 3-5 shows the linear calibration line for an example calibration of the drag direction. One can see that the calibration is very linear. A calibration file (calib.mat) is located with each set of the raw data located on the Tow Tank server.

The Kistler force sensors used in this experiment had some problems associated with proper sensor connection and flooding in the actual sensor. In most test cases, noise caused by these issues resulted in improper force measurements on one side of the cylinder. The forces reported in this thesis are therefore only comprised from force measurements from one force sensor and forces are normalized by half the cylinder span. This results in a potential increased error in actual force measurement and an inability to calculate a correlation between force measurements.

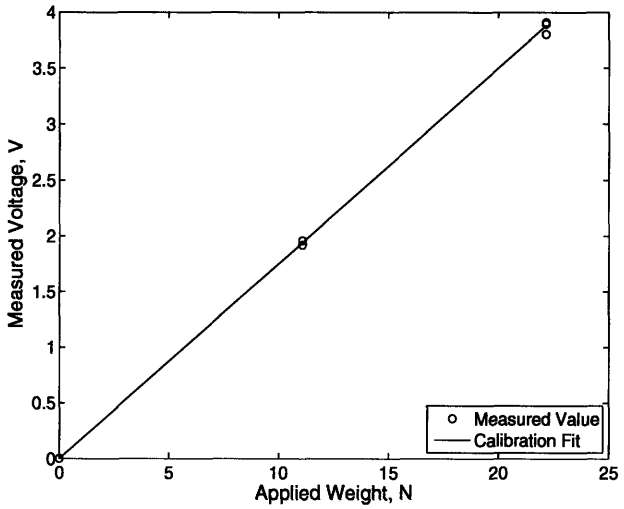

Figure 3-5: Sample calibration of the drag direction. Shows the application of three forces repeated three times. Sensor is repeatable and voltage output increases linearly with increased force.

3.2.4 Spring Bank

The spring bank acts as a central point for which all springs and linear motors connect to the test apparatus. The spring bank is located at the center of the structural tube of the test cylinder apparatus so that all spring forces and linear motor forces are applied at virtually the same point. This balances the forces exerted on the guide bearings, keeping the system from locking when in motion. The spring bank is shown in Figure 3-6. Small extension springs are used to set the natural frequency of the structure in each direction. The extension springs allow for small adjustments to the natural frequency of the structure when tuning the system to various natural frequency ratios.

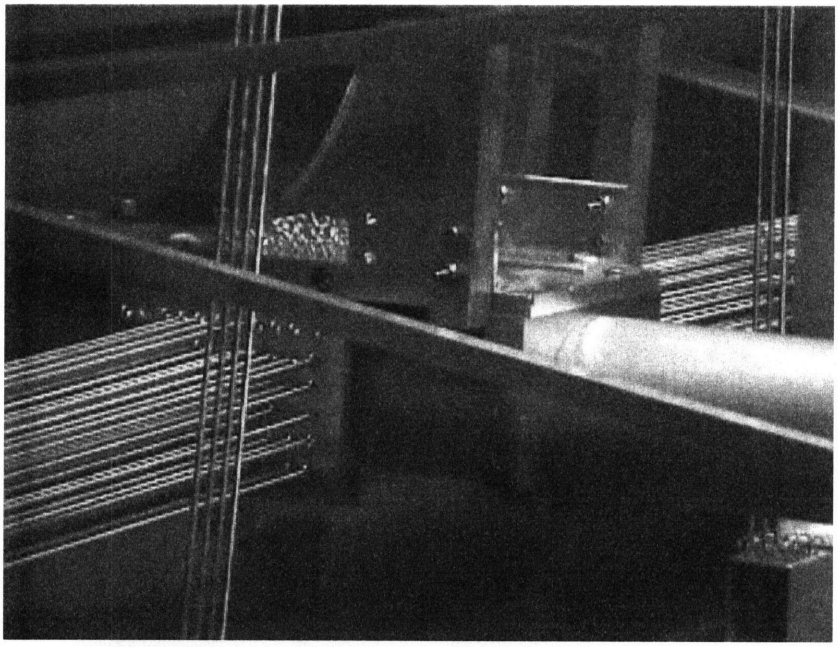

Figure 3-6: Close-up picture of spring bank.

The extension springs have an unstretched length of one meter and a stretched length near 1.3 meters. Since all of the springs are connected to the spring bank

at the same point, the spring constants in the transverse and in-line directions are lightly coupled, i.e. deflections in the in-line direction will cause changes in the spring constant of the transverse direction. Making the spring length as long as possible reduces the coupling effect between directions. At the lowest spring constant used, the spring constant in the transverse or in-line direction changes by less than 5 percent of the linear value. This translates to less than 2 percent change in the natural frequency of the system.

The in-line extension springs are attached to welded aluminum arms that stretch forward and behind the test apparatus. These in-line springs must be adjusted such that the cylinder is aligned in the center of the guide bearing assembly under the mean drag forces when the cylinder is being towed. This position is dependent on the in-line stiffness of the system. Transverse extension springs help offset the weight of the structure or pull the structure down to center the cylinder. The extension springs that oppose gravity are attached to a stationary vertical arm that extends above the test apparatus, and directly connects to the spring bank. Extension springs that pull the cylinder down are attached to stationary arms extending just above the surface of the water. These springs attach to a tall vertical arm that is connected to the moving portion of the apparatus such that a down force is applied by extending these springs. The in-line and transverse springs are shown in Fig. 3-2.

3.2.5 Linear Motors

The linear bearings in the guide railing system exhibit a large amount of non-linear damping due to friction in the bearings and small misalignment between the bearings over the large span of the tank. When perturbed in air, the spring-mass system in the transverse direction typically has a linear damping ratio between 6 and 8 percent. This damping ratio is very large compared with typical damping ratios for ocean structures (less than 1 percent), so linear motors were added to help cancel structural damping in the system.

The linear motors used in this experiment were Linmot model PS01 23x80 motors. Two motors were used, one in the transverse direction and one in the in-line direction,

with each motor fixed 1 m from the spring bank. The linear motors were attached to the spring bank with long, lightweight, carbon fiber tubes such that damping correction forces would be stiffly transmitted to the spring bank. The motors were mounted on pivoting hinges to allow for the motion of the cylinder and were located as far from the spring bank as possible in order to limit coupling between in-line and transverse damping corrections.

The actual damping force in the bearings is difficult to measure because it changes with time, system use, and system setup. The true damping forces in the bearings are caused by both dynamic and static friction components that change depending on the alignment of the actual rolling balls in each bearing along with the dynamic position of the system itself. A simplified predictive damping force model was used for estimating the damping to produce a motor force output. The damping force models for the transverse (y-direction) and in-line (x-direction) motions were as follows, where $F_{y-motor}$ is the transverse motor force, and $F_{x-motor}$ is the in-line motor force:

$$F_{y-motor} = C_1\dot{y} + C_2 sgn(\dot{y})|\dot{y}|^p \tag{3.4}$$

$$F_{x-motor} = C_3\dot{x} + C_4 sgn(\dot{x})|\dot{x}|^p \tag{3.5}$$

C_1 and C_3 are gains for countering the linear damping in the system, which is primarily due to flexing structural components in the bearings. C_2 and C_4 are gains for countering the non-linear damping in the system. This portion of the motor force is modeled as Coulomb damping, where there is a constant force opposing the direction of motion. This friction is apparent in the bearings where there is surface contact between the bearing rollers and the rails. The constant p is a number less than 0.5, which determines the smoothness of the function's transition through zero velocity. The velocity of the cylinder was measured in the transverse and in-line directions using linear velocity transducers. Conservative values for motor gains were chosen to avoid pumping too much energy into the system, resulting in negative damping.

Determining Damping

Since the cylinder must remain centered on the railing system in order to properly run experiments, the natural frequency of the system must be determined with the test cylinder immersed in water. In order to determine the natural frequency of the system, the cylinder is perturbed to a large amplitude and allowed to oscillate freely. The position of the cylinder is measured, resulting in a decaying amplitude oscillation. Determining the logarithmic decrement of the decaying amplitude, allows one to estimate a value for the linear damping in the system [50]. The damping ratio can be determined from consecutive cycles in the decaying oscillation, such that a damping ratio can be found for each cycle of oscillation of the cylinder. In the case of perfectly linear damping, the damping ratio will be equal for every cylinder oscillation. Non-linear damping will cause the damping ratio to change as a function of the oscillation amplitude.

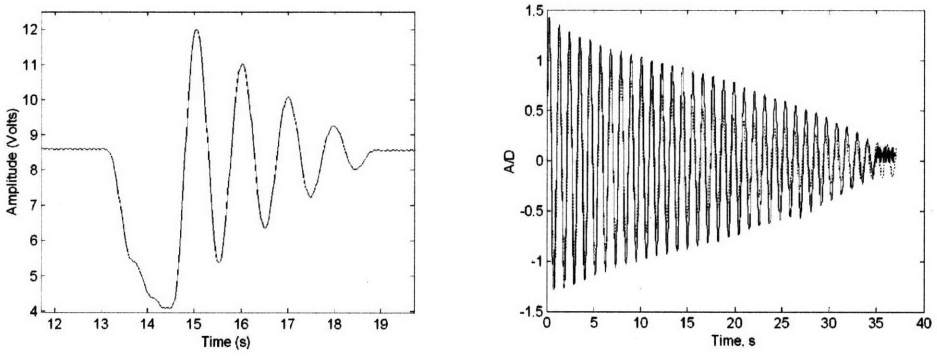

(a) Without Linear Motor (b) With Linear Motor

Figure 3-7: Pluck tests showing improved low damping response of the system with the linear motor attached. Case (a) is performed without a linear motor attached. Case (b) - solid line indicates case with linear motor attached, dotted line indicates analytic solution to the single degree of freedom spring-mass-dashpot equation with one percent damping ratio.

Two example pluck tests are shown in Fig. 3-7 a and b. The first figure shows an example pluck test with damping ratios between 6 and 8 percent depending on the oscillation amplitude. In this case, the linear motors are not attached and the damping is much too high for performing experiments. In Fig. 3-7 b, a linear motor

has been attached and the damping ratio has been decreased to roughly one percent for amplitudes greater than 0.4 cylinder diameters. The solid line shows the measured cylinder motions, while the dotted line indicates the analytic solution of a linear system with equivalent linear damping of one percent. The two curves are similar for high amplitude motions, but as the amplitude of motions decreases, the actual system reaches a point where static friction forces are too strong and the system comes to rest. Figure 3-8 shows the damping ratio as a function of amplitude in this case. One can see how the computed linear damping ratio increases as the amplitude of motion becomes small. Figure 3-9 shows a similar trend with both in-line and transverse linear motors attached. Because of this trend, the damping for a given run is defined as the average value of the cyclically computed damping. The dotted line in Figure 3-9 indicates this average damping value for the particular arrangement of springs.

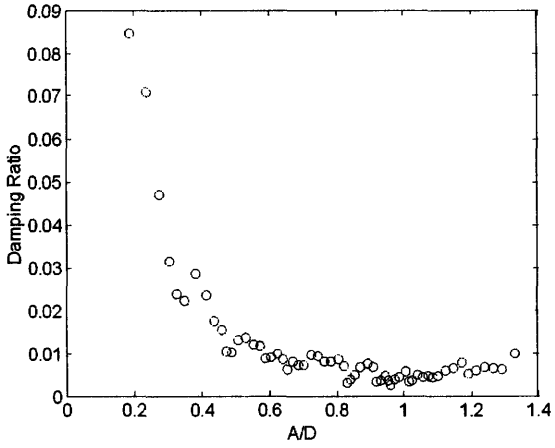

Figure 3-8: Damping ratio as a function of oscillation amplitude for freely vibrating transverse motions. In-line direction is fixed (uncoupled)

3.2.6 Test matrix

The system was tuned to six different frequency ratios and towed at nominal reduced velocities between 3 and 12. The frequency ratio is defined as the ratio between the in-line natural frequency and the transverse natural frequency. For each frequency ratio, a stiffness test was performed to determine the spring constant in each direction.

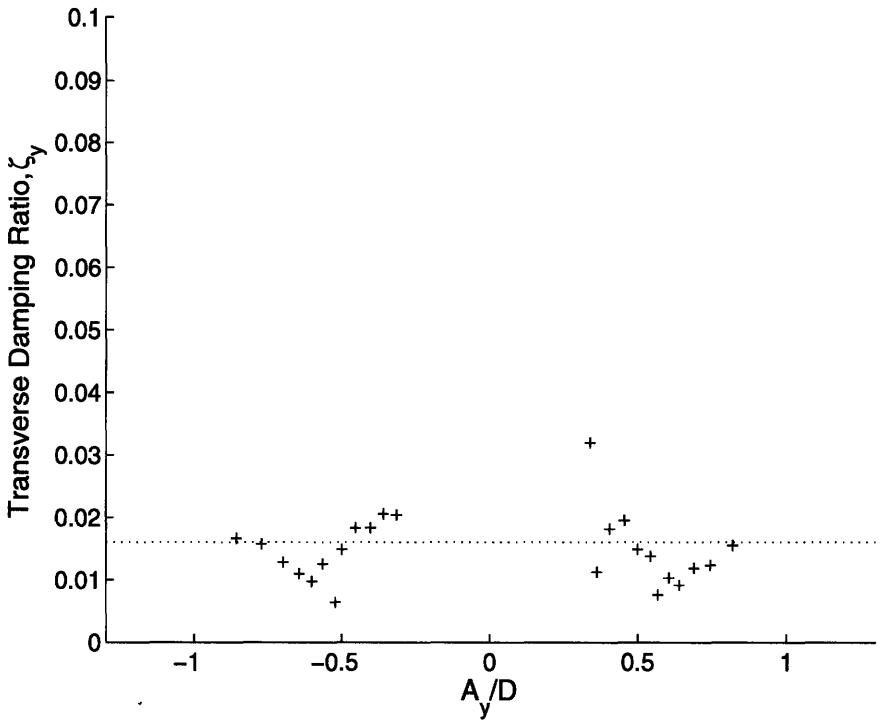

Figure 3-9: Damping ratio as a function of oscillation amplitude for freely vibrating transverse motions. In-line direction is not fixed. Nominal natural frequency ratio is 1.52. Dotted line indicates the average value of damping ratio.

The moving mass in each direction was calculated from the stiffness and frequency in each direction. Damping in still water was also determined from pluck tests. The structural characteristics for each frequency ratio are shown in Table 3.2.6, where f_{ny} is the transverse natural frequency, ζ_y is the mean transverse damping, ζ_x is the mean in-line damping, m_y^* is the transverse mass ratio, m_x^* is the in-line mass ratio, and $m_y^*\zeta_y$ is the mass-damping parameter.

3.3 Free vibration test results

3.3.1 Validation of Test Method - 1 DOF

In order to validate the method for using linear motors to cancel damping in the system, a set of one degree of freedom free vibration experiments is performed and compared with results from Smogeli [57] and Khalak and Williamson [34]. Nominal

Ratio	f_{ny} (Hz)	ζ_y (%)	ζ_x (%)	m_y^*	m_x^*	$m_y^*\zeta_y$
1.00	0.715	2.2	2.2	3.8	3.3	0.084
1.22	0.799	1.3	1.7	3.9	3.8	0.051
1.37	0.894	1.1	2.5	3.9	3.7	0.043
1.52	0.977	1.6	3.2	4.0	3.6	0.064
1.67	0.698	2.6	2.9	5.5	5.3	0.14
1.90	0.704	6.2	2.5	5.7	5.0	0.35

Table 3.1: Tuned natural frequencies, damping, and mass characteristics

reduced velocity is varied from 3 to 17. The mass ratio is 3 and the damping for the system is less than one percent for transverse non-dimensional amplitude greater than 0.4 (see Figure 3-8). The Reynolds number in the present study and Smogeli experiment are comparable since both tests were performed in the MIT Towing Tank with comparable speeds and equivalent cylinder diameter (Re ranges from 15,000 to 45,000). Figure 3-10 shows the resulting curve of transverse amplitude as a function of nominal reduced velocity for the three experiments.

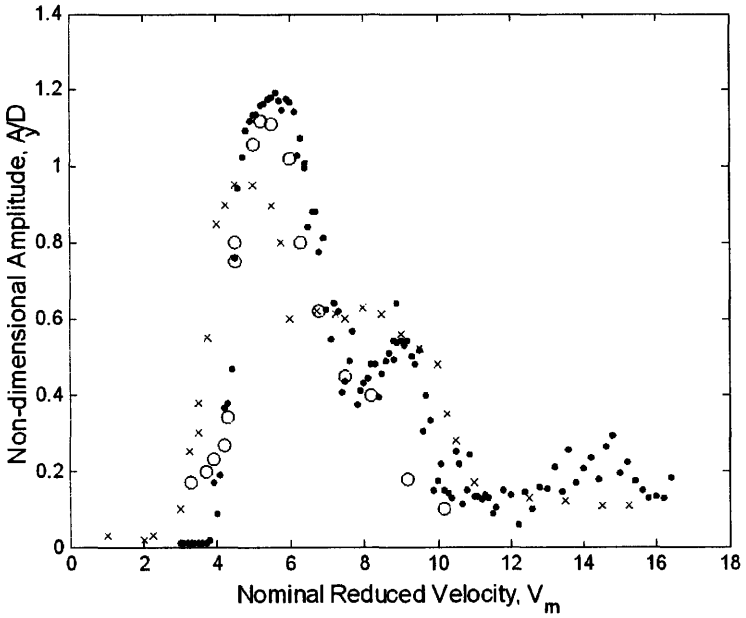

Figure 3-10: Transverse amplitudes from one degree of freedom oscillations. • - present study, o - Smogeli [57], x - Khalak and Williamson [34]

The response compares well with Smogeli's force-feedback experiment over the

lower reduced velocities, although Smogeli's data does not show the plateau in amplitudes that occurs for reduced velocities between 7 and 10 as in Khalak and Williamson [34]. The present study displays this plateau as well, indicating that although the damping is not perfectly linear when corrected with the linear motors, the data is comparable to previous experiments for the range of amplitudes in which damping is shown to be nearly linear. Preceding data is therefore considered useful only for amplitudes above the threshold where the damping is linear. This cutoff occurs in the two degree of freedom experiments for transverse and in-line amplitudes of approximately $A_y/D = 0.3$ and $A_x/D = 0.1$.

3.3.2 Time Traces

The motions and forces associated with these two degree of freedom experiments were fairly regular in amplitude for most cases. For example, beating phenomena which is known to occur at some reduced velocities for a one degree of freedom cylinder were not observed for the two degree of freedom motions. Instead, at low nominal frequency ratio, in-line motions experienced a multiple frequency response.

Fig. 3-11 shows two example cases of the time traces obtained for nominal frequency ratios of 1.0 and 1.9 respectively at nominal reduced velocity of 6.5. Additional time traces are included in Appendix A. Third harmonic forces are clearly evident in the instantaneous lift coefficient measurements.

3.3.3 Motion Amplitudes - 2 DOF

Figure 3-12 shows the peak amplitudes of in-line and transverse motion for varied reduced velocity and varied nominal natural frequency ratio. At a natural frequency ratio of one, the peak amplitudes of transverse motion are very large, peaking with amplitudes in excess of $A_y/D = 1.35$. In this particular experiment, the guide railings had a physical limit of $A_y/D = 1.35$, denoted by the dotted line in Fig. 3-12. For this reason, the amplitude levels out at 1.35. At higher reduced velocity, transverse amplitudes level off at a value near 0.6.

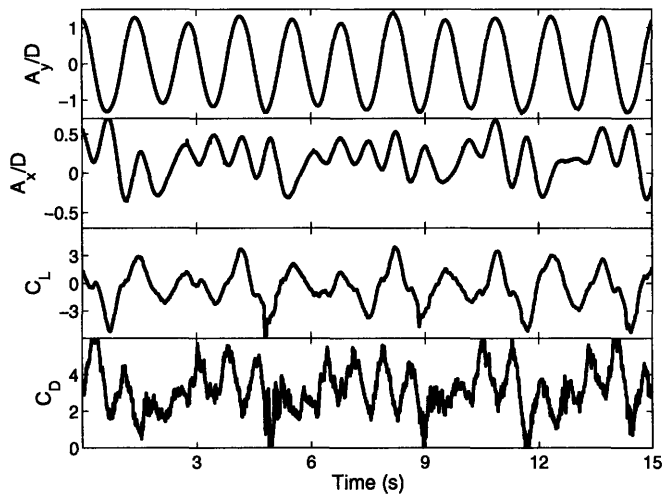

(a) $V_{rn} = 6.5, f_{nx}/f_{ny} = 1.0$

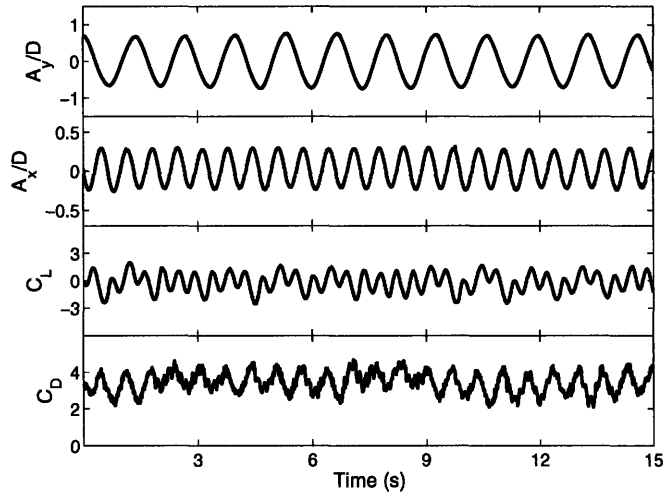

(b) $V_{rn} = 6.5, f_{nx}/f_{ny} = 1.9$

Figure 3-11: Sample time traces from free vibration experiments showing transverse motion, in-line motion, lift coefficient, and drag coefficient.

As the nominal natural frequency ratio increases, the general trend of transverse amplitude stays relatively the same. At low reduced velocity there is little or no transverse motion. As reduced velocity increases, peak amplitudes increase rapidly to a peak value near or in excess of 1.35 diameters. Beyond this peak value at higher reduced velocities, motion amplitudes level off at lower values between 0.5 and 1 diameter of motion. This general trend exists for all nominal frequency ratios except $f_{nx}/f_{ny} = 1.9$, where two distinct peaks in the transverse amplitude curve exist. The

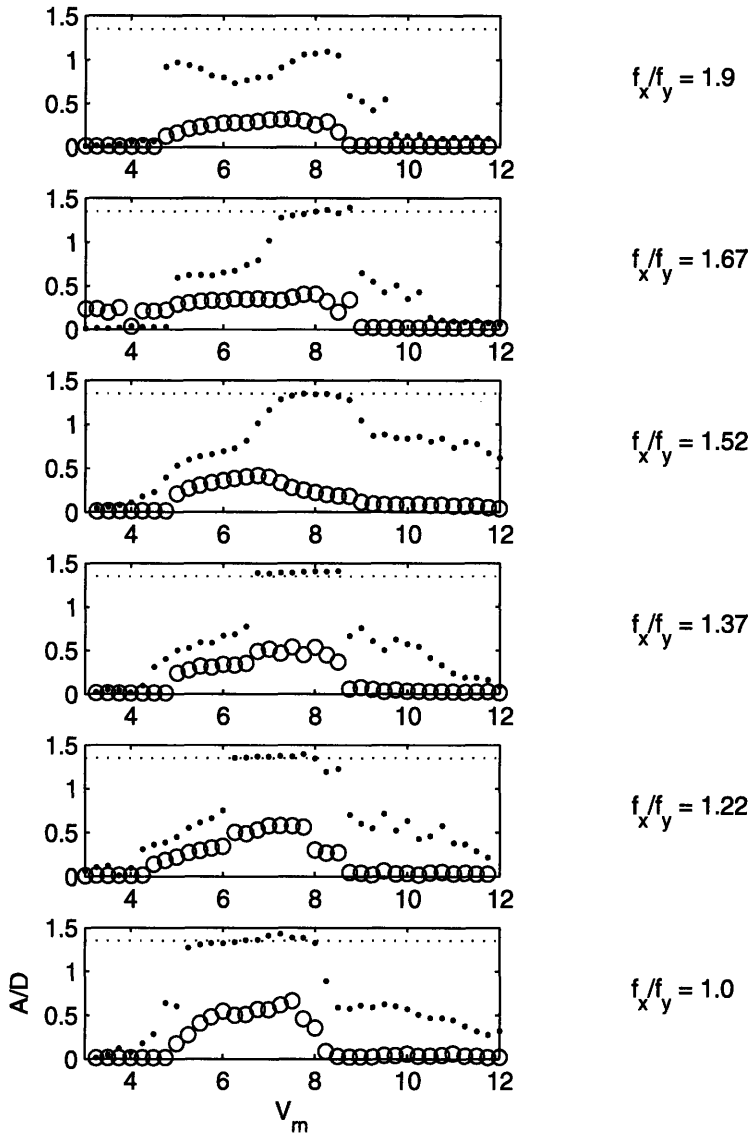

Figure 3-12: Transverse and in-line non-dimensional amplitudes for various nominal natural frequency ratios. • - A_y/D, ○ - A_x/D

slight difference in each of these curves, however, is the reduced velocity at which each peak amplitude exists.

As nominal frequency ratio increases, the maximum amplitude for each curve shifts to higher nominal reduced velocity. For instance, at a nominal frequency ratio of 1, maximum amplitudes of 1.35 diameters are recorded for nominal reduced velocities as low as 5. As the frequency ratio increases to 1.52, the peak amplitude of 1.35 now

occurs at a nominal reduced velocity of 7. At the highest nominal frequency ratio of 1.9, the maximum amplitude near 1.2 diameters occurs at a nominal reduced velocity of 8.

In-line motions of the cylinder were observed to be approximately one-third the size of transverse motions in most cases where there was significant in-line motion; however, in-line oscillations could be as high as half the transverse oscillation amplitude. The maximum value of in-line motion does not always occur at the same reduced velocity as the transverse motion, an observation that was also made by Jauvtis and Williamson [30]. For example, at a nominal frequency ratio of 1.52, maximum in-line motion of 0.5 diameters occurs near a reduced velocity of 6.5, while the maximum transverse motion of 1.35 diameters occurs at a reduced velocity of 7.

Comparison of Motions with Literature

Cylinder motions for $f_{nx}/f_{ny} = 1$ and $f_{nx}/f_{ny} = 1.9$ and compared with the studies of Sarpkaya [53] and Jauvtis and Williamson [30]. Fig. 3-13 shows the comparison for a frequency ratio of 1. The transverse motion amplitude is plotted on the vertical axis, while the parameter $V_r St$ is plotted on the horizontal axis. V_r is the true reduced velocity and St is the Strouhal number for the stationary cylinder in a uniform flow. This parameter is equivalent to the ratio between the vortex shedding frequency and the oscillation frequency of the cylinder. For both the present study and Sarpkaya [53], the mass ratios were slightly different in each direction, while for Jauvtis and Williamson [30], the mass ratio was the same in each direction. For the present study, the Reynolds number ranged from 16,000 to 60,000, while Sarpkaya [53] cites a Reynolds number of 35,000 and Jauvtis and Williamson [30] had a Reynolds number ranging from 7,200 to 15,400. The mass-damping parameter for the present study was 0.084 in this case. Mass-damping was not reported in Sarpkaya [53], while the mass-damping for Jauvtis and Williamson [30] was significantly lower than the present study, with a reported value of 0.0064.

One can see distinct differences between each data set. The present study shows large amplitude transverse motions between $V_r St = 1$ and $V_r St = 1.4$, with the

maximum response occurring near $V_rSt = 1.4$. The study of Sarpkaya [53] has its maximum peak at $V_rSt = 1.4$ as well, however the maximum response for Jauvtis and Williamson [30] occurs at $V_rSt = 1.6$. The relative shape of the present study curve matches well with Jauvtis and Williamson [30], with a distinct upper branch and lower branch of cylinder motions. Mass ratio and added mass play a very important role in the observed response of the system. The difference in the reduced velocity associated with the peak amplitude is due to the different mass characteristics. For instance, Jauvtis and Williamson [30] had precisely the same mass in each direction of motion, meaning that some specific combination of in-line added mass and cross-flow added mass would be necessary to excite the system under lock-in conditions. In the present study and Sarpkaya [53], the mass in each direction was not equal, however changes to the spring constant allowed each direction to have equivalent natural frequencies. This means that a different combination of in-line and transverse added mass would be necessary to drive the system to a lock-in condition in these cases, resulting in a different cylinder response. The wide range of possible two degree of freedom motions is more easily seen in the forced vibration study of Chapter 5.

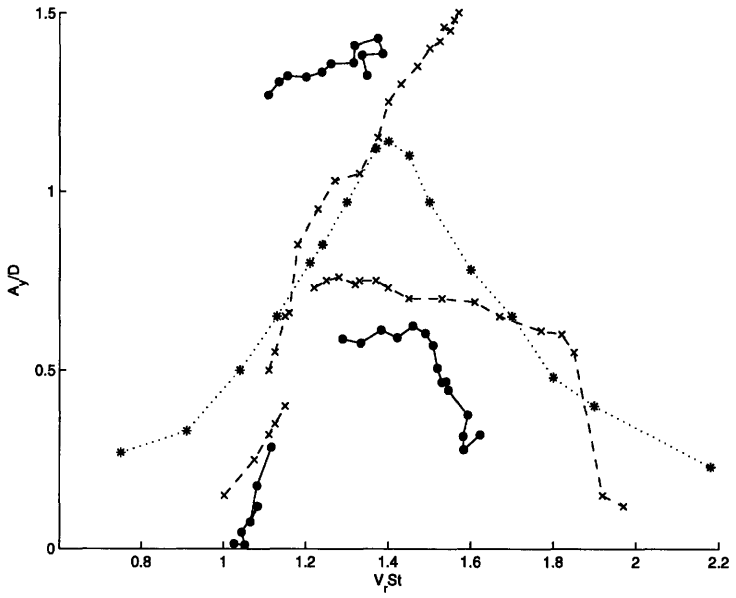

Figure 3-13: Comparison of two degree of freedom motions with 1:1 nominal natural frequency ratio. • - present study, ∗ - Sarpkaya [53], x - Jauvtis and Williamson [30].

Fig. 3-14 shows the present results, for frequency ratio 1.9, compared with the results of Sarpkaya [53], for frequency ratio 2.0. Again, the mass ratios were slightly different in each direction for both sets of experiments. The Reynolds number in the present study ranged from 11,000 to 44,000, while Reynolds number in [53] was 35,000. The mass-damping for the present study was fairly high, with a value of 0.35, while Sarpkaya [53] did not report the mass-damping.

The double peak observed by Sarpkaya [53] is seen in the present study as well, however the range of V_rSt for the present study is much smaller than for Sarpkaya. Amplitudes are larger from the present study due to the small mass ratio and low damping. The results of Sarpkaya tend towards higher amplitudes as V_rSt approaches a values of 2, where in the present study, motions begin to drop off at a value of $V_rSt = 1.4$. Forced motions of the cylinder shown in Chapter 5 will show that both of these transverse motion possibilities are possible for free vibrations dependent on the effective added mass. A direct comparison between the transverse motions of the two experiments may be very different simply based on the structural properties of the experimental apparatus.

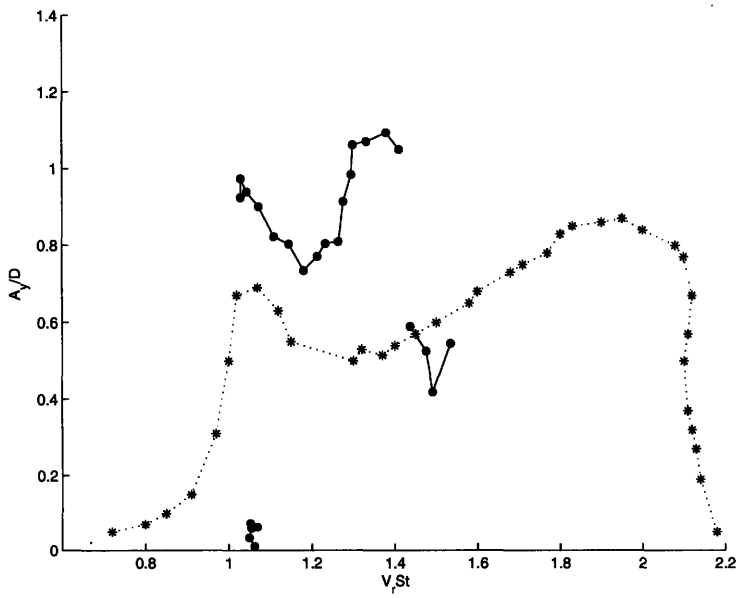

Figure 3-14: Comparison of two degree of freedom motions with 2:1 nominal natural frequency ratio. • - present study (1.9:1), $*$ - Sarpkaya [53] (2:1)

Phase between in-line and transverse motion

The phase between in-line and transverse motion, θ, is defined according to the definition given by Jauvtis and Williamson [30], the same definition given in Chapter 2, Fig. 2-5. The phase θ defines the shape of the cylinder motion for a two degree of freedom motion.

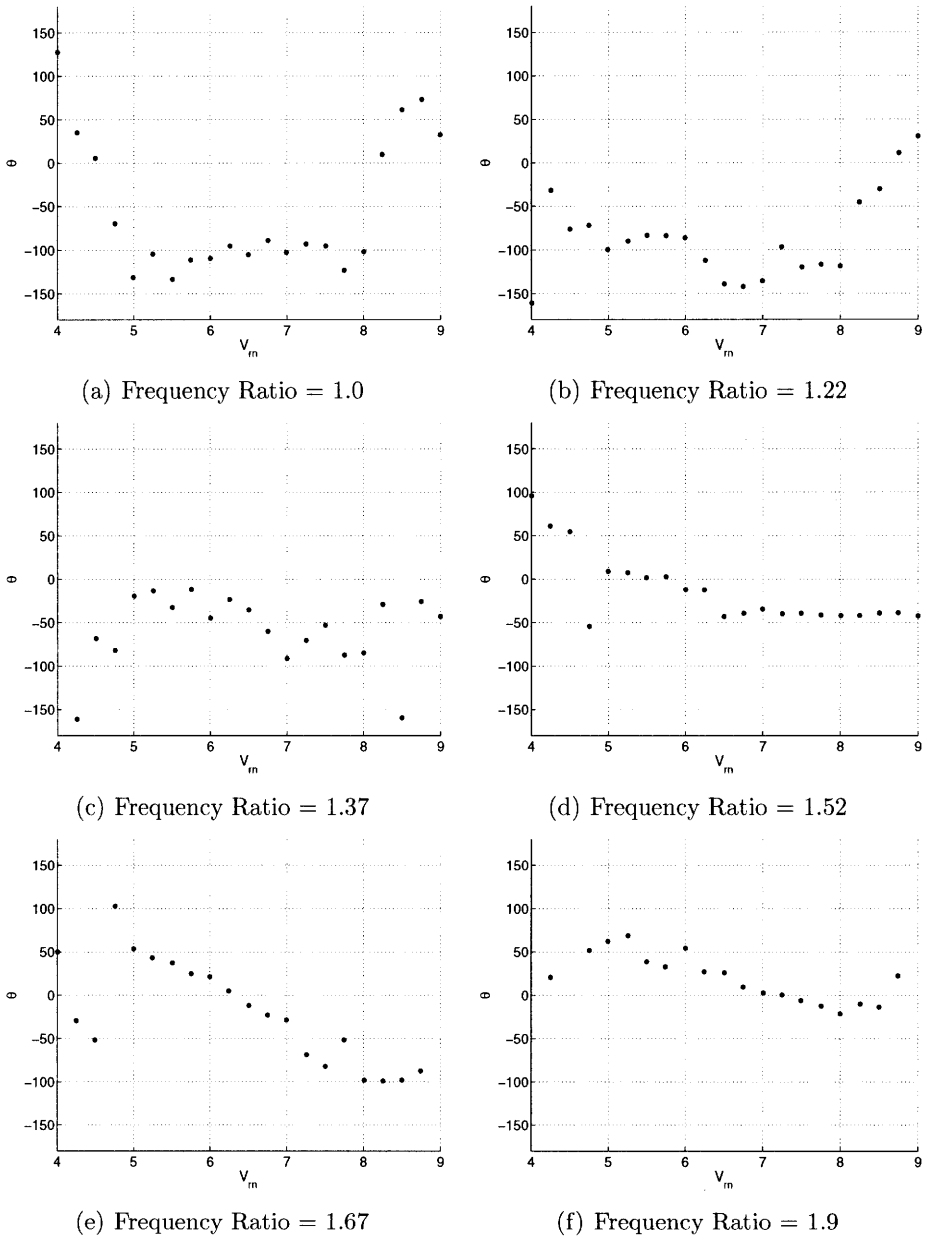

(a) Frequency Ratio = 1.0

(b) Frequency Ratio = 1.22

(c) Frequency Ratio = 1.37

(d) Frequency Ratio = 1.52

(e) Frequency Ratio = 1.67

(f) Frequency Ratio = 1.9

Figure 3-15: Phase angle between in-line motion and transverse motion, θ, in degrees.

The phase between in-line and transverse motion primarily occurs between values of -90 degrees (downstream facing crescent) and 90 degrees (upstream facing crescent) for all nominal natural frequency ratios. At the lower frequency ratios, the phase is near -100 degrees for some motions. When the in-line motion is regular, however, the phase tends to transition almost linearly with increasing reduced velocity. This phase transition results in crescent shapes or figure eights with lobes pointed upstream at low reduced velocity and crescent shapes or lobes pointed downstream at higher reduced velocities. Phases near -90 degrees are consistent with the largest transverse cylinder motions, while phases near 0 degrees are consistent with the largest magnitudes of third harmonic forces as seen in the following section.

3.3.4 Force Measurements

Drag and lift forces are significantly affected by particular cylinder motions as the wake interacts with the cylinder. In one degree of freedom vibrations, the mean drag on the cylinder typically is shown to increase with cylinder motions as the larger cylinder oscillations create a larger wake deficit [18]. In two degree of freedom motions, the mean drag coefficient is still dependent on the transverse motion of the cylinder, however in-line motion can enhance fluctuating drag components or change wake shedding patterns, altering the drag on the cylinder.

Fig. 3-16 shows the mean drag coefficients and fluctuating drag coefficients for the performed free vibration experiments as a function of nominal reduced velocity. The mean drag is slightly larger for lower nominal frequency ratio since transverse amplitudes were larger in these cases. Fluctuating drag coefficients show an interesting trend for a nominal frequency ratio of 1.9. There are two peaks in the amplitude response in this case. The fluctuating drag coefficient also shows two peaks in magnitude corresponding to the transverse amplitude peaks. As the transverse motion increases in this case, the fluctuating drag component increases as well. The mean drag, however, does not follow this trend in this case. As the transverse amplitude peaks at a nominal reduced velocity near 5, the mean drag is increasing, while the fluctuating drag begins to decrease. This same trend occurs for $f_{nx}/f_{ny} = 1.67$.

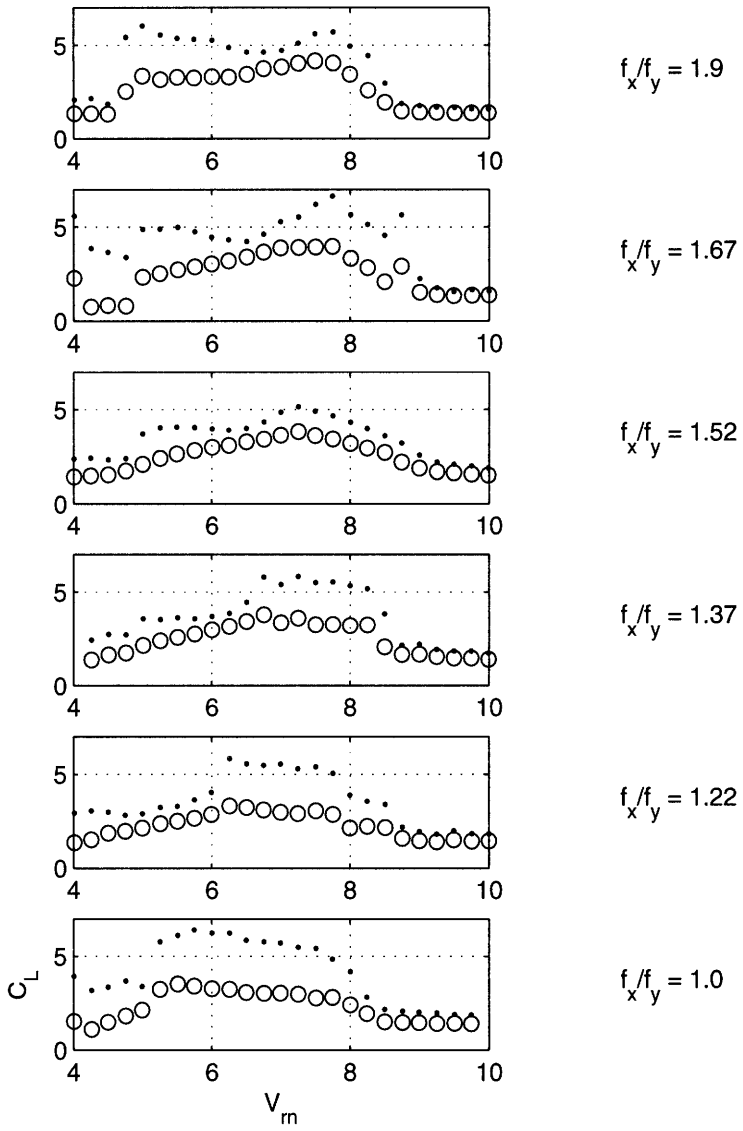

Figure 3-16: Drag coefficient magnitudes for various nominal frequency ratios. ○ - Mean drag, ● - Peak value of drag fluctuation.

Lift forces in one degree of freedom cylinder vibrations are typically treated as single frequency forces since the magnitude of higher harmonic forces are negligible compared to the magnitude of the fundamental frequency component. In two degree of freedom oscillations, significant third harmonic components of force exist, such that it is necessary to report both first harmonic and third harmonic magnitudes of lift coefficient. The root mean square of the first and third harmonic portions of the

lift coefficient signal are calculated as the square root of the area under the individual harmonic spikes in the power spectral density.

Fig. 3-17 shows the magnitudes of first and third harmonic portions of lift for the various nominal frequency ratios. At all frequency ratios, the third harmonic portion of lift coefficient takes on peak values between 1 and 1.5. The maximum value of third harmonic lift increases slightly as nominal frequency ratio increases. The magnitude of the first harmonic portion of lift varies largely with nominal frequency ratio and reduced velocity, however, such that the third harmonic portion of lift is comparatively small for nominal frequency ratios near 1, but very large and possibly dominant for frequency ratios near 2. This finding is a large departure from one degree of freedom cylinder oscillations where higher harmonic forces are typically ignored.

The effective added mass coefficient associated with in-line and transverse motions are shown in Figs. 3-18 and 3-19 respectively. Added mass coefficients are only shown for large amplitude motions (larger than $A/D = 0.2$), since the amplitude of motion appears in the denominator of the added mass calculation and added mass estimates will blow up as motion amplitude goes to zero.

The added mass curves show a similar trend regardless of frequency ratio or direction of motion. At low reduced velocities, the added mass starts with some large value. As reduced velocity increases, the added mass trends nearly linearly towards zero. At high reduced velocity the added mass coefficient levels off at a negative values. An exception occurs for the in-line added mass with a frequency ratio of 1, where the added mass coefficient is nearly always negative. The transition to a negative transverse added mass for a frequency ratio of 1.9 also occurs at a much lower reduced velocity than in other frequency ratio cases.

The wide variation in effective added mass in both in-line and transverse directions illustrates the large excitation region where the wake locks-in to the excitation frequency from equation 2.4. This effective added mass plays an important role in driving the system towards a resonant condition in both the in-line and transverse directions.

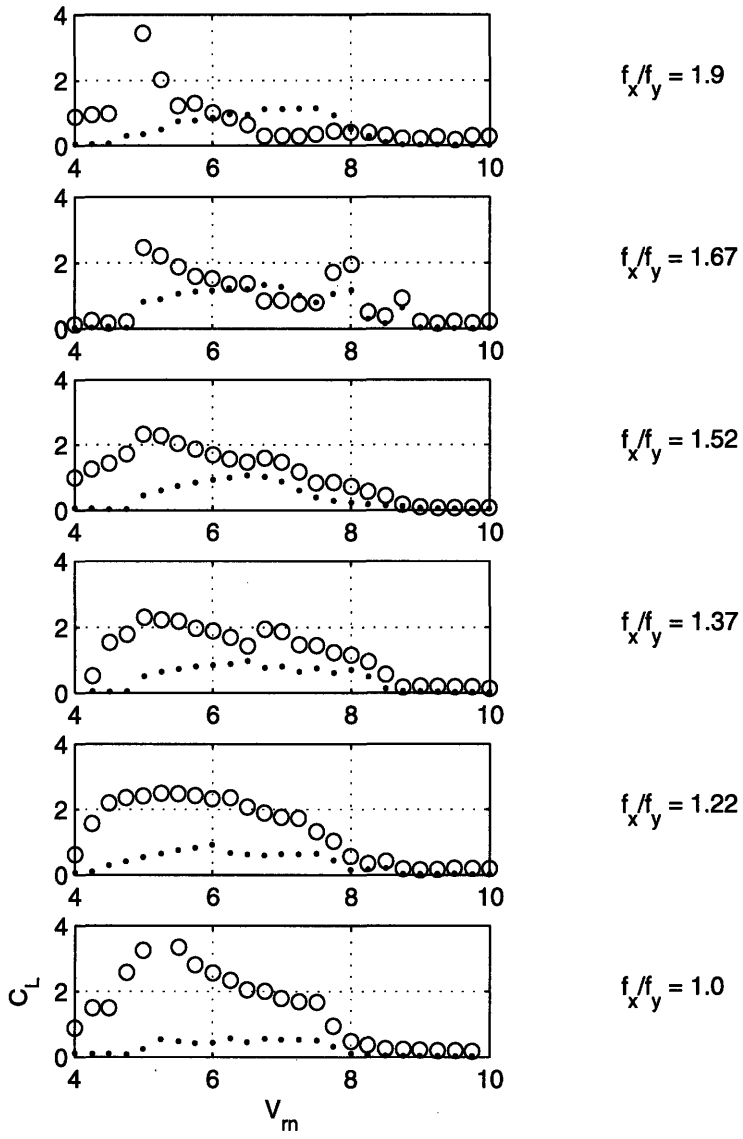

Figure 3-17: Lift coefficient magnitudes for various nominal frequency ratios. o - First harmonic magnitude, • - Third harmonic magnitude.

Phase between force and motion

The phase between force and motion is defined as the phase angle for which the force measurement lags the motion, given that both the force and motion are sinusoidal. In one degree of freedom motions, the phase angle is typically near zero for lightly damped systems at reduced velocities below 6. As reduced velocity increases, the phase angle rapidly switches to 180 degrees as the wake transitions from a '2S' mode

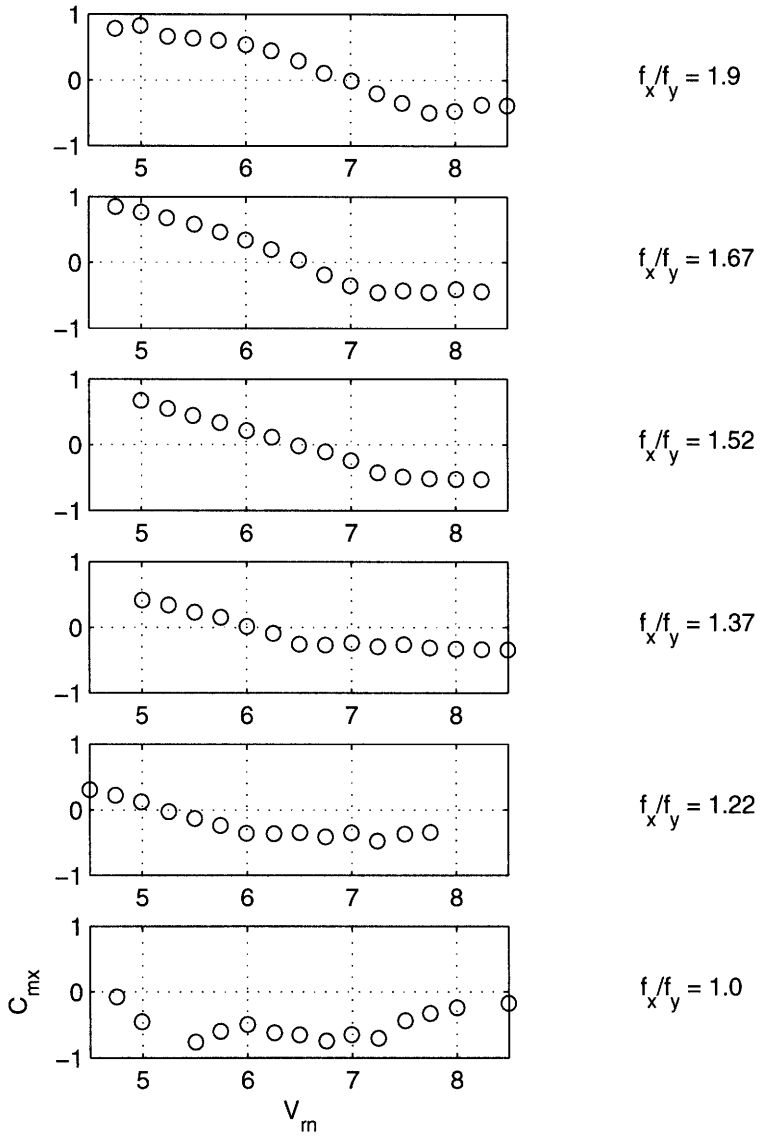

Figure 3-18: In-line added mass coefficient for various nominal frequency ratios.

to a '2P' mode. The counter rotating vortex pairs of the '2P' shedding mode results in a shift in the phase between lift and transverse motion. In the two degree of freedom case, a similar transition occurs, however the particular structural parameters of the system can change the particular wake formation and hence change the reduced velocity for which a phase transition occurs.

Fig. 3-20 shows the calculated phase between the first harmonic portion of lift and the transverse motion. The first harmonic portion of lift is only used for the phase

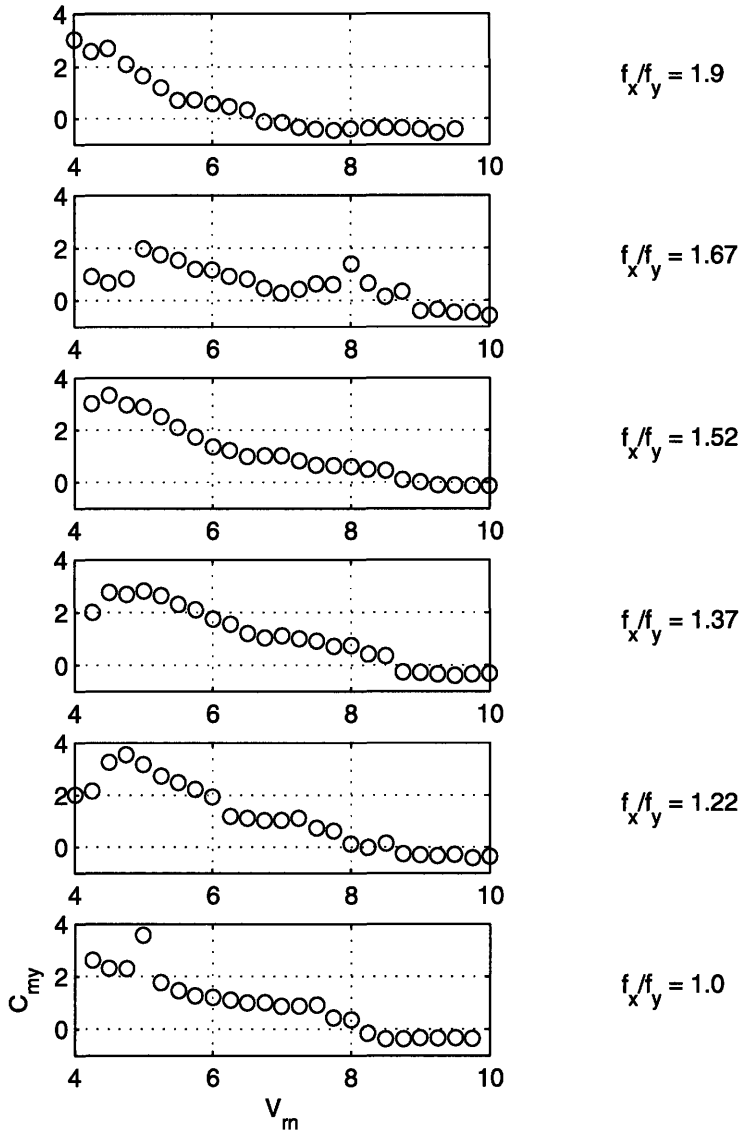

Figure 3-19: Transverse added mass coefficient for various nominal frequency ratios.

calculation since there is no third harmonic motion of the cylinder to reference third harmonic phase. For all frequency ratios below $f_{nx}/f_{ny} = 1.67$, the phase transitions from zero degrees to 180 degrees as in the one degree of freedom case, however, the transition point is shown to occur at higher reduced velocity as nominal frequency ratio increases. For instance, at a frequency ratio of 1.0, the phase transitions near a nominal reduced velocity of 8, and at a frequency ratio of 1.67, the phase transitions near reduced velocity 9. At the highest frequency ratio of 1.9, the system behaves

differently and phase transition occurs earlier. This transition, however is a bit deceptive because the first harmonic portion of lift becomes very small in this region and the third harmonic portion of lift is actually dominant in this region. The phase becomes better established at a reduced velocity of 8 where the lift coefficient is again dominated by the first harmonic.

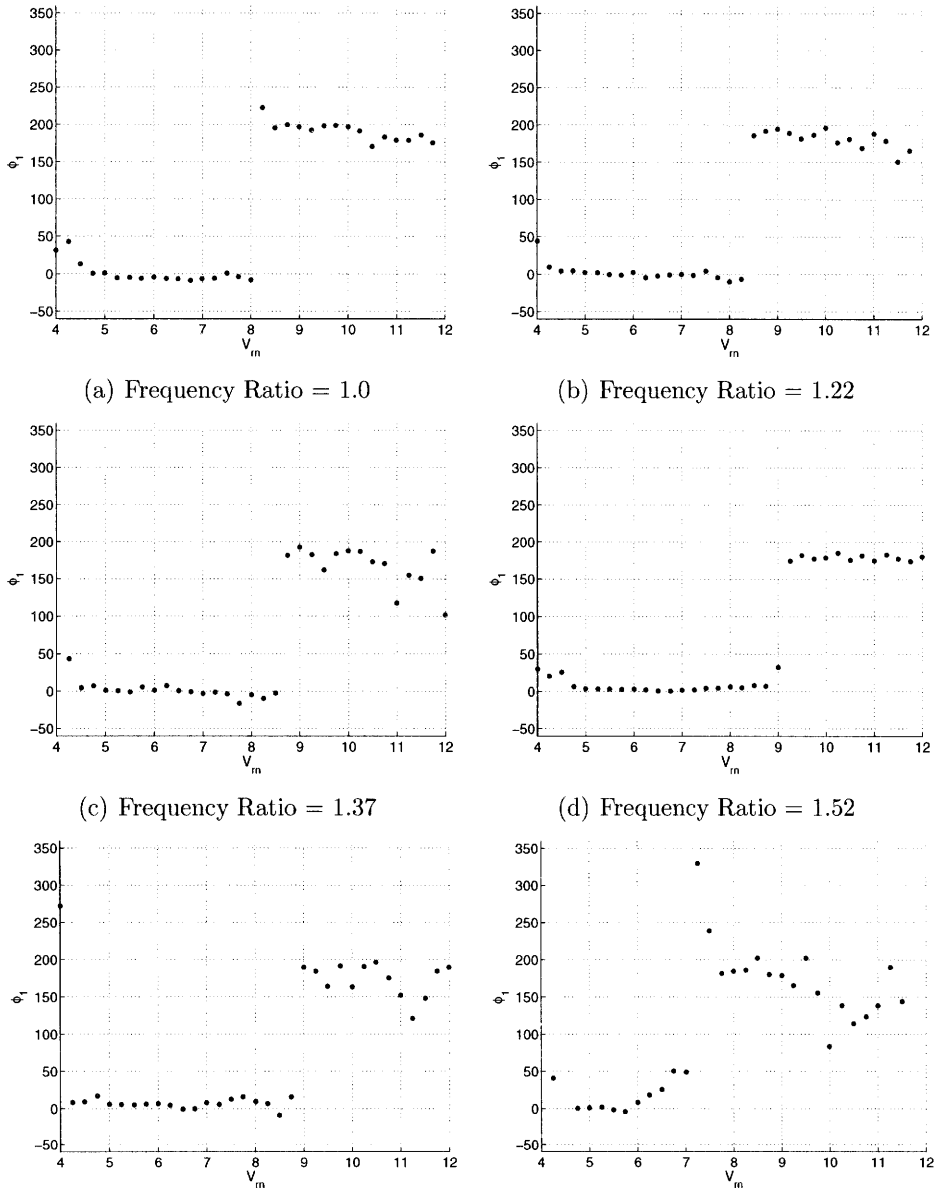

(a) Frequency Ratio = 1.0

(b) Frequency Ratio = 1.22

(c) Frequency Ratio = 1.37

(d) Frequency Ratio = 1.52

(e) Frequency Ratio = 1.67

(f) Frequency Ratio = 1.9

Figure 3-20: Phase angle between first harmonic lift force and transverse motion, ϕ, in degrees.

For two degree of freedom motions, one can also consider the phase between the fluctuating component of drag and in-line motion. Fig, 3-21 shows the phase relations between drag and in-line motion for the experiments. The same trend occurs for the in-line direction where the phase angle transitions from zero degrees to 180 degrees. At the lowest frequency ratio of 1.0, the transition occurs near a reduced velocity of 5, while the transition occurs near a reduced of 7 for the highest frequency ratio of 1.9. Some variability exists in the phase at the highest and lowest reduced velocities where in-line motions were very small.

Frequency Analysis

An analysis of the frequency components of the motion and force signals is necessary to show the various frequency components in each signal. As mentioned earlier, the lift force in particular consisted of large amplitude third harmonic components of lift that do not exist in one degree of freedom experiments. Figs. 3-22 - 3-27 show contours drawn from spectra of transverse motion, in-line motion, instantaneous lift coefficient, and instantaneous fluctuating drag coefficient. The contours indicate the regions where peaks in the frequency spectra occur, illustrating how the different frequency components change as a function of nominal reduced velocity. All frequencies are normalized by the transverse natural frequency such that dominant frequencies in lift will be first and third harmonics and dominant frequencies in drag will be second and fourth harmonics.

Some features of the observed frequency properties from these experiments are independent of the nominal natural frequency ratio. In all cases, the transverse motion of the cylinder occurs at the fundamental frequency, where $f/f_{ny} \approx 1$. This is an important observation since a third harmonic force in the lift direction is observed in many of the experimental cases. Since no third harmonic exists in the motion measurement, the third harmonic force seen in the lift force cannot be attributed to cylinder motions at the third harmonic frequency. Similarly, the third harmonic forces are not exciting a third harmonic motion of the cylinder. This is expected since the cylinder has only one tuned natural frequency in the transverse direction. There is

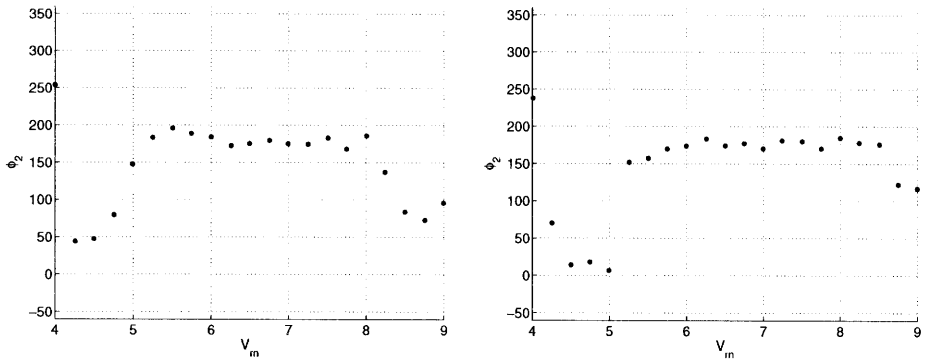

(a) Frequency Ratio = 1.0

(b) Frequency Ratio = 1.22

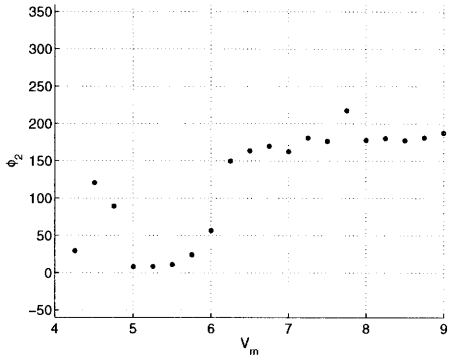

(c) Frequency Ratio = 1.37

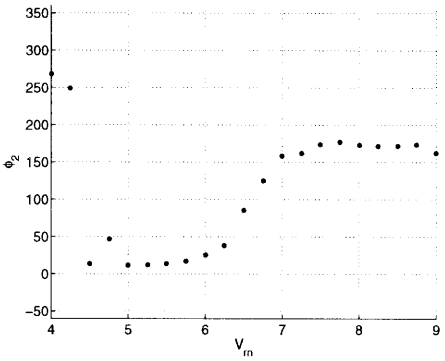

(d) Frequency Ratio = 1.52

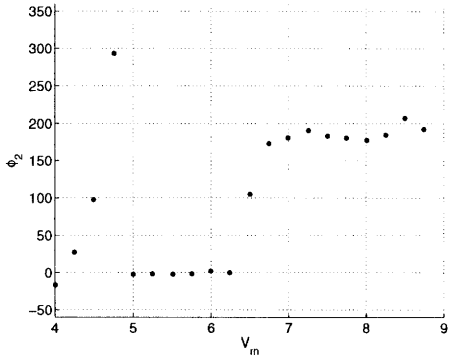

(e) Frequency Ratio = 1.67

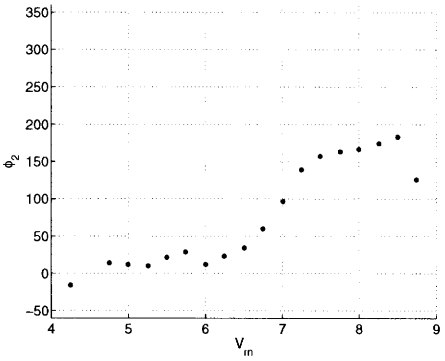

(f) Frequency Ratio = 1.9

Figure 3-21: Phase angle between second harmonic fluctuating drag force and in-line motion, ϕ_2, in degrees.

no third harmonic natural frequency to excite. The consequence of this observation is that any added mass coefficient associated with the third harmonic force must be zero and all third harmonic forces are due to vortex shedding in the wake of the cylinder and the interaction between the vortices and the cylinder's particular motion.

When the in-line motions are regular and repeatable, the cylinder has a distinct

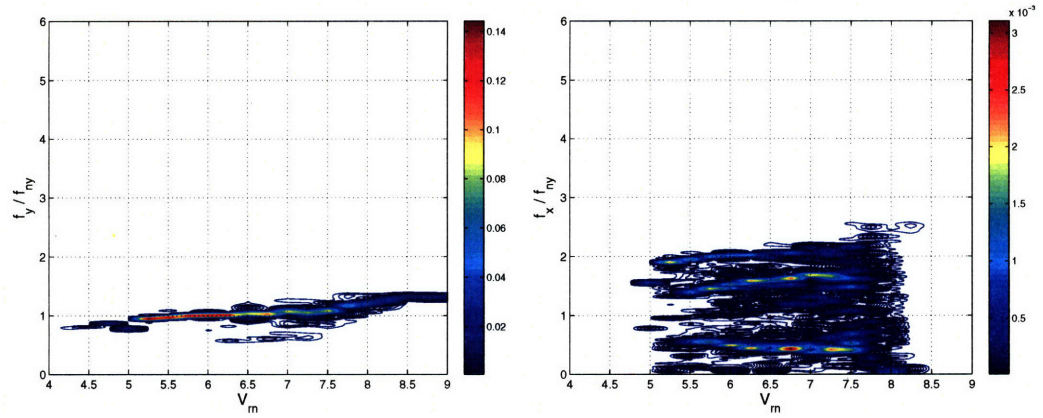

(a) Transverse Motion

(b) In-line Motion

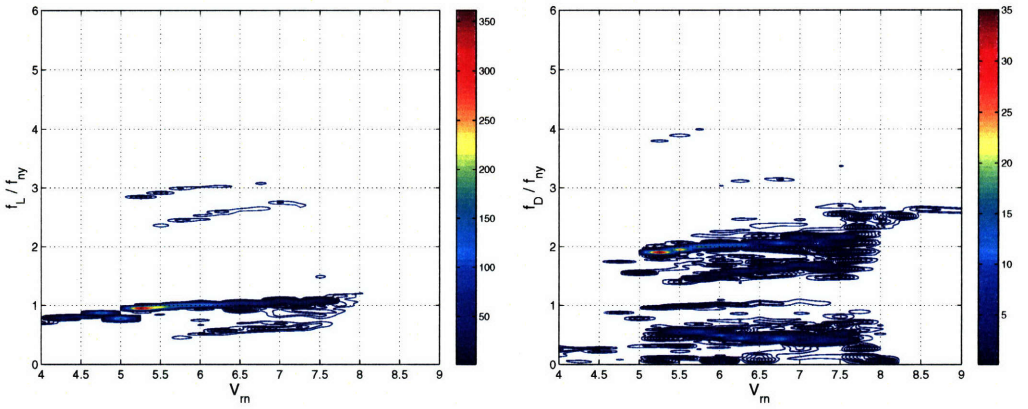

(c) Lift Coefficient

(d) Drag Coefficient

Figure 3-22: Contours of Power Spectral Density Magnitudes for transverse motion, in-line motion, instantaneous lift coefficient, and fluctuating drag coefficient for $f_{nx}/f_{ny} = 1.0$. Harmonic components of forces can be seen by the dense, colored lines formed by the contours.

frequency of in-line motion that occurs near $f/f_{ny} \approx 2$. Again, in these cases, this is the only frequency of motion in the in-line direction. For frequency ratios of 1.0, 1.22, and 1.37, fractional harmonic frequencies occur at $f/f_{ny} = 0.5$ and $f/f_{ny} = 1.5$. These fractional frequencies are particularly strong for a nominal frequency ratio of 1.0 and can be seen clearly in the preceding time traces. Multiple dominant frequencies in the in-line direction result in very irregular motions of the cylinder. As the frequency ratio increases, the second harmonic frequency becomes more dominant until it is the only frequency of motion in the in-line direction.

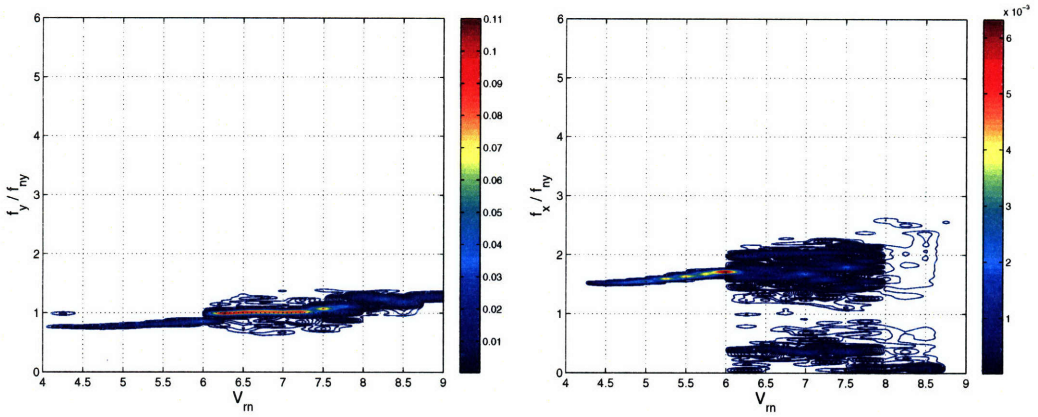

(a) Transverse Motion

(b) In-line Motion

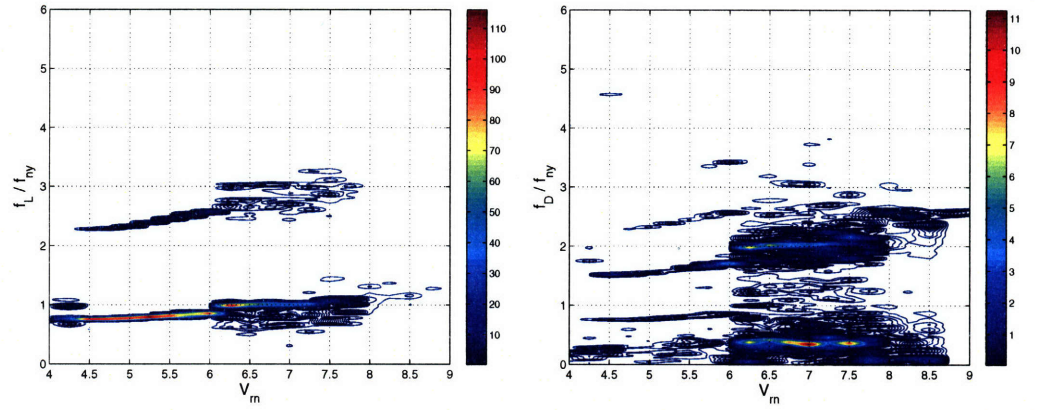

(c) Lift Coefficient

(d) Drag Coefficient

Figure 3-23: Contours of Power Spectral Density Magnitudes for transverse motion, in-line motion, instantaneous lift coefficient, and fluctuating drag coefficient for $f_{nx}/f_{ny} = 1.22$. Harmonic components of forces can be seen by the dense, colored lines formed by the contours.

The lift force in each case shows distinct first and third harmonic forces depending on the nominal natural frequency ratio. The third harmonic forces tend to occur at reduced velocities where the in-line motion is large. This can clearly be seen by comparing the peak contours of in-line motion with the reduced velocity location of the third harmonics in lift. A clear relationship exists between in-line motion and third harmonic forces. In the two frequency ratio cases of 1.52 and 1.67, an additional fifth harmonic line can be from the frequency spectrum. This fifth harmonic is very small, less than 1/300 of the peak spectrum values and at the same order of magnitude

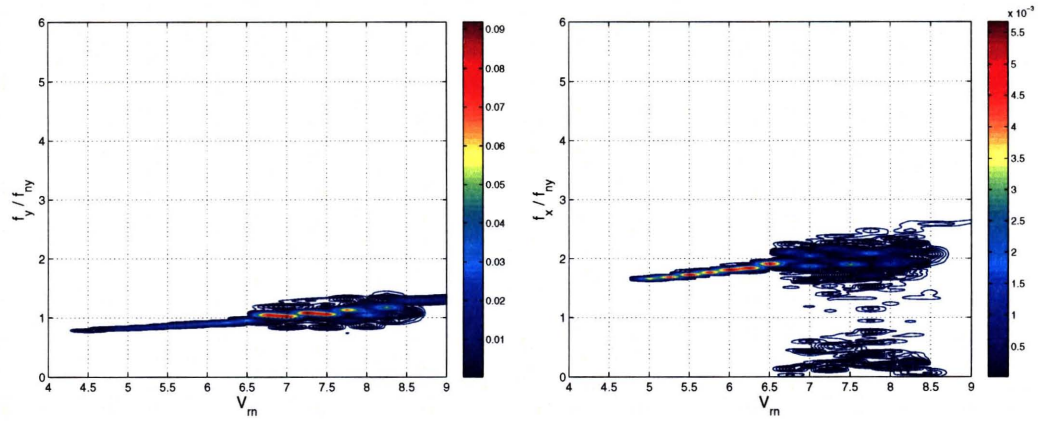

(a) Transverse Motion

(b) In-line Motion

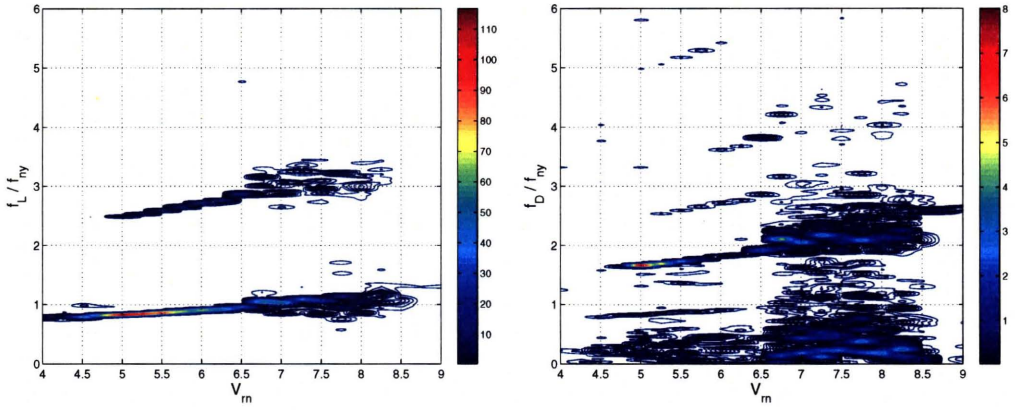

(c) Lift Coefficient

(d) Drag Coefficient

Figure 3-24: Contours of Power Spectral Density Magnitudes for transverse motion, in-line motion, instantaneous lift coefficient, and fluctuating drag coefficient for $f_{nx}/f_{ny} = 1.37$. Harmonic components of forces can be seen by the dense, colored lines formed by the contours.

as noise in the spectra. The fifth harmonic appears, however, only for cases where the in-line motion is extremely large (the largest in-line motions were observed for frequency ratios of 1.52 and 1.67). Fifth harmonics must occur due to a similar mechanism that causes third harmonic forcing of the cylinder.

The drag spectra indicate similar messy spectra at smaller nominal frequency ratios because of the multiple dominant frequencies in the in-line direction. Similar to the observations in lift, the drag displays a very small fourth harmonic which is on the same order as the noise in the spectra.

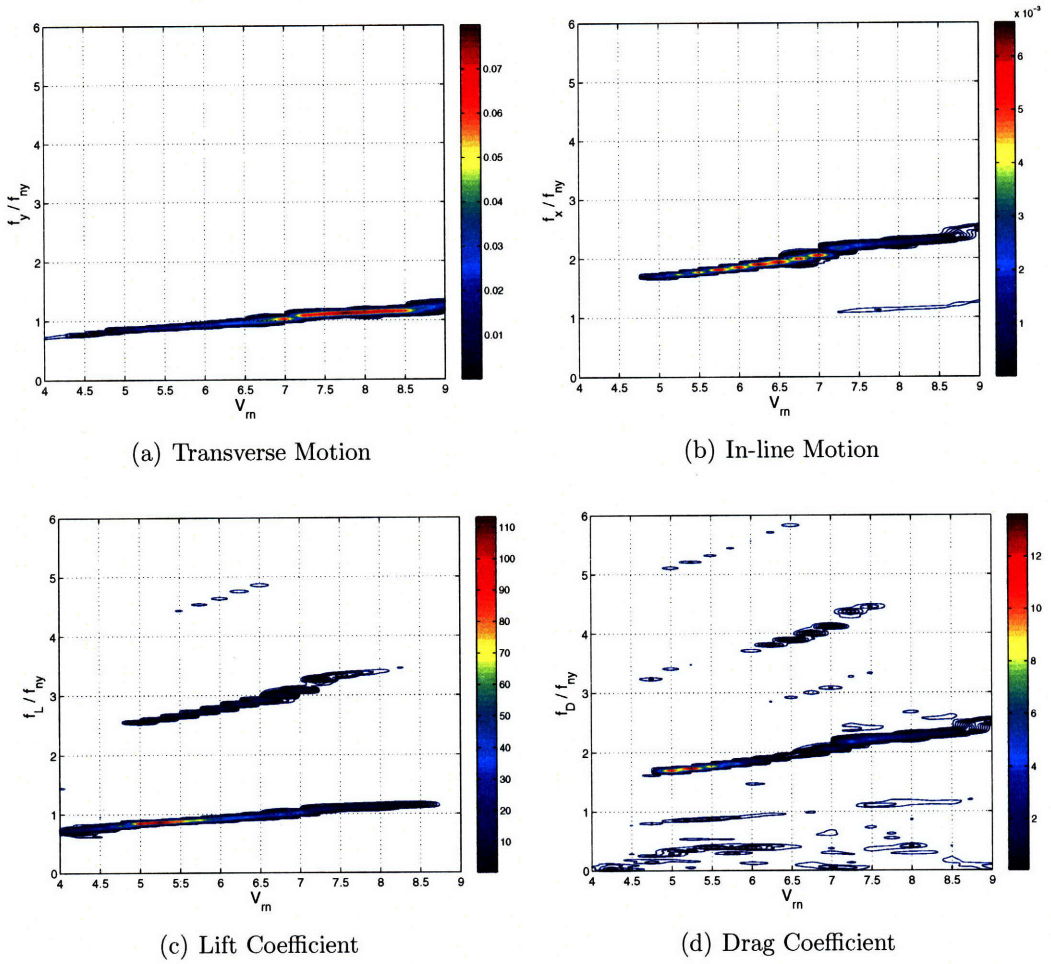

(a) Transverse Motion

(b) In-line Motion

(c) Lift Coefficient

(d) Drag Coefficient

Figure 3-25: Contours of Power Spectral Density Magnitudes for transverse motion, in-line motion, instantaneous lift coefficient, and fluctuating drag coefficient for $f_{nx}/f_{ny} = 1.52$. Harmonic components of forces can be seen by the dense, colored lines formed by the contours.

Fig. 3-28 shows a three dimensional version of the normalized lift frequency spectra for $f_{nx}/f_{ny} = 1.9$. One can clearly see the region of dominant third harmonic force, where the first harmonic component is nearly non-existent. Reduced velocities of concern exist where large combined first and third components of force exist, since the sum of these components can drive the peak amplitude of lift forces to very large values.

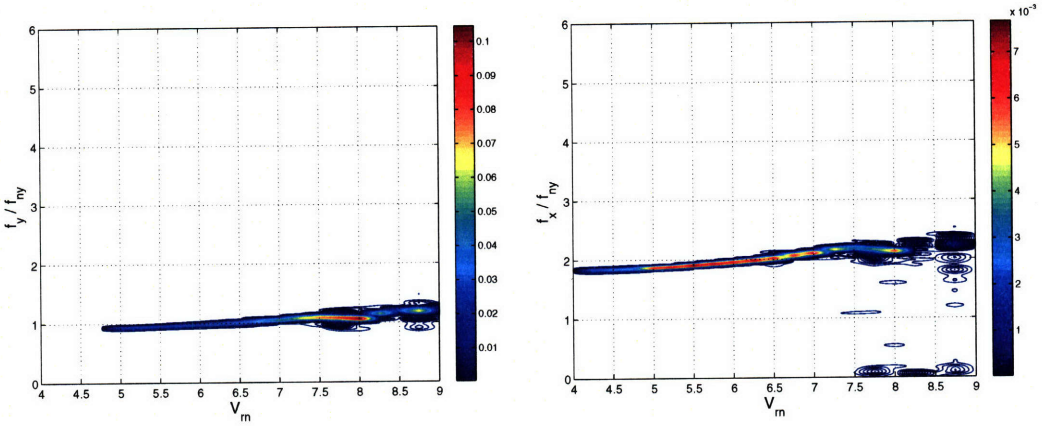

(a) Transverse Motion

(b) In-line Motion

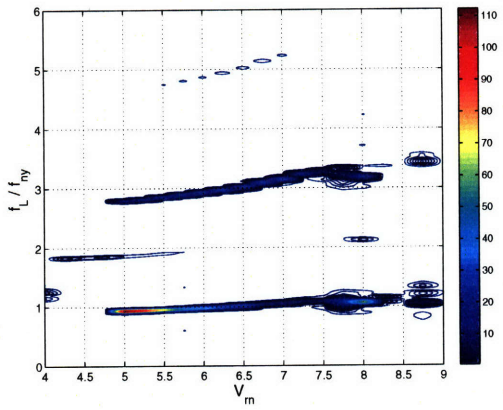

(c) Lift Coefficient

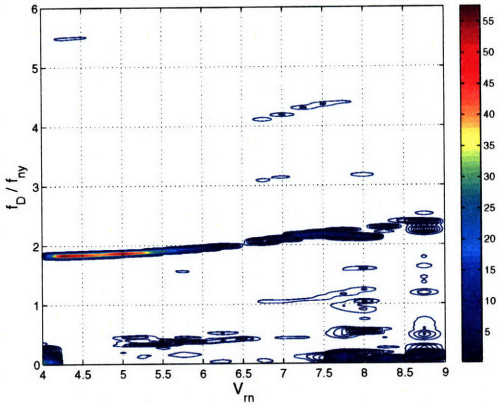

(d) Drag Coefficient

Figure 3-26: Contours of Power Spectral Density Magnitudes for transverse motion, in-line motion, instantaneous lift coefficient, and fluctuating drag coefficient for $f_{nx}/f_{ny} = 1.67$. Harmonic components of forces can be seen by the dense, colored lines formed by the contours.

3.3.5 Error Analysis through power balance

The flow of power in this experiment manifests itself in three forms: power from the fluid, power lost to linear and nonlinear damping, and power input from the linear motors. It is desirable that the power lost to structural damping equals the power input from the motor so that the average fluid power is zero. The fluid can act either as a source or a sink, removing power from the system or providing power to move the cylinder. Average fluid power is calculated as in equation 3.6, where T is the length of a test run, $\mathbf{L}$ is lift force, $\mathbf{D}$ is drag force fluctuation, $\dot{\mathbf{y}}$ is transverse velocity, and

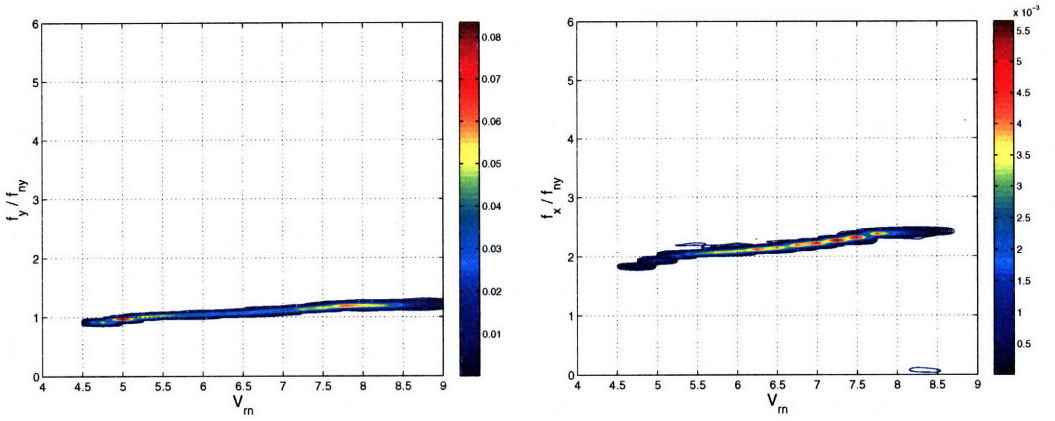

(a) Transverse Motion

(b) In-line Motion

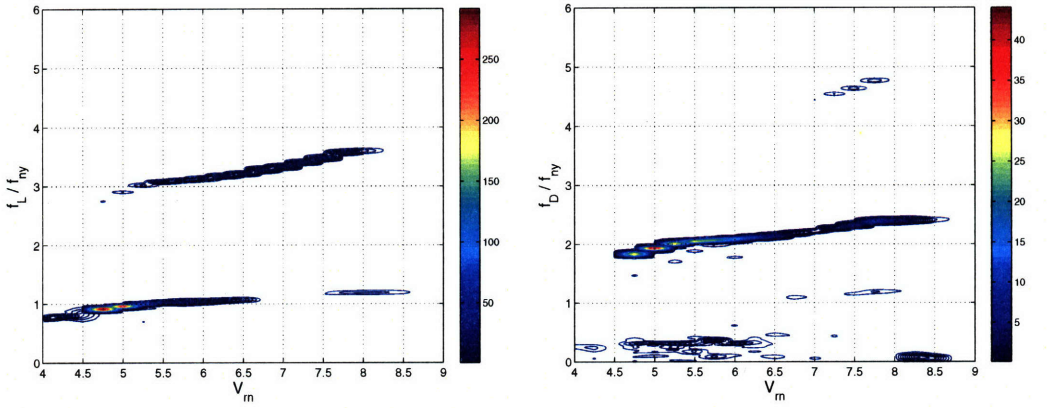

(c) Lift Coefficient

(d) Drag Coefficient

Figure 3-27: Contours of Power Spectral Density Magnitudes for transverse motion, in-line motion, instantaneous lift coefficient, and fluctuating drag coefficient for $f_{nx}/f_{ny} = 1.9$. Harmonic components of forces can be seen by the dense, colored lines formed by the contours.

$\dot{\mathbf{x}}$ is in-line velocity fluctuation:

$$P_{fluid} = \frac{1}{T}\int_0^T (\mathbf{L}\dot{\mathbf{y}} + \mathbf{D}\dot{\mathbf{x}})\, dt \tag{3.6}$$

The total average power over one run must equal zero:

$$0 = P_{fluid} + P_{damping} + P_{motors} \tag{3.7}$$

Assuming a system with no damping, i.e. the linear motors have negated the

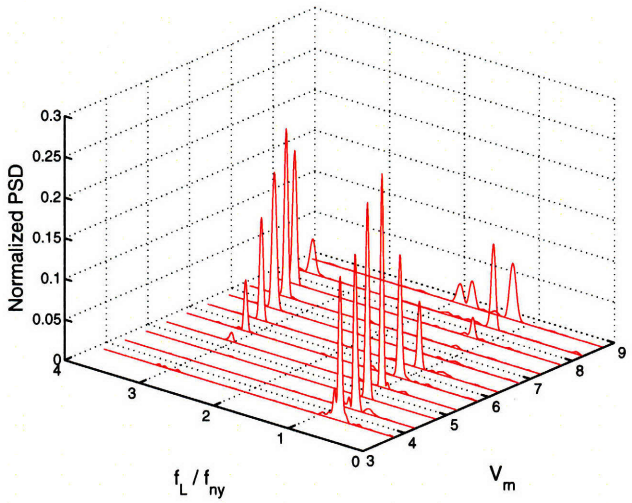

Figure 3-28: Normalized power spectral density of lift coefficient at various reduced velocities, $f_{nx}/f_{ny} = 1.9$. Figure shows how the third harmonic spectral component becomes dominant over certain reduced velocities.

damping in the system, then P_{fluid} must be equal to zero. P_{fluid} is known to be non-zero from the calculation in equation 3.6, hence damping cancelation is not exact. To quantify the error, one must first calculate the total power available in the system, P_{total}, estimated from the available kinetic energy.

$$P_{total} = \max(\frac{d}{dt}(\frac{1}{2}m_y\dot{\mathbf{y}}^2 + \frac{1}{2}m_x\dot{\mathbf{x}}^2)) \tag{3.8}$$

Dividing the error in power by the total power available generates a percent error, ϵ_{error}.

$$\epsilon_{error} = \frac{P_{fluid}}{P_{total}} \tag{3.9}$$

It is possible for ϵ_{error} to be negative, referring to a system with negative damping. Zero ϵ_{error} is indicative of a good test run. Positive ϵ_{error} means that damping is positive. The large values of ϵ_{error} shown in Figure 3-29 correspond to small motions, which are overcome by the damping force. Since the damping in the system is not controlled perfectly and the pluck tests do not provide a perfect description of oscillatory damping, ϵ_{error} was not always zero.

Fig. 3-29 shows the value of ϵ_{error} for each frequency ratio. The error is less than three percent in most cases and has only been calculated for non-dimensional amplitudes greater than 0.1, since small motion amplitudes with little available kinetic energy will cause this metric to be very large.

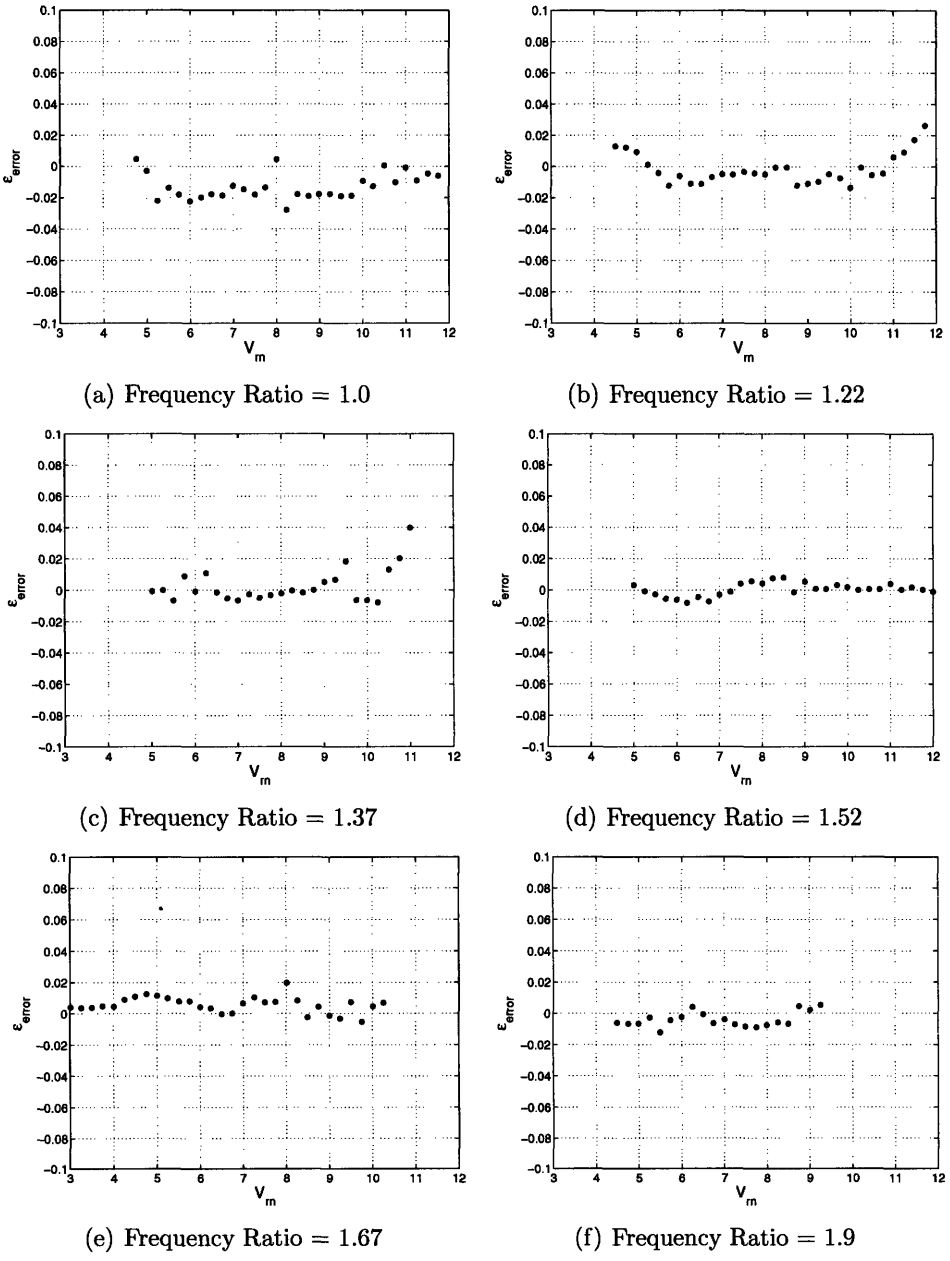

(a) Frequency Ratio = 1.0

(b) Frequency Ratio = 1.22

(c) Frequency Ratio = 1.37

(d) Frequency Ratio = 1.52

(e) Frequency Ratio = 1.67

(f) Frequency Ratio = 1.9

Figure 3-29: Error in power balance for given frequency ratio.

3.3.6 Comparison with Direct Numerical Simulation

The results of free vibration experiments are also compared with computational fluid dynamic experiments performed by Prof. Dong from Purdue University and Prof. Karniadakis from Brown University. A direct numerical simulation (DNS) is performed using the methods from Karniadakis and Sherwin [33] and Dong and Karniadakis [12] at Reynolds numbers of 1000 and 10,000. The cylinder motions for nominal frequency ratio 1.9 and nominal reduced velocity 7.25 (where maximum dominant third harmonic forces occur) are forced to study the effect on the third harmonic portion of lift. A free vibration analysis at similar true reduced velocity is performed as well.

The DNS studies show that for prescribed motions with phase the opposite phase (180 degrees out of phase) of the observed free vibrations, the third harmonic of the lift force is more pronounced at low Reynolds number (e.g. 1000), and that its intensity decreases as the Reynolds number increases to 10,000. On the other hand, for a trajectory matching that of the free vibrations ($\theta = 0$ deg), the intensity of the third harmonic component increases with increasing Reynolds number. Simulations with free vibrations of the cylinder at $f_{nx}/f_{ny} = 2$ confirm that the phase of the motion is near $\theta = 0$, in agreement with the experimental results which are obtained at higher Reynolds number. Fig. 3-30 shows the lift force spectrum for an example case, where the third harmonic component is twice as large as the fundamental component. The lift force spectrum from the DNS results compares well with the observed free vibration experimental results.

The DNS simulations allowed for visualization of the cylinder wake as well. Fig. 3-31 shows a three dimensional visualization of the wake behind the rigid cylinder in free vibrations at a true reduced velocity near 5.5. Iso-surfaces of pressure are shown to indicate the regions of vortex formation. A triplet of three vortices form per half cycle of cylinder motion in this case. One very large vortex is forming directly behind the cylinder and two smaller vortices are indicated with numbered labels. The spanwise coherence of each vortex is well-established in this case. This figure compares

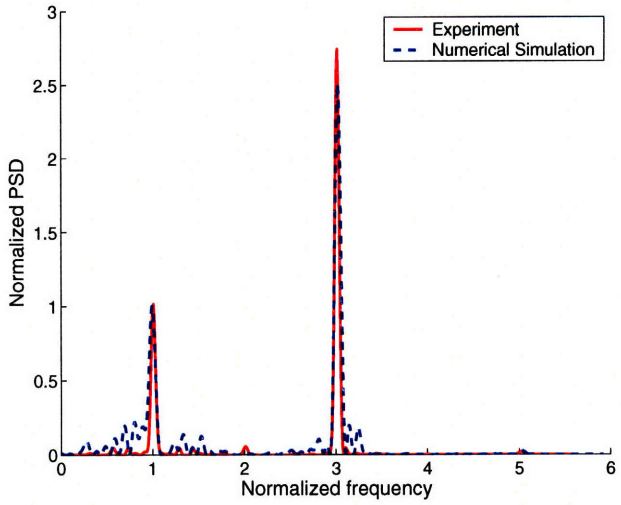

Figure 3-30: Comparison of Lift coefficient spectra in present experimental study and DNS study for $f_{nx}/f_{ny} = 1.9, V_{rn} = 6.5$.

well with PIV observations shown in Chapter 4.

3.4 Discussion on free vibrations

The free vibrations of a circular cylinder in two degrees of freedom are significantly more complex than the one degree of freedom counterpart. Additional in-line motions change the wake formation and the dynamic interaction between the cylinder and shed vortices. Additionally, the sinusoidal motion in the in-line direction introduces two additional variables in the amplitude of in-line motion and the phase between in-line and transverse motion.

3.4.1 Cylinder Orbital

In a two degree of freedom sinusoidal oscillation, there are three parameters governing the spatial motion of the cylinder, the transverse amplitude, in-line amplitude, and phase between transverse and in-line motion, as discussed in Chapter 2. A useful way to display all of these parameters for a given test run is to show the cylinder orbital. A cylinder orbital shows the motion of the cylinder in a coordinate system fixed to the carriage, such that the cylinder appears to move with a figure eight or crescent

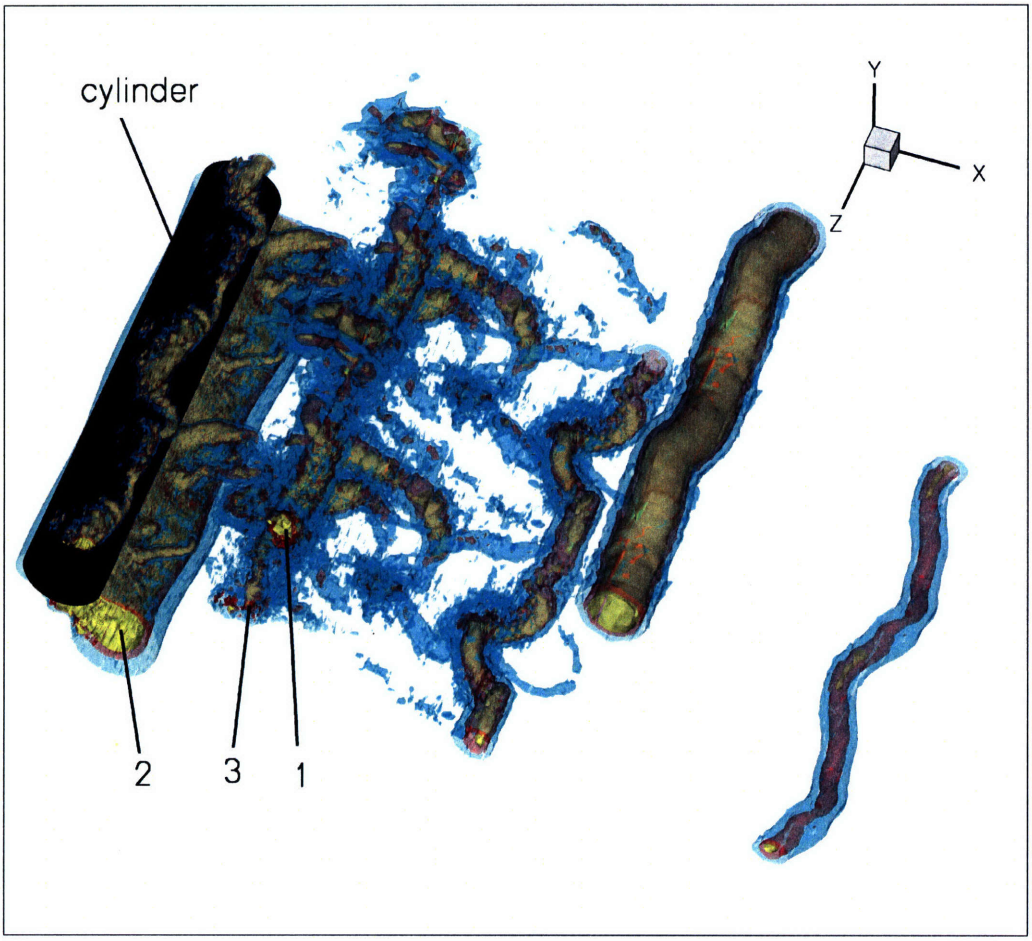

Figure 3-31: 3-D visualization of wake behind rigid cylinder from DNS through iso-surfaces of pressure, demonstrating the spatial persistence of vortex triplets; $f_{nx}/f_{ny} = 2$, $V_{rn} = 5.45$. Numbers 1,2, and 3 indicate the vortices in one vortex triplet. Figure courtesy of Prof. Dong (Purdue University) and Prof. Karniadakis (Brown University).

shape. Figure 3-32 shows the orbital motion for all experiments with significant in-line motion. The orbits are plotted for each nominal frequency ratio and nominal reduced velocity. The orbits shown in Figure 3-32 display the time history of cylinder motions for transverse motions that did not hit the guide railing over at least three cycles of motion. Black orbits show cylinder motions where the cylinder is moving upstream at the top and bottom of its motion; Blue orbits show motions where the cylinder is moving downstream at the top and bottom of its motion. The flow direction is left to right. The contours in the background of the figure display the percentage of third

harmonic force magnitude in lift.

Plotting cylinder orbits in this fashion indicates a number of striking features about these particular free vibration experiments. One distinct characteristic of the cylinder motions is that downstream crescent shaped motions (corresponding to $\theta \approx -90$ degrees) are typical for the largest transverse amplitudes. Similarly, third harmonic forces are more dominant if the motion is a figure eight shape with the cylinder moving upstream at the extreme transverse motions (corresponding to $\theta \approx 0$ degrees).

When the cylinder orbital motion is very regular, the observed excitation frequency in the in-line direction is always twice the frequency of motion in the transverse direction. This is clearly shown in Fig. 3-32 by the regular, repeatable orbit shapes at the higher nominal frequency ratios. If the cylinder motions are always excited with twice the transverse motion frequency in the in-line direction, then how does nominal frequency ratio affect the orbit shape of the cylinder? More simply, why do different orbit shapes exist for different nominal frequency ratios? It appears as though a regular transition occurs such that for a given reduced velocity, θ shifts to more positive values as nominal natural frequency ratio increases.

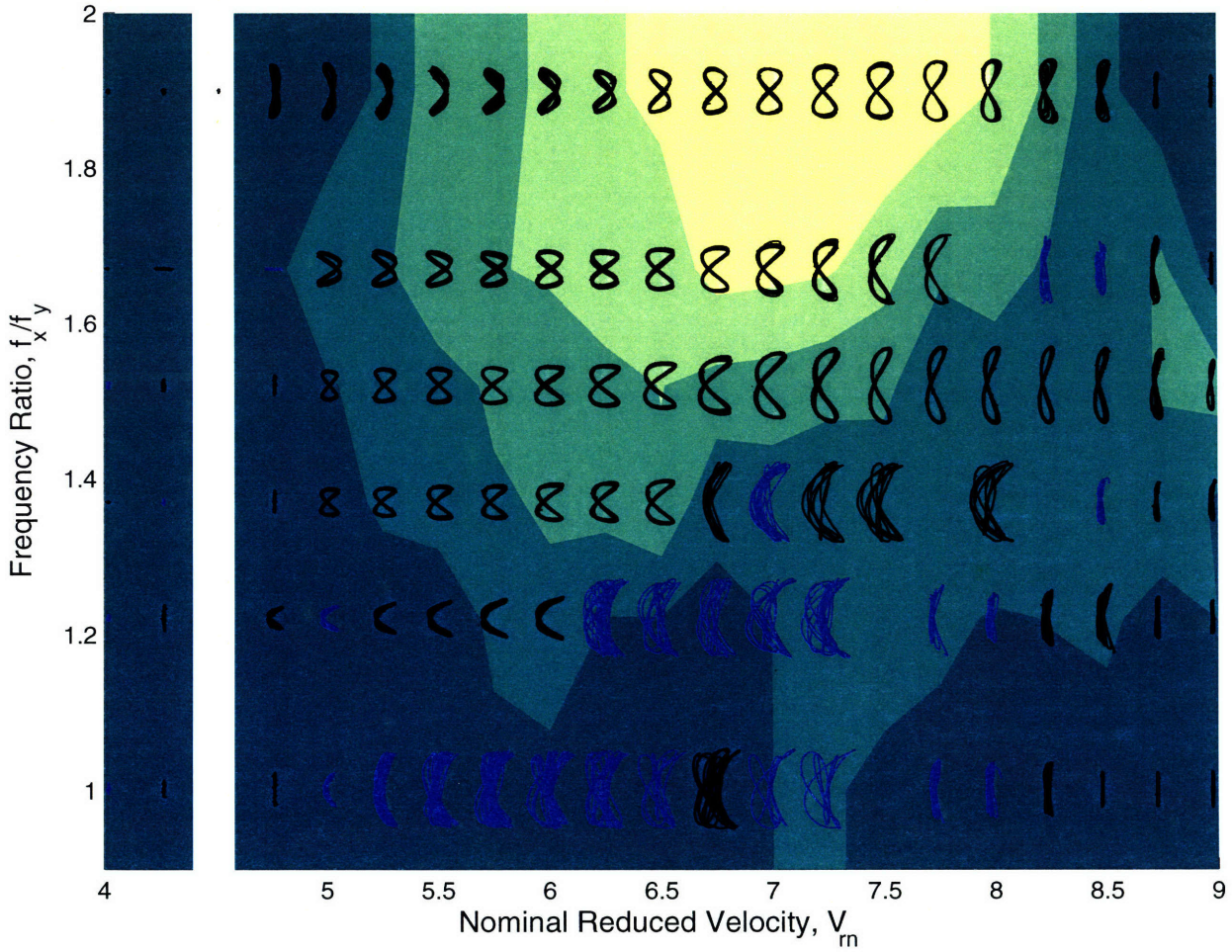

Figure 3-32: Cylinder orbital trajectories overlaid on the third harmonic magnitude of the lift force. Blue - Trajectory moves downstream at the top of the figure-eight (C: Clockwise); black - trajectory moves upstream at the top of figure-eight (CC: Counter-clockwise); flow is left to right. Contours indicate the third harmonic lift coefficient magnitude over the total lift coefficient magnitude. Darkest green denotes a third harmonic magnitude less than 25 percent of the total lift; lightest yellow denotes a third harmonic magnitude greater than 75 percent of the total lift.

3.4.2 Excitation frequencies

The variation in phases and motion amplitudes between various nominal frequency ratios is a function of the effective added mass achieved in each particular oscillation. The wake behind the cylinder interacts dynamically with the structural properties of the cylinder to achieve particular steady-state oscillations. Although the cylinder is restricted to move in two directions of motion, the phasing between these two motions can act as a feedback mechanism with the wake, such that vortex formation in wake can drive the system to have an effective natural frequency ratio of 2.

Figs. 3-33 and 3-34 show the dominant motion frequencies associated with each nominal natural frequency ratio. The open squares indicate the frequencies as they are traditionally normalized by the respective natural frequencies in each direction. Since the system has a low mass ratio, the non-dimensional frequency does not have a value equal to one during lock-in since the added mass can largely change the excitation frequency of the system. The closed circles show the same observed motion frequencies normalized by the excitation frequency as given in equation 2.4. Although the added mass is a function of reduced velocity, this normalization more clearly shows the region of lock-in, where the non-dimensional frequency becomes flat. Lock-in occurs where this value is equal to one and dual lock-in (lock-in in both in-line and transverse directions) will occur where both the in-line non-dimensional frequency and transverse non-dimensional frequencies are equal to one.

This condition of dual lock-in only actually occurs for a nominal frequency ratio of 1.9, where the added mass is capable of driving the system to this dual lock-in condition. For all other frequency ratios, however, lock-in occurs for transverse motions, but not in the in-line direction. The in-line direction is driven in such a way that it reaches a condition close to lock-in, but the oscillation frequency is not equal to the effective natural frequency. This is better illustrated in Fig. 3-35 where the ratio between effective natural frequencies is shown. The values show the ratio between the in-line excitation and transverse excitation frequencies as calculated from equation 2.4.

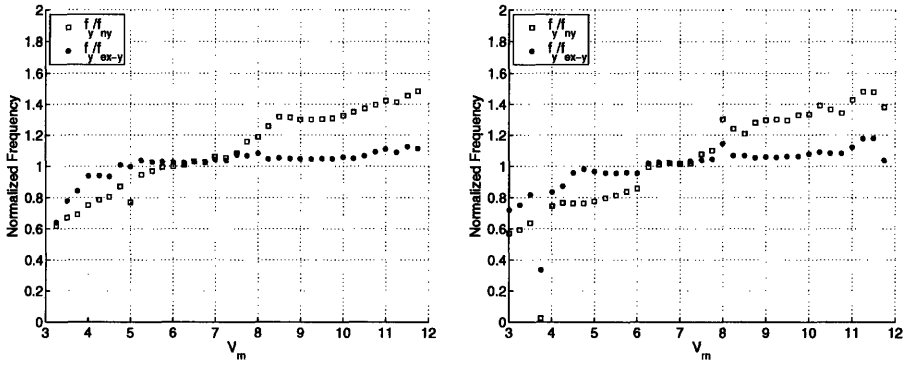

(a) Frequency Ratio = 1.0

(b) Frequency Ratio = 1.22

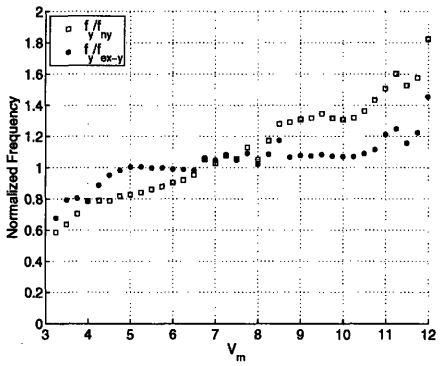

(c) Frequency Ratio = 1.37

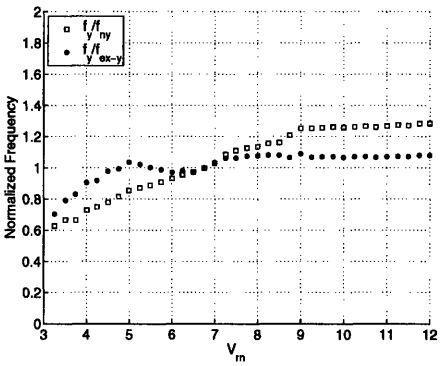

(d) Frequency Ratio = 1.52

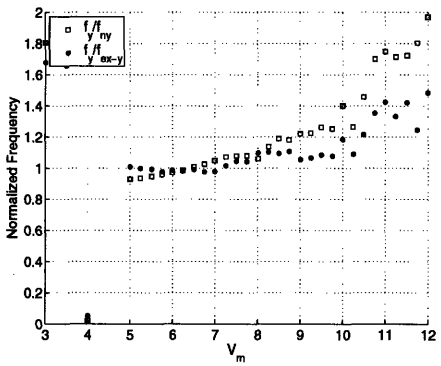

(e) Frequency Ratio = 1.67

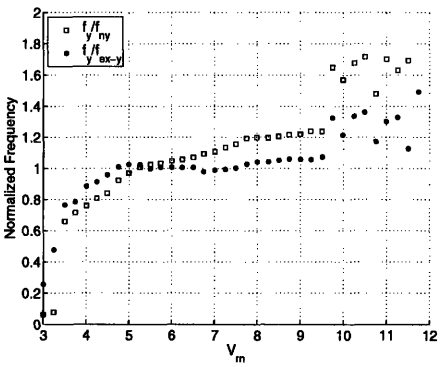

(f) Frequency Ratio = 1.9

Figure 3-33: Non-dimensional frequencies for each nominal frequency ratio in cross-flow direction. □ - Measured transverse motion frequency normalized by the transverse natural frequency. • - Measured transverse motion frequency normalized by the transverse natural frequency adjusted for added mass effects.

Points showing a frequency ratio of 0 occur where in-line motions did not exist or the in-line motions were multi-frequency (for a frequency ratio of 1.0). This figure shows that regardless of the nominal natural frequency ratio, added mass effects

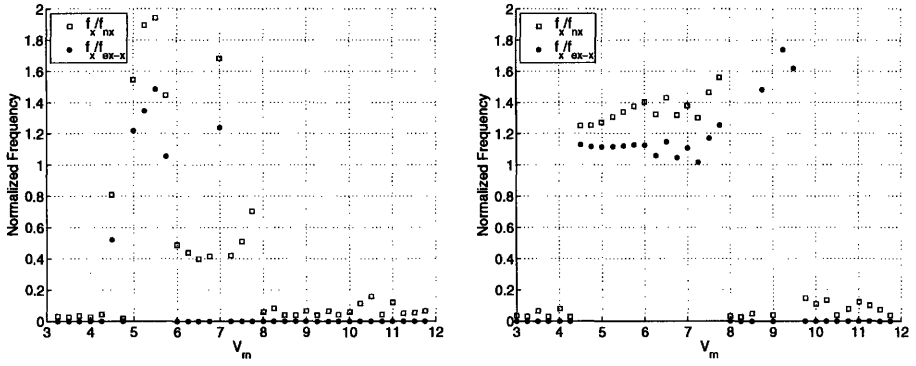

(a) Frequency Ratio = 1.0

(b) Frequency Ratio = 1.22

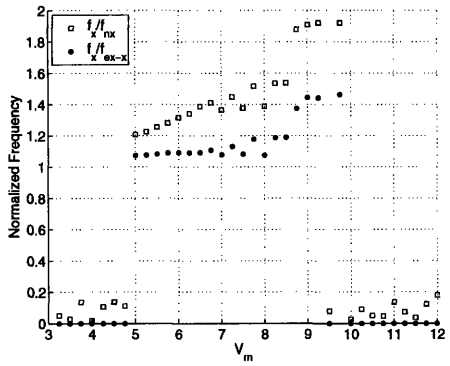

(c) Frequency Ratio = 1.37

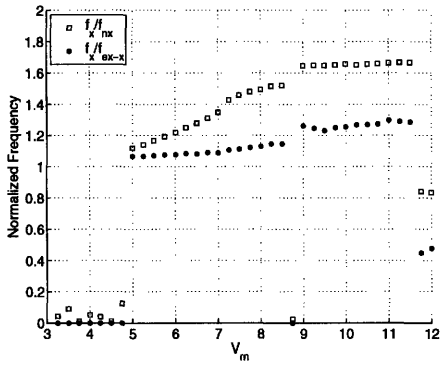

(d) Frequency Ratio = 1.52

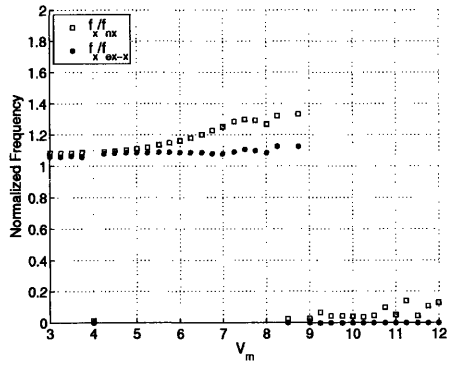

(e) Frequency Ratio = 1.67

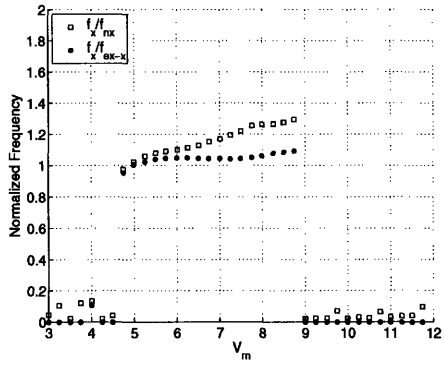

(f) Frequency Ratio = 1.9

Figure 3-34: Non-dimensional frequencies for each nominal frequency ratio in in-line direction. □ - Measured in-line motion frequency normalized by the in-line natural frequency. • - Measured in-line motion frequency normalized by the in-line natural frequency adjusted for added mass effects.

always drive the system towards an effective natural frequency ratio of 2. In all cases, the effective natural frequency ratio lies between a value of 1.5 and 2, where the nominal natural frequency ratios ranged between 1 and 1.9.

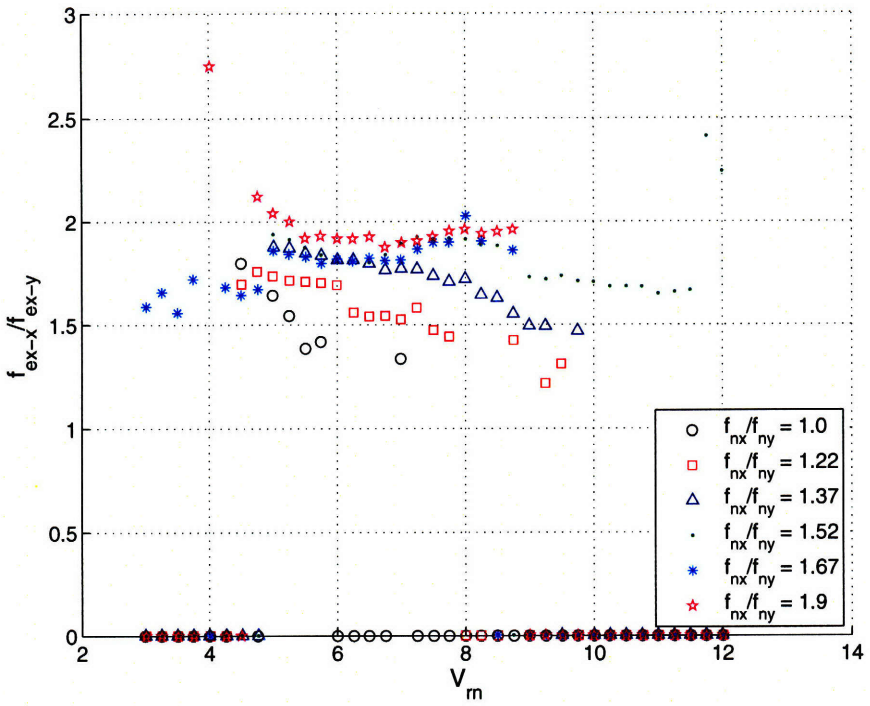

Figure 3-35: Effective natural frequency ratio for each nominal natural frequency ratio. Effective natural frequency ratio moves towards a value of 2 in all cases.

Effective added mass is a function of the cylinder's motions interacting with vortex shedding in the wake, since both vortices and cylinder motions through the dense fluid can alter the inertial forces experienced by the cylinder. It may not be possible in every flow condition for the cylinder to interact with the wake in such a way that both the in-line and transverse directions can undergo lock-in. In fact, it seems that more likely this condition should not be necessary since energy can transfer easily between the two degrees of freedom. Additionally, the motions of the cylinder and particular vortex formation in the wake limit the possible in-line and transverse added mass combinations possible to achieve dual lock-in. Lock-in in the in-line direction therefore does not always occur for two degree of freedom oscillations even though the in-line motion almost always occurs with twice the frequency of the transverse motion.

The interesting condition, however is that the system is always driven towards an effective natural frequency ratio of 2 and if the nominal natural frequency of the

system is near 2, the system can achieve a condition of dual lock-in. As mentioned earlier, very long, string-like structures such as deep water risers always have a condition where the nominal natural frequency ratio can have a value of 2. This condition is unavoidable for very long structures. One may expect that lock-in in both in-line and transverse directions may occur on deep water marine risers.

The condition of dual lock-in also presents an interesting assumption that can be made for predicting the motions of particular structures. This issue will be addressed in Chapter 5, where a dual lock-in assumption is used in conjunction with a database of forced cylinder motions to predict the rigid cylinder motions.

3.4.3 Implications of Large Third Harmonic Forces

The appearance of large third harmonic lift forces on a cylinder undergoing two degree of freedom motions is significance because of the impact on estimation of fatigue life. The fatigue life of ocean structures is affected significantly by additional high frequency harmonics because fatigue curves exhibit a high-power functional dependence on the stress level. In steel structures, for example, it is typical to model the fatigue process as in equation 3.10.

$$N \times S^b = A \tag{3.10}$$

In this equation, N is the number of cycles to fatigue, S is the stress amplitude, and A and b are constants, with $b = 4$ [28]. The stress amplitude is directly related to the fluid force on the structure. Hence, when a high frequency stress is added to the basic harmonic of roughly the same magnitude as the first harmonic, fatigue life is decreased by a factor of 2^4. Additionally, the higher frequency forcing of the third harmonic force will increase loading cycles, leading to a reduction in fatigue life as well. Understanding the conditions under which third harmonic forces exist is essential to appropriately predicting the fatigue life of marine risers.

This example assumes a direct magnitude relation between the observed hydrodynamic forces and the applied stresses in the riser material. This assumption does

not necessarily hold true since material stresses in the riser will be a function of both bending stress in the material due to riser motions and shear stress in the material. Flexible cylinder experiments indicate large magnitude third harmonic components of strain [32, 44], however the direct relation between the hydrodynamic force and the observed stress in the material is not known for these experiments. Further studies are necessary to solidify the relationship between hydrodynamic forces and material stresses in order to properly estimate fatigue life from hydrodynamic force measurement. The order of magnitude estimate above is based on an assumption that stress magnitudes are proportional to hydrodynamic force magnitudes.

Chapter 4

Cylinder Wake Visualization

Understanding the forces associated with vortex-induced vibrations requires an understanding of the wake behind the vibrating cylinder. The forces associated with vortex-induced vibrations are strongly dependent on the vorticity shed in the wake of the cylinder. Quantitative flow visualization of the wake behind an oscillating cylinder allows one to see the patterns of vortex shedding which occur behind the cylinder while giving quantitative information about the velocities in the wake of the cylinder. The particular method of Digital Particle Image Velocimetry (DPIV) is used in the wake visualizations of these experiments. In all experiments where DPIV is performed, the same experimental equipment and technique is used.

Three experiments are performed with wake visualization in order to observe the wake of a cylinder in a free stream excited in two degree of freedom motions. The purpose of these experiments is to understand why higher harmonic forces appear in the lift direction as seen in Chapter 3. Additionally, recent experiments of [30] have shown that the wake behind a cylinder oscillating in two degrees of freedom can display a '2T' mode with two triplets of vortices forming per cycle of transverse motion. Visualization is used to investigate whether the '2T' mode is related to higher harmonic forcing in the wake of the cylinder.

4.1 General DPIV Setup

4.1.1 Digital Particle Image Velocimetry (DPIV)

Digital Particle Image Velocimetry (DPIV) is a technique for quantitatively visualizing the motion of a fluid. The technique has advanced significantly in the past 20 years due to advances in camera equipment, lasers, and image processing techniques [37]. The basic equipment for performing a DPIV measurement is a camera, laser with light sheet optics, seeding particles, and PIV image processing software.

In a basic PIV experiment, the fluid is seeded with reflective, neutrally buoyant particles that will be visible when illuminated by laser light. Lasers typically produce a small beam of light, so optics are used to change the beam into a thin sheet of light that can illuminate many particles in one plane. The laser light sheet is aligned in the fluid such that the plane of fluid which one wants to view is illuminated by the laser. The camera is positioned perpendicular to the light sheet in order to view the illuminated particles.

By pulsing the laser in very short time intervals, successive images are recorded by the camera. The images can be broken into smaller pieces, called interrogation windows, which are compared using a correlation technique. The interrogation window is chosen to be small enough such that particles are moving with nearly rigid body motion (translating and rotating), but large enough such that a distinct constellation of particles can be discerned. Each interrogation window then allows one to calculate the vector movement of particle constellations. When this process is performed over the entire frame of two images, a vector field of the flow is obtained. Fig. 4-1 shows the general setup of a sample PIV system.

4.1.2 DPIV Equipment

High Speed Camera

The camera used for all experiments was an Imager Pro HS, high speed digital camera, supplied by LaVision. The camera is capable of taking pictures at 638 Hz at the

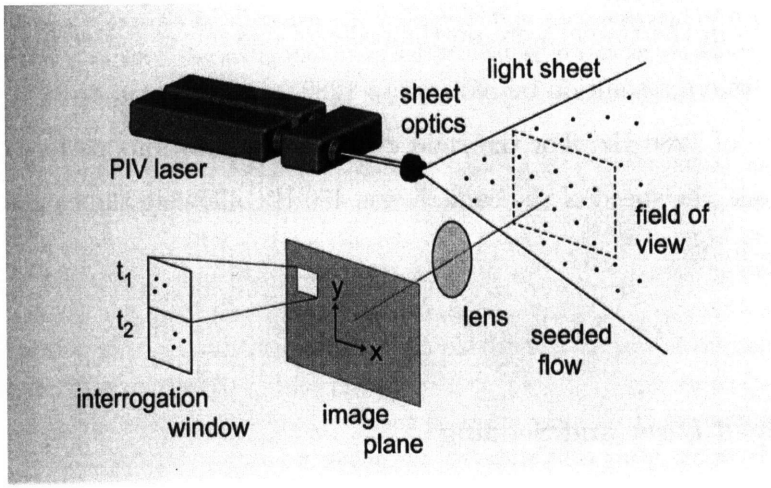

Figure 4-1: General setup for DPIV system from LaVision Manual [37].

full resolution of 1280 x 1024 pixels. Since the camera is digital, the stored frame resolution can be reduced in order to increase the frame rate. Since the camera is a high speed camera, there is only one image frame taken per laser pulse. Low-speed PIV cameras typically expose half of one image at a time to produce a double frame photo. This allows the exposure between sides of the image to occur over a very small period of time (on the order of nanoseconds). With a dual-pulsing laser, this produces pairs of closely time-spaced frames at a rate of around 15 Hz. The high speed camera, however, takes successive full resolution images at the rate of the closely spaced time frames, thus the frame rate of the camera is equal to the frame rate of the resulting set of PIV images.

The movement of particles in the frame of the camera then determines what frame rate is necessary for the high speed camera. A typical rule of thumb for setting the frame rate of the camera requires that there are at least 12-15 particles visible per interrogation window and the particles should not move more than one third of the interrogation window between frames [37]. A more detailed analysis of particle density and interrogation window size is found in Willert and Gharib [72].

For experiments performed with flexible cylinders in the MIT Water Tunnel, the flow speeds in the tunnel were on the order of one meter per second. This required that the camera resolution be reduced to 1280 x 500 pixels in order to have a camera frame rate of 1280 Hz. For the rigid cylinder visualizations performed in the small towing tank, the speed of the camera was 450 Hz, allowing the camera to obtain full resolution images.

High Speed Laser and Seeding

The laser used in all PIV visualizations was a Quantronix Darwin 527 Series diode-pumped, Q-switched, Nd:YLF laser. This is a high speed laser, meaning that it is a single laser capable of being pulsed at high frequency. The laser performs optimally with the highest power output at a pulse frequency of 1000 Hz. Increasing or decreasing this frequency causes a significant drop in the output power and available light from the laser. In both experiments in the water tunnel and the small towing tank, the laser pulse frequency was at 1280 Hz or 450 Hz, meaning optimal lighting conditions were not achieved. This problem was alleviated by the use of silver coated particles.

The seeding particles were Conduct-O-Fil ceramic spherical particles (AGSL150-30TRD and AG-SF20) obtained from Potters Industries Inc. The particles had a mean size of 93 microns and 45 microns, respectively, and were coated with 30 % and 18 % silver concentration. Traditional spherical glass beads on the order of 10 microns performed poorly at reflecting light from the high speed laser, since this laser has a lower power output than traditional lower speed PIV lasers. The silver concentration helped with reflecting more laser light, distinctly illuminating particles suspended in the water. The larger particles were neutrally buoyant with a density of 1.01 grams per cubic centimeter. The 45 micron particles were slightly buoyant, with a density of 0.8 grams per cubic centimeter, however a sufficient number of particles remained suspended in the fluid for experiments.

PIV Processing and Software

The software used for PIV processing was DaVis version 7 supplied by LaVision. This software uses the same processing techniques described in Willert and Gharib [72], but offers a variety of image processing, vector field processing, filtering, and parameter calculation routines [38, 37]. A very basic processing routine was chosen to obtain general features of the wake with less emphasis on obtaining exact measurements of velocity in the wake.

In the flexible cylinder experiments, the diameter of the cylinder was 1 cm. The resulting flow structures in the wake of this cylinder required a final interrogation window size of 32x32 pixels. The vector field was computed using a multi-pass cross-correlation of interrogation windows, starting with a window size of 64x64 pixels and ending with the final interrogation window size (32x32 pixels). The larger interrogation window produced a reference vector to improve vector calculations at smaller window sizes [37]. A fifty percent overlap was used in defining interrogation windows in order to increase the number of calculated vectors. Windows were not weighted and vectors were calculated using a standard 2D-FFT method with no zero-padding.

In the rigid cylinder visualization experiments, the same processing techniques were used except for a final interrogation window size of 64x64 pixels. The larger image size and larger cylinder resulted in wake features that were better captured by the larger interrogation window. Very small interrogation windows can lead to spurious vectors and false correlations as the interrogation window particle density decreases [72]. An additional description of PIV processing methods is given by Anderson [1].

4.1.3 Image Calibration

Velocity fields were calibrated by appropriately scaling the image size and orientation of the high speed camera. A calibration plate was used which had an array of small plus signs spaced 27 mm apart. Due to the constraints of the water tunnel and small towing tank, the camera had to be positioned such that there was a slight angle to the

camera, viewing the back side of the cylinder. An aspherical lens was also used with the camera to obtain the right image magnification in some cases. This magnification causes deformities to occur around the edges of the image. Calibrating the image allows for the images to be corrected for lens deformities and camera angle while scaling the image properly.

The calibration is done using the Calibration Wizard in the DaVis 7 software [36]. After the calibration plate is aligned with the laser sheet, a calibration image can be taken. Knowing the dimensions and spacing of the symbols on the calibration plate, one can find all of the plus symbols in the calibration image and correct the image for camera angle and lens distortion.

4.1.4 Vector Error

Errors in the measured displacement of particle constellations versus the true displacement occur as a result of interpolation when estimating the correlation peak from compared interrogation windows and from distortion of the particle constellation within an interrogation window (non-rigid body motion of particles) [72]. More modern processing techniques can improve error due to these types of problems [23], however these methods are not used in the following visualizations. The primary concern for the visualizations found in this thesis were to identify large-scale features in the wake of a cylinder oscillating in two degrees of freedom, not to accurately determine velocities in the wake of the cylinder, hence moderate errors in the measurement of velocity were acceptable as long as these errors did not change the large-scale features of the wake. Based on the analysis of [72], considering a particle density of between 10 and 20 particles for each interrogation window, the relative velocity error is estimated to be 6% of the actual velocity.

4.2 Flexible Cylinder in Water Tunnel

A flexible cylinder excited by vortex shedding will have excitation in both in-line and transverse directions since the flexible cylinder in compliant in both directions. The

experiments from Chapter 3 showed that a cylinder with a natural frequency ratio of 2:1 exhibits large third harmonic forces. In order to visualize the wake behind a cylinder with a 2:1 natural frequency ratio, we first consider a flexible cylinder which has multiple natural frequencies.

A flexible cylinder under tension will act much like a string under tension, exhibiting a fundamental natural frequency according to Equation 3.3, where f_{string} is the fundamental natural frequency, L is the length of the string, T is the tension in the string, and M is the mass per length of the string.

$$f_{string} = \frac{1}{2L}\sqrt{\frac{T}{M}} \tag{4.1}$$

Higher harmonic natural frequencies will be multiples of the fundamental frequency. Assuming sinusoidal mode shapes for a string, the fundamental mode shape will look like a half sinusoid and the second harmonic will be a full sinusoidal shape as illustrated in Figure 4-2. If we want to consider a portion of the flexible cylinder that is excited by the first harmonic frequency in the transverse direction and the second harmonic frequency in the in-line direction, such that the natural frequency ratio is 2, we can consider the point along the cylinder where an anti-node of the second harmonic occurs. This point, occurring at one quarter the length of the string or three quarters the length of the string, will have excitation from both the first and second modes of the string. If vortex shedding in the wake of the flexible cylinder excites the first mode of the string in the transverse direction and the second mode of the string in the in-line direction, the point one quarter of the length along the string may exhibit similarities to rigid cylinder vibrations with a natural frequency ratio of 2.

One problem with this assumption occurs when one considers the entire length of the string. If we are observing excitation of the flexible cylinder at the one quarter point along the length of the cylinder, the orbital motion of the cylinder should exhibit a pattern similar to those observed in Chapter 3, i.e. crescent or figure eight shapes. In the rigid cylinder, free vibration experiments, figure eight motion had a preferred

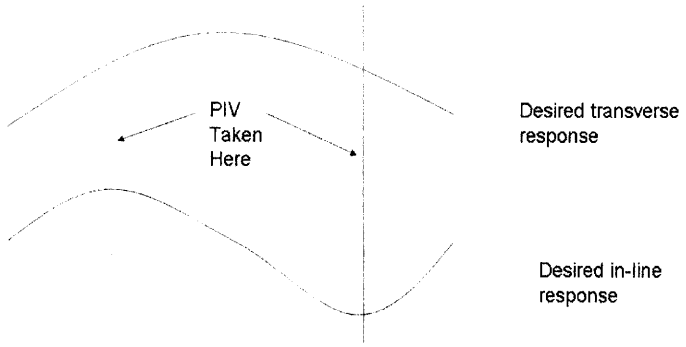

Figure 4-2: Desired wake modes of the flexible cylinder and position of PIV laser.

direction where the cylinder would always move upstream at the extreme transverse motions. If a flexible cylinder truly has resonant excitation of the first harmonic in the transverse direction and resonant excitation of the second harmonic in the in-line direction, at the quarter point along the length, the cylinder will move in a figure eight with upstream motion at the transverse extremes, but at the three quarters point along the length, the cylinder must move in the opposite direction, with downstream motions at the transverse extremes. This would indicate that the flexible cylinder cannot have a preferred direction of motion if resonance of both modes occurs.

4.2.1 Experimental Setup

The flexible cylinder experiment was performed in the MIT Water Tunnel. The water tunnel has a working test section of 0.5 m by 0.5 m and tests were performed at speeds between 0.5 and 1.5 m/s. The tunnel has less than 2 percent fluctuation in mean velocity as determined by water velocity measurement using Laser Doppler Velocimetry (LDV).

The flexible cylinder was molded from PMC-780 urethane rubber. The unstretched

diameter was 1 cm and the unstretched length was 0.35 m. The cylinder was stretched along the width of the tunnel test section to set the natural frequencies such that the fundamental frequency of the cylinder was calculated to be 25 Hz, the stretched diameter was 0.90 cm, and the stretched length was 0.43 m. The mass ratio of the cylinder was 1.3. Structural damping in air was estimated to be less that one percent based on the decay of cylinder motions in the camera picture plane.

The cylinder was not outfitted with any motion sensors. All measurements were made from camera images. Cylinder motions were reconstructed based on the cylinder motions observed in the camera frames. It was not possible to observe time-correlated span-wise motions of the cylinder in these experiments, hence results are reported for individual sections along the length of the riser. The PIV laser was positioned to observe a two dimensional section of the wake behind the cylinder at one quarter or three quarters along the length of the cylinder. The position of the PIV laser is shown in 4-2.

4.2.2 Results - Flexible Cylinder Wake

For all observed motions of the flexible cylinder, both at the quarter point and three quarters point along the length of the cylinder, motions were irregular, characteristic of non-resonant conditions or traveling waves along the length of the cylinder. Figure 4-3 shows the wake and motions of the cylinder at the three quarters point along the length over various points in time with reduced velocity 5.9 and Reynolds number 9600. Immediately apparent is the irregular shape of the motion orbital as shown in the X-Y plot of each frame. This irregular orbit shape changes as one progresses in time, such that the shape is not repeatable. This is significantly different from the orbit shapes observed for the freely vibrating rigid cylinder with a natural frequency ratio of 2.

Although the orbit shape is not repeatable and asymmetric, the cylinder tends to prefer motions resembling a figure eight shape. The motions resembling the figure eight shape are similar in phase to the motions observed for the free vibrations such that the cylinder moves upstream at the extreme transverse points in the orbit. These

shapes correspond to the figure eight shape with phase near 0. In Figures 4-3 - 4-5 we see this phenomenon where the orbits are non-repeating, yet the cylinder has a tendency to exhibit this zero phase figure eight motion.

The tendency to exhibit this type of figure eight motion seems to be a natural state of cylinder's interaction with the wake. Similar motions have been observed for a cylinder freely rising through a fluid by Horowitz and Williamson [25]. For this flexible cylinder, which has a low number of excited modes, the mode shape is asymmetric, while drag loading on the cylinder is symmetric along the length. The asymmetry of the in-line mode shape means that the natural motion of the cylinder competes on either side of the central node, such that both directions want to move in a figure eight with phase 0, yet both sides cannot resonate under that condition. This results in non-resonant vibrations where the cylinder tries to move in a figure eight, but stalls or doesn't complete the motion over more than one cycle. This could be indicative of traveling waves or reflections at the ends of the cylinder.

The irregular motions of the flexible cylinder results in irregular wake formations as well. Figures 4-3 - 4-5 show the wake behind the cylinder at various times over the course of 24 cycles of motion. Since the cylinder vibrates with such erratic motions, wake formations are not regular, forming unbalanced half cycles of vortex shedding. Occurrences of anywhere from one to five vortices shed per half cycle are observed. Since forces were not measured and the span-wise motion of the cylinder is unknown, it is impossible to tell whether the cylinder is responding to fluid forces or whether the cylinder is being forced in motion to produce the resulting wakes. If traveling waves or reflections of waves are altering the motions of the cylinder in the wake, it is likely that cylinder has both positive and negative energy transfer to the fluid over the various different cycles of motion. Without a more detailed exploration of the entire flexible cylinder's interaction with the fluid, it is not possible to make many conclusions about the motions of the cylinder.

The wake of the flexible cylinder displays all of the characterized modes of vortex shedding characterized by [16, 30, 76]. Over the particular moments in time shown in Figure 4-3, one observes pairs, triplets, and quintuplets of vortices shedding over

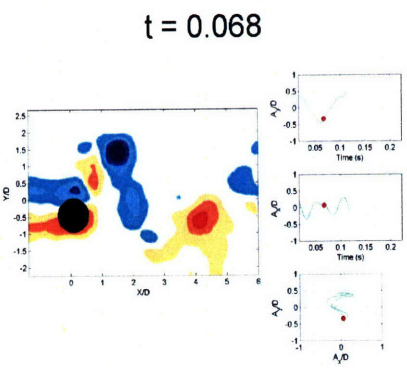

(a) t = 0.068 s, Triplet

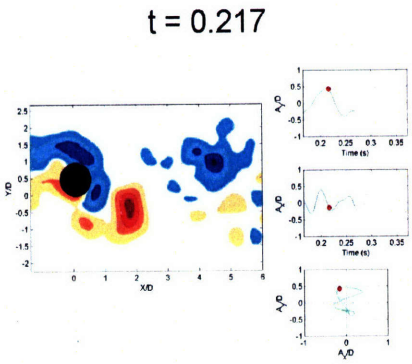

(b) t = 0.217 s, Triplet

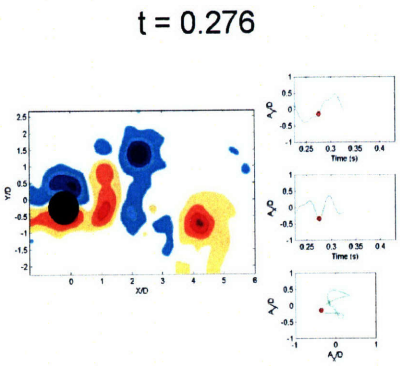

(c) t = 0.276 s, Quintuplet

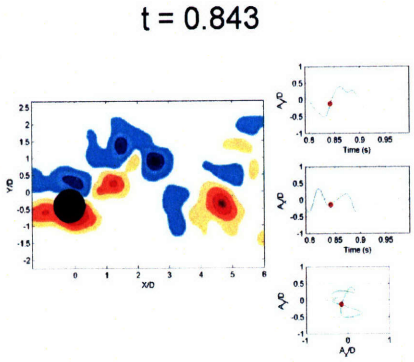

(d) t = 0.843 s, Triplet

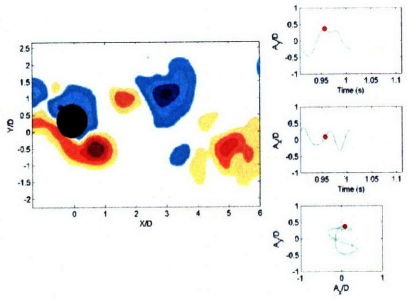

(e) t = 0.957 s, Pair

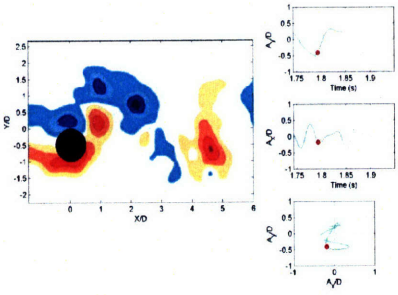

(f) t = 1.79 s, Triplet

Figure 4-3: Flexible cylinder wake at $V_r = 5.9$. Various shedding occurrences of pairs,triplets, and quintuplets. Time indicates the number of seconds from the beginning of recorded history of shedding.

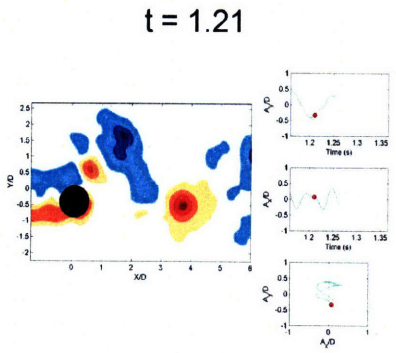

(a) t = 1.21 s

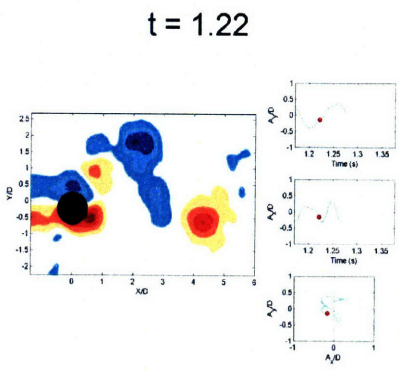

(b) t = 1.22 s

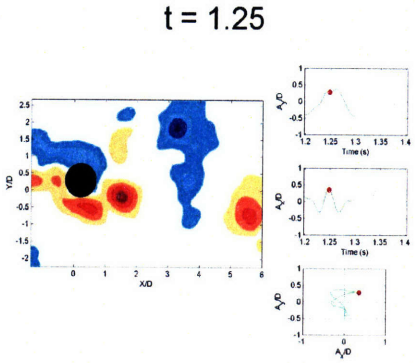

(c) t = 1.25 s

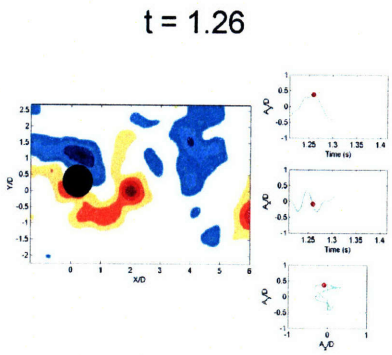

(d) t = 1.26 s

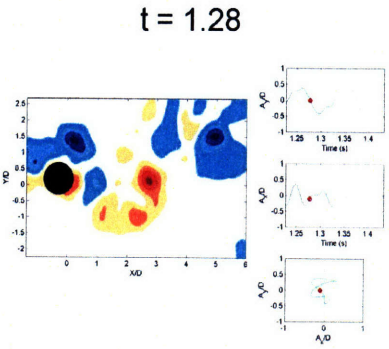

(e) t = 1.28 s

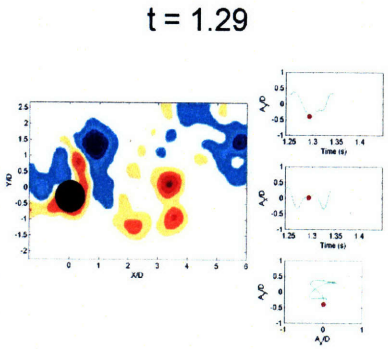

(f) t = 1.29 s

Figure 4-4: Flexible cylinder wake at $V_r = 5.9$. Formation of multiple vortices over one cycle of motion. Time indicates the number of seconds from the beginning of recorded history of shedding.

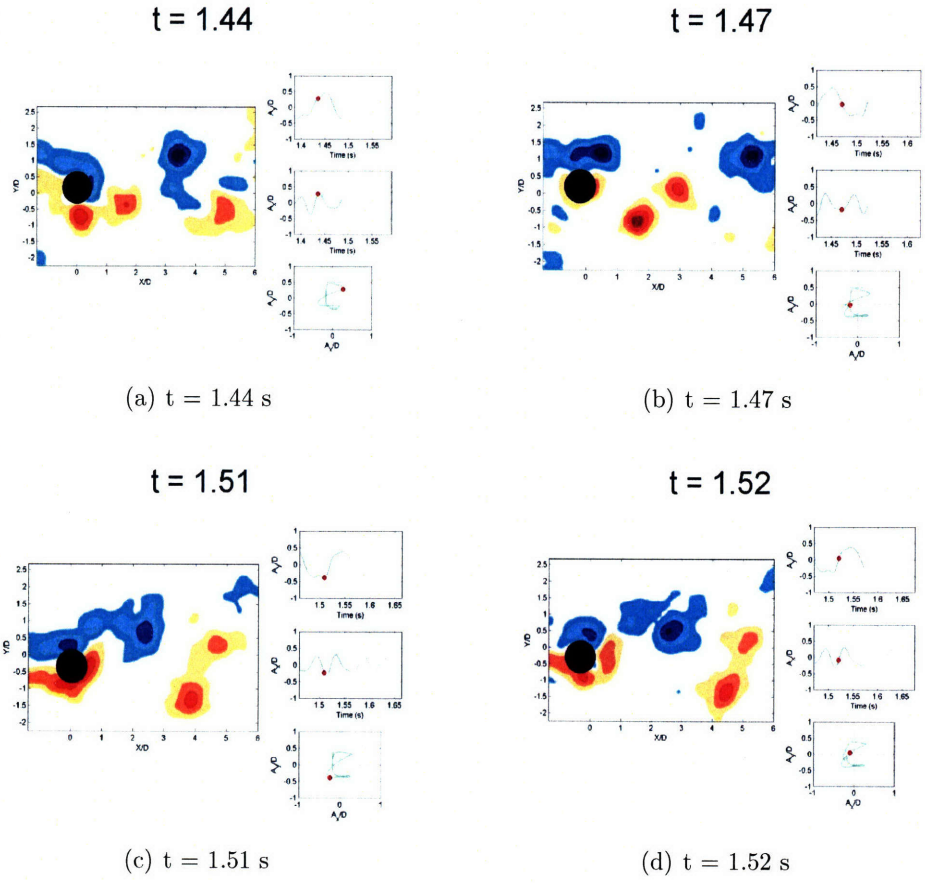

(a) t = 1.44 s

(b) t = 1.47 s

(c) t = 1.51 s

(d) t = 1.52 s

Figure 4-5: Flexible cylinder wake at $V_r = 5.9$. Formation of coupled pairs of vortices over one cycle of motion. Time indicates the number of seconds from the beginning of recorded history of shedding.

a half cycle of motion. Figure 4-4 shows consecutive time steps as an occurrence of multiple vortices are shed over one cycle of motion. Here one can see that the bottom half cycle forms three co-rotating vortices. Figure 4-5 shows the formation of the '2C' mode, where coupled pairs of vortices shed over one cycle of motion. This mode has previously been shown to form behind a pivoted rigid cylinder [16].

Figure 4-6 shows the number of occurrences of each wake pattern over the recorded cycles of motion. This does not represent a statistically significant number of cycles, but does show the predominance of the triplet shedding pattern. It is possible that the triplet shedding pattern is related to the figure eight pattern since this shedding pattern is predominant in the wake of the flexible cylinder and the flexible cylinder

has a tendency to exhibit figure eight motion, however this assumption cannot clearly be made without regular cylinder motions.

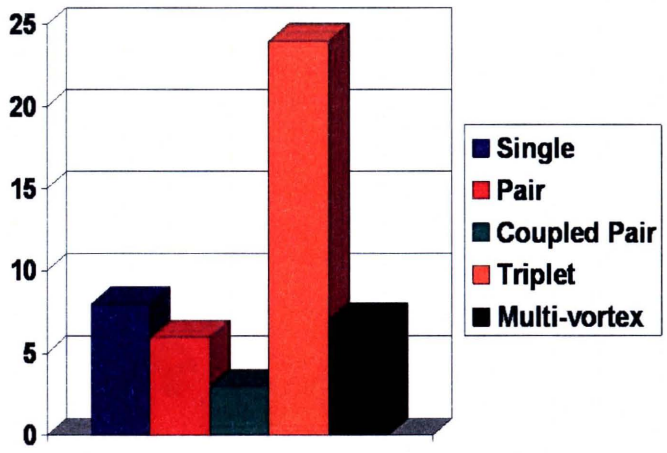

Figure 4-6: Occurrences of vortex shedding patterns over 48 half cycles of motion at $V_r = 5.9$. Vertical axis is number of occurrences.

Since the motions of the flexible cylinder are irregular, it is not possible to make a connection between wake formations and the third harmonic forces associated with the rigid cylinder free vibrations. The motions and wake of the flexible cylinder show the true complexity of vortex induced vibrations when the fluid structure interaction is three-dimensional.

The asymmetry of the in-line mode shape leads to irregular motions as the cylinder cannot resonate in the in-line direction. A flexible cylinder with an odd in-line mode shape is necessary to obtain regular oscillations in the in-line direction. This can be done for low mode flexible cylinder by tuning the natural frequencies of the flexible cylinder.

4.3 Flexible Beam Cylinder in Water Tunnel

The flexible cylinder experiment was unable to produce repeatable oscillations of the cylinder since the in-line mode shape was asymmetric and excitation of this mode shape could not be achieved. In order to use a flexible cylinder to observe the wake of a system with a natural frequency ratio of 2, one must have a flexible cylinder where the in-line natural frequency is twice the transverse natural frequency, but the in-line mode shape is symmetric. This can be achieved by 'tuning' the flexible cylinder by molding a beam through the center of the cylinder.

In the case of a cylinder with a beam molded through the center, the system is bending dominated and the natural frequency is determined by the structural characteristics of the beam. The first mode natural frequency of the beam is determined according to Equation 4.2, where f_{beam} is the natural frequency of the beam, E is the elastic modulus of the beam material, I is the area moment of inertia of the beam, L is the beam length, and M is the mass per unit length of the beam.

$$f_{beam} = \frac{\pi}{2}\sqrt{\frac{EI}{L^3 M}} \tag{4.2}$$

In the case of a beam, the moment of inertia, I, can be different in the in-line and transverse directions if the shape of the beam is oblong or rectangular. By making the moment of inertia four times larger in the in-line direction than the transverse direction, one obtains a beam with a first harmonic natural frequency in the in-line direction that is twice the natural frequency in the transverse direction. Both directions have odd mode shapes where the antinode occurs at the center of the beam.

4.3.1 Experimental Apparatus

The beam in the flexible beam cylinder was a 1/4 in x 1/8 in rectangular beam that is 0.46 m long. The same rubber material from the flexible cylinder experiment was used to mold a circular cylinder around the beam. The diameter of the cylinder was 12 cm and the resulting mass ratio of the entire beam was 2.3. The resulting natural frequency of the cylinder was 10.7 Hz and the damping was again estimated to be less

than one percent. In order to ensure the beam would vibrate with the same modes shapes as a string, it was necessary to have pinned end conditions on either side of the beam in the experimental setup. To mount the beam in the water tunnel, one sliding universal joint was fixed to one end of the beam cylinder and a fixed universal joint was connected to the other end.

Figure 4-7 shows the desired mode shapes for the beam cylinder along with the cross section of the cylinder. PIV measurements were taken at the half length of the cylinder in order to view the maximum oscillation amplitudes. The frame rate and pulse rate of the PIV camera and laser were set between frequencies of 1000 Hz and 1800 Hz, depending on the flow speed in the tunnel. Resolution of the camera needed to be changed accordingly. Flow speeds in the tunnel ranged from 0.5 to 1.5 m/s.

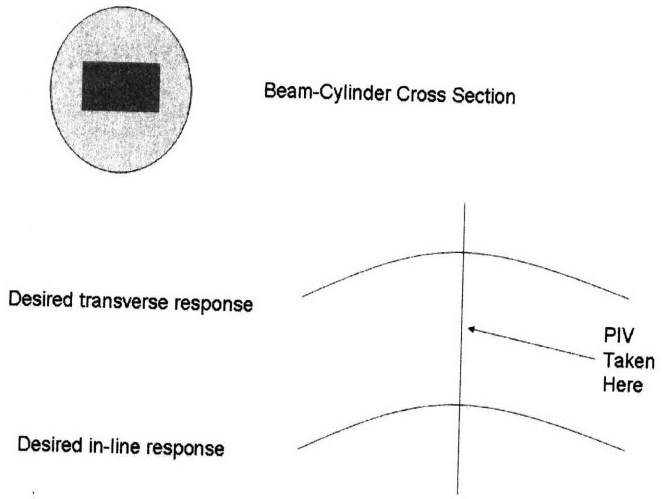

Figure 4-7: Cross-section and mode shapes of the flexible beam cylinder.

4.3.2 Results - Flexible Beam Cylinder

Motions of the flexible beam cylinder are regular, symmetric, and periodic as opposed to the motions of the flexible string cylinder. Figure 4-8 shows the measured A_y/D, A_x/D, and orbit shape for various reduced velocities. One can see that the motions

of the beam cylinder exhibit very similar shapes and amplitudes to those observed for the free vibrations of the rigid cylinder with $f_{nx}/f_{ny} = 1.9$ in Chapter 3. Transverse motions of the cylinder reach a peak at low reduced velocities near 5, level off, then increase in amplitude again at high reduced velocities. The in-line motion of the cylinder is very large in this case, reaching amplitudes in excess of $A_x/D = 0.5$.

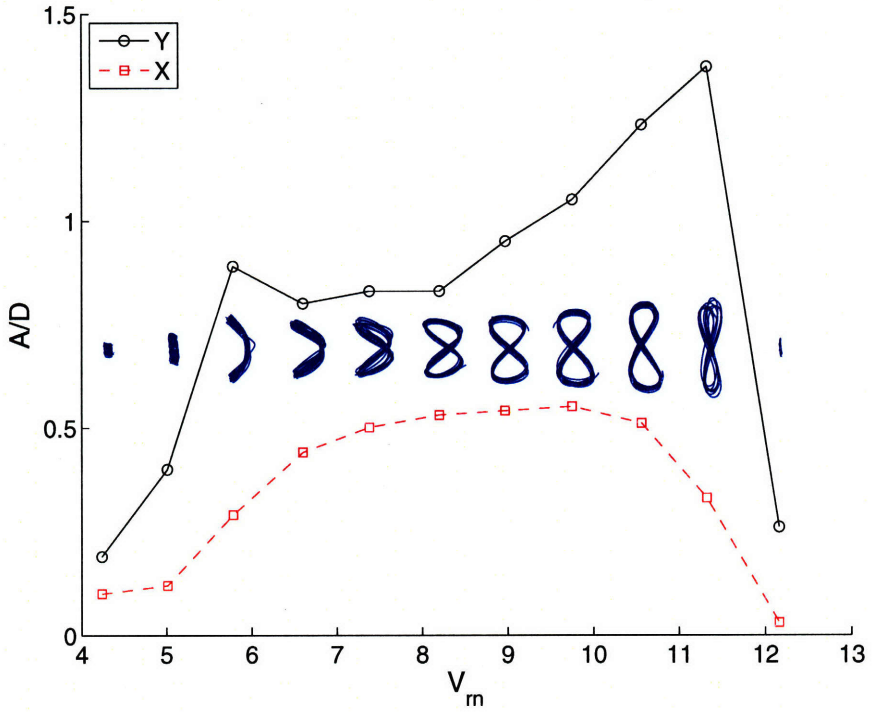

Figure 4-8: Non-dimensional amplitudes and orbit shapes for flexible beam cylinder motions at the midpoint of the beam. Motions are very similar to those observed for the elastically mounted, rigid cylinder with $f_{nx}/f_{ny} = 1.9$.

The motions of the flexible beam cylinder are very similar to the motions observed in rigid cylinder free vibrations, so we may expect that the wake of the flexible beam cylinder is similar to the wake of the rigid cylinder. Figs. 4-9 and 4-10 show the phase averaged wake of the cylinder for two different reduced velocities, $V_r = 6.03$ and $V_r = 7.38$. Phase averaging is used in this case because the motions of the cylinder were very repeatable. Additionally, the PIV images were fairly low resolution due to the high frame rates used to obtain the images. Phase averaging helps to smooth out some of the noise inherent in low resolution PIV images. Phase averaging is done

over 20-30 cycles of motion depending on the maximum number of cycles obtained through the visualization.

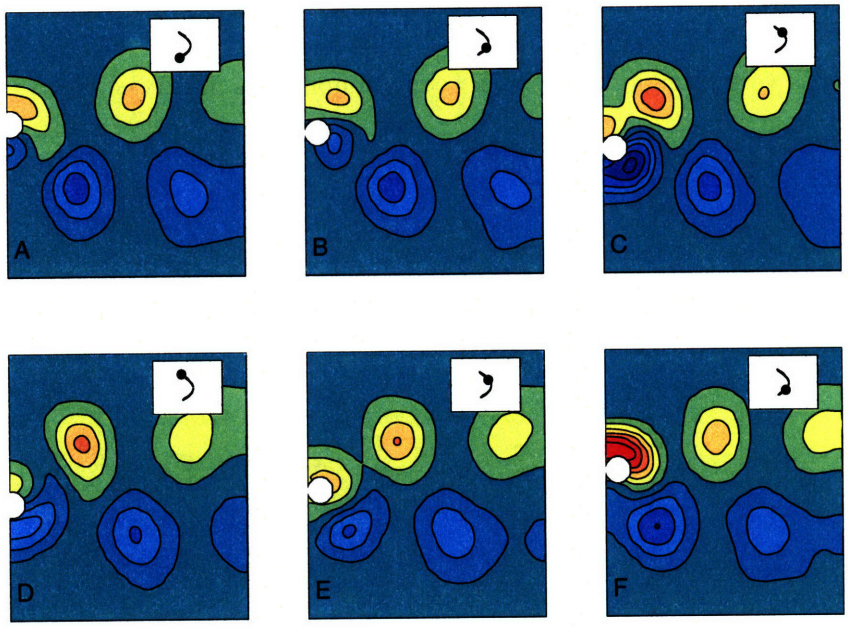

Figure 4-9: Wake beam flexible beam cylinder at midpoint of beam, $V_r = 6.03$. Wake resembles '2S' shedding pattern. Contours show non-dimensional vorticity, $\omega D/U = \pm 0.1, \pm 0.3, \pm 0.5, ...$

One can see that at the lower reduced velocity, the phase averaged wake of the beam cylinder appears to form a '2S' pattern. As reduced velocity increases, a '2P' pattern emerges with one weak vortex and one strong vortex making up the pair. The strength of the paired vortices becomes more even as reduced velocity increases further. Under these regular motions of the beam cylinder, a '2T' shedding pattern does not appear to form. It is difficult to say that the actual shedding pattern is paired vortices, however, because phase averaging will smooth out areas where discrete vortices may exist. If two vortices of like-sign rotation exist in the wake at a certain point in the cycle and we phase average these vortices, they may appear as one vortex after phase averaging since the vortices may not always shed and propagate in the exact same location of the wake each time. With low resolution images, this distinction becomes even more difficult to make.

The wake of the beam cylinder indicates that a cylinder with a natural frequency

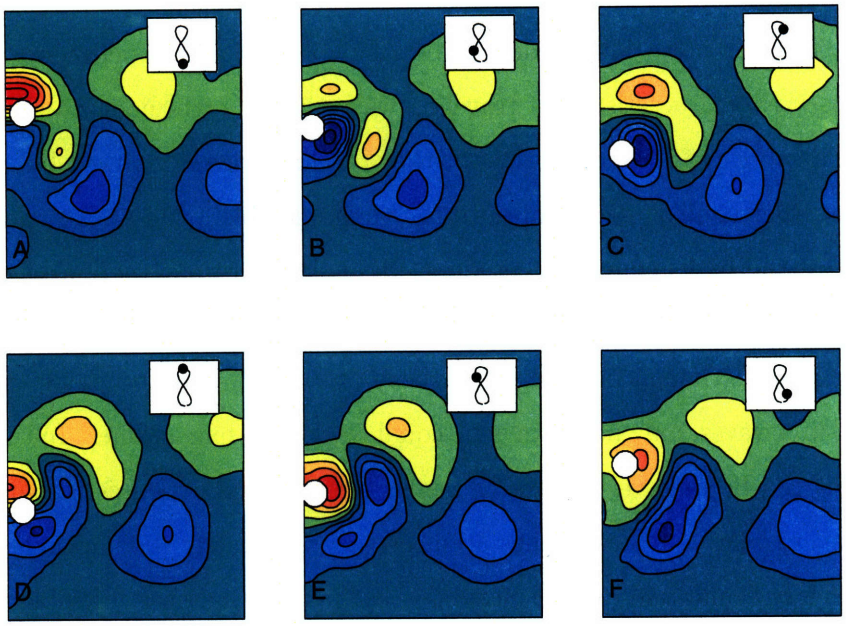

Figure 4-10: Wake beam flexible beam cylinder at midpoint of beam, $V_r = 7.38$. Wake resembles '2P' shedding pattern. Contours show non-dimensional vorticity, $\omega D/U = \pm 0.1, \pm 0.3, \pm 0.5, ...$

ratio of 2 may shed wake patterns similar to those observed behind a cylinder oscillating in one degree of freedom. In the case of the two degree of freedom motions, however, there is still an unexplained third harmonic force. Force measurements are required in conjunction with wake visualization to truly see how these wake patterns affect the lift forces exerted on the cylinder.

4.3.3 Discussion on Flexible Cylinder Experiments

The observation of cylinder motions for the two flexible cylinders tested raise new questions about the nature of vortex-induced vibrations. For instance, is the vortex-induced vibration of the flexible cylinder chaotic, random, or deterministic? In the case of the low mode number cylinder with tuned modes, we see very regular cylinder motions, while the tension-dominated system displays very irregular cylinder motions. The particular structural characteristics play an important role in the observed behavior of the cylinder.

Flexible risers in field experiments show the existence of traveling waves in the

riser ([44, 32]). Can low mode number, flexible cylinder experiments help explain the observed characteristics of traveling waves in the high mode number riser? The appearance of repeatable motions in the traveling waves observed by Jhingran [32] indicate that similar orbit shapes to the tuned flexible cylinder can travel along the length of the high mode number riser. In contrast, reconstruction of riser motions from experiments performed by the Norwegian Deepwater Programme (NDP) [44], indicate that although traveling waves may exist, the phase speed of cross-flow waves and in-line waves, may not always be equal or close to one another. In this case, orbit motions can become very irregular , as in the observed experiments with the purely flexible cylinder. Further studies are necessary to identify the particular mechanism for which irregular and regular motions occur in a marine riser. Flexible riser motions will be affected by a number of conditions including the ability of the riser to achieve local dual resonance, the effect of the riser end points on wave reflection, and the particular shear flow conditions seen by the riser.

4.4 Rigid Cylinder in Small Towing Tank

Experiments were performed in a small flow visualization towing tank in order to visualize the wake of a rigid cylinder oscillating in two degrees of freedom. The purpose of this experiment was to use the visualization of vorticity in the wake of the cylinder in order to explain the presence of the third harmonic force in lift force measurements while directly measuring the lift force on the cylinder.

The flow visualizations performed in the small tank are divided into two sections: Equivalent free vibrations and forced vibrations. In the equivalent free vibration experiments, the kinematic motions of the cylinder from the observed, self-excited vibrations of Chapter 3 were re-created through forced oscillations and the wake is observed. In the forced vibration experiments, parameters such as reduced velocity, amplitude, and phase between in-line and transverse motion, are varied to observe the effect on vortex formation in the wake.

4.4.1 Experimental Setup

The small, flow visualization towing tank is 2.4 m long, 0.75 m wide, and 0.7 m deep. The tank is filled with clear, deionized water. A small towing carriage rides along the top of the tank. Figure 4-11 shows a drawing of the small tank with the carriage. The carriage is made of aluminum and carries two linear motors and the flow visualization equipment.

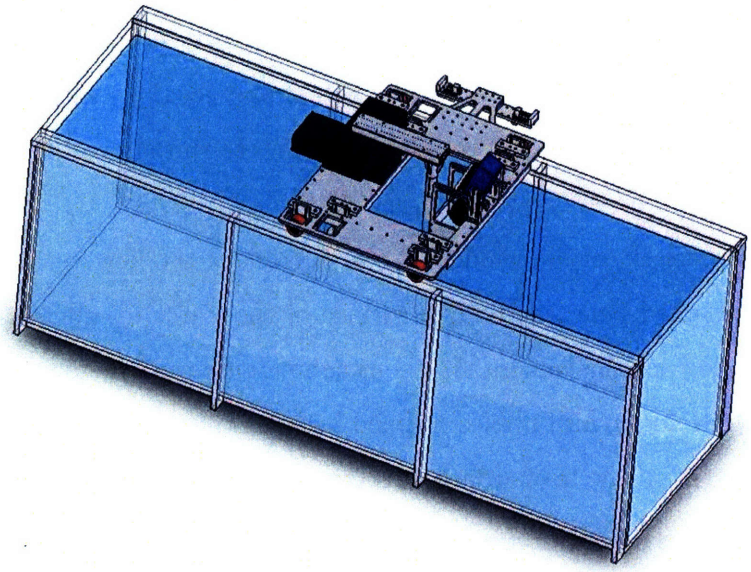

Figure 4-11: Computer model of small towing tank.

Small Tank Linear Motors

The linear motors mounted on the carriage for the small towing tank are Parker Trilogy, open-ended linear motors. The motors are arranged perpendicularly allowing forced motion in the in-line (towing direction) and cross-flow directions. The cross-flow motion motor is mounted on top of the in-line motor, allowing smooth forced motions in both directions. The motors are shown in Figure 4-12.

The motors are controlled by the PMAC software, located on the small towing tank computer. Motion files are downloaded to the PMAC control card which sends

the control signals to the linear motors. The linear motors are powered by amplifiers which were provided by the linear motor vendor.

Flow Visualization Box

The flow visualization equipment used in this experiment was the same as that used in the flexible cylinder experiments from the previous section. A small box with an acrylic window was mounted to the back side of the test carriage in order to hold the PIV camera. The box contains adjustable supports such that the camera can be adjusted to focus the PIV images. The power supply for the camera mounted directly to the carriage with velcro and camera cables were run above the tank to the PIV processing computer, as shown in Figure 4-12.

The transparent acrylic window in the bottom of the flow visualization box was slightly submerged beneath the free surface of the water in order to obtain a clean viewing window for the camera. Without submerging this window, the camera focus may be altered due to air bubbles trapped between the water surface and the window or from changes on the free surface of the water.

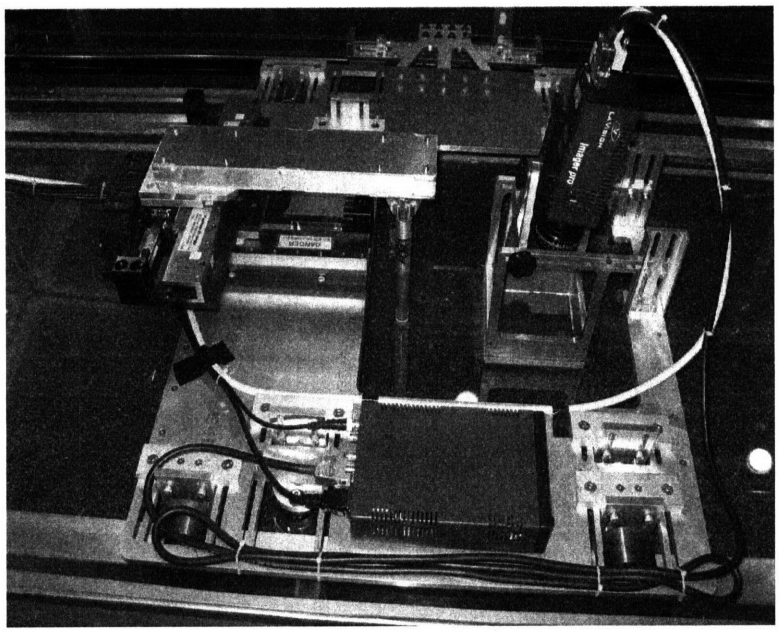

Figure 4-12: Small tank carriage, linear motors, and PIV camera configuration.

Test Cylinder

The test cylinder for these experiments was a hollow aluminum cylinder that spanned the entire depth of the testing tank. The diameter of the cylinder was 0.0381 m (1.5 inches) in order to maximize Reynolds number and minimize the forcing frequency for forced motions. The span was 0.6858 m (27 inches). The cylinder was plugged in order to keep water out of the test cylinder. Plugging the test cylinder allows for the linear motors to work at higher frequencies and amplitudes since the total moving mass of the system is less. Test cylinders were either painted black or anodized with a black finish in order to minimize light reflection on the surface of the cylinder. This helped to improve flow velocity measurements near the cylinder surface.

The test cylinder was mounted on a cantilever arm that extends back from the linear motors. A hole in the middle of the main carriage frame allows the test cylinder to extend from the cantilever arm into the water. A six-axis force sensor is mounted between the cantilever arm and the test cylinder. This arrangement is shown in Fig. 4-13.

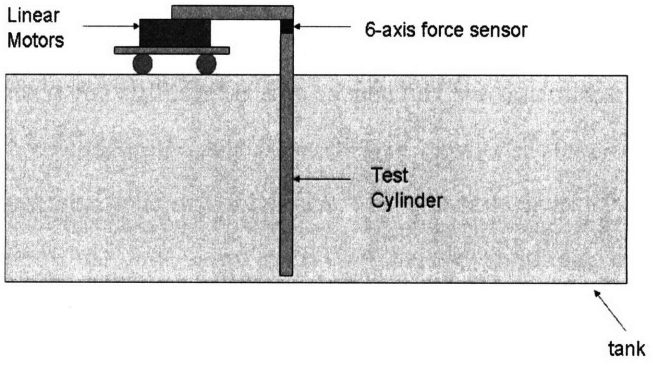

Figure 4-13: Test cylinder arrangement in small towing tank.

Force Sensor

Since the test cylinder was mounted on a cantilever arm and the force sensor was located between the cantilever and the test cylinder, forces from the fluid would cause large moments at the point where forces were being measured. Since large moments can effect the measurement of forces on the three-axis Kistler sensors that were used previously in the free vibration experiments of Chapter 3, it was necessary to use a force sensor that could log moments as well as forces.

The force sensor used in all of the small tank experiments was a JR3 model 20E12A-125 six-axis load transducer. The sensor has a load capacity of 110 N in each force axis and 5 N-m in each moment axis. The sensor comes equipped with an AC to DC power converter and an amplifier with various analog filtering capabilities for high frequency noise.

The sensor outputs voltages proportional to directions F_x, F_y, F_z, M_x, M_y, M_z, where F is an applied force and M is an applied moment. The force sensor measures forces and moments based on strain gauges mounted strategically within the sensor. This arrangement of strain gauges, as is typical with all six-axis force sensors, causes strong cross-coupling between channels in the sensor. It is therefore necessary to calibrate the sensor using a six-axis calibration matrix to accommodate cross-coupling between sensor channels.

A factory calibration for the sensor was originally sent with the sensor; however, this calibration matrix is very sensitive to the conditions of the experiment itself, particularly in the way that the sensor is loaded in the experiment. From discussions with the sensor manufacturer, it was discovered that the factory calibration is determined by loading each axis independently, very close to the center of the sensor. Independently loading axes near the center of the sensor will only result in a useful calibration matrix if all measured loads are applied in the same way. Additionally, independently loading the axes near the center of the force sensor will produce very poor estimations of the cross-coupling between dependently loaded axes such as x-force and y-moment or y-force and x-moment. If loads are applied far away from the

sensor, it is very likely that cross-coupling terms in the calibration matrix will be very different from those in the factory calibration. It was therefore necessary to obtain a new calibration matrix based on the conditions of the experimental setup.

Force Sensor Calibration

In all applications of this force sensor, the robot side of the sensor is mounted to the cantilevered arm, connected to linear motors. The test cylinder is connected to the tool side of the force sensor. Figure 4-14 shows a schematic of the force sensor with the cantilevered arm and the test cylinder. The hydrodynamic force on the cylinder when being towed will be applied roughly at the center of the span of the cylinder as indicated in Figure 4-14. Since the applied force is very far from the center of the cylinder, the factory calibration matrix will not be accurate in determining the forces from voltages, since the cross-coupling will not be accurately represented by the calibration matrix. Applying a constant load at various lengths away from the location of the sensor shows that the predicted force drops off linearly when it should stay constant if the factory calibration is used. This shows that a linear portion of the force is missing from the calibration which can be attributed to the cross-coupling between applied force and measured moment.

To obtain a new calibration matrix, the important forces are first identified. It is necessary to measure lift and drag on the cylinder so forces F_x and F_y must be known. With such a large moment arm on the sensor, it is likely that these forces will largely be affected by the applied moments, so we must also accurately know M_x and M_y. For asymmetric measurements, such as with a foil or cylinder with attachments, it may be necessary to know M_z as well. F_z is not an important measurement for our setup because there will be no applied F_z in the experiments, except for the static buoyant force of the cylinder. Since F_z will not change in the experiments, it is not necessary to determine the effect of F_z on the other channels. This leaves us with the need to determine a five by five calibration matrix (or six by six with a row of zeros for F_z).

For calibration, the sensor was attached to the cantilever arm and the test cylinder

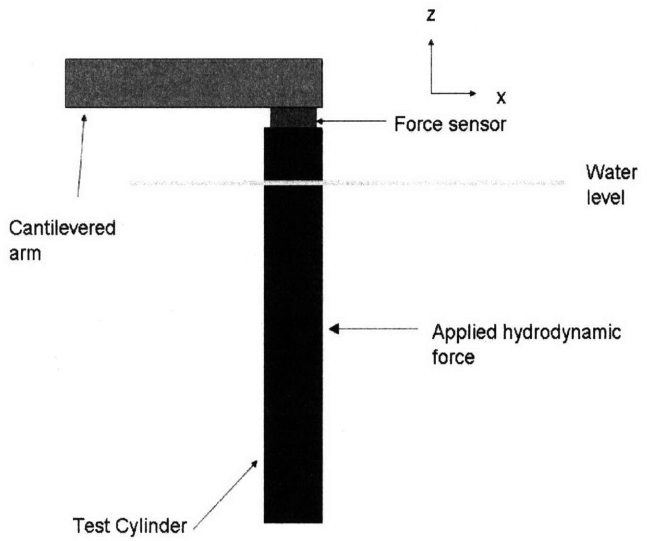

Figure 4-14: Test cylinder arrangement schematic

as in the experimental setup (Figure 4-14). The cantilever arm, sensor, and test cylinder were all leveled with respect to one another to ensure that the sensor was not rotated with respect to the test cylinder. If the force sensor has linear output voltage regardless of its zero value, the test apparatus can be aligned so that weights can be hung from the test cylinder at various positions in different axes. Figure 4-15a shows a schematic of the apparatus alignment for determining F_x, M_y, and M_z. Seven weights were applied at eight different moment arms for determining F_x and M_y. M_z was varied with seven weights at five moment arms along the cylinder length and one moment arm off the cylinder center. Each measurement was individually zeroed. Figure 4-15b shows the apparatus arrangement for determining F_y, M_x, and M_z. The same procedure was used for determining these coefficients.

Knowing the forces and moments applied on the cylinder and the voltages measured, we can determine the calibration matrix through the relation in Equation 4.3.

$$F = C * V \tag{4.3}$$

F is a 6×182 (number of measurements) matrix of known applied forces, C is

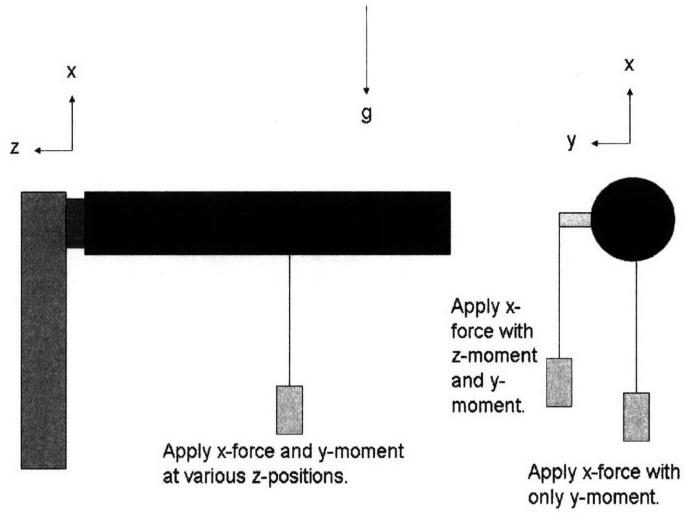

(a) Drag calibration

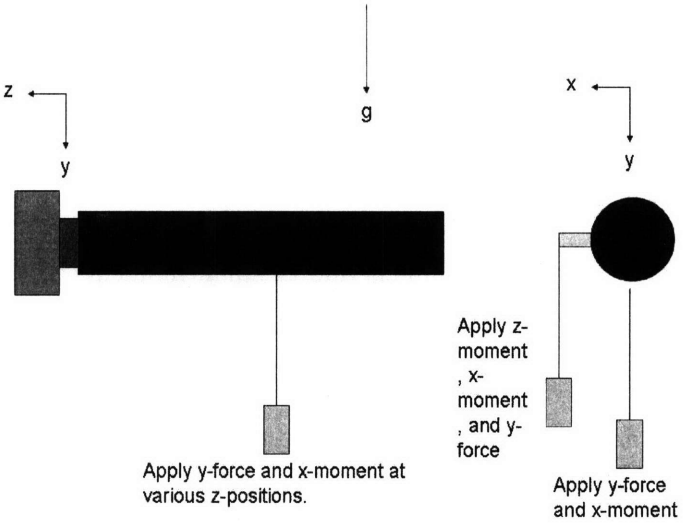

(b) Lift calibration

Figure 4-15: Schematics of calibration weight application in lift and drag directions.

the 6×6 calibration matrix, and V is a 6×182 (number of measurements) matrix of measured voltages that have been zeroed. Solving for C gives the calibration matrix in units of force/volt. The calibration matrix determined by this method is given in

Table 4.4.1.

	F_x	F_y	F_z	M_x	M_y	M_z
F_x	12.971	−0.233	−1.607	−1.007	−0.264	0.985
F_y	0.030	13.104	−4.779	0.208	−1.467	1.067
F_z	0	0	0	0	0	0
M_x	−0.113	0.012	−4.664	0.486	0.113	0.195
M_y	0.051	−0.005	2.139	0.073	0.627	−0.104
M_z	0.036	0.027	1.776	0.059	−0.055	−0.701

Table 4.1: Six-axis calibration matrix

Figure 4-16 shows the measured forces and moments from the calibration plotted against the actual forces and moments applied in the calibration for a number of points. The measured value is determined using the calibration matrix to convert the voltages to forces and moments. The ideal line shows the line of slope one, in which all points should lie if the measured force matches the applied force. F_x, F_y, M_x, and M_y all behave well in this plot, indicating that the calibration works well over this range. M_z has some deviation from the ideal curve because of non-linearity in some of the cross-coupling coefficients. Part of the problem with M_z occurs because of very poor sensitivity in cross-coupled channels at very small moments. There is little variability in the cross channels due to small moments in M_z, which makes it difficult to accurately determine a linear slope. This is most likely due to the fact that for M_z, we are operating right at the lower limits of the sensor's sensitivity. M_z is not an important measurement in oscillating cylinder experiments since there is no applied M_z from fluid forces, so a detailed error analysis of measurements in M_z is not necessary.

Verification of Cantilevered Experiment - Span-wise Visualization

The experimental setup requires that the cantilevered test cylinder passes through the free surface at the top of the testing tank and terminates near the bottom of the testing tank. End plates are not used in this experiment. Since the cylinder is cantilevered on the force sensor, end plates would generate forces that would appear

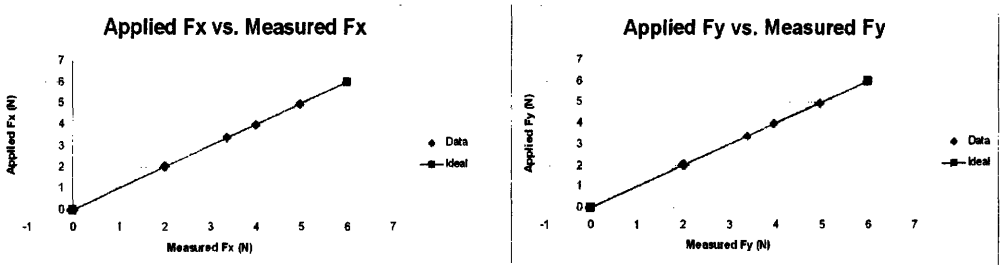

(a) F_x

(b) F_y

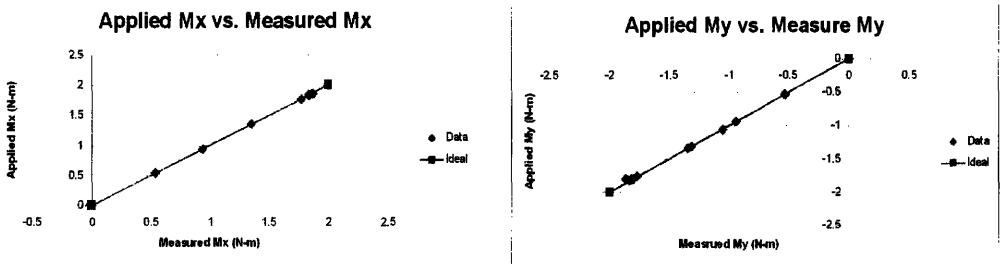

(c) M_x

(d) M_y

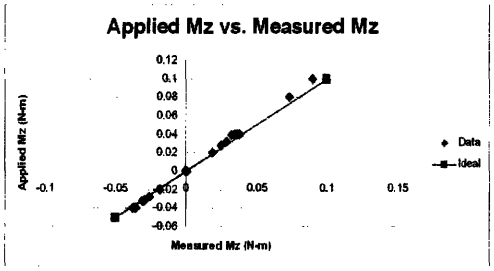

(e) M_z

Figure 4-16: Calibration fit for six-axis force sensor channels

directly in the measurement of force. Small misalignments of the endplates will cause large changes in the measured force due to the presence of the end plate at the very end of the cylinder.

Slaouti and Gerrard [56] showed that the wall of the testing tank serves as a sufficient end condition for vortex termination if the cylinder is within 0.2 diameters of the wall. The test cylinder was arranged to be less than this distance from the bottom of the tank in all experiments. Slaouti and Gerrard [56] also showed that the free surface can be used as a sufficient end condition if the surface is not contaminated with a significant number of dust particles or surface changing substance, such as detergent. In order to show that the free surface and bottom do not largely affect the termination of vortices at the ends of the cylinder, a span-wise visualization technique was employed.

A lead precipitation technique similar to that outlined in Honji et al [24] and employed by Techet [63] was used for visualizing fluid structures in the span-wise direction. Thin lead tape was lined span-wise along the leading edge of the cylinder, while thin copper tape was placed span-wise along the trailing edge of the cylinder. The lead tape and copper tape were connected to a power supply, with the lead acting as the anode and the copper as the cathode. Table salt was mixed with the tank water to make the water conductive. When the power supply is turned on, and a moderate DC voltage is applied, the lead gives up electrons to the copper and lead begins to precipitate into the water.

As the cylinder moves forward through the water, lead precipitates into the water, but is contained within vortices that shed from the boundary layer of the cylinder. By shining a laser into the tank with the laser sheet parallel to the test cylinder, shed vortices that pass through the sheet will be illuminated as the laser light reflects off the lead particles. Figure 4-17 illustrates the arrangements of the lead precipitation experiment.

Figure 4-18 shows the span-wise shedding of vortices for a non-oscillating cylinder and an oscillating cylinder. The lines of vortex tubes are primarily vertical in each case, meaning that the flow is primarily two dimensional. The free surface and bottom of the test cylinder do not cause large curvature in the span-wise vortices near the cylinder, meaning that force measurements can be normalized by the entire submerged span of the cylinder.

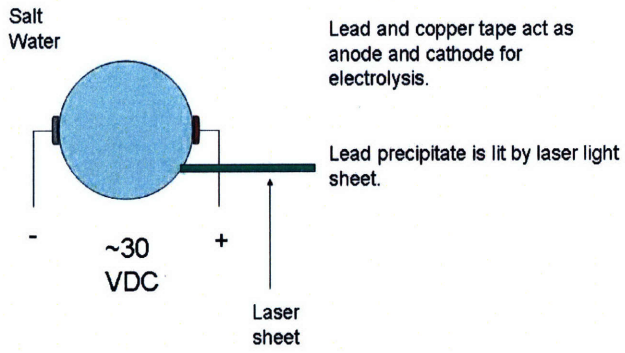

Figure 4-17: Lead precipitation experimental setup

4.4.2 Equivalent Self-Excited Vibration Visualization

Since the self-excited vibration experiments from Chapter 3 did not involve visualization from the wake, it was not possible to determine the cause of large third harmonic lift forces. Additionally, it was unknown whether the wake from these large amplitude vibrations displays similar shedding characteristics to those of a cylinder oscillating in one degree of freedom. To estimate the wake of the free vibrations, the small visualization tank was used to force kinematically equivalent motions to the observed self-excited vibrations in an environment where flow visualization could easily be performed. Additionally, forces could be measured concurrent with the wake visualizations.

Equivalent motions of the self-excited motions are obtained by assuming sinusoidal motion of the cylinder. The in-line amplitude, transverse amplitude, and phase between in-line and transverse motions were calculated, as reported in Chapter 3. Applying these amplitudes and phases to forced sinusoidal motions gives motion very similar to observed free vibrations. Reduced velocity is matched to kinematically scale oscillation frequency and forward velocity. Reynolds number is not matched perfectly

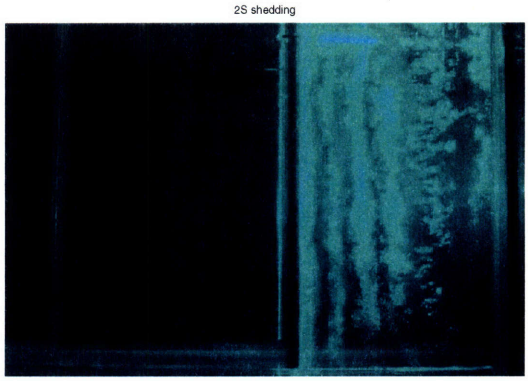

(a) Image 1

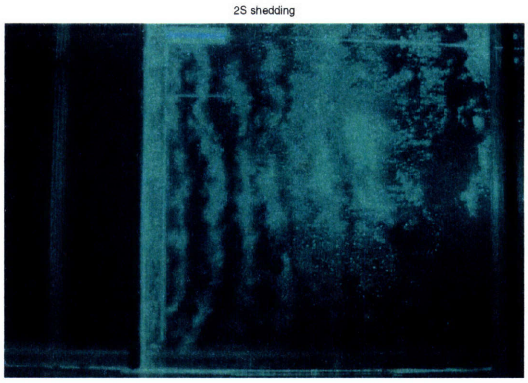

(b) Image 2

Figure 4-18: Span-wise visualization of vortex shedding for non-oscillating cylinder. Wake shows '2S' shedding with nearly straight span-wise vortex tubes near the cylinder.

as the Reynolds number in small tank experiments ranged from 6800-11,000, while Reynolds numbers in the large tank ranged from 11,000 to 65,000.

The particular free vibrations that were replicated in this experiment are outlined in red boxes in Figure 4-19. These particular cases were chosen for visualization based on the orbital shape of motion, true reduced velocity, and force characteristics, such that a range of these parameters were covered. Visualizations not shown in the following text are included in Appendix A.

Comparison of Forces from Free Vibrations

Although free vibrations are compliant, where amplitudes and frequency may vary over the course of many oscillations, the equivalent free vibration motions may be

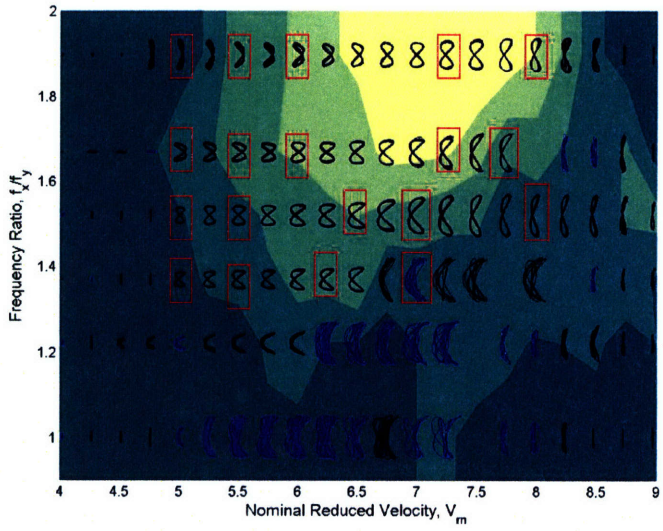

Figure 4-19: Free Vibration Orbitals. Red boxes indicate free vibrations replicated through forced oscillations.

assumed to form a similar wake to free vibration experiments if the measured hydrodynamic forces are similar. We would expect that if kinematic motions of the cylinder are perfectly matched, fluid excitation forces and added mass forces will be similar regardless of forced oscillation or self-excited oscillation.

Fig. 4-20 shows comparisons of first harmonic and third harmonic lift coefficient magnitudes measured from the free vibration experiments and equivalent forced motion experiments. The bars indicate standard deviation of the measured amplitudes over the entire test run. The comparison shows that in some instances, there is a good match between the measured lift coefficients, particularly in motions equivalent to those observed for a frequency ratio of 1.9 (Figs. 4-20a and b). The forced vibration experiments tend to have a higher measured third harmonic force compared with the free vibrations, although this is not true for every experiment performed. Lift coefficient magnitudes are typically within a magnitude of 0.5 between forced and self-excited motions.

In some instances, large discrepancies in lift coefficients exist between the self-excited and forced measurements. For motions equivalent to the frequency ratio 1.67

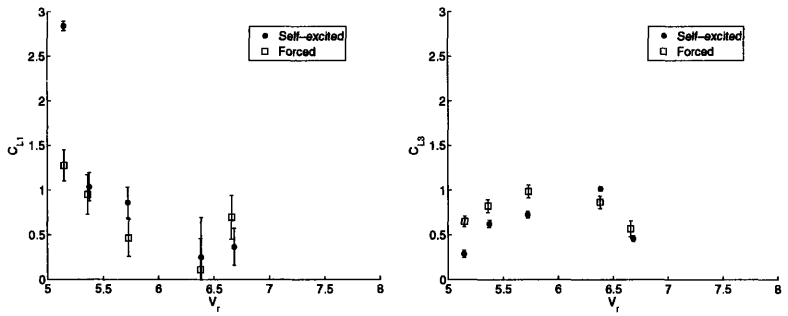

(a) C_{L1}, Equivalent $f_x/f_y = 1.9$

(b) C_{L3}, Equivalent $f_x/f_y = 1.9$

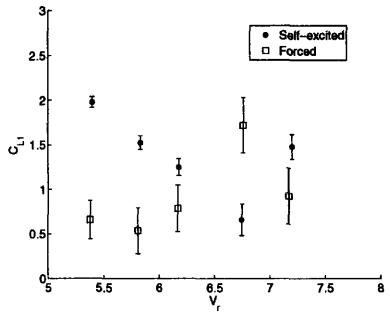

(c) C_{L1}, Equivalent $f_x/f_y = 1.67$

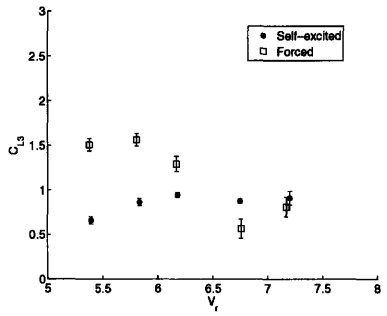

(d) C_{L3}, Equivalent $f_x/f_y = 1.67$

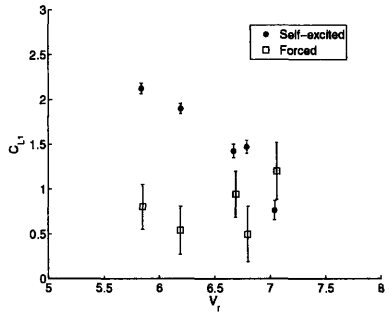

(e) C_{L1}, Equivalent $f_x/f_y = 1.52$

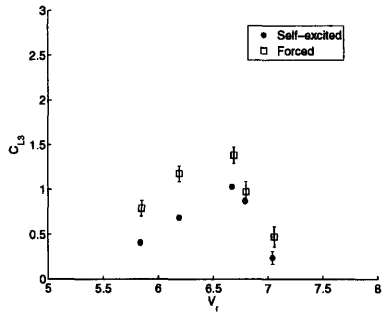

(f) C_{L3}, Equivalent $f_x/f_y = 1.52$

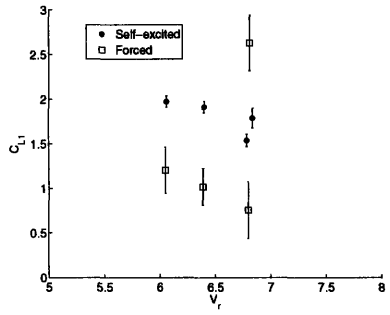

(g) C_{L1}, Equivalent $f_x/f_y = 1.37$

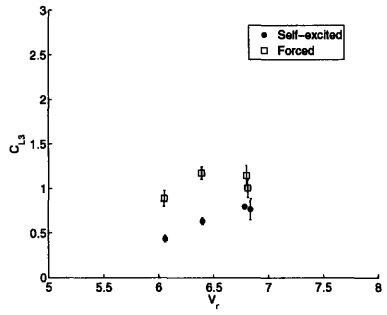

(h) C_{L3}, Equivalent $f_x/f_y = 1.37$

Figure 4-20: Comparison of Lift Coefficient Magnitudes for Free and Forced Oscillations. Error bars show the standard deviation of coefficient magnitudes.

cases, at low reduced velocities, one sees a high C_{L3} value for forced vibrations and a low value for free vibrations (see Fig. 4-20d). The trend is opposite for values of C_{L1}. A number of issues exist with each experiment that could explain this type of trend. As noted in Chapter 3, only one force sensor was working properly for many of the free vibration experiments. Since the third harmonic force is related to the vortex shedding in the wake, while the first harmonic force is related to vortex shedding and added mass, it is possible that degenerate shedding of vortices in the wake of the free vibration experiment could have caused a dominant first harmonic force to appear on one force sensor.

Reynolds number is also known to effect the magnitude of fluctuating lift coefficient for both stationary cylinders and vibrating cylinders in a free stream. Zdravkovich [78] shows that the fluctuating lift coefficient on a towed stationary cylinder can vary between 0.1 and 1 for Reynolds numbers between 1000 and 10,000. Similarly Govardhan and Williamson [20] showed there is a strong Reynolds number dependence on lift coefficient magnitudes and vibration amplitudes for an oscillating cylinder. As Reynolds number increases, peak vibration amplitudes and peak lift coefficients tend to increase. Additionally, the number of experiments for which visualizations were performed are very small, lending to potentially large error due to outliers.

In a free vibration, the compliance of the system allows for changes in the oscillation frequency and amplitude of the oscillation. The effective added mass associated with the oscillation actually changes dynamically as the system oscillates, hence the effective natural frequency of the system is constantly changing and the system remains in a dynamic equilibrium, constantly adjusting for the dynamic fluid forces. Although the fluid forces are dynamic in nature, if motions of the cylinder are periodic or nearly periodic, we can determine average force coefficients over individual periods of oscillation, hence we can determine a value of lift coefficient in phase with velocity or effective added mass coefficient for a given time history of cylinder motions. These coefficients rely on the assumption that the cylinder oscillation frequency is stationary and amplitudes of motion are stationary, which is not quite true for a compliant free vibration. In the case of a forced vibration, the motion of the cylinder

is prescribed, hence oscillation frequencies and amplitudes remain constant and the derived force coefficients will be exact. In order to truly compare forces measured from free vibration with forces measured from forced vibration, it may be necessary to consider a band of frequencies over which the free vibration occurs, hence it may not be correct to only consider one fixed reduced velocity for a given free vibration. In that case, it may be necessary to consider several forced vibrations in the vicinity of the free vibration parameters to make a good comparison of measured forces. It is shown in Chapter 5 that there is good comparison with free vibration measurements and forced vibration measurements if the number of forced vibration measurements is large and spans the region of potential free vibrations. In this case, it is possible to predict the free vibration motions by correctly determining the fluid forces necessary for a particular motion.

It is impossible to know if there was degenerate vortex shedding, if Reynolds number dependence on lift coefficients in this experiment causes problems, or if the number of data points was too small without further experimentation, so comparisons where forces do not match properly will not be treated as true visualizations of the free vibration. With this assumption, visualizations for the equivalent motions with frequency ratio 1.9 are shown along with individually chosen motions. Selected visualization of the remaining free vibration motions are included in Appendix C.

Equivalent Self-Excited Motion Wake Visualizations, $f_{nx}/f_{ny} = 1.9$

The wake visualization for motions equivalent to $V_{rn} = 7.25$ are shown in Fig. 4-21. The true reduced velocity in this case is 6.38 and the motion of the cylinder is a figure eight with the cylinder moving upstream at the extreme transverse amplitudes ($\theta \approx 0$). The forces measured for this case exhibit a dominant third harmonic, where the first harmonic force magnitude is very small. The wake that forms behind the cylinder in this case appears to be very similar to the '2P' wake of Williamson and Roshko [76], although the wake is not as well-formed as typical '2P' wakes. As the cylinder moves transversely, a clockwise vortex forms upstream of the cylinder since the cylinder is moving downstream with in-line motion. The vortex travels around

the cylinder and sheds to the bottom side of the cylinder as the cylinder begins to move in the opposite transverse direction. As the clockwise vortex sheds, one or two small counterclockwise vortices are pinched off from the boundary layer, which quickly disperses in the wake. This pair of clockwise and counterclockwise vorticity makes up a similar pair to that of the '2P' mode. If two counterclockwise vortices are pinched off due to the movement of the clockwise vortex around the cylinder, the wake is not quite a '2P' mode, but could be considered similar to the '2T' mode observed by Jauvtis and Williamson [30]. This mode does not quite form a triplet of vortices packed together as with Jauvtis and Williamson [30], but instead resembles a train of vortices that shed from the cylinder as it executes transverse motion. When the cylinder changes transverse direction, a train of opposite vorticity sheds and either two or three vortices of the same rotation are observed to shed in succession. A similar shedding pattern is reported in a free vibration simulation by Pontaza et al [49], where a freely vibrating cylinder is shown to oscillate with very similar motions to those in Fig. 4-21. In that case, a '2T' shedding pattern formed in the wake of the cylinder.

In this particular case of vortex shedding, the pairs or triplets of vortices are not equivalent in magnitude and one vortex dominates the wake over one half cycle of motion. This dominant vortex is nearly 10 times larger in magnitude than other features in wake and it stays in close proximity to the cylinder during the shedding process. This vortex and its counterpart in the other half of the cycle will largely determine the forces on the cylinder caused by vortex shedding.

Motions of the cylinder with slightly different phase and reduced velocity exhibit similar shedding characteristics to the $V_r = 6.38$ case. Figs. 4-22 - 4-25 show the wake behind the cylinder for nominal reduced velocities $V_{rn} = 5, 5.5, 6, 8$, true reduced velocity of $V_r = 5.15, 5.36, 5.73, 6.66$. Each of these cases exhibit a similar train of vorticity that sheds from the cylinder through transverse motion. As the cylinder reaches the apex of its motion, moving forward against the free stream, a large vortex moves around the cylinder and sheds downstream. For each of these cases, the phase between in-line and transverse motion lies between positive 45 degrees, at the low

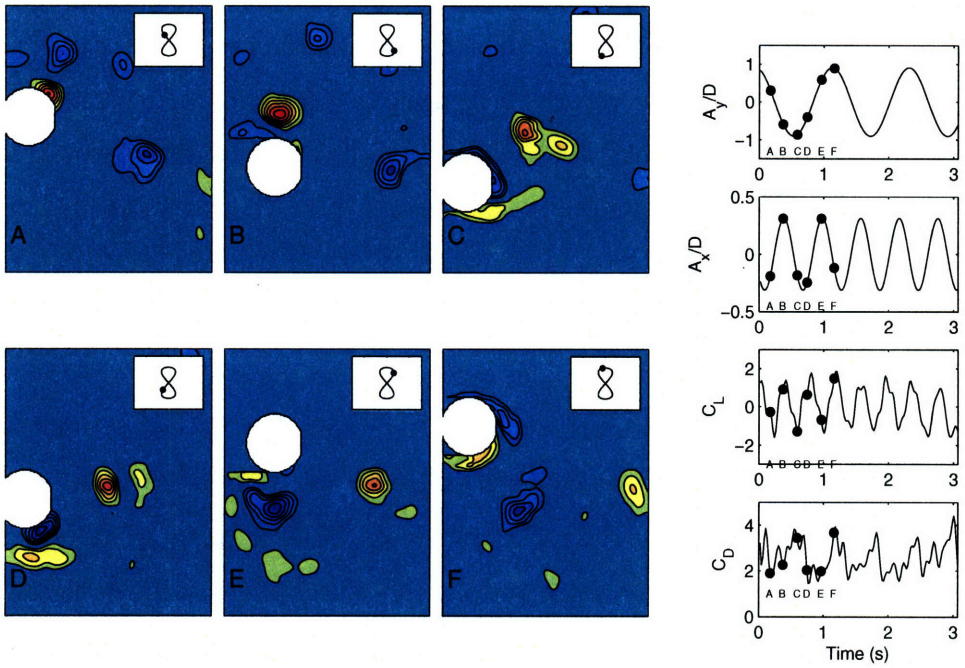

Figure 4-21: Flow Visualization of $f_x/f_y = 1.9$, $V_{rn} = 7.25$, $V_r = 6.38$. Vorticity contours show non-dimensional vorticity, $\frac{\omega D}{U} = \pm 3, \pm 5, \pm 7, \ldots$

reduced velocity, and negative 45 degrees, at the high reduced velocity. This slight change in the phase between these motions causes the forces associated with the dominant large vortex to have different phases.

In all of the shown cases, the dominant, large vortex begins to move downstream as the cylinder passes through the midpoint of its orbit. The shape of the orbit, however changes the relative position of the vortex with respect to the cylinder. With relative position in mind, one can see that in Fig. 4-22, the vortex train which forms in the wake of the cylinder is nearly vertical, if one were to draw a line through the similarly colored vorticity shedding in the wake. As reduced velocity increases and the phase between in-line and transverse motion decreases, the shedding train becomes more horizontal. At the highest reduced velocity, in Figure 4-25, the train is almost completely horizontal. This occurs since most of the vorticity sheds as the cylinder moves upstream. At the lower reduced velocity, the upstream motion is very steep, causing the train to be more vertical. As the orbit becomes more like a figure eight, the train of vorticity generally becomes more horizontal.

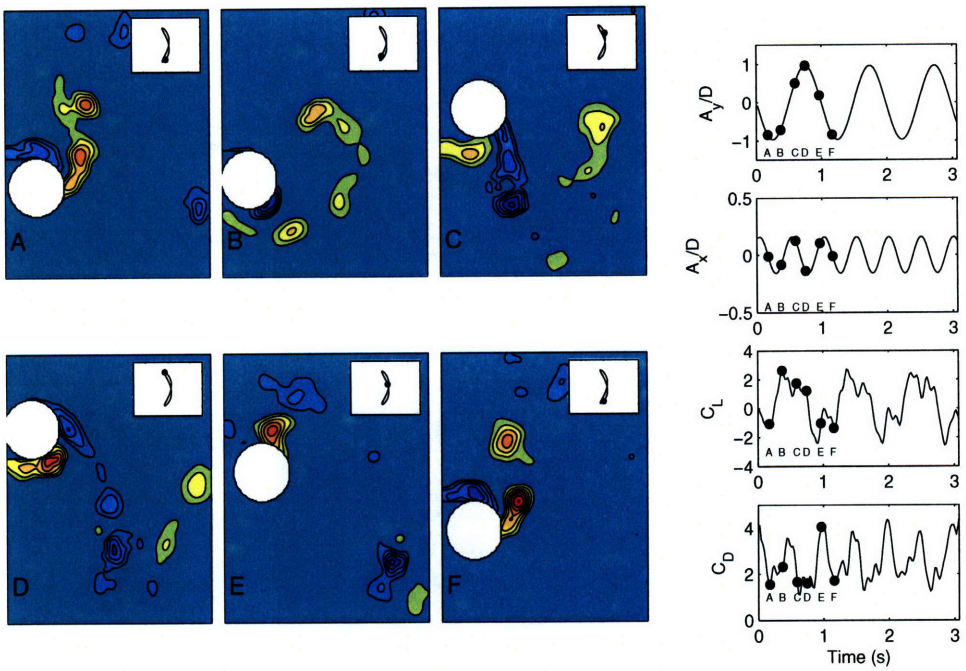

Figure 4-22: Flow Visualization of $f_x/f_y = 1.9$, $V_{rn} = 5$, $V_r = 5.15$. Vorticity contours show non-dimensional vorticity, $\frac{\omega D}{U} = \pm 3, \pm 5, \pm 7, \ldots$

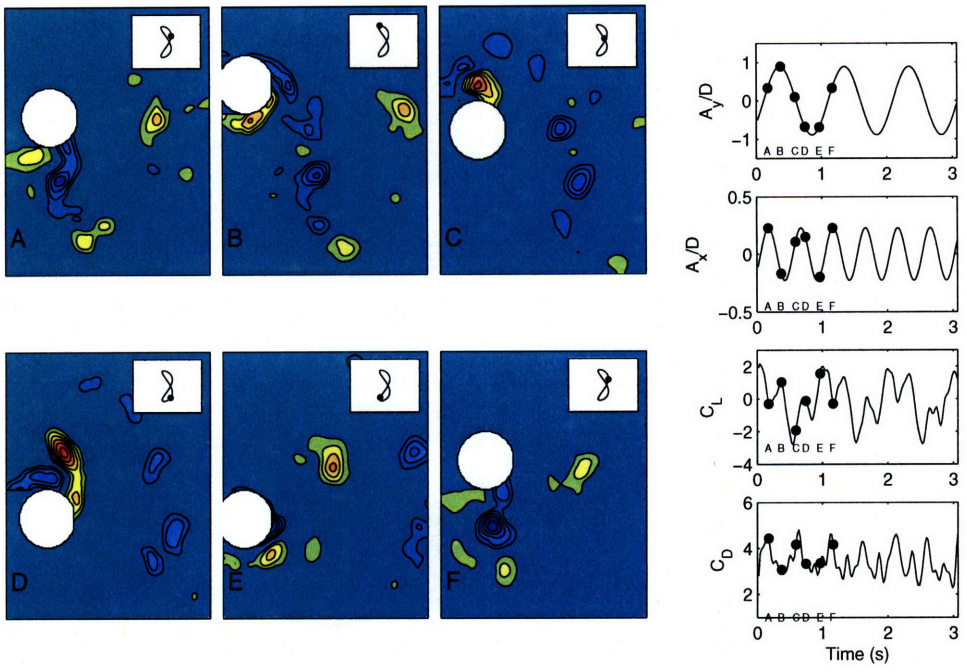

Figure 4-23: Flow Visualization of $f_x/f_y = 1.9$, $V_{rn} = 5.5$, $V_r = 5.36$. Vorticity contours show non-dimensional vorticity, $\frac{\omega D}{U} = \pm 3, \pm 5, \pm 7, \ldots$

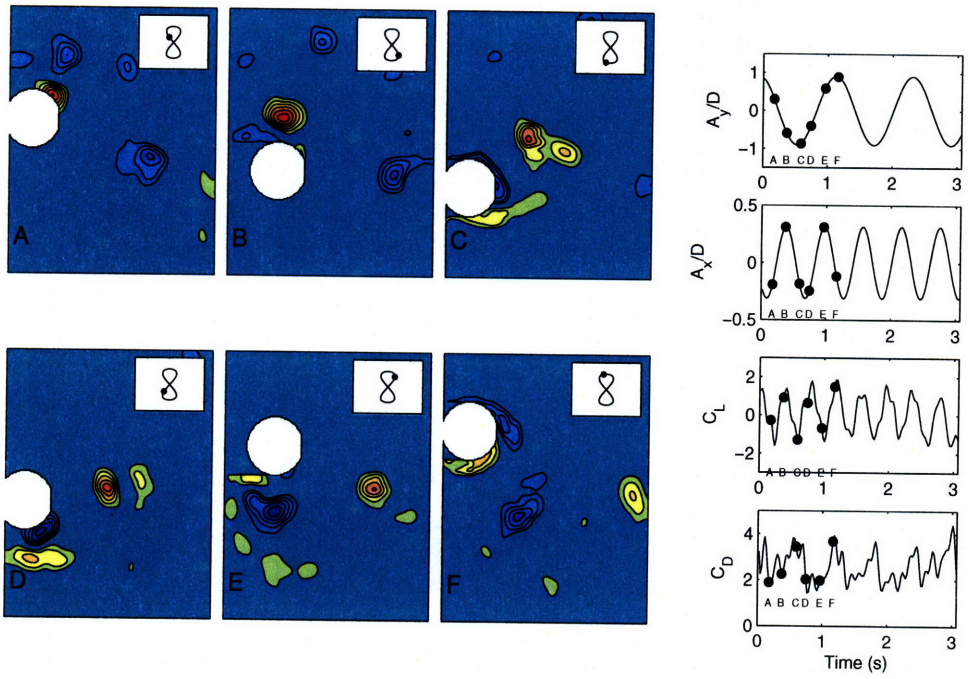

Figure 4-24: Flow Visualization of $f_x/f_y = 1.9$, $V_{rn} = 6$, $V_r = 5.73$. Vorticity contours show non-dimensional vorticity, $\frac{\omega D}{U} = \pm 3, \pm 5, \pm 7, \ldots$

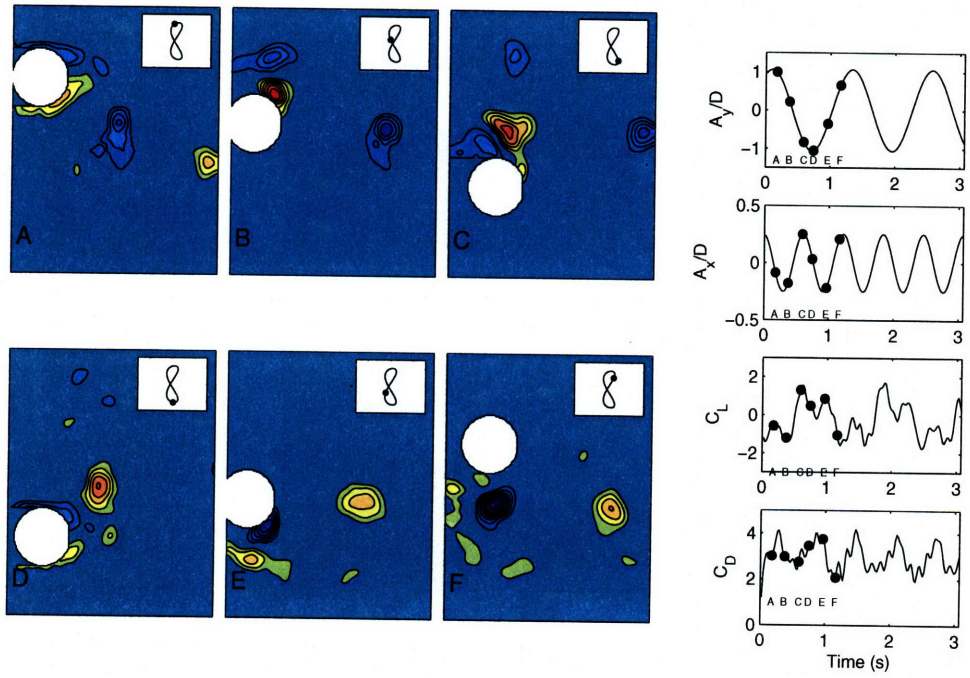

Figure 4-25: Flow Visualization of $f_x/f_y = 1.9$, $V_{rn} = 8$, $V_r = 6.66$. Vorticity contours show non-dimensional vorticity, $\frac{\omega D}{U} = \pm 3, \pm 5, \pm 7, \ldots$

The change in forces on the cylinder can be seen in each figure as well. A clear shift in the phase of the third harmonic portion of the force occurs. As the positioning between the dominant vortex and orbit of the cylinder change, the phase of the third harmonic force changes. Additional wake visualizations of equivalent free vibration motions are shown in Appendix C.

In the visualization of the wake behind the flexible cylinder, groups of multiple vortices with four or five vortices per group were seen to shed in the wake of the cylinder. These multiple vortex groups are not observed in the visualization of the equivalent free vibration wake. In PIV processing, it is difficult to resolve multiple small vortices when also resolving the entire wake behind the cylinder. Hence, multiple vortices may appear as one vortex depending on the particular processing algorithm used and the quality of the pictures obtained. Additionally, the irregularity of the flexible cylinder motions enhances the shedding of multiple vortex groups. The regular, repeatable motions of the elastically mounted rigid cylinder leads to a nearly repeatable wake shedding pattern with only '2P' or '2T' type shedding.

Explanation of the Third Harmonic Force

The third harmonic force in lift can be explained if we consider a simplified version of the cylinder wake. In Figure 4-21, we see that although the wake appears similar to a '2P' wake mode, there is one dominant vortex shed per half cycle. This dominant vortex is an order of magnitude larger in vorticity strength than other vortices in the wake. For the purpose of explaining the third harmonic force, these strong vortices will only be considered.

At a Reynolds number of 8760, inertial forces are much larger than frictional forces and measured lift forces will be composed of a force associated with acceleration of the fluid (added mass force) and forces exerted on the cylinder by vortices in the wake. This simplified representation is shown in Equation 4.4.

$$F = F_{addedmass} + \sum F_{vortex-n} \tag{4.4}$$

If we assume that frictional forces are negligible and the flow is primarily two dimensional, we can consider an equivalent potential flow representation of the wake. A number of studies have used a similar method for estimating fluid forces based on the observed wake [21, 39, 73]. Using the circle theorem and Blausius formula from Milne-Thompson [40], we can derive the formula for the lift and drag forces on a cylinder in the presence of a vortex, given in equations 4.5 and 4.6. This derivation is given in Appendix B.

$$L_{vortex-n} = \rho\Gamma_n a^2\left(\frac{u_n(x_n^2 - y_n^2) + 2v_n x_n y_n}{(x_n^2 + y_n^2)^2}\right) \tag{4.5}$$

$$D_{vortex-n} = \rho\Gamma_n a^2\left(\frac{v_n(x_n^2 - y_n^2) - 2u_n x_n y_n}{(x_n^2 + y_n^2)^2}\right) \tag{4.6}$$

In each of these equations, n denotes a specific vortex in the wake, the total force is determined as a sum over n. Velocities u and v are relative velocities of the vortex with respect to the cylinder. Positions x and y are relative positions of the vortex with respect to a coordinate system centered on the cylinder. The density of the fluid is denoted by ρ, the circulation of the vortex is Γ, and a is the radius of the cylinder. Including the forces exerted due to acceleration of the fluid, the lift force is written as Equation 4.7.

$$F_y = \rho\pi\frac{D^2}{4}\dot{U} + \sum_n \rho\Gamma_n a^2\left(\frac{u_n(x_n^2 - y_n^2) + 2v_n x_n y_n}{(x_n^2 + y_n^2)^2}\right) \tag{4.7}$$

In this representation of the fluid forces acting on the cylinder, added mass forces are a function of the changing free stream velocity. In the coordinate system fixed to the cylinder, the free stream velocity, U, will simply change as a function of the cylinder motions. Therefore, added mass forces will occur at the same frequency as the acceleration of the cylinder. In the transverse direction, added mass forces will contribute a lift force at the fundamental frequency of transverse motion; in the in-line direction, added mass forces will contribute a force at the fundamental frequency of in-line motion (twice the frequency of transverse motion). This shows that third

harmonic forces cannot be attributed to an added mass force if the cylinder has no motion excitation at the third harmonic frequency. Third harmonic forces must therefore be attributed to the vortex force of equation 4.5.

If we consider only one vortex shedding per half cycle while the cylinder moves in a figure eight pattern, we see a shedding pattern similar to that shown in Fig. 4-24. Fig. 4-26 shows a schematic of six points in the cycle of shedding as two vortices are shed from the cylinder. Using the arguments of Jauvtis and Williamson [30], defining the impulse force on the cylinder due to vortex motion in the wake, we can illustrate how third harmonic forces persist in Fig. 4-26. The direction of the in-line relative velocity is indicated on each vortex and the direction of the lift force caused by that vortex is indicated as well. In frame A, the cylinder is beginning to moving transversely downward and downstream in the in-line direction. A red vortex has just shed from the cylinder and has not yet begun to move downstream. The relative velocity of this vortex with respect to the cylinder is upstream and the lift force exerted on the cylinder is downward. In frame B, the red vortex has begun to move downstream and a blue vortex is beginning to form upstream of the cylinder. The red vortex is still dominant, but the relative velocity of this vortex with respect to the cylinder is now downstream. This results in a lift force pointing upward. The blue vortex is now well-formed in frame C and is the closest vortex to the cylinder. This vortex has a relative velocity downstream, but its opposite sign of circulation causes the lift force to be pointing down. This means that the lift force has fluctuated three times over the course of one half cycle. Continuing through the cycle in frames D-F, one can see that there is a total of six lift force fluctuations over the course of one cycle of motion. Six sign changes in lift correspond to a third harmonic force. In essence, the transverse motion of the cylinder results in two sign changes of the lift force due to the alternate shedding of vortices. The in-line motion of the cylinder results in four sign changes of the lift force due to the change in relative velocity of the shed vortex with respect to the cylinder.

This representation of the vortex force is extremely simplified to explain fluctuations in the lift force. The proximity of vortices with respect to the cylinder and

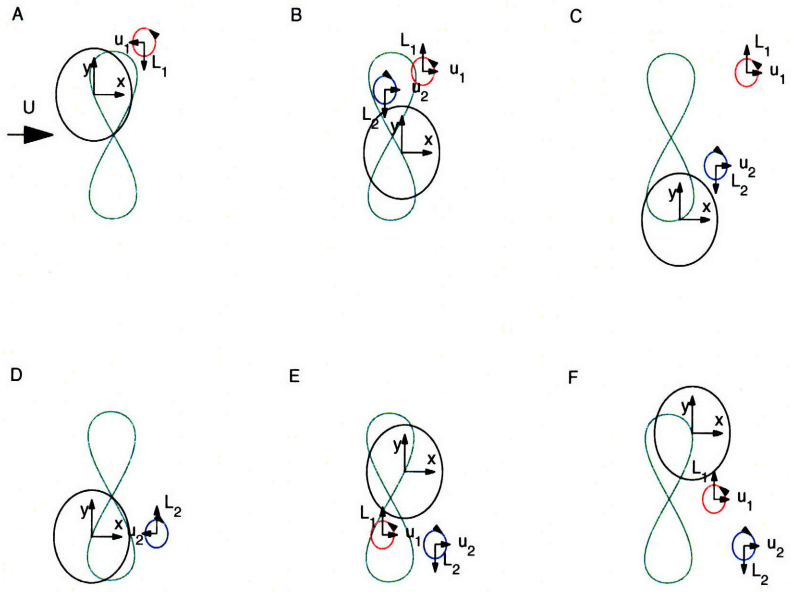

Figure 4-26: Schematic of simplified vortex shedding behind a cylinder with figure eight orbital shape.

strength of the vortices play a significant role in determining the actual magnitude of forces exerted on the cylinder. Similarly, the phase of the cylinder motion plays an important role since the relative positions and velocities of vortices with respect to the cylinder will change if the orbital chape of the cylinder changes.

If we track the large vortices in the wake of the equivalent free vibration from Fig. 4-24, we can generate values for the relative velocities and positions of each vortex with respect to the cylinder. Integrating the vorticity over the area of each vortex, we can estimate the circulation of that vortex. Using the estimated circulation and relative position and velocities, we can use Equation 4.7 to calculate a lift force on the cylinder due to potential flow vortices in the wake and ideal added mass. Fig. 4-27 shows this calculation for the equivalent free vibration case with $V_r = 5.73$ (see Fig. 4-24). The black line indicates the measured lift coefficient obtained from the six-axis force sensor. The dashed red line shows the total lift force calculated from the potential flow approximation. One can see that the potential flow approximation is not perfect since the flow is not truly two dimensional and the PIV image plane may not perfectly match the phase of the total force exerted on the cylinder. This problem

is known to occur anytime forces from a three dimensional process are estimated from an incomplete measurement of the velocity field [62]. More accurate measurement of forces from the wake can be obtained based on more complete velocity field information forward of the cylinder [46, 66]. The frequency match between the potential flow estimate and the measured lift force is very good, and in some portions of the cycle the curves are nearly identical.

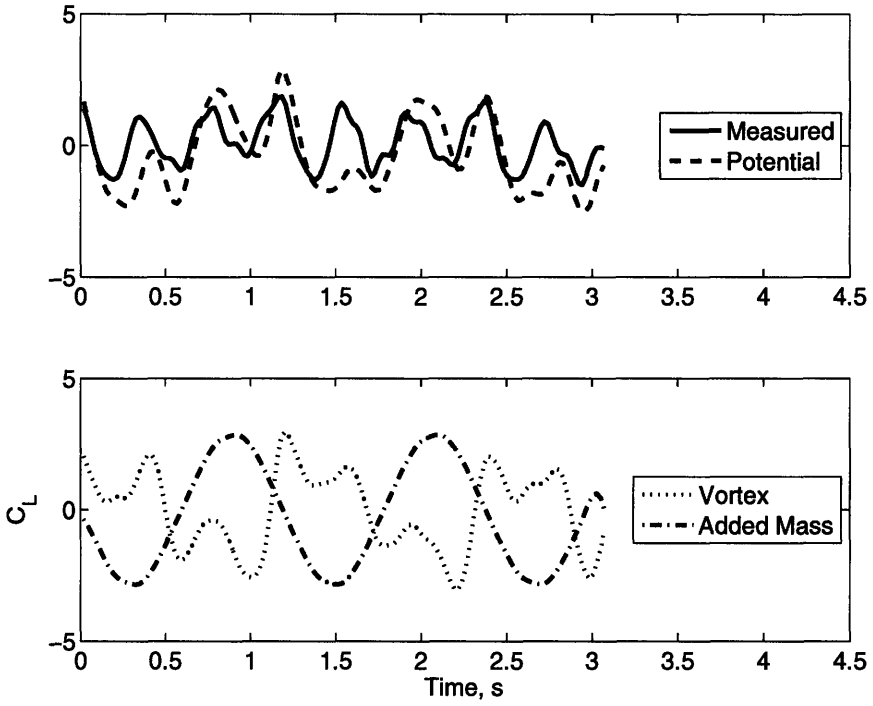

Figure 4-27: Potential flow estimate of lift forces on the cylinder for $V_r = 5.73$

In Fig. 4-27, the potential flow force is also broken into its two components, the added mass force (dash-dot line) and the vortex force (dotted line). The added mass force has no components of third harmonic as expected since this value is only a function of the relative cylinder acceleration. The vortex force clearly contains a first and third harmonic component of force due to the shedding of vortices and the relative motion of these vortices with respect to the cylinder. In this particular case, the peak of the added mass force almost perfectly lines up with the trough of the first harmonic portion of the vortex force. When added together, we see that the added mass force and first harmonic portion of the vortex force almost completely cancel

one another, resulting in a total lift force dominated by the third harmonic.

If we look at the forces associated with the wake observed in Fig. 4-23, we see that the lift force has a larger component of first harmonic force. Fig. 4-28 shows the same potential flow estimate applied to the wake in this case. Here we see that the vortex force and added mass force look very similar to the forces observed in Fig. 4-27, but the phase between these two forces is slightly different. When added together, the first harmonic portion of lift is much larger in this case.

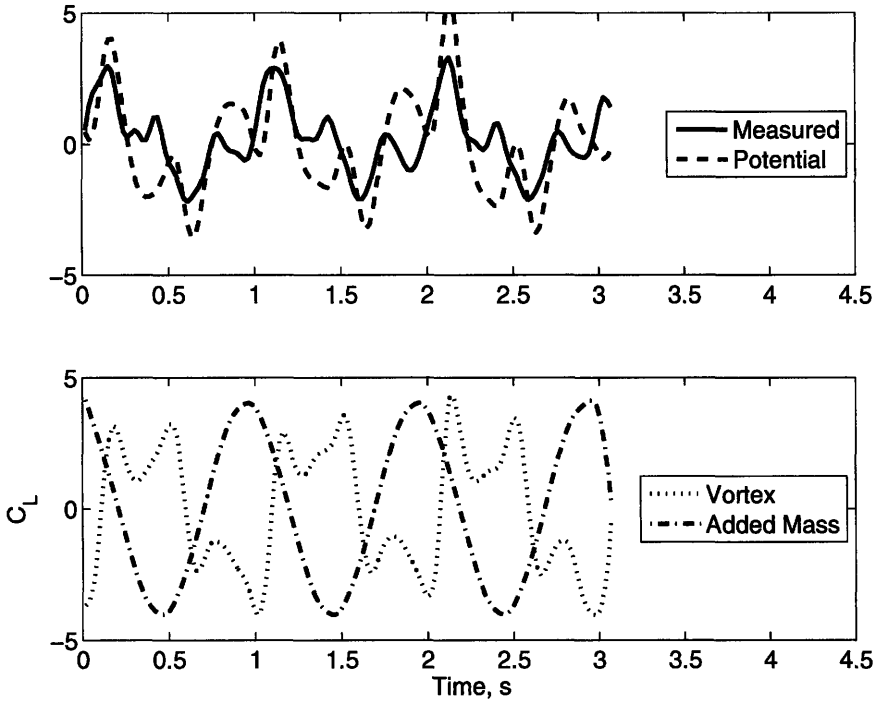

Figure 4-28: Potential flow estimate of lift forces on the cylinder for $V_r = 5.36$

From this potential flow estimate of the wake, we can see that the dominance of the third harmonic portion of lift is largely a function of the phase of vortex shedding. The third harmonic itself is shown to come from the relative motion of vortices in the wake with respect to the cylinder. Since the cylinder has in-line motions, there are additional fluctuations in the relative velocity between shed vortices and the cylinder. The third harmonic is not necessarily related to the number of vortices shed in the wake, although the magnitude of the third harmonic may be larger with more vorticity in the wake. Higher harmonics such as the fifth or seventh harmonic could

be explained by considering additional downstream vortices and their contribution to the lift force on the cylinder. Since these vortices are very far away from the cylinder, they make a negligible contribution to lift and are not significant in the measurement of lift.

4.5 Forced Vibrations of Rigid Cylinder

Third harmonic forces in lift have been shown to be largely a function of the cylinder motions, particularly in-line motions, and the phase of vortex shedding. One question that one might ask is how these forces and the resulting wake will change if the motion parameters governing the vibration are perturbed. For instance, will larger in-line motions cause larger amplitude third harmonic forces? How does phase between in-line and transverse motion affect the wake behind the cylinder?

The questions could be answered by doing an exhaustive flow visualization across the entire parameter space of motions. Williamson and Roshko [76] showed how the wake of the one degree of freedom system changes as a function of transverse amplitude and reduced velocity. This type of exhaustive visualization of the cylinder wake in the two degree of freedom case would be very time consuming and difficult since two degree of freedom motions are governed primarily by four parameters, in-line motion (A_x/D), transverse motion (A_y/D), phase between in-line and transverse motions (θ), and reduced velocity (V_r). In order to simplify the parameter space to consider, only cylinder motions that have a dominant third harmonic associated with the motion are considered, since the third harmonic is the predominant theme of this thesis.

The free vibration case analyzed in the previous section, where $V_r = 6.4$ and $f_x/f_y = 1.9$ serves as the base motion for my forced vibration study. This case had $A_y/D = 0.91$, $A_x/D = 0.31$, and $\theta = 0$. In this section, this base motion of the cylinder is perturbed in three ways, phase variation, amplitude variation, and reduced velocity variation. In each case, the wake is observed using PIV visualization as in the previous sections. Forces on the cylinder are measured as well.

In varying phase, the in-line and transverse amplitudes of the cylinder motion are held constant, equal to the values reported above. The reduced velocity is held at 6.4 and the 9 tests are performed varying the phase between in-line and cross-flow motions from -180 degrees to 180 degrees in increments of 45 degrees. Variation of amplitudes is performed by holding the phase of motion constant at 0 degrees and holding the reduced velocity constant at 6.4. The in-line amplitude is varied from 0.15 to 0.45 in increments of 0.075 while the transverse amplitude is varied from 0.5 to 1.5 in increments of 0.25. These motions are based on the observed free vibration magnitudes and they result in a total of 25 test cases. In varying reduced velocity, amplitudes and phase were again held constant at the values denoted above and the reduced velocity was varied from 4 to 7 in increments of 1. The towing velocity in all forced experiments was 0.2 m/s and the Reynolds number was 7620.

This variation of parameters is a more expansive variation than the two degree of freedom forced motions performed by Jeon and Gharib [31]. In those experiments, the in-line and transverse amplitudes of motion were much smaller than those observed for low mass ratio, low damping vibrations. The phase of motions in the experiments of Jeon and Gharib [31] were limited to phases between -45 and 45 degrees.

4.5.1 Phase Variation

Varying the phase of motion for the cylinder in two degree of freedom motion has a significant impact on both the measured forces on the cylinder and the wake structure behind the cylinder. Fig. 4-29 shows the power spectral density of the total lift force signal measured from the forced oscillations of the cylinder at each specified phase. At zero phase, the equivalent free vibration motions, there is nearly zero first harmonic component of the lift force and the amplitude of the third harmonic component of lift is close to 1. As the phase increases to more positive values towards 180 degrees, the first harmonic component of the total lift force grows rapidly. The third harmonic portion of lift grows as well and a small fifth harmonic component can be seen. These larger amplitude forces are primarily due to larger magnitude vorticity in the wake of the cylinder as the cylinder is forced through these extreme motions and due to the

phase relation of vortex shedding with respect to the cylinder motions.

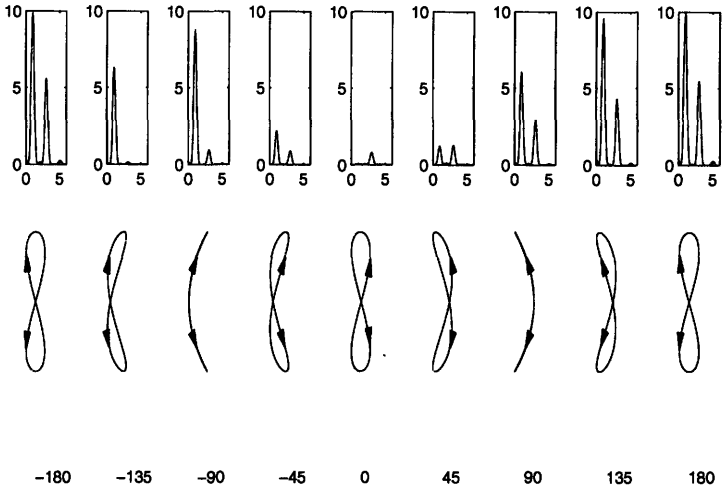

Figure 4-29: Power spectral densities of lift coefficient for varied phase angles of motion. $A_y/D = 0.91, A_x/D = 0.31, V_r = 6.4$.

As phase runs through negative values towards -180 degrees, the first harmonic force grows in magnitude again. At -135 degrees, there is almost no third harmonic force present. The reason for the disappearance of the third harmonic force can be shown by the observed wake modes. At -180 degrees, the forces are exactly the same as with 180 degrees since the cylinder motions are equivalent.

If we break the first harmonic component of lift into components of lift in phase with velocity, C_{Lv}, and effective added mass coefficient, C_m, we can see how phase significantly alters these values (see Fig. 4-30). In the two degree of freedom forced motion, since energy can transfer from within the closed system through both in-line and transverse motions, it is better to consider the normalized average power over one cycle of motion. When this value is positive, it indicates the region where a free vibration can potentially occur. One can see that the large forces associated with cylinder motions away from zero phase occur due to the fact that the normalized average power is fairly large and negative. This means that the linear motors are pumping a large amount of energy into the fluid by forcing the cylinder through the fluid. The relevance of measuring fluid forces due to the forced motions of a cylinder is discussed in Chapter 5.

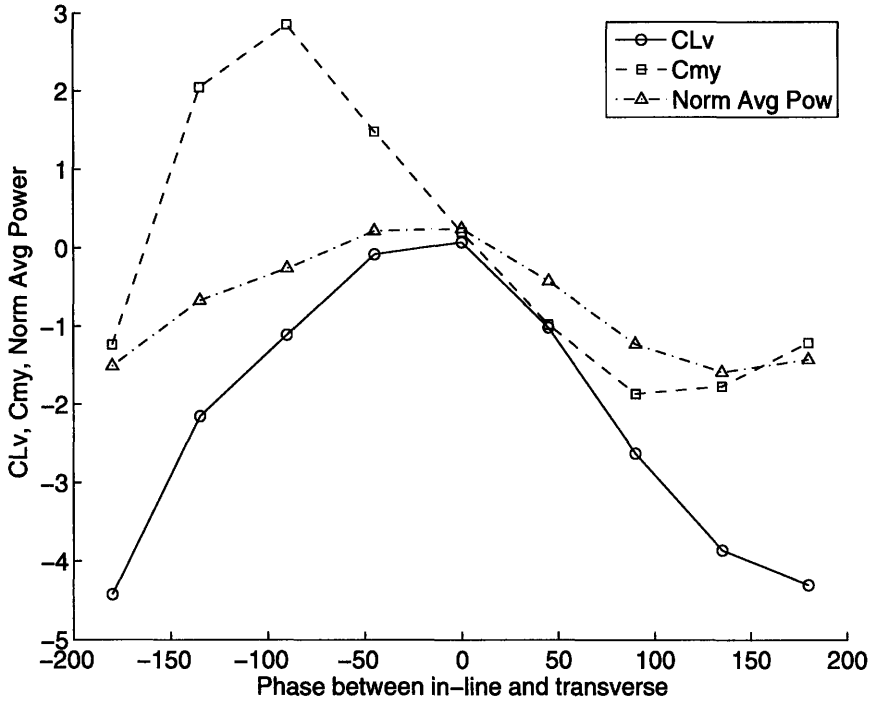

Figure 4-30: Components of the first harmonic portion of lift force for varied phase angles. $Y/D = 0.91, X/D = 0.31, V_r = 6.4$.

The effect of motion phase angle on the wake of the cylinder for the given fixed amplitude and reduced velocity is very distinct in some cases. Fig. 4-21 shows the cylinder wake for the cylinder motions with zero phase angle. As the phase angle increases, the wake shows a streak of vorticity that sheds as the cylinder goes through its transverse motions. As opposed to shedding one large vortex over the course of transverse motion, the cylinder sheds two large like-sign vortices. In the extreme case of the phase being 180 degrees (Fig. 4-31), there is almost a third like-signed vortex that sheds at the apex of the transverse motion. The large like-sign vortices spin together and coalesce in the wake. This type of wake is similar to the '2T' pattern observed by Jauvtis and Williamson [30], but the vortices are not tightly packed as a grouped triplet. Since the strength of this vorticity is very large, the forces exerted on the cylinder are very large as well. The wakes for intermediate positive phases are shown in Appendix C.

At a phase angle of -45 degrees, the wake of the cylinder takes on a '2P' pattern.

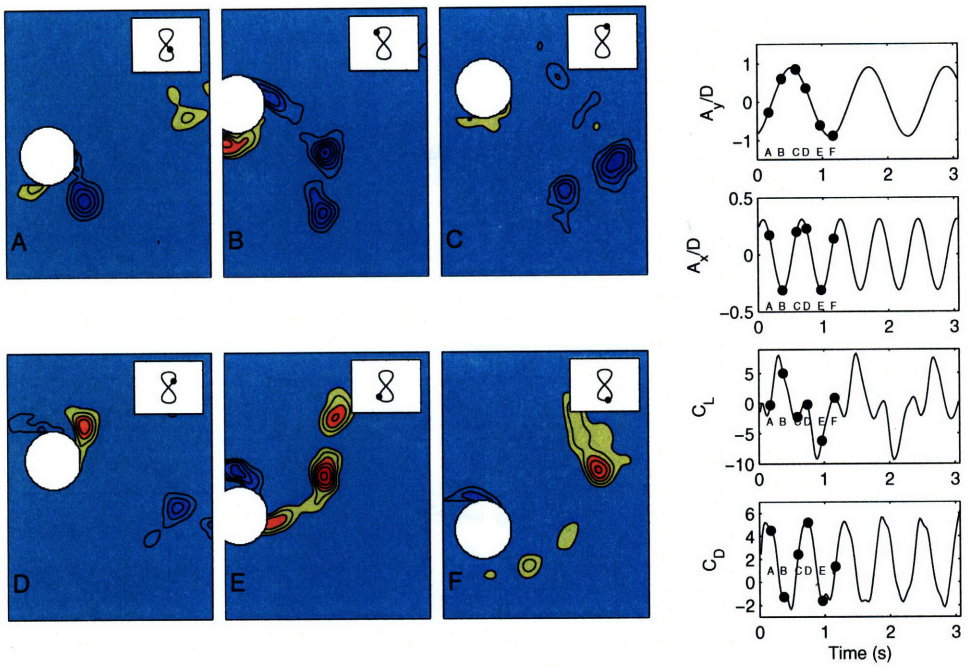

Figure 4-31: Cylinder wake for $\theta = 180$ degrees. $A_y/D = 0.91, A_x/D = 0.31, V_r = 6.4$.Vorticity contours show non-dimensional vorticity, $\frac{\omega D}{U} = \pm 3, \pm 5, \pm 7, \ldots$.

At more negative phases, however, the pattern switches to a '2S' pattern. For phases of both -90 and -135 degrees, the cylinder only sheds two single vortices per cycle and the shed vortices do not cross the centerline of the wake. Fig. 4-32 shows the wake of the cylinder for $\theta = -135$ degrees. One noticeable difference with this case is that the lift force on the cylinder is primarily composed of first harmonic forcing, with very little third harmonic component. This occurs because the vortex sheds as the cylinder reaches it apex of transverse motion. At this point, the cylinder is also beginning to move downstream as it is caught in the free stream on the upper or lower side of the cylinder, so the relative velocity of the vortex with respect to the cylinder does not change. By the time the in-line motion of the cylinder changes again, the shed vortex has moved downstream and is now relatively far away from the cylinder. The change in relative velocity of the vortex has less of an effect and the third harmonic portion of the force is very small. Additional wakes for negative phase motions are shown in Appendix C.

One can conclude from these phase representations that the third harmonic force is

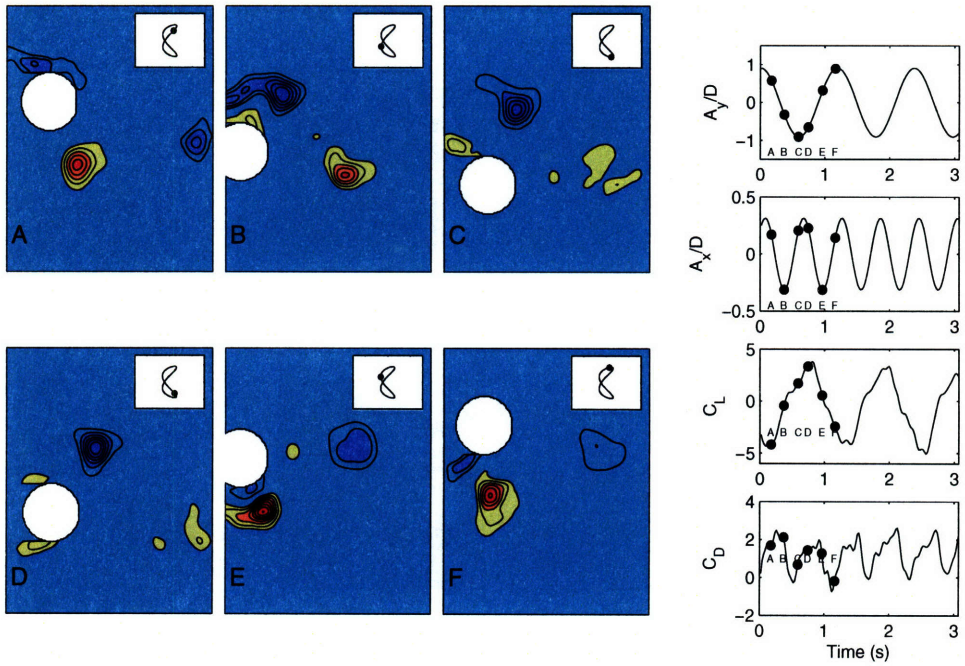

Figure 4-32: Cylinder wake for $\theta = -135$ degrees. $A_y/D = 0.91, A_x/D = 0.31, V_r = 6.4$.Vorticity contours show non-dimensional vorticity, $\frac{\omega D}{U} = \pm 3, \pm 5, \pm 7, \ldots$.

largely related to the '2P' or '2T' shedding mode. In each of these modes, one vortex must pass from one side of the cylinder around to the other side of the cylinder, remaining in close proximity to the cylinder. This allows for the in-line motion of the cylinder to effectively change the relative velocity of the vortex with respect to the cylinder while the vortex is in close proximity to the cylinder. In the '2S' mode, it is still possible to have a third harmonic force, but it is less likely if the vortex sheds at such a way that the vortex relative velocity does not change significantly while the vortex is near the cylinder.

4.5.2 Amplitude Variation

Variation of amplitude on the base two degree of freedom motions of the cylinder resulted in significant changes in force measurements as well. Figure 4-33 shows the individual lift coefficient spectra for each combination of in-line and transverse amplitude. The free vibration amplitude again corresponds to $A_y/D = 0.91$ and

$A_x/D = 0.31$. There is a general trend in the spectra in relation to increasing in-line amplitude. As in-line amplitude increases, the magnitude of the third harmonic force increases, regardless of the transverse amplitude of motion. This is expected since larger in-line motions will result in larger changes in the relative velocities of vortices shed in the wake of the cylinder. Increasing the transverse amplitude of motion generally results in an increase in first harmonic portion of the force and a decrease in the third harmonic portion of the force. Although this trend is not necessarily true for all reduced velocities or phases, it is interesting that the third harmonic decreases as the transverse amplitude becomes large. This may occur since shed vortices will be further away from the cylinder if transverse motions are large, reducing the force exerted on the cylinder, but this hypothesis must be justified by the wake.

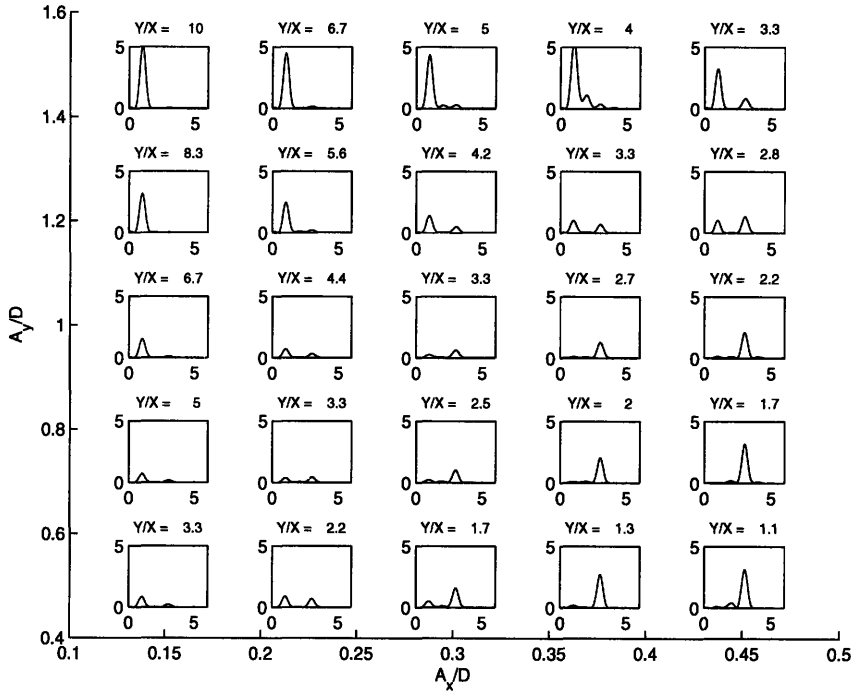

Figure 4-33: Power spectral densities of lift coefficient for varied amplitudes of motion. $\theta = 0$ degrees, $V_r = 6.4$.

In general, increased in-line motion causes the wake of the cylinder, under any tested combination of amplitudes, to look like a '2P' or '2T' mode, depending on the transverse amplitude of motion. At this reduced velocity, for small in-line amplitudes,

the '2P' mode consists of one strong vortex and one weak vortex. The strong vortex is the first vortex shed per half cycle so this vortex quickly moves away from the cylinder and in-line motion has little effect on producing a large third harmonic force. The stronger vortices can clearly be seen in the example case shown in Figure 4-34. For larger in-line motions, both vortices in the pair have a large magnitude of vorticity. The second vortex shed in the half cycle is now very close to the cylinder as it fluctuates in the in-line direction, producing a large change in relative velocity near the cylinder. The larger strength vortices are distinguished in Figure 4-35.

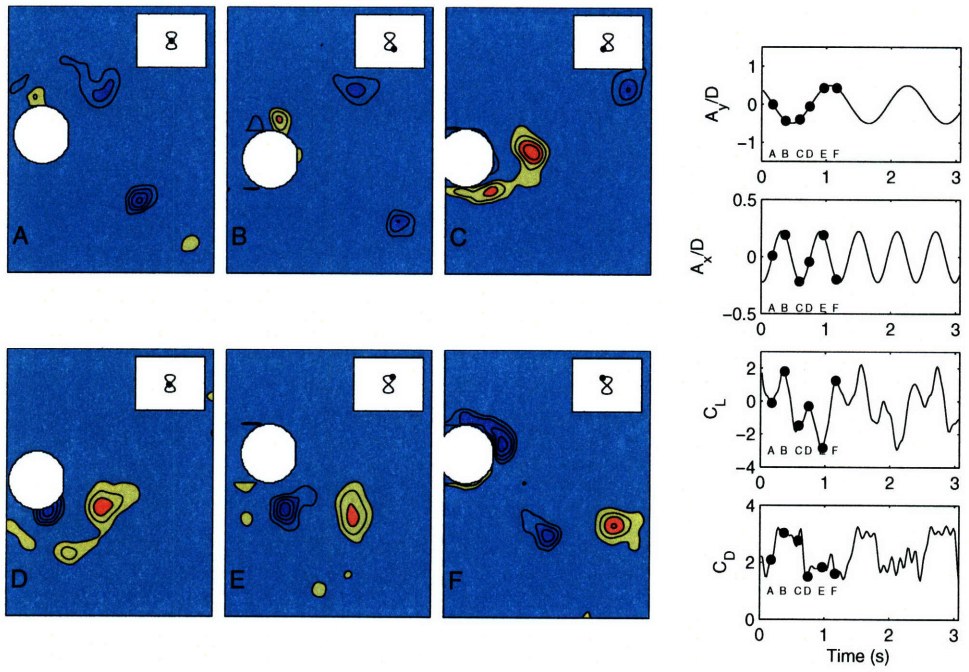

Figure 4-34: Cylinder wake '2P' mode formation (one weak vortex, one strong vortex in pair).$A_y/D = 0.5, A_x/D = 0.225, \theta = 0$ degrees, $V_r = 6.4$. Vorticity contours show non-dimensional vorticity, $\frac{\omega D}{U} = \pm 3, \pm 5, \pm 7, \ldots$.

For large transverse and in-line motions, the wake was quite messy and it was difficult to distinguish distinct modes in the wake. Selected visualizations of the wake over the various amplitude combinations are included in Appendix C.

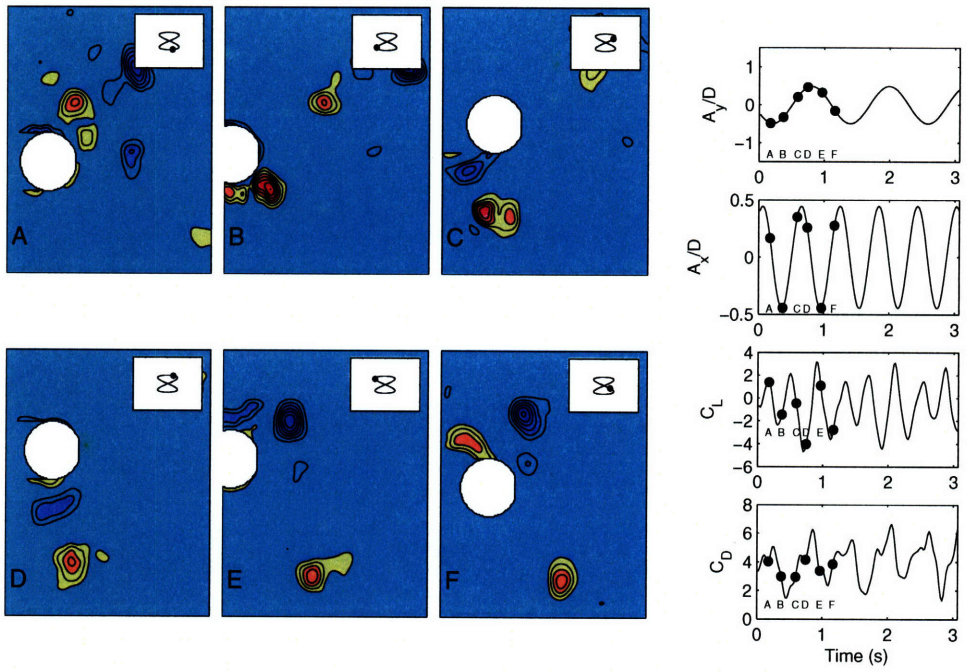

Figure 4-35: Cylinder wake '2P' mode formation (two strong vortices in pair). $A_y/D = 0.5, A_x/D = 0.45, \theta = 0$ degrees, $V_r = 6.4$. Vorticity contours show non-dimensional vorticity, $\frac{\omega D}{U} = \pm 3, \pm 5, \pm 7, \ldots$.

4.5.3 Reduced Velocity Variation

For fixed amplitudes and fixed phase, variation of reduced velocity did not seem to significantly alter the shedding pattern in the wake at given phase and amplitudes of oscillation. Reduced velocity did change the frequency of shedding such that the wavelength between shed vortices was smaller for lower reduced velocity, however the basic pattern did not seem to change significantly. The wake maintained a '2P' pattern similar to that observed for the equivalent free vibration base case, where there was one large vortex and one smaller vortex making up the pair in the '2P' pattern. At a reduced velocity of 4, the cylinder actually collided with many vortices in the wake since there was not sufficient time for shed vortices to propagate downstream. As reduced velocity increases, shed vortices are more spread out downstream. The width of the wake remained relatively constant regardless of reduced velocity. Selected visualizations of reduce velocity variations are included in Appendix C.

Chapter 5

Forced Vibration Database

The vibration of very long ocean structures is very complicated as ocean currents and structural properties vary with depth. It is typical that ocean structures may be excited in free vibration over only a small section of the structure [61, 69]. Energy transferred span-wise along the structure may lead to forced vibrations elsewhere in the structure. The free vibrations of a rigid cylinder as part of a simple spring-mass-dashpot system are limited to motions in which the average total power integrated over one cycle of motion must be equal to zero. Forced vibrations at a cross section of a marine riser may not have an average power equal to zero as energy can travel along the length of the flexible riser. If one wants to predict possible forces seen by a marine riser, it is therefore relevant to consider both free vibrations from experimentation and possible forced vibrations.

The analysis of two degree of freedom free vibrations in previous chapters has shown that one degree of freedom assumptions can be flawed when predicting the forces and amplitudes associated with two degree of freedom vortex induced vibrations. Free vibrations in two degrees of freedom result in much larger peak amplitudes of transverse motion and lift forces may contain large amplitude third harmonic portions, dependent on the cylinder orbit and wake structure.

To account for the effects of two degree of freedom motions on vortex induced vibrations, a new force model is proposed, containing higher harmonic components. In order to determine the force coefficients for this force model, a matrix of forced

vibrations are performed spanning the relevant non-dimensional parameters. Forced motions of a rigid cylinder are performed while measuring the resulting forces. The forced vibration apparatus described in Chapter 4 is used for these experiments.

5.1 Database Parameters

5.1.1 Motion Definitions

Cylinder vibrations in two degrees of freedom can be categorized into a number of different possibilities: 1) Vibrations where the in-line frequency is exactly twice the transverse frequency (orbit shapes are repeatable), 2) Vibrations where the in-line frequency has discrete frequency content that is not twice the transverse frequency (orbit shapes are repeatable), 3) chaotic vibrations (orbit shapes are non-repeatable). The purpose of this database is to gain an initial understanding of the fluid forces associated with repeatable, single frequency vibrations, hence all motions have a fixed in-line to transverse frequency ratio of two.

Vortex induced vibrations typically produce sinusoidal motions, so database motions are based on sinusoidal cylinder motions. Equations 5.1 and 5.2 show the sinusoids used to describe the forced cylinder motions. The frequency of these motions, ω, is determined according to the reduced velocity, V_r in equation 5.3.

$$\frac{y}{D} = \frac{A_y}{D} cos(\omega t) \tag{5.1}$$

$$\frac{x}{D} = \frac{A_x}{D} cos(2\omega t + \theta) \tag{5.2}$$

$$V_r = U/(2\pi\omega D) \tag{5.3}$$

One major difference between one degree of freedom forced vibration experiments and two degree of freedom experiments is the significantly larger number of control parameters. In one degree of freedom experiments, the transverse amplitude and

reduced velocity can be varied to cover possible resonant motions of the cylinder. In two degrees of freedom, the addition of in-line motion adds a necessary variation in in-line motion, A_x/D, along with a variation in the phase relationship between in-line and transverse motion. This phase relationship is denoted by θ in Equation 5.2. The phase between in-line and transverse motion determines the direction in which the path of the cylinder is traveling when observing from a coordinate system fixed to the carriage.

The transverse motion non-dimensional amplitude, A_y/D, is varied with six values over a range from 0.25 to 1.5. This range is determined from the range of motions observed in free vibration experiments. In-line non-dimensional amplitude, A_x/D, ranges from 0 to 0.75, again according to observations from field and lab experiments. The phase parameter, θ, was shown to vary between -90 and 90 degrees in the free vibration experiments of chapter 3, however Jauvtis and Williamson [30] experienced phases over an even broader range. To ensure a complete investigation of the parameter space, θ is varied from -180 to 180 degrees in increments of 45 degrees. Eight values of reduced velocity were investigated in the range from 4.5 to 8 based on the observed reduced velocities from free vibration experiments. The total motion parameter space is defined by 6 transverse amplitudes, 6 in-line amplitudes, 8 phases between in-line and transverse motions, and 8 reduced velocities, for a total of 2304 experimental runs. The Reynolds number is held constant at a value of 8760 for reduced velocities greater than or equal to 6 and the Reynolds number is 6860 for reduced velocities less than 6. The Reynolds number cannot be held constant for all motions due to frequency constraints on the experimental apparatus.

5.1.2 Force Definitions

Assuming that the dominant lift force occurs at the fundamental frequency of cylinder motion as in one degree of freedom cylinder oscillations is not sufficient for describing lift and drag forces seen in two degree of freedom oscillations. Higher harmonic components of lift and drag must be included in the model of forces in order to account for these differences. Equations 5.4 and 5.5 show models for lift and drag

coefficients that include higher harmonic forces. The number of the harmonic is denoted by the force magnitude subscripts. Additional harmonics could be added if necessary, although measured harmonics in these experiments are shown to be insignificant beyond the fifth harmonic.

$$C_L = C_{L1}cos(\omega t + \phi_1) + C_{L3}cos(3\omega t + \phi_3) + C_{L5}cos(5\omega t + \phi_5) + \ldots \quad (5.4)$$

$$C_D = C_{Dmean} + C_{D2}cos(2\omega t + \phi_2) + C_{D4}cos(4\omega t + \phi_4) + \ldots \quad (5.5)$$

The phases shown in equations 5.4 and 5.5 are referenced to the cylinder motions. For instance, ϕ_1 is the phase between first harmonic force and transverse motion. This phase is the same as defined for a one degree of freedom vibration as in Chapter 2. The phase, ϕ_3, refers to the phase between third harmonic force and transverse motion. As shown in equation 5.1, the transverse motion of the cylinder has no third harmonic component, so the value of ϕ_3 refers to the phase between the third harmonic force and the first harmonic motion. Since the third harmonic has three times the frequency of the first harmonic, the associated phase between force and motion will repeat three times over the course of one cycle of transverse motion. Therefore, ϕ_3 must repeat every 120 degrees as opposed to every 360 degrees. Similarly, ϕ_5 will repeat every 72 degrees. The phases in the drag equation are referenced to the in-line motion.

5.1.3 Added Mass, C_m

The magnitudes and phases of equations 5.4 and 5.5 can be determined by directly measuring the resulting forces from forced vibrations. The traditional way of representing these forces, as described in [3, 52] breaks the lift into forces in phase with acceleration and forces in phase with velocity. The force in phase with acceleration can be used to determine a representative added mass coefficient. In two degree of

freedom rigid cylinder oscillations, the third harmonic force is not related to third harmonic cylinder oscillations since these motions do not exist. Therefore, added mass can still be determined from the portion of the lift in phase with cylinder accelerations.

The added mass coefficient can then be computed by equating the added mass force with the force in phase with acceleration.

$$m_{ay} Y \omega^2 cos(\omega t) = L_1 cos(\phi_1) cos(\omega t) \tag{5.6}$$

If we non-dimensionalize and rearrange to solve for the added mass coefficient, we obtain:

$$C_{my} = \frac{-2U^2 C_{L1} cos(\phi_1)}{\pi (Y/D) D^2 \omega^2} \tag{5.7}$$

Since high even harmonic forces in the in-line direction are small in comparison to the second harmonic, the added mass in the in-line direction can be shown to be calculated in the same manner as the traditional C_{my}, where ω is the fundamental transverse frequency of motion.

$$C_{mx} = \frac{-2U^2 (C_{D2} cos(\phi_2))}{\pi (Y/D) D^2 (2\omega)^2} \tag{5.8}$$

5.1.4 Average Power

Fluid forces associated with vortex induced vibrations will cause excitation of motion or dissipation of motion depending on the flow of power in the system. In a free vibration, energy can either flow from the fluid to the spring mass system, exciting the spring mass system, causing motions to grow, or energy can flow from the spring mass system to the fluid, damping motions of the cylinder. In a free vibration, the flow of energy fluctuates over the course of vibrations, however, if the cylinder oscillations are regular and repeatable, the total average power calculated over one cycle of motion must be equal to zero. This must be true in order to satisfy conservation of energy. If the average power over one cycle of motion is positive, then the net energy in the

system must be growing. In order to store that energy, the springs in the system must deflect more, hence vibrations will be growing. Similarly, if the average power over one cycle is negative, energy must be flowing out of the system, hence motions will decrease. If motion amplitudes are constant, the average power over one cycle will be zero as the energy into the system balances the energy out of the system.

In the case of forced vibrations, the motions of the cylinder are fixed, hence, the system cannot adjust amplitudes to ensure that the average power over one cycle is zero. Therefore, in forced vibrations the average power can take on values positive or negative depending on the actual cylinder motions. The region where forced vibrations show an average power equal to zero indicate the theoretical region over which a free vibration may occur. This region is theoretical since a free vibration is compliant and hence will not always have the same amplitude of motion over individual cycles. It will be shown, however, that the theoretical free vibration region as predicted from forced vibrations is a fairly good match.

The average power over one cycle of motion is defined as the integral in time over one cycle of motion of the total force times the velocity. The power is normalized to produce an average power coefficient, C_{ap}.

$$C_{ap} = \frac{\frac{1}{t_2-t_1}\int_{t_1}^{t_2}(\mathbf{F}\cdot\mathbf{v})dt}{\frac{1}{2}\rho U^3 DS} \tag{5.9}$$

Expanding equation 5.9 in terms of the lift and drag allows one to see differences between the average power for a one degree of freedom vibration and a two degree of freedom vibration, where D_f is the fluctuating component of drag.

$$C_{ap} = \frac{\frac{1}{t_2-t_1}\int_{t_1}^{t_2}(\mathbf{L}\cdot\dot{\mathbf{y}} + \mathbf{D_f}\cdot\dot{\mathbf{x}})dt}{\frac{1}{2}\rho U^3 DS} \tag{5.10}$$

In a one degree of freedom vibration, there is no in-line motion, hence the $\dot{x}$ is zero and forces in the drag direction do not contribute to the calculated average power. In this case, equation 5.10 reduces to an expression similar to the inner product representation of C_{Lv}. The normalization is slightly different, however C_{Lv} and C_{ap} would be directly related by a scalar value.

In a two degree of free vibration, an energy balance must be accomplished considering motions in both the in-line and transverse directions. It is possible, in this case, for energy to flow in through transverse excitation and out through in-line excitation, or vice versa. Phase between these motions plays an important role in determining the direction of energy flow. A simple trigonometric expansion of in-line motions shows the important role of the phase, θ, on the average power calculation.

$$x = Xcos(\theta)cos(2\omega t) - Xsin(\theta)sin(2\omega t) \tag{5.11}$$

Changes in θ can cause the form of x to be significantly different, looking like a cosine for $\theta = 0$ and looking like a sine for $\theta = \pi/2$. Average power must therefore be sensitive to the phase between in-line and transverse motions.

5.2 Forced Vibration Results

The varied parameters of the forced vibration database create a four dimensional space spanning in-line amplitude, transverse amplitude, phase between in-line and transverse motions, and reduced velocity. Holding one of the parameters constant, such as reduced velocity, allows for a three dimensional parameter space. The space is then defined by the motion amplitudes and the phase between motions. Measured force values or values derived from forces can then be assigned to the corresponding points in the three dimensional parameter space. Iso-surfaces of force derived values are then plotted in three dimensional space to show the effect of two degree of freedom cylinder motion on measured fluid forces for the following sections. The three dimensional figures are intended to help visualize force coefficients throughout the entire parameter space. Appendix D gives the force contours for fixed reduced velocity and fixed phase for measurements of C_{L3}, C_{ap}, C_{my}, and C_{mx}. The contours int he appendix are a more quantitative representation of the forced motion database.

5.2.1 Constant V_r

Reduced velocity, V_r, was varied in increments of 0.5 from 4.5 to 8. Fig. 5-1 shows iso-surfaces of average power for each reduced velocity between 5 and 7.5. The green surface in each figure denotes the zero average power surface where free vibrations would theoretically occur. In general, the average power iso-surfaces form a bulging paraboloid-like surface that encompasses many combinations of in-line motion, transverse motion, and phase. The zero average power region grows within the parameter space as reduced velocity increases. The increase in size of the zero power region indicates a large number of theoretically possible free vibrations, however the structural characteristics of a free vibration will further limit these possible motions.

If the zero power contours are viewed from an angle showing transverse amplitude versus phase angle, one can see how the maximum transverse amplitude possible, changes with phase. As reduced velocity increases. the maximum transverse amplitude increases, while phase decreases. The forced vibration database shows possible free vibration amplitudes in excess of $A_y/D = 1.4$, consistent with observed amplitudes greater than $A_y/D = 1.5$ from [30] and amplitudes greater than $A_y/D = 1.4$ from Dahl et al [10].

One major difference between one degree of freedom cylinder vibrations and two degree of freedom vibrations is the condition of resonance and lock-in. In a one degree of freedom vibration, all energy transfer between the fluid and cylinder can be defined in the transverse direction. Therefore, as added mass alters the effective natural frequency such that the vortex shedding frequency locks-in with the effective natural frequency for a low mass ratio system, the system reaches a resonant condition at the added mass adjusted natural frequency. In two degree of freedom vibrations, it is not necessary that both or either of the in-line and transverse directions reach a resonant condition with zero total power flow in a particular direction since power can flow from one direction to another. It is possible that transverse motions are excited by structural resonance, while in-line motions are forced with a negative power input, extracting energy from the transverse oscillations. This phenomenon is illustrated

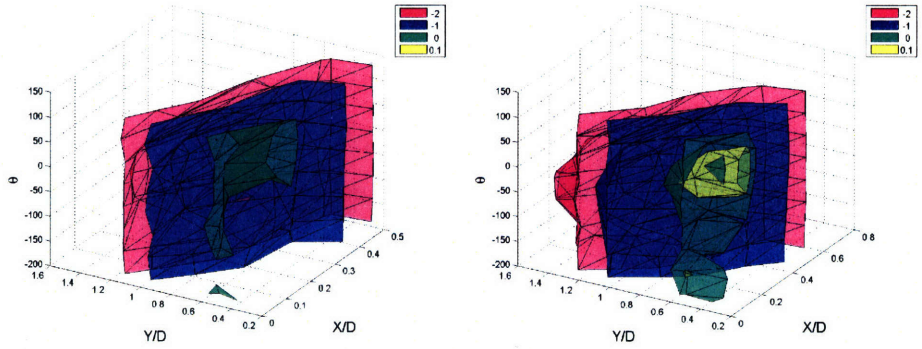

(a) $V_r = 5$

(b) $V_r = 5.5$

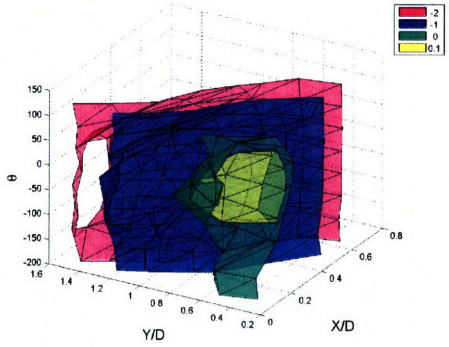

(c) $V_r = 6$

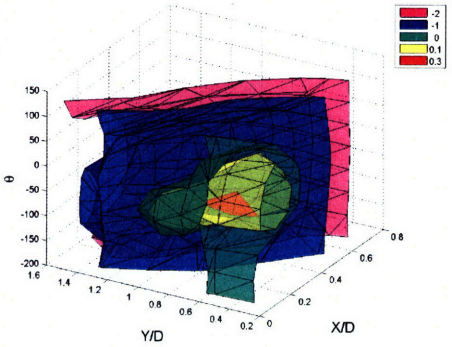

(d) $V_r = 6.5$

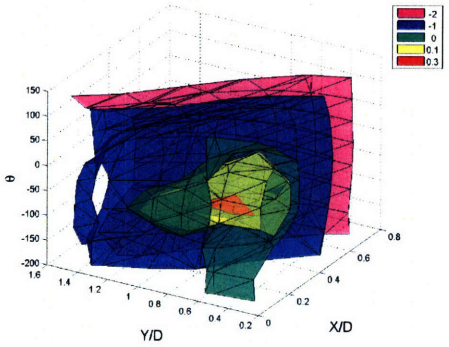

(e) $V_r = 7$

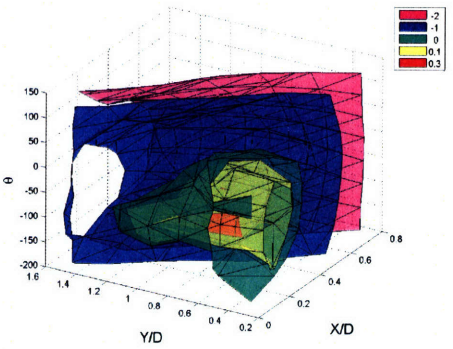

(f) $V_r = 7.5$

Figure 5-1: Normalized average power iso-surfaces

in Figs. 5-2 and 5-3, which shows iso-surfaces of traditional C_{Lv} and C_{Dv}. When these parameters are combined, one obtains the average power figures from above. Individually, one can see that for the majority of the parameter space, C_{Dv} is almost always negative. This means that in-line motions are almost always being forced with negative power input, regardless of the transverse motions. In contrast, C_{Lv}

is positive over specific regions of the parameter space. This indicates that for free vibrations, the transverse direction is resonant with positive power input, but the in-line motions are almost always undergoing forced vibration with negative power input and the motions are at twice the frequency of transverse motion.

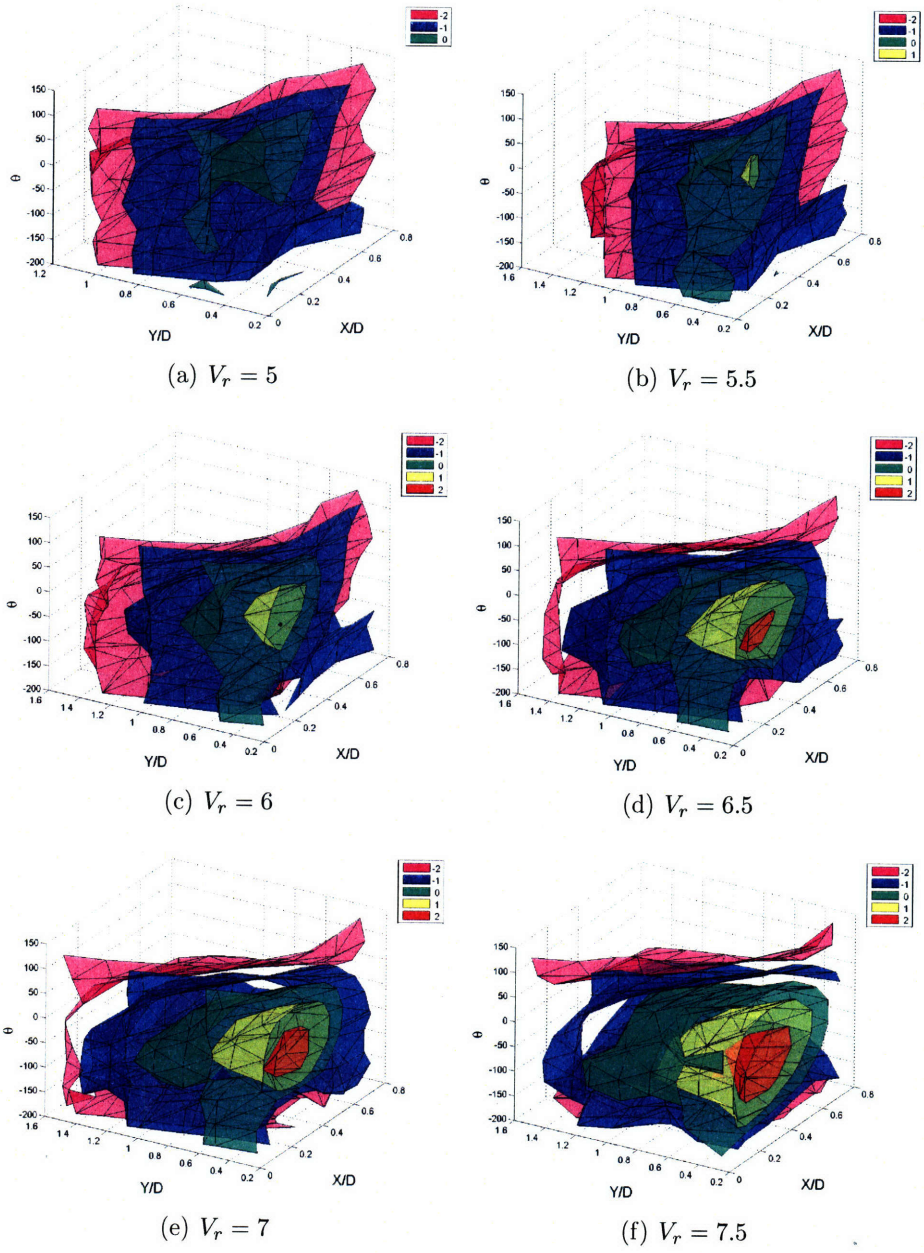

(a) $V_r = 5$ (b) $V_r = 5.5$

(c) $V_r = 6$ (d) $V_r = 6.5$

(e) $V_r = 7$ (f) $V_r = 7.5$

Figure 5-2: Iso-surfaces of lift coefficient in phase with velocity for various reduced velocities.

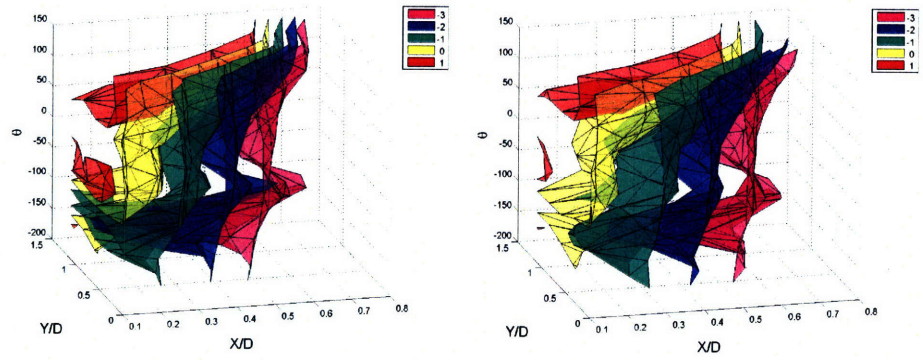

(a) $V_r = 5$ (b) $V_r = 5.5$

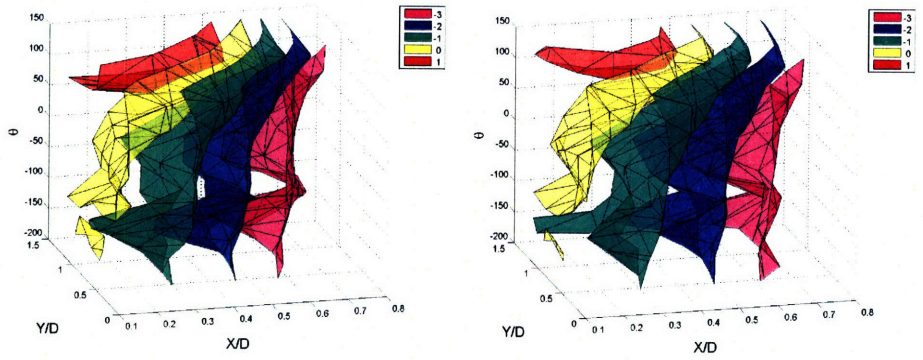

(c) $V_r = 6$ (d) $V_r = 6.5$

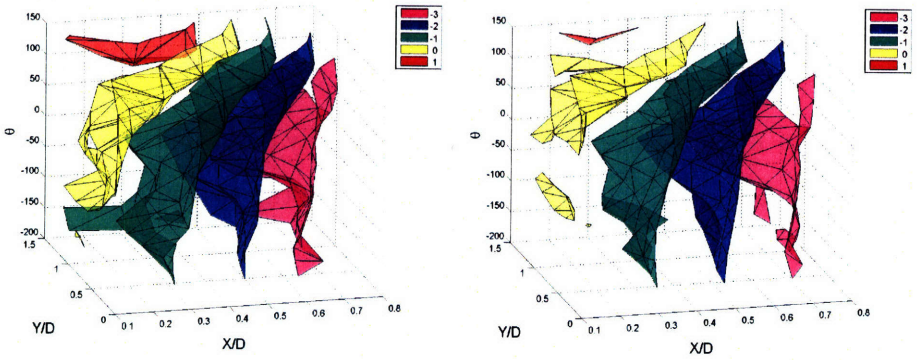

(e) $V_r = 7$ (f) $V_r = 7.5$

Figure 5-3: Iso-surfaces of fluctuating drag coefficient in phase with velocity for various reduced velocities.

Since the in-line motion of the cylinder is almost always forced with negative power input, it is not necessarily a good assumption to assume that added mass in the in-line and transverse directions change such that the effective natural frequency of the system in each direction is equal to the frequency of motion. Since the wake of

the cylinder preferentially locks-in to the effective natural frequency in the transverse direction, lock-in of in-line cylinder motions occurs coincidentally. In the free vibration, the system will naturally adjust to drive in-line motions towards a condition of lock-in, however, this condition is not necessarily achievable under all given structural conditions. In 3, however, we shoed that the effective natural frequency ratio of the system will naturally approach a value of two regardless of the nominal structural natural frequencies in each direction.

The appearance of third harmonic forces in lift from two degree of freedom motions were the main reason for constructing this database since previous databases do not include higher harmonic force measurements. Fig. 5-4 shows the magnitude of the third harmonic force for each reduced velocity in the database. One can see that the third harmonic lift coefficient can reach significant values of 1 or 2 in the region where average power is positive. If the motions along one particular point in a riser cause the average power to be negative, the third harmonic force coefficients can be even larger.

Certain motion combinations result in small third harmonic forces. For instance, for reduced velocity 6, small transverse amplitudes, and large in-line amplitudes, there is a pocket of small third harmonic coefficient for θ -135 degrees. Regions like this exist for all reduced velocities and are likely consistent with wake formations similar to those discussed in Chapter 4. Apart from these small pockets of change, the third harmonic almost increases linearly as a function of in-line motion, as evidenced by the nearly vertical colored planes in Fig. 5-4. This tends to indicate that third harmonic forces will primarily be large in regions along a flexible riser where large in-line motions exist.

Drag Force

The drag force in the wake of an oscillating cylinder typically increases as a function of motion amplitudes since larger cylinder motions create a larger wake deficit behind the cylinder. Gopalkrishnan [18] gives an equation for estimating the mean drag coefficient based on transverse oscillation amplitude for one degree of freedom

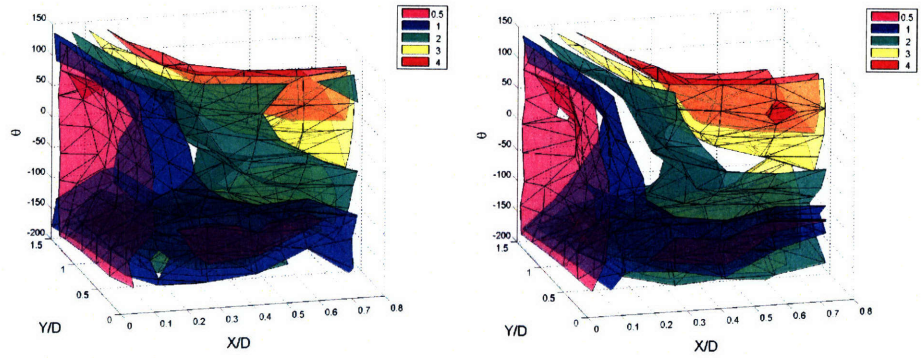

(a) $V_r = 5$ (b) $V_r = 5.5$

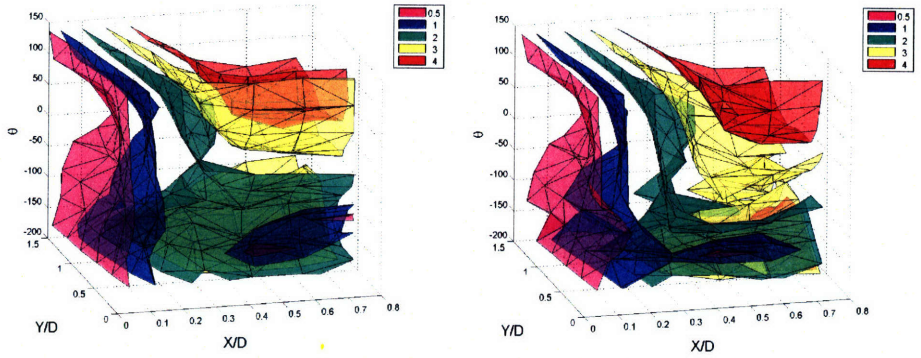

(c) $V_r = 6$ (d) $V_r = 6.5$

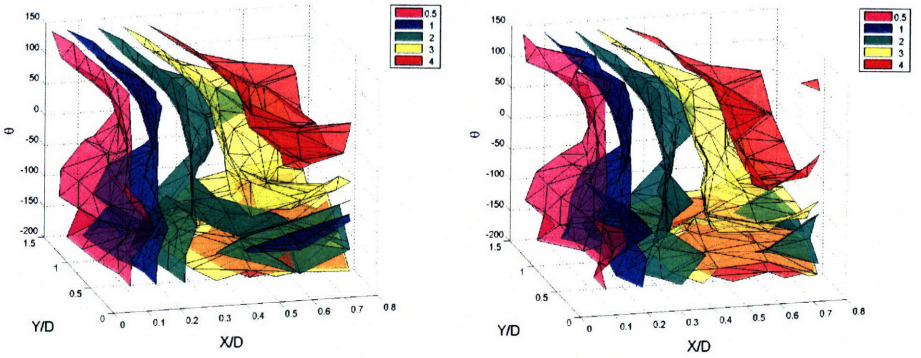

(e) $V_r = 7$ (f) $V_r = 7.5$

Figure 5-4: Iso-surfaces of third harmonic lift coefficient for various reduced velocities.

vortex induced vibrations. Forced oscillations of the cylinder in both the in-line and transverse direction show that the mean drag is affected by both motion amplitude and the phase between the motions.

Fig. 5-5 shows iso-surfaces of mean drag coefficient determined from force cylinder

motions. In general, regardless of reduced velocity, the mean drag increases as a function of both in-line and transverse motion. The largest mean drag coefficients exist for large transverse and in-line amplitudes. Drag coefficients increase with only transverse motion or only in-line motion, however the gradient in drag coefficient is not as large in these fixed directions. Drag coefficients are slightly larger than those observed by Gopalkrishnan [18] for a one degree of freedom system due to in-line motions.

One interesting feature in the surfaces of mean drag is a local minimum which occurs for $\theta \ -135$ degrees. For nearly all reduced velocities, the mean drag coefficient is fairly small in this region. This phase corresponds to the motions shown in Fig. 4-32, where the wake takes on a '2S' pattern. The width of the wake, in this case, is small compared to the width of the wake at other phase angles, such as in Fig. 4-21. In each of these cases, the amplitudes of motion are the same and only the phase is shifted. The local minimum in drag can simply be attributed to a change in the wake mode caused by the phasing of in-line motions with respect to transverse motions.

Added Mass Coefficients

Added mass coefficients computed for the in-line direction and transverse direction are shown in Figs. 5-6 and 5-7. The added mass coefficient in the in-line direction varies largely between values of -1 and 1 within the parameter space of the database. This variability is consistent with the observations from free vibrations in Chapter 3, where in-line added mass was shown to vary between -1 and 1 over the range of reduced velocities observed. The interesting aspect of the in-line added mass, however, is that this variability occurs for fixed reduced velocity, as shown in Fig. 5-6. In the free vibration case, the specific in-line added mass corresponds to a specific reduced velocity. From forced vibrations, we can see, however, that several motion combinations for a fixed reduced velocity may produce an equivalent added mass. This is important, as it shows that several different motion combinations can possibly alter the effective natural frequency of the in-line direction with the same resulting frequency characteristics at a given reduced velocity. The transverse motion

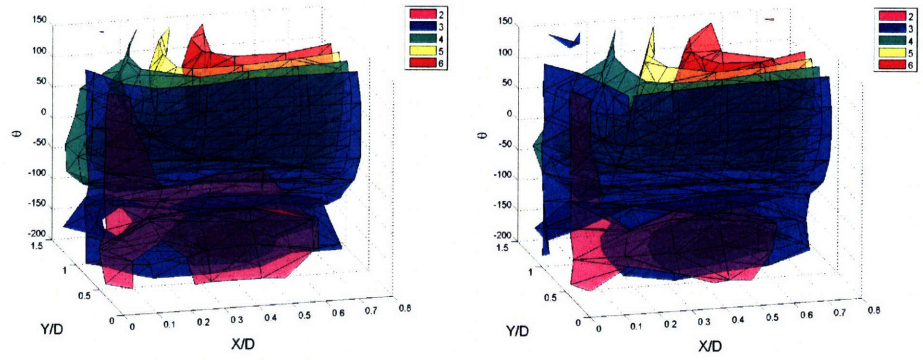

(a) $V_r = 5$ (b) $V_r = 5.5$

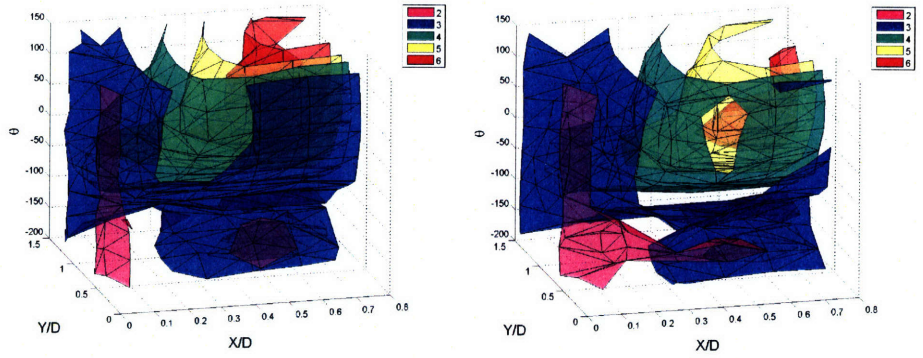

(c) $V_r = 6$ (d) $V_r = 6.5$

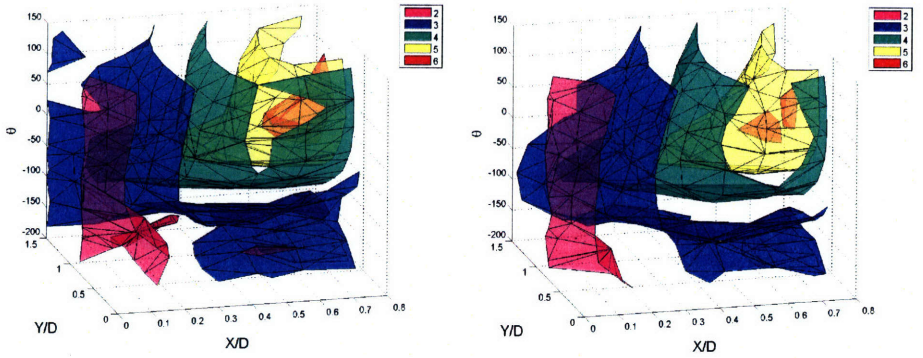

(e) $V_r = 7$ (f) $V_r = 7.5$

Figure 5-5: Iso-surfaces of mean drag coefficient for various reduced velocities.

characteristics will play an important role in determining the specific motions of the cylinder in a specific free vibration.

C_{my} is very sensitive to cylinder motions, particularly the phase angle between in-line and transverse motions. The iso-surfaces of Fig. 5-7 are closely packed together,

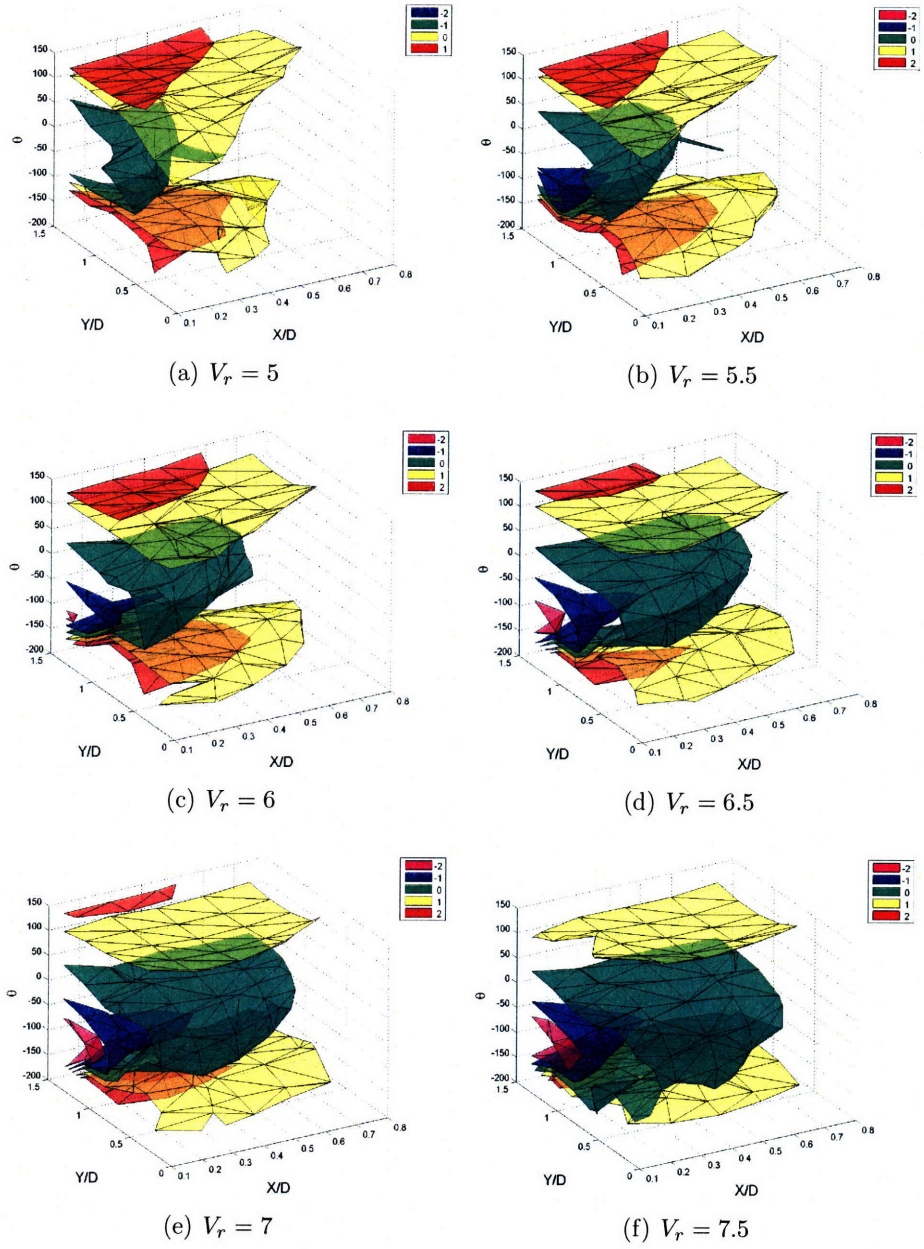

(a) $V_r = 5$ (b) $V_r = 5.5$

(c) $V_r = 6$ (d) $V_r = 6.5$

(e) $V_r = 7$ (f) $V_r = 7.5$

Figure 5-6: Iso-surfaces of in-line added mass coefficient for various reduced velocities.

resulting in large changes in added mass with small changes in phase. As reduced velocity increases, transverse added mass begins to take on more constant values through the motion parameter space. This is consistent with observations from free vibrations, where added mass typically levels off at constant values at high reduced velocities.

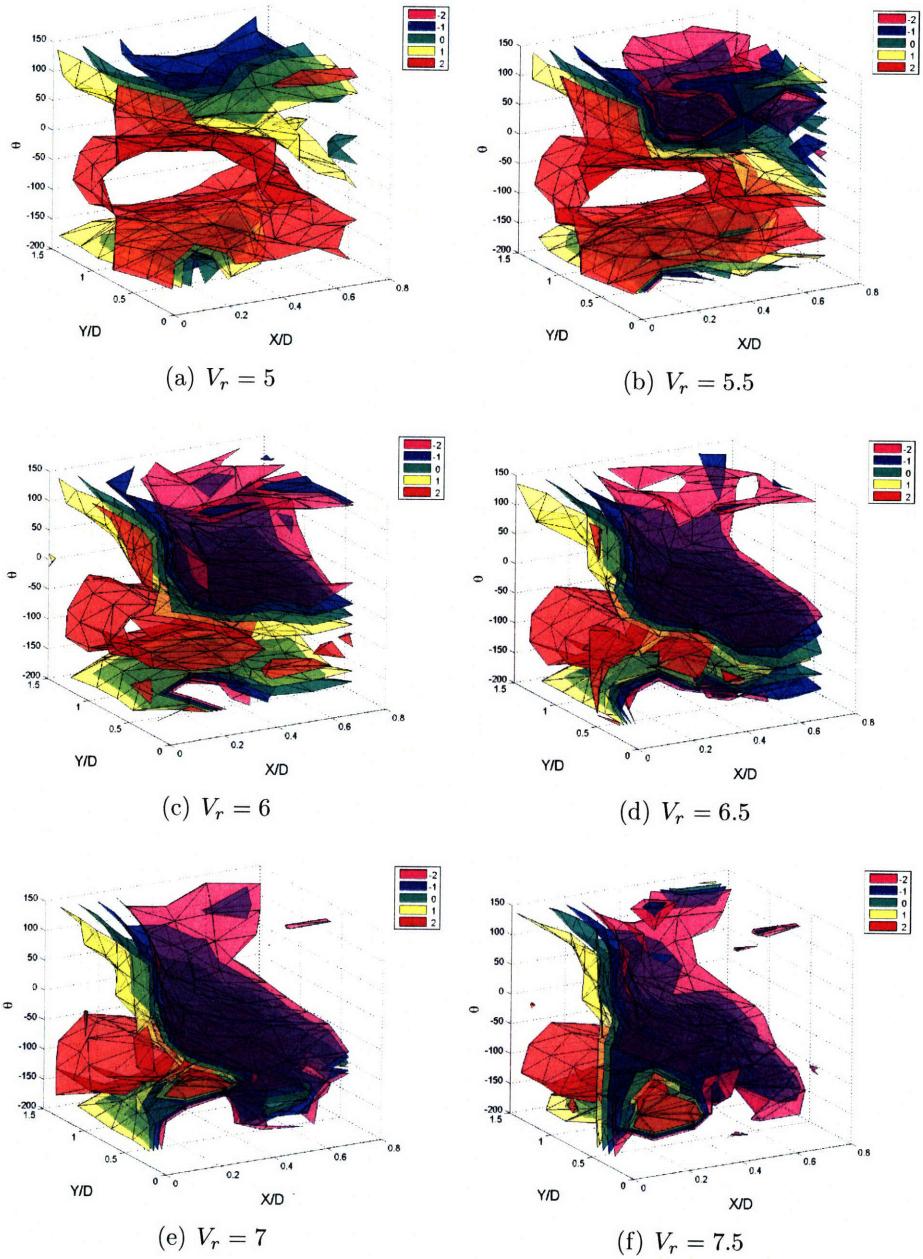

(a) $V_r = 5$ (b) $V_r = 5.5$

(c) $V_r = 6$ (d) $V_r = 6.5$

(e) $V_r = 7$ (f) $V_r = 7.5$

Figure 5-7: Iso-surfaces of transverse added mass coefficient for various reduced velocities.

5.2.2 Constant θ

Previously, we have viewed the force coefficient parameter space with reduced velocity held constant. In one degree of freedom experiments, amplitudes and forces are

typically depicted as a function of reduced velocity. Holding phase constant and varying reduced velocity within the three dimensional parameter space allows one to view the effects of reduced velocity on force derived parameters such as the zero average power manifold.

Iso-surfaces of zero average power for various phase angles are shown in Fig. 5-8, where reduced velocity is now the vertical axis in this case. This set of images shows how the region where free vibrations may occur changes as a function of the phase angle. As the phase angle changes from positive 135 degrees towards negative phase angles, the zero power region moves to higher reduced velocities and moves towards the axis with zero in-line motion. At phase angles near 45 degrees, the entire reduced velocity space has possible free vibrations. In contrast, at a phase angle of -90 degrees, the primary zero power region exists only at reduced velocities higher than 7 or for motions with only transverse oscillations.

One interesting feature occurs at a fixed phase angle of -135 degrees. Two distinct split regions of zero power occur in this case near a reduced velocity of 8. One region consists of motions with relatively large transverse motions and some in-line motion, while the second region mainly occurs with no in-line motion. This type of split region may lead to a large discontinuity in amplitudes as a function of reduced velocity, where two distinct oscillation patterns may be possible. This type of phenomenon is known to occur under different experimental conditions. It was shown by Fujarra et al [17] that the tip motions of a cantilevered cylinder may exhibit two different modes at very high reduced velocities. In this case, this is not quite the same phenomenon and is more closely related to the branches observed by Jauvtis and Williamson [30]. In two degree of freedom oscillations with a nominal natural frequency ratio of 1.0, Jauvtis and Williamson [30] observed a distinct super upper branch and lower branch of oscillations. The super upper branch consists of motions with phases near -135 degrees (crescent shape with lobes facing downstream) and very large transverse motions ($A_y/D \approx 1.5$), while the lower branch has virtually no in-line motion and the transverse motions were much smaller ($A_y/D \approx 0.7$).

Fig. 5-9 consists of four views of a composite plot of several zero power manifolds

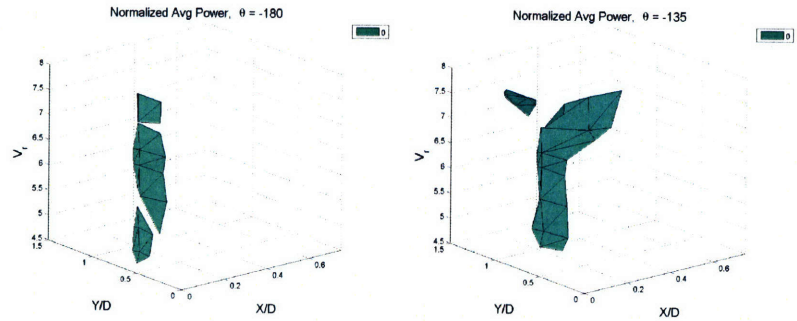

(a) $\theta = -180deg$

(b) $\theta = -135deg$

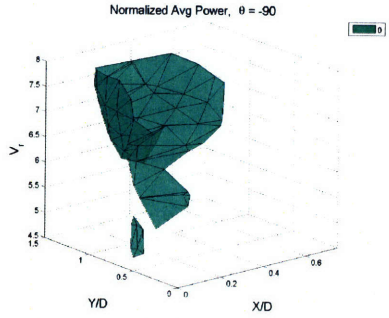

(c) $\theta = -90deg$

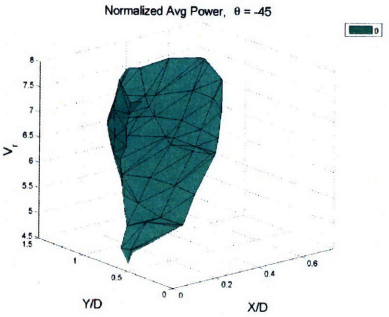

(d) $\theta = -45deg$

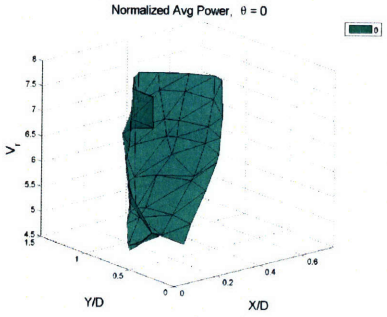

(e) $\theta = 0deg$

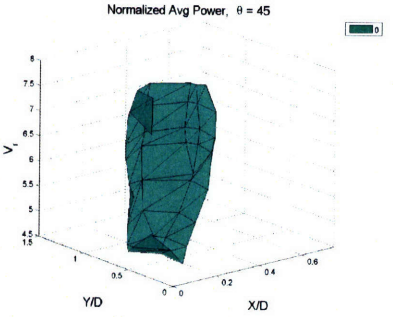

(f) $\theta = 45deg$

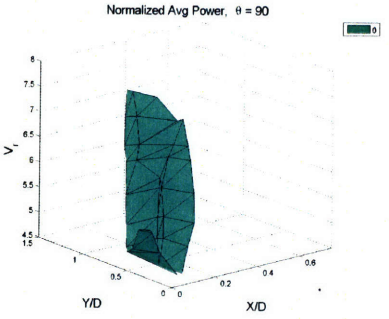

(g) $\theta = 90deg$

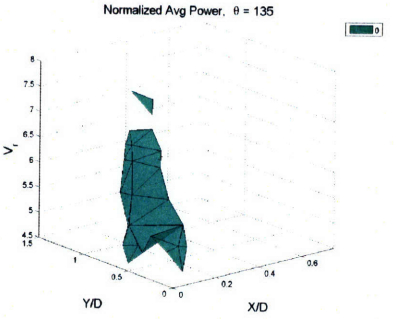

(h) $\theta = 135deg$

Figure 5-8: Iso-surfaces of zero average power for various phase angles, θ.

for various motion phase angles combined with a few points from the upper and super upper branches of Jauvtis and Williamson [30]. The data points are color coded according to the nearest phase angle, for example, a phase angle between -112.5 and -67.5 degrees will appear yellow. The points from Jauvtis and Williamson [30] follow closely along the manifolds, indicating that the surfaces closely indicate regions where free vibrations may occur. The path of these particular data points indicate a particular path based on the motions and phases resulting from particular mass characteristics of the Jauvtis and Williamson [30] experiment. One can see that points corresponding to phase angles near -135 degrees are moving towards the high amplitude portion of the orange and yellow surfaces. This particular path is unique to this experiment, however altering the structural characteristics of the system will result in a different path of points through this parameter space.

Fig. 5-10 shows the same space as in Fig. 5-9, except motions from the free vibration experiments of Chapter 3 are plotted for $f_{nx}/f_{ny} = 1.9$. One can see the drastically different path that these data points take as they curve around the zero power surfaces. The transition through this space is still smooth and the path still remains close to the zero power surface. Both cases from Figs. 5-9 and 5-10 represent valid paths for a free vibration, however the structural properties of the system are very different in each free vibration.

Since two degree of freedom free vibrations show a tendency to lie close to the zero average power curves, one may be able to use these surfaces to predict the particular steady-state motion of a rigid cylinder under free vibration. One can see that different structural characteristics of the free vibration lead to very different motions of the cylinder and very different paths taken through this three dimensional parameter space. Using simple assumptions, can one predict these motions with only the known structural characteristics at hand?

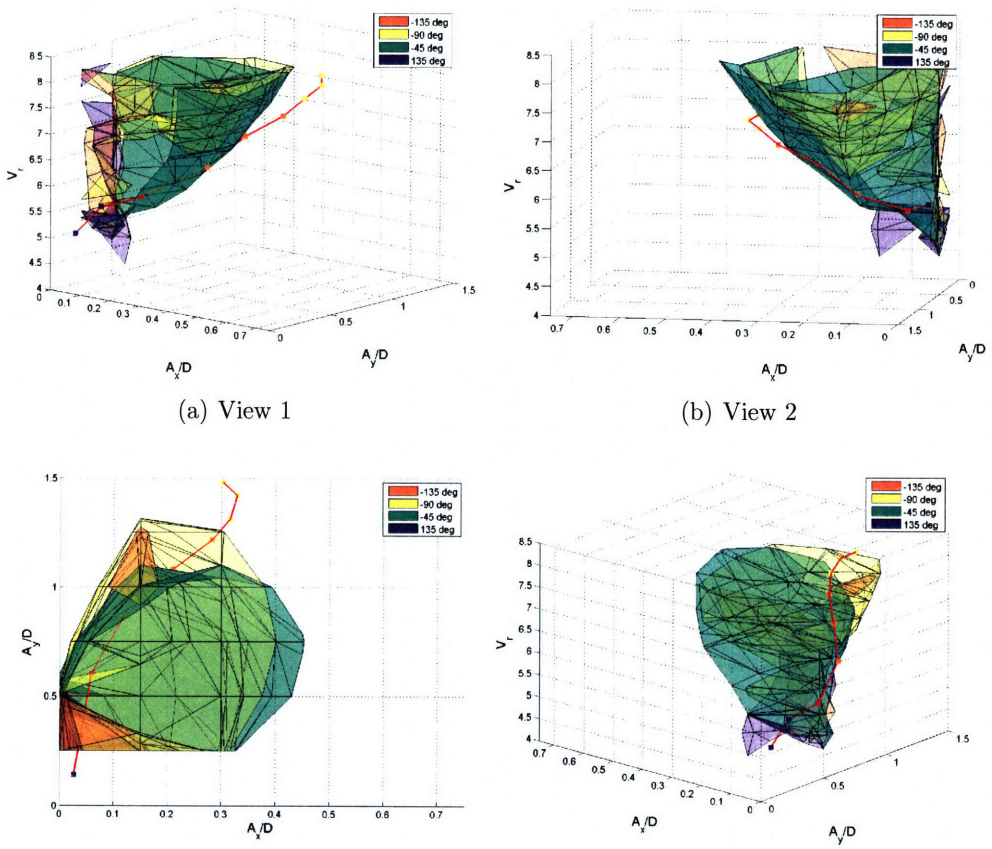

(a) View 1

(b) View 2

(c) View 3

(d) View 4

Figure 5-9: Free vibration points from Jauvtis and Williamson [30] for $f_{nx}/f_{ny} = 1.0$ in 3-D motion parameter space. Iso-surfaces show average power = 0 surfaces for phase, θ, at -45,0, and 45 degrees. Reduced velocity is varied on the vertical axis. Phase angles of data points are $\pm$ 22.5 degrees of the indicated phase from color.

5.3 Predicting Free Vibrations

The average power plots from the previous section show that the potential free vibrations of a cylinder in two degrees of freedom can take on a large number of amplitude and phase combinations. In the free vibration experiments from Chapter 3, it was shown that under various structural conditions, different cylinder amplitudes and phases were observed for similar reduced velocities. Can the steady state cylinder motions from free vibration experiments be predicted using the forced vibration database? How do we determine the points on the zero average power manifold for which a specific free vibration should occur?

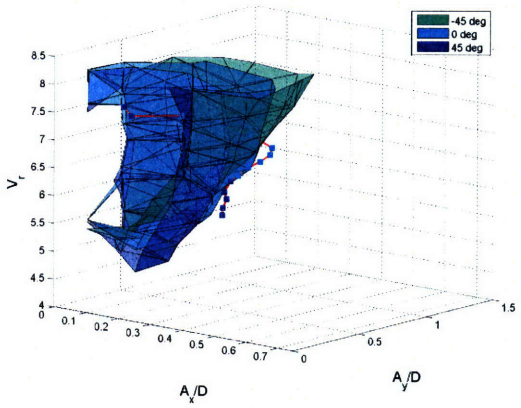

(a) View 1

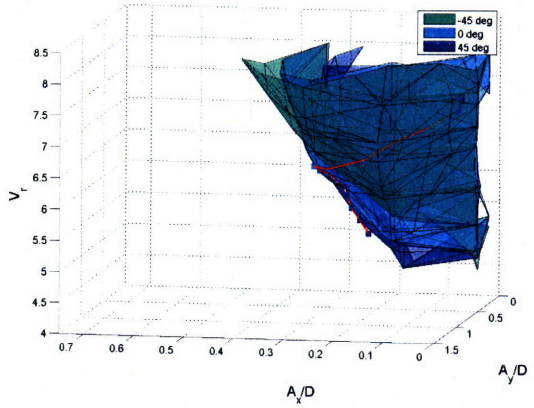

(b) View 2

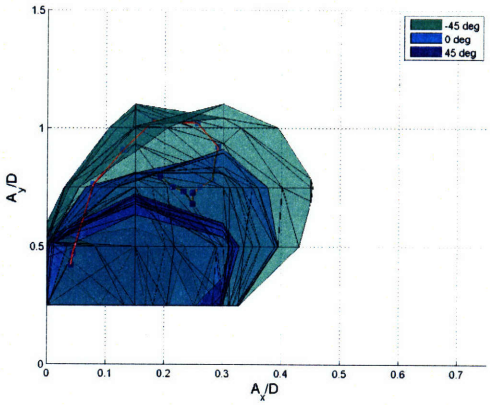

(c) View 3

Figure 5-10: Free vibration points in 3-D motion parameter space. Iso-surfaces show average power = 0 surfaces for phase, θ, at -45,0, and 45 degrees. Reduced velocity is varied on the vertical axis. Figure shows how points smoothly transition along the zero power surfaces as θ changes. Phase angles of data points are $\pm$ 22.5 degrees of the indicated phase from color.

From an engineering design standpoint, the known quantities of the problem include the structural characteristics of the vibrating structure and the flow conditions for which the structure will be subjected. It is assumed that one must know the mass, stiffness, damping, and natural frequency of the structure in order to predict it's motions. Similarly, one must know the flow velocities for which the structure will be subjected. Since vortex-induced vibrations occur for a range of true reduced velocities near 6, with known flow velocity, one can choose a range of reduced velocities

for which oscillations will occur, defining the cylinder's oscillation frequency.

Free vibration experiments also showed that for two degree of freedom cylinder oscillations, the observed oscillation frequencies almost always had a fixed in-line to transverse frequency ratio of 2. It is necessary to assume that the same will happen for predicted cylinder motions in this case since all database motions were performed with an in-line to transverse motion frequency ratio of 2.

5.3.1 Lock-in assumption and free vibration assumption

It was shown in Chapter 3 that for a cylinder with structural characteristics such that the nominal natural frequency ratio was near 2, the effective added mass associated with the cylinder motions would adjust such that the effective natural frequency ratio or excitation frequency ratio was 2. If we assume that the cylinder undergoes lock-in with the fluid wake, this requires that the oscillation frequencies of the cylinder in the in-line and transverse directions must be equal to the effective natural frequency defined in equation 2.4. Since the oscillation frequency of the cylinder is unknown a priori, we must make predictions for a range of reduced velocities to cover the range of possible motions. By determining a range of reduced velocities to consider, we can set the oscillation frequency given a certain flow speed. The only remaining unknown parameter is the added mass, which can easily be found as in equation 5.12. The added mass is found independently for each direction of motion where ω_{ex} in the in-line direction is twice the frequency as the transverse direction.

$$m_a = \frac{k}{\omega_{ex}^2} - m \tag{5.12}$$

Assuming lock-in for a particular reduced velocity allows one to directly solve for the added mass necessary for this assumption to occur.The added mass in the in-line direction and the added mass in the transverse direction give two known parameters for predicting the cylinder's motions at a particular reduced velocity.

In order for steady-state oscillations to occur for the self-excited oscillations of a cylinder, the average power calculated over one cycle of motion must be equal to

zero. This requirement ensures that oscillations are not increasing or decreasing in amplitude and is a physical requirement for a free vibration. The zero power manifolds calculated in the previous section display the points within the forced vibration database for which this condition holds. This results in three known parameters, in-line added mass, transverse added mass, and zero average power, that govern the particular motions for a cylinder with particular structural characteristics at a particular reduced velocity.

5.3.2 Prediction Method

The three known parameters of in-line added mass, transverse added mass, and zero average power are measured, known quantities for all experiments contained in the force coefficient database. These parameters each define an iso-surface within the three-dimensional parameter space for fixed reduced velocity defined by in-line amplitude, transverse amplitude, and phase between in-line and transverse motion. When the system reaches its steady state oscillation, if lock-in occurs, then the oscillation condition must lie on each of these three surfaces. Fig. 5-11 shows an example case of the three surfaces drawn in the three dimensional space. Since the steady state oscillation condition must lie on all three surfaces, the intersection of the surfaces defines the predicted steady-state oscillation of the cylinder. The intersection of three planar surfaces is one point, as long as the curvature of the surfaces does not cause them to intersect along multiple lines.

The surfaces show in Fig. 5-11 are computer generated surfaces formed by the gridded points of the database. Determining an equation for each surface is very difficult or impossible, thus the intersection of the surfaces can't be found by setting equations equal to one another. Additionally, it is not necessary that all three surfaces intersect and the coarse grid spacing of the test matrix may cause surface intersections to be distorted. If surfaces do not intersect, then it is assumed that the system will oscillate under the conditions for which the three surfaces are closest to one another.

In order to solve for the predicted cylinder oscillation, a simple error function is defined to determine how close a given datum in the database is from the predicted

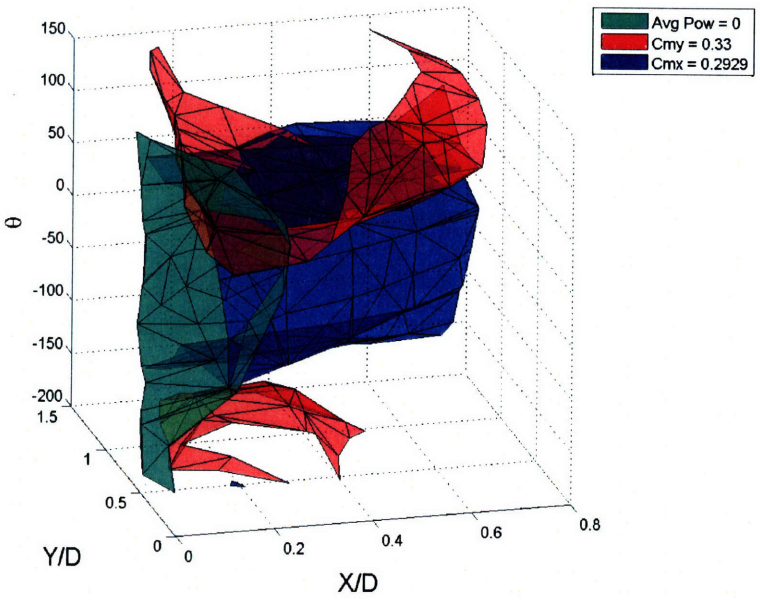

Figure 5-11: Intersecting surfaces of constant C_{mx}, C_{my}, and average power. Intersection point represents the predicted free vibration condition for specific structural characteristics of flexibly mounted rigid cylinder.

parameters. The general form of the error function, d, is shown in equation 5.13, where C_{mx},C_{my}, and C_{ap} are the in-line added mass coefficient, transverse added mass coefficient, and average power coefficient respectively. The term $-pred$ refers to the predicted values as determined from the lock-in assumption and free vibration assumption (e.g. $C_{ap-pred} = 0$ for zero damping), and $-database$ refers to the values at a given point in the database. The equation coefficients a, b, and c are scaling multipliers to ensure that the differences are scaled appropriately with respect to one another.

$$d = a|C_{mx-pred} - C_{mx-database}| + b|C_{mx-pred} - C_{mx-database}| + c|C_{ap-pred} - C_{ap-database}| \tag{5.13}$$

In reality, added mass values are a function of reduced velocity, meaning that the equation coefficients a, b, and c from equation 5.13 must be a function of reduced velocity. For simplicity, these coefficients are treated as constant regardless of the

reduced velocity since the ratio of in-line added mass to transverse added mass does not change dramatically as a function of reduced velocity. The particular values used in the results shown are $a = 1$, $b = 3$, and $c = 1$. The value of a is set to one in order to act as the reference parameter. The value of b is set to three since the in-line added mass is typically shown to be between one-half and one-third the size of the transverse added mass. This is seen in Figs. 3-18 and 3-19 from the free vibration experiments. The value of c is set to one since the average power for a system with zero damping is zero and the average power coefficients are much larger than added mass coefficients. Therefore, any average power coefficient away from zero will have a large error function. This is the most important parameter to match since matching the average power over one cycle is a physical requirement of the free vibration.

Once the prediction parameters are determined for a given reduced velocity, the error function is determined for each point in the database. Database values are linearly interpolated in order to generate intermediate amplitude and phase estimates. A linear interpolation is used for simplicity and speed. More complex interpolation of the sparse database may provide improved prediction estimates. Similarly, more complex search algorithms or error functions may improve prediction estimates. The particular linear interpolation used in the shown results interpolates the entire four dimensional test matrix twice.

With the error function determined for each point in the database, the minimum value of the error function is determined and the corresponding motion parameters are the prediction of the cylinder's motions. The search for the minimum of the error function is limited to values within one interpolated grid point of the chosen reduced velocity. The same process is performed over a range of reduced velocities to determine how the motion parameters vary as a function of reduced velocity.

Figs. 5-12 - 5-14 show predictions from the forced motion database compared with the observed motions from the free vibration experiments from Chapter 3. These predictions utilize the assumption that the excitation frequencies for each system will have a ratio of 2. The grid spacing on each figure shows the grid spacing of the experimental points in the database, emphasizing the sparseness of the grid.

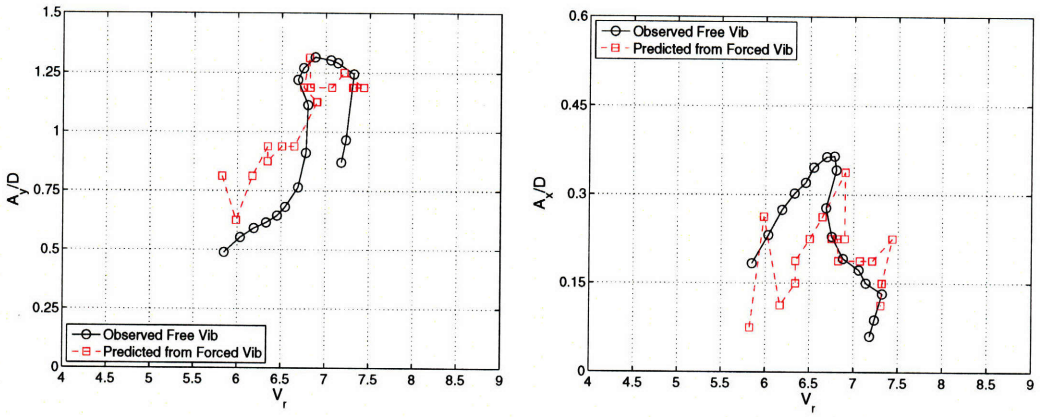

(a) A_y/D Prediction

(b) A_x/D Prediction

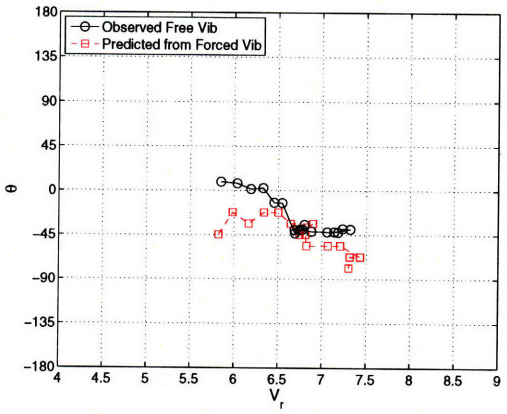

(c) θ Prediction

Figure 5-12: Prediction of motion parameters for $f_{nx}/f_{ny} = 1.52$ from forced motion database. Assumption that $f_{ex-x}/f_{ex-y} = 2$

The prediction for Fig. 5-12 indicates the major trends of the free vibrations, although the exact amplitudes and phases do not match perfectly. In this case, the assumption that the in-line excitation frequency occurs at twice the transverse excitation frequency may not be the best assumption for obtaining a good prediction. Fig. 3-35 shows that the in-line to transverse excitation frequency ratio for $f_{nx}/f_{ny} = 1.52$ is more likely a value near 1.9. The in-line direction is not undergoing lock-in for the free vibration case, so the prediction is flawed. It is important to note, however, that even with the discrepancy in excitation frequency, the prediction still does relatively well at predicting the free vibration motions. Most of the prediction values lie within one grid spacing of the actual free vibration case. The grid spacing

acts as the limiting error for each prediction case.

Fig. 5-13 shows predictions of the free vibration motions for $f_{nx}/f_{ny} = 1.67$. Again, the prediction magnitudes do not match perfectly with the observed free vibrations, although the main trends of each curve are still captured with the prediction. The discrepancy in magnitudes occurs again due to the lock-in assumption. It was shown in Chapter 3 that the in-line natural frequency did not lock-in for this frequency ratio, but rather had an equivalent natural frequency ratio near 1.9.

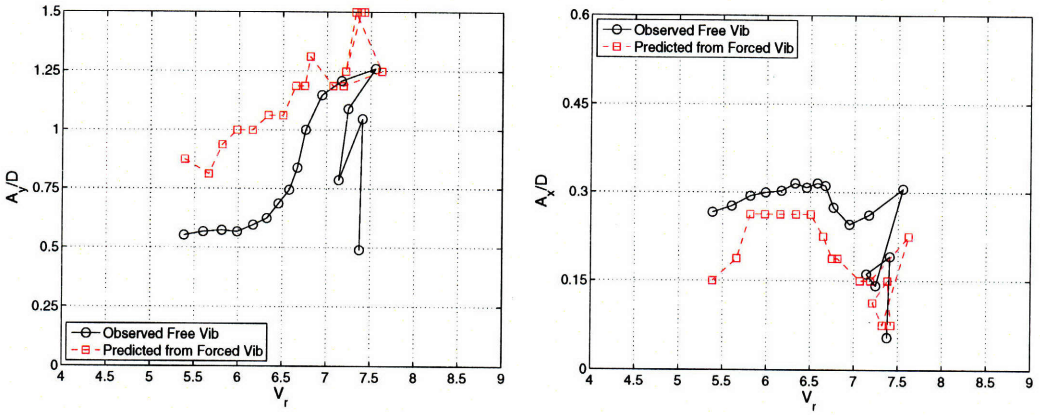

(a) A_y/D Prediction

(b) A_x/D Prediction

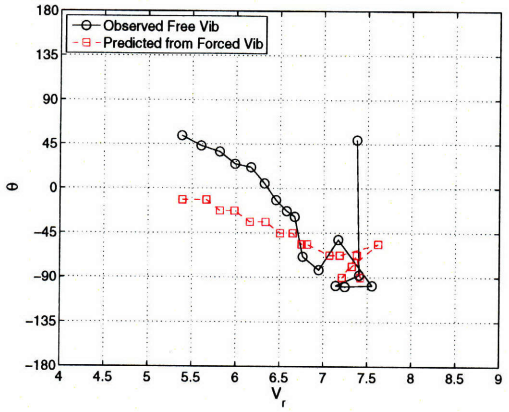

(c) θ Prediction

Figure 5-13: Prediction of motion parameters for $f_{nx}/f_{ny} = 1.67$ from forced motion database. Assumption that $f_{ex-x}/f_{ex-y} = 2$

The prediction for $f_{nx}/f_{ny} = 1.9$ works very well compared to the observed free vibration motions, as seen in Fig. 5-14. The major feature of the transverse amplitude from the free vibrations is the double peaks that appear as a function of reduced

velocity. As seen from the figure, the prediction shows the double humps, although larger amplitudes in the second peak are predicted. The relative error of the transverse amplitude prediction is less than two percent of the actual value for the middle reduced velocities and less than twenty percent of the observed values for the higher reduced velocities. The relative error still remains smaller than the error associated with the test matrix grid spacing. A break down in the prediction occurs for reduced velocities greater than 7. At these high reduced velocities, the assumption of lock-in is no longer valid, so the prediction method breaks down. At this point a more detailed prediction method is necessary that accounts for the complete fluid structure interaction in time.

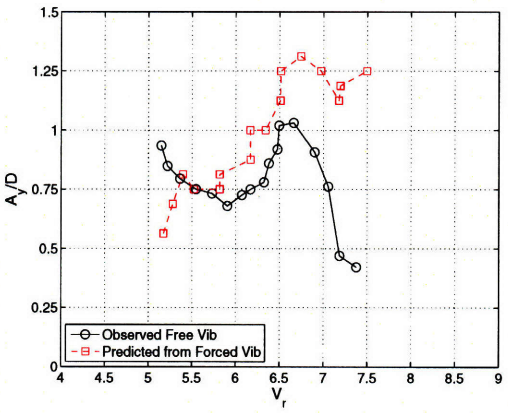

(a) A_y/D Prediction

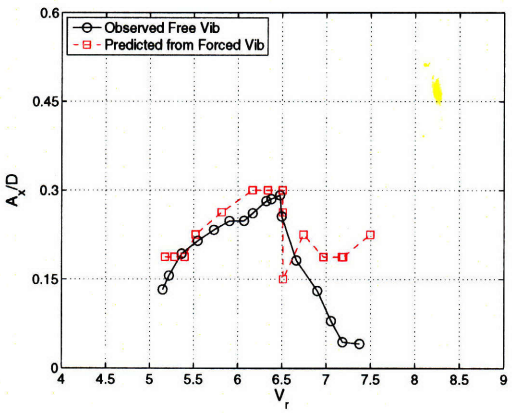

(b) A_x/D Prediction

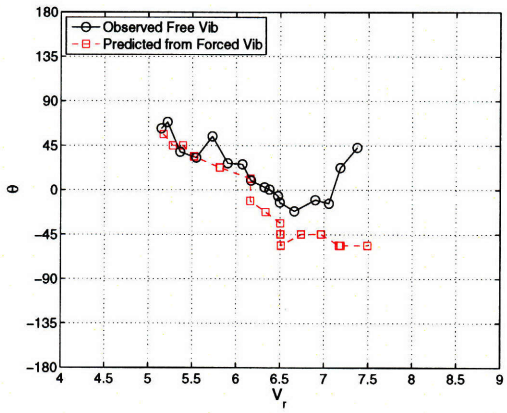

(c) θ Prediction

Figure 5-14: Prediction of motion parameters for $f_{nx}/f_{ny} = 1.9$ from forced motion database. Assumption that $f_{ex-x}/f_{ex-y} = 2$

In-line motion and phase is also predicted well in the $f_{nx}/f_{ny} = 1.9$ case since

the dual lock-in assumption is more suited for both directions of motion. In this case, the equivalent natural frequency ratio calculated from free vibration motions was between 1.93 and 2, depending on the particular reduced velocity. This results in a better prediction match.

In order to better predict cylinder motions for lower frequency ratios, one can simply adjust the equivalent natural frequency ratio used in the prediction. By doing so, one no longer assumes that lock-in must occur in both in-line and transverse directions, however, one must know a priori, the appropriate equivalent natural frequency for in-line motions, assuming that the transverse motions remain locked-in. In Chapter 3, we saw that the condition of dual resonance drives the free vibrations towards a natural frequency ratio of 2, however this ratio does not always equal 2. In Fig. 3-35, the effective natural frequency ratio was closer to 1.9 for a nominal ratio of 1.52. Fig. 5-15 shows motion amplitude and phase predictions for $f_{nx}/f_{ny} = 1.52$, under the assumption that $f_{ex-x} = 1.9 f_{ex-y}$.

Altering the excitation frequency in the in-line direction shows that the prediction is quite sensitive to this parameter as the predictions for $f_{nx}/f_{ny} = 1.52$ improve. The relative error of motion predictions reduces to less than 10 percent of the observed in-line and transverse motions when the in-line excitation frequency is reduced, consistent with the excitation frequency observed in free vibrations. In-line motions and phase are improved as well. A similar improvement occurs in the prediction of transverse motion for $f_{nx}/f_{ny} = 1.67$, as seen in Fig. 5-16.

Although prediction of the transverse motion is improved for $f_{nx}/f_{ny} = 1.67$ when the in-line excitation frequency is reduced, the prediction of in-line motion and phase is not necessarily improved. This occurs since the in-line excitation frequency is not really a constant, but rather a function of reduced velocity as seen in the free vibration experiments. Therefore, changing the effective natural frequency in the in-line direction may improve estimates for some points while causing more error in others. Errors in this assumption of in-line excitation frequency are more easily seen in Fig. 5-17, for $f_{nx}/f_{ny} = 1.9$.

In this case, the excitation frequency in the in-line direction is no longer a good

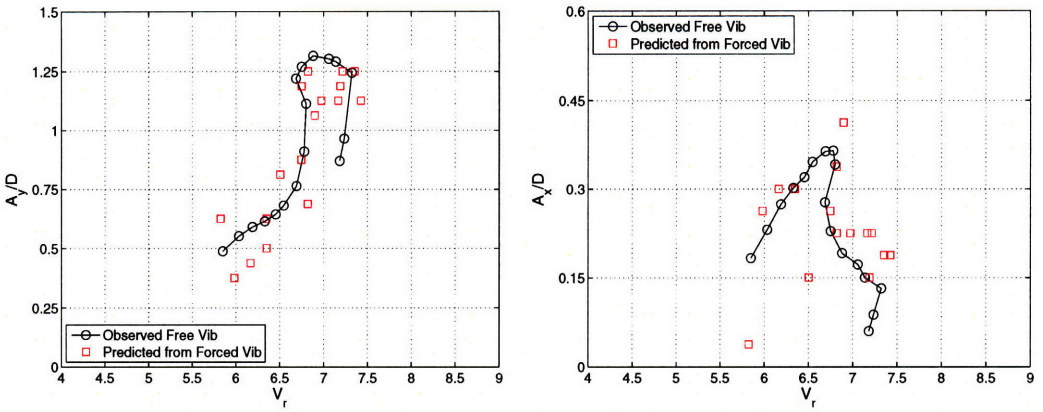

(a) A_y/D Prediction

(b) A_x/D Prediction

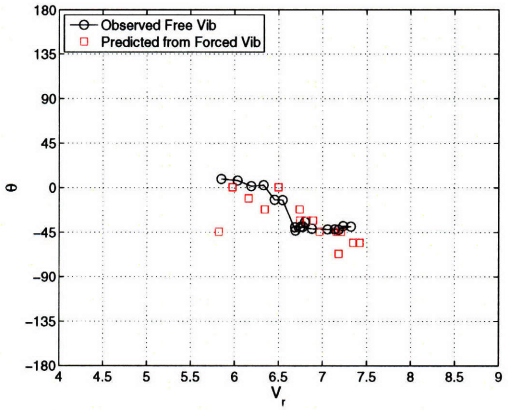

(c) θ Prediction

Figure 5-15: Prediction of motion parameters for $f_{nx}/f_{ny} = 1.52$ from forced motion database. Assumption that $f_{ex-x}/f_{ex-y} = 1.9$

estimate for determining the proper added mass of the system. Transverse motions still match relatively well with the observed free vibrations although the two peaks of the free vibrations are no longer apparent. In-line motions no longer match well with the observations from free vibrations.

This study of the prediction parameters shows that it is essential to understand the appropriate mass characteristics of the system as well as the appropriate lock-in conditions of the cylinder. The condition of lock-in in the in-line direction is important for determining the steady-state motions of the cylinder since slight alterations in this term can result in changed predictions of the motions.

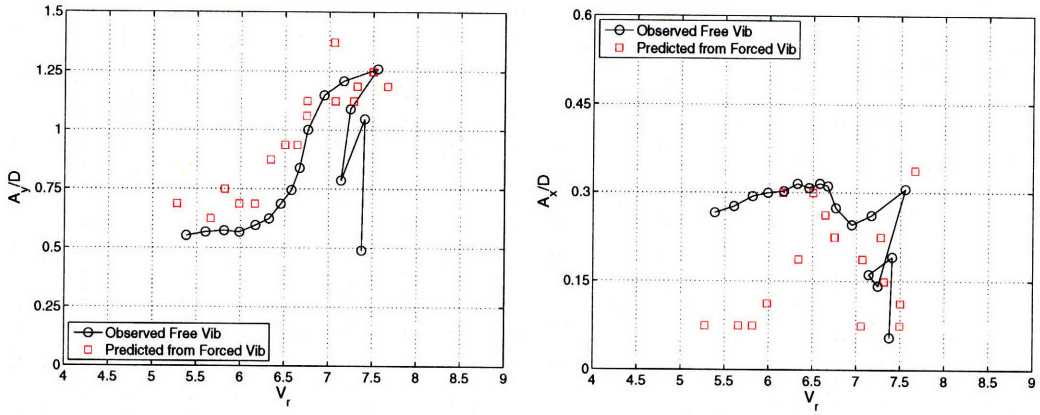

(a) A_y/D Prediction

(b) A_x/D Prediction

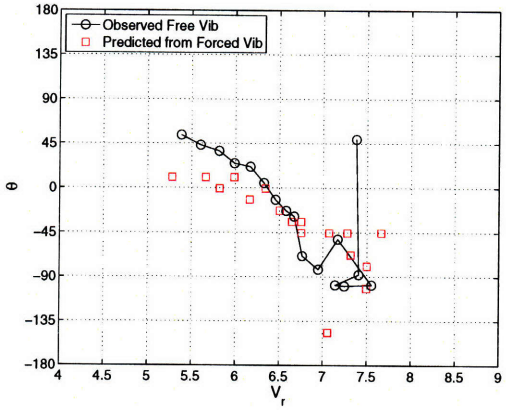

(c) θ Prediction

Figure 5-16: Prediction of motion parameters for $f_{nx}/f_{ny} = 1.67$ from forced motion database. Assumption that $f_{ex-x}/f_{ex-y} = 1.9$

5.3.3 Discussion on Prediction of Flexibly Mounted Rigid Cylinder Motions

As seen in the previous section, accurate prediction of cylinder motions is dependent on the condition of in-line lock-in. The assumption that lock-in occurs in both the in-line and transverse directions has been shown to only truly be valid for a system with a nominal natural frequency ratio near 2. In a string-like, marine riser this condition is valid for any point along the length of the riser. It is possible that a dual lock-in assumption may be used for predicting riser motions of a long flexible riser.

In the case of the flexible riser, however it is not required that the average power

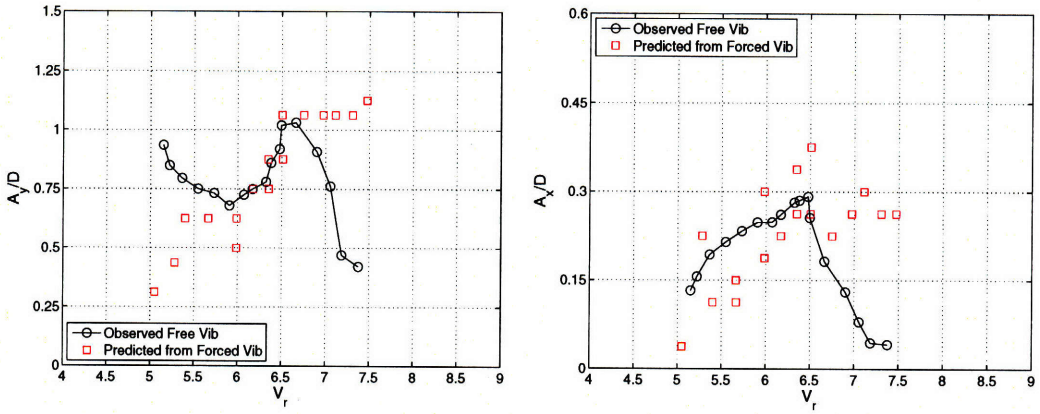

(a) A_y/D Prediction

(b) A_x/D Prediction

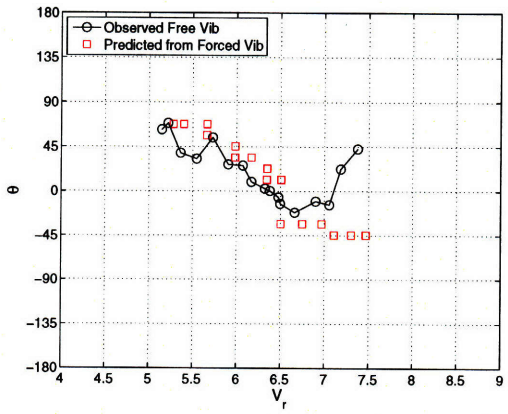

(c) θ Prediction

Figure 5-17: Prediction of motion parameters for $f_{nx}/f_{ny} = 1.9$ from forced motion database. Assumption that $f_{ex-x}/f_{ex-y} = 1.9$

over one cycle of motion be equal to zero for any given cross section along the length of the riser. Instead, average power must be balanced along the span of the riser such that energy pumped in at some point along the length of the riser must be dissipated elsewhere on the riser span. The prediction of complete riser motions must consider additional assumptions to estimate motions along the span.

One important aspect of motion predictions shown in the previous section is that although the prediction is somewhat sensitive to the choice of the excitation frequency, which determines the predicted added mass necessary to excite motions in each direction, the assumption of dual lock-in is still acceptable for predicting the cylinder motions. In order to make a perfect prediction, the true excitation condition

of the in-line motion must be known, which is a function of reduced velocity. The true excitation frequency of the in-line direction can only be known by performing a free vibration experiment beforehand, eliminating the need for a prediction in the first place. The assumption of lock-in provides a sufficient estimated condition that can predict the cylinder motions for any nominal frequency ratio given that the free vibration oscillates close to a condition of lock-in.

The forced vibration database is successful at predicting cylinder motions using very simplified assumptions about the dynamic interaction of the flexibly mounted cylinder and its wake along with a very sparse test matrix. A more refined test matrix would certainly improve estimations of cylinder motions. A more refined test matrix may also allow for an improved prediction method that doesn't require lock-in of the in-line motion. Balancing equations of motion in the frequency domain would certainly be able to predict steady-state motions of the cylinder without relying on a specific effective natural frequency assumption since the observed in-line frequency of motion is always twice the transverse frequency of motion, while the effective natural frequency is dependent on the fluid forces. This method does not work well for a sparse matrix of data points since the time trace of forces and motions is necessary for determining the frequency spectra associated with each test run. Interpolation of the test matrix does a poor job at producing quality estimates of the force and motion frequency spectra in this case, thus predictions are limited to occurring at the actual grid points of the database.

5.4 Distributed force on a flexible cylinder

Two established methods exist for dealing with vortex induced vibrations of a flexible marine riser. One can either try to get rid of vibrations altogether by using a VIV suppression device (this topic is discussed in Chapter 6), or one can deal with the vibrations by monitoring riser motions and predicting the fatigue life of the riser, removing it from operation before failure.

Logging the motions of a flexible riser is a fairly common engineering practice done

through strain and accelerometer measurements. The measurement of these values can give an exact measurement of particular motions at sensor locations along the length of the riser and in the case of tension-dominant systems, an estimate of the equation of motion for the riser can be used to estimate the fluid forces acting on the riser at that location. Knowing the material stress or fluid forces at a given location along the length of a riser allows one to make an estimate of fatigue life based on the observed time-dependent stress on the material at that point. This estimate, however ignores the possibility that high stress locations may exist elsewhere along the riser span, where a sensor may not be located.

It is therefore desirable to estimate the distributed force along the length of a riser, such that one can estimate fatigue life as a function of span length along the riser. This motivation has fueled the research of Mukundan [44] in conjunction with this study. Mukundan [44] has developed a method for reconstructing time-dependent riser motions along the length of a long, flexible riser using limited, finite, sensor measurements along the span of the riser. This reconstruction results in a continuous estimate of riser motions along the length of the riser.

Reconstruction does well at producing a unique representation of the riser motions, however prediction of the lift force measurement along the span of the riser is limited to an estimate of first harmonic forces occurring at the frequency of transverse motion. High frequency motions are lost in the reconstruction process, hence distributed third harmonic lift forces cannot be reproduced as a function of span. Since the third harmonic force may contribute significantly to a reduction in fatigue life, it is desirable to know the spatial distribution of third harmonic lift forces.

Flow visualization and force measurement behind the rigid cylinder has shown that the third harmonic lift force is primarily a function of in-line motion of the cylinder. Large third harmonic forces occur when significant in-line motion of the cylinder causes significant fluctuations in lift, dependent on the phase between in-line and transverse motion. One can therefore expect that the distribution of third harmonic forces along the length of a riser will likely occur with roughly the same spatial distribution as the first harmonic force, since third harmonic motion of the

cylinder is not necessary to excite third harmonic forces. The third harmonic forces are caused by the same fluid vortex structure that causes first harmonic forces. This hypothesis is based on hydrodynamic assumptions from observed fluid phenomena, however Mukundan [44] makes a similar assertion based on a small test of different spatially distributed forcing functions with an assumed equation of motion for the riser. Additionally, since third harmonic forces are shown to increase almost linearly as a function of in-line motion, one can expect large third harmonic forces to exist where large in-line motions exist. This assumption is not universally true, however, since the third harmonic force can still be slightly altered by the phase relationship between in-line and transverse motions.

5.4.1 Quasi-steady fluid flow assumption

In order to estimate the distributed third harmonic force along the length of a flexible riser, a quasi-steady fluid flow assumption is used, similar to strip theory. Strip theory approximates the fluid flow around an object by assuming that the flow is locally two dimensional. Strip theory is used in many situations on cylindrical bodies such as slender pilings, ship hulls or mooring cables to approximate three dimensional force coefficients [45]. A quasi-steady assumption assumes that a long slender object can be broken into finite pieces where the fluid flow across each piece is uniform and steady. This method allows for an estimate of fluid forces acting in a sheared flow. The method works relatively well for stiff structures, however very long, oscillating structures with complicated sheared flows may suffer from a two-dimensional flow assumption. For instance, a cylinder oscillating in one degree of freedom in a sheared flow exhibits a complex wake that transitions from a '2S' shedding pattern to a '2P' shedding pattern [26]. This transition is difficult to model with two dimensional slices since a two dimensional flow may fluctuate between the two shedding patterns. Similarly, a long flexible riser is free to move in six degrees of freedom, meaning axial flow along the length of the riser may occur simply as a function of the riser oscillations. This flow cannot be approximated using a two dimensional assumption.

Although a quasi-steady flow assumption may not perfectly predict forces along

the entire length of a riser in shear flow, it still provides an order of magnitude estimate in the absence of a complete three dimensional riser model coupled with fluid dynamics. Prediction methods using experimentally obtained force coefficients such as those outlined by Gopalkrishnan [18], use a quasi-steady flow assumption, assuming that the flow over small portions of a riser are uniform and steady. This method will also provide a reasonable estimate of forces where steady motions of the cylinder occur. The forces on a cylinder experiencing motions that travel along the length of the riser may not be approximated well with a quasi-steady flow assumption, however steady oscillations of the cylinder may produce a regular, repeatable wake that may be approximated with a quasi-steady flow assumption. One might expect, therefore, that a quasi-steady fluid flow assumption may be able to indicate regions along the span of a riser where large third harmonic forces may dominate.

5.4.2 Estimate of distributed forces on example case

To estimate the distributed forces along the length of a flexible riser, an example case of a riser reconstruction was used from the Norwegian Deepwater Programme (NDP) High Mode VIV Tests analyzed in Mukundan [44] and Modarres-Sadeghi et al [41]. In this experiment, a 38 m long flexible pipe is subjected to a shear flow by being towed at an angle in a cylindrical arc. The arc motion allows for slow fluid velocities to occur at the pivot point of the flexible cylinder, while high velocities are achieved at the other end of the cylinder. Various strain gages and accelerometers are placed along the length of the riser, measuring strain and acceleration at discrete points along the length of the riser. Riser motions are reconstructed from the strain and accelerometer signals using Mukundan's reconstruction algorithm [44].

The particular example used in this case is for a sheared flow, where the 10th mode of the cylinder is excited in the span. The sheared flow in this case, produces oscillations that remain steady over a few cycles of motion such that traveling waves along the riser span are limited. The motion reconstruction gives values of A_x/D, A_y/D, and θ as continuous functions of the span. V_r is a continuous function of the span due to the shear flow. The force coefficient database is linearly interpolated in

order to generate a sufficient grid of motion parameters to match to the continuous parameters given by the motion reconstruction. The closest motion parameters from the database corresponding to the in-line motion, transverse motion, phase between motions, and reduced velocity from the reconstruction are determined and the corresponding force parameters are chosen as the magnitude of force at the given point along the length of the flexible riser.

Fig. 5-18 shows the reconstruction of lift coefficient magnitudes along the length of the flexible cylinder using the quasi-steady flow assumption. The figure only shows non-dimensional span length between 0 and 0.45 since the force coefficient database is limited to reduced velocities between 4.5 and 8. Force coefficient magnitudes of the first harmonic and third harmonic components of lift force are shown.

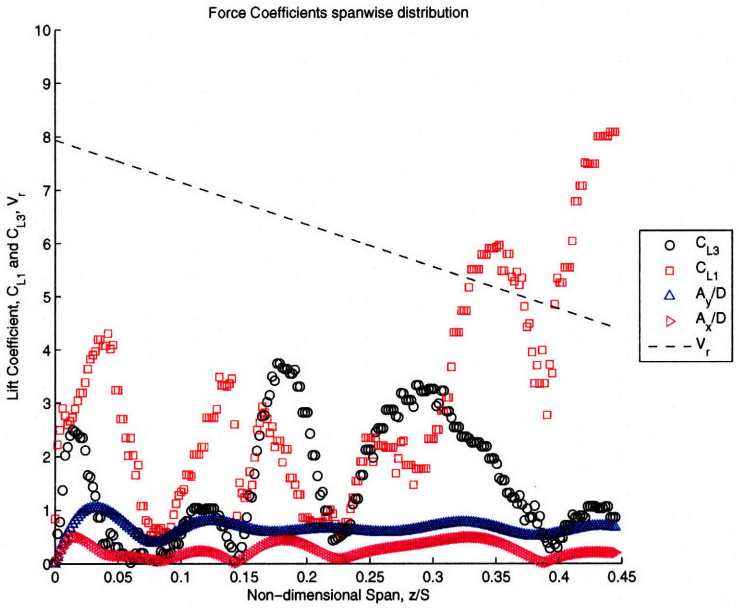

Figure 5-18: Reconstruction of lift force coefficient magnitudes along the length of flexible cylinder. Flexible cylinder experiment from Marintek data set with sheared flow. Estimates of force coefficients are only made in reduced velocity regions contained in the forced motion database. Black dotted line indicates the reduced velocity as a function of span.

Immediately apparent in Fig. 5-18 is the spatial distribution of the third harmonic force. Since the cylinder is excited in the 10th mode in this case, 5 peaks in the reconstructed transverse amplitude are apparent over the half span shown in Fig.

5-18. The third harmonic component of force also displays five peaks in the force magnitude. The third harmonic occurs with the same spatial distribution of the first harmonic force and transverse motion, although the peaks of third harmonic do not necessarily occur at the same place as peaks in the first harmonic force and transverse motion. The third harmonic portion of force is instead large in regions where in-line motion is large.

In this particular case, the sheared flow means that reduced velocity varies along the length of the riser. This results in different magnitudes of first and third harmonic forces with respect to one another along the length of the riser. One can see that at low reduced velocity, the motions are such that first harmonic forces are very large and third harmonic forces are relatively small in comparison. At intermediate reduced velocities near 6.5, the third harmonic becomes dominant and the first harmonic portion of force is small in comparison. As reduced velocity increases, the first harmonic portion of force again becomes dominant. This phenomenon matches the same phenomenon observed in the free vibration experiments from Chapter 3. The top line of motions from 3-32 shows how the third harmonic portion of lift becomes dominant for reduced velocities near 6.5 when the nominal frequency ratio of the system is near 2. This indicates that the flexible cylinder may in fact be excited with a condition of dual lock-in.

Chapter 6

Vortex Induced Vibration Suppression

Previous chapters have dealt with the problem of vortex formation behind a cylinder in a free stream of fluid and how these vortices dynamically interact with the structural characteristics of the cylinder to cause vibrations. In engineering applications, where vortex-induced vibrations exist, it is desirable to minimize these vibrations to extend the fatigue life of marine structures such as risers, undersea pipelines, and cabling.

There are two major consequences of vortex induced vibrations that can cause operational problems for offshore structures. One issue, discussed briefly in 3, is the problem of reduced fatigue life. Forces from the vibrations of long marine risers over a long period of time, can lead to fatigue damage in the structural material of the riser. The third harmonic forces analyzed in previous chapters will enhance the reduction of fatigue life, leading to structural failure earlier than expected. Devices for suppressing vortex induced vibrations must be able to reduce the oscillation amplitudes and forces associated with vortex shedding in order to limit fatigue damage on offshore structures. A second major problem caused by vortex induced vibrations is the enhancement of drag loads on the structure. Offshore drilling cannot occur when high drag loads exist on the drilling risers since high drag loads cause significant deflection of the riser. It is desirable that vortex suppression devices are therefore

capable of limiting or reducing the drag coefficient of the structure while suppressing vortex shedding.

Many methods exist for suppressing vortex shedding while limiting or reducing drag on the structure. Cost and manufacturing ease become an important factor in how many of these types of devices can be fitted onto existing structures or built into the design of new structures. Various methods of vortex suppression are discussed in the following sections.

Two passive methods of vortex suppression are analyzed experimentally in the context of two degree of freedom vortex induced vibrations. The two methods analyzed in this chapter are 1) placing holes along the span of the cylinder, passively introducing a jet into the cylinder wake, and 2) placing strakes along the outside of the cylinder to break up vortex correlation length. Resulting forces are measured using each method and these forces are compared with a bare cylinder and with the resulting forces on a cylinder oscillating in one degree of freedom. Flow visualization behind each suppression device is also performed.

6.1 Background - VIV Suppression Devices

Many VIV suppression methods exist for altering the fluid flow around a cylinder to inhibit vortex shedding. The methods used for vortex suppression can be divided into two groups, active control methods and passive control methods. Active control methods utilize an external source of energy to impart momentum into the fluid, controlling the flow with an external power source. This may be achieved by motoring a device to deflect the fluid flow in a certain direction or by pumping fluid into areas around the cylinder to impart momentum changes in the fluid. The latter method has been used to successfully suppress vortex-induced vibrations of a cylinder while reducing drag on the cylinder through the use of radial water jets in the experiments of Skaugset and Larsen [55]. A sucking and blowing method used in simulations by Dong and Karniadakis [13] has been shown to successfully reduce fluctuating lift coefficient magnitudes on a stationary cylinder while achieving very low drag coefficients.

The penalty for active methods of vortex suppression is that in engineering applications, active methods of suppression become expensive to install or construct and become complicated to engineer and control. Additionally active methods of suppression require external energy to control the flow, thus costing money and resources to operate and maintain. In contrast, passive methods of VIV suppression attempt to inhibit vortex-induced vibrations by either controlling the flow with a self-positioning device or a stationary device fixed to the cylinder. Passive devices can still be costly in the field, however the lack of an external power source makes them more attractive as a viable solution for controlling VIV.

Two typical passive control devices that are fixed directly to the cylinder and remain stationary are strakes and vortex generating tabs. Zdravkovich [77] compiled a series of experiments on such passive devices identifying drag coefficients and reduction in lift coefficient on stationary cylinders in a free stream. Since large lift forces occur when vortex shedding is well correlated along the span of the cylinder, strakes and vortex generators work by breaking up vortex correlation along the length. For strakes, vortex shedding is forced to occur at the specific edge of the strake, while vortex generators attempt to break up the formation of vortex tubes in the wake by shedding additional vorticity in the wake. In both cases, a drag mechanism is used to prohibit vortex-induced vibrations. The typical problem with strakes is that they are expensive to manufacture for very long cylinders and they have a fairly high drag coefficient associated with them. A cylinder with strakes is chosen as one of the passive methods used in this study because of its widespread use in ocean engineering applications.

Additional passive control devices that attempt to reduce drag on the cylinder are fairings. Fairings are used to direct the flow around the cylinder such that the cylinder becomes a stream-lined body that does not suffer from vortex shedding in the wake. Fairings cause problems in ocean engineering applications since they require a directional orientation to the flow. In order to direct the orientation of a fairing, bearings must be used so the fairing can align itself to the flow. This makes fairings quite expensive. Additionally, a fairing that does not align to the flow may have

problems associated with torsional instabilities and galloping.

The second device used in this study is a passive flow control device intended to reduce drag while suppressing vortex formation. Olsen and Rajagopalan [48] showed that if a slit is placed through a cylinder in the direction of fluid flow, a stationary cylinder shows a decrease in the vortex shedding frequency while the drag coefficient is reduced to almost half that of an equivalent bare cylinder. Similar to the blowing mechanism of Dong and Karniadakis [13], the hole passively creates a jet that interferes with the unstable vortex street. This method of vortex suppression is modified to a three dimensional form by placing holes along the length of a rigid cylinder rather than putting a slit through the cylinder, which causes the flow to be completely two-dimensional. This method is compared with the traditional strake and bare cylinder to investigate whether this passive control method is feasible for suppressing VIV in only cross-flow oscillations and in two degree of freedom oscillations.

6.2 Experimental Description

The apparatus used for studying vortex suppression methods was the same forced vibration apparatus described in Chapter 4. This apparatus was used in order to obtain flow visualization of the wake behind each test cylinder. One disadvantage in using forced vibrations to analyze VIV suppression devices is that the effect of the device on suppressing vibrations must be inferred from fluid force measurements rather than observed, as with a free vibration. Gopalkrishnan [18] used this method for evaluating the effectiveness of a haired fairing by considering changes in contours of C_{Lv} from forced motions compared with similar contours obtained for the bare cylinder.

In this experiment, the two VIV suppression devices are tested and compared with oscillations of a bare cylinder. In each case, the cylinders with suppression devices are compared to a bare cylinder with equivalent diameter and length. The bare cylinder dimensions are the same as in previous forced oscillations in this study, with a cylinder diameter of 0.0381 m (1.5 in), and a span of 0.686 m. Fluid forces in the lift and drag

directions are recorded and flow visualization is performed on individually significant experiments.

6.2.1 Hole Cylinder

One of the tested devices is a cylinder with holes drilled directly through the cylinder to allow fluid to pass through the cylinder. The holes through the cylinder are intended to mimic a two dimensional cylinder with a slit through the center, however the two dimensional version does not translate well to a useful three dimensional experiment. Instead, holes are used in place of the slit.

The holes in the cylinder are aligned in-line with the incoming flow, such that a jet will be created in the wake behind the cylinder due to the acceleration of fluid through the holes. The intention of this device is that the instability of the jet forming in the wake of the cylinder will passively interact with the instability of vortex shedding in the wake, resulting in a wake without vortex shedding.

Two configurations of holes are used in this experiment, one where holes are 16 percent of the cylinder diameter, and the other with holes 25 percent of the cylinder diameter. Hole diameter affects the exit velocity of fluid from the hole, resulting in a stronger or weaker jet in the wake of the cylinder. Fig. 6-1 shows a picture of the test cylinder with holes. The test cylinder is hollow to limit the moving mass and inertial forces exerted on the linear motors. Plastic tubing is inserted through each hole to ensure that the cylinder will not flood.

The spacing between holes on the test cylinder is 50 percent of the cylinder diameter. This spacing is chosen to maximize the number of holes along the length, while keeping the structural integrity of the cylinder intact.

6.2.2 Strake Cylinder

The cylinder with strakes is outfitted with three strakes that helically wind down the span of the cylinder. The strakes are equally spaced around the cylinder such that they are located 120 degrees apart. The strake height is fixed at 25 percent of

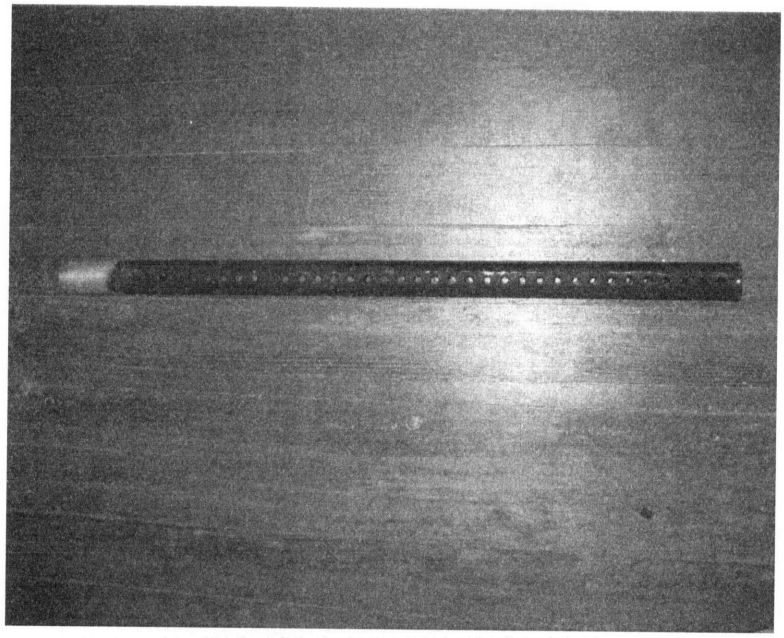

Figure 6-1: Picture of test cylinder with holes drilled along the length.

the cylinder diameter and the strake width is 12.5 percent of the cylinder diameter. The pitch ratio (P/D) of an individual strake is 15, such that the strake makes one revolution around the cylinder every 15 diameters. Since three strakes are used on the cylinder, the effective pitch ratio is 5, since one of the strakes will be crossing a given radial point on the cylinder every 5 diameters. Fig. 6-2 shows the test cylinder outfitted with strakes.

6.2.3 Test Matrix

Many previous studies on VIV suppression devices have focused on suppressing transverse oscillations of the cylinder only. For comparison purposes, two sets of tests are performed for each suppression device configuration with only cross-flow motion and with in-line and cross-flow motion. This generates comparisons to show whether devices effective for suppressing cross-flow motion are still as effective when the cylinder is free to oscillate in-line to the flow as well.

The cross-flow motion tests consist of 60 tests in a range of reduced velocities between 5 and 8.5. Cross-flow amplitude is varied from 0.2 to 1 cylinder diameter.

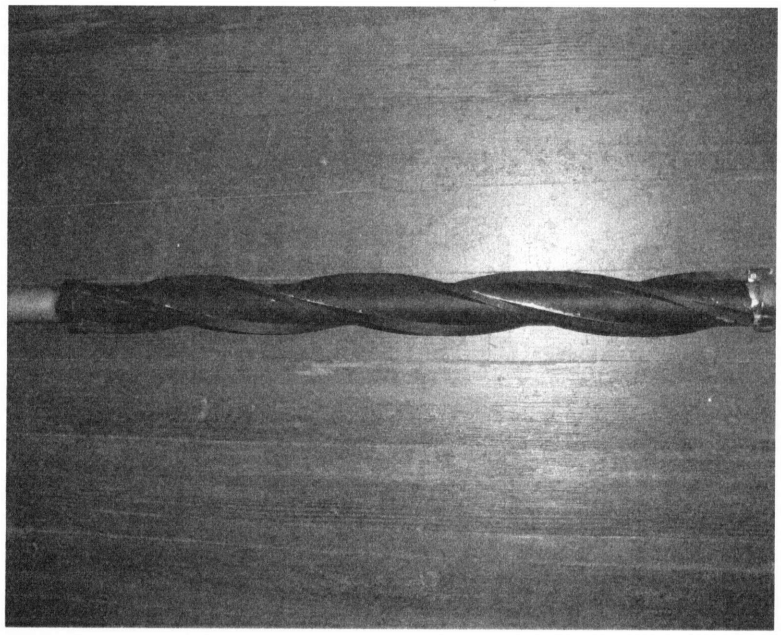

Figure 6-2: Picture of cylinder test cylinder with strakes. Individual strakes have a $P/D = 15$ and three strakes provide an effective P/D of 5.

This creates a small series of experiments in the range of reduced velocity where largest amplitude vibrations may be expected. Drag and lift forces are measured using the same six-axis sensor from Chapters 4 and 5.

For cross-flow and in-line motion of the cylinder, 60 tests are performed across the same reduced velocity range as the one degree of freedom tests, V_r between 5 and 8.5. In-line motion introduces two new variables of motion, the in-line amplitude and the phase between in-line and transverse motions. In order to simplify the data set and avoid running a comparable number of experiments to those in Chapter 5, the phase between motions is fixed at a value of 0 degrees. One of the initial goals of this study was to see how third harmonic forces are affected by the presence of vortex suppression devices. A phase of 0 degrees is chosen since a local maximum of third harmonic forces was shown to exist for this phase. In-line motion is also fixed as a function of transverse motion in order to simplify the parameter space. In-line motion is set to be one-half the magnitude of the transverse motion, e.g. a forced transverse motion of $A_y/D = 0.8$ will have a forced in-line motion of $A_x/D = 0.4$. This relationship is based on the worst case relationship of these parameters observed

in free vibration experiments. Due to the limitation of the parameter space for the in-line motion and phase, it is important to note that the results presented in this chapter are very limited in truly showing the effectiveness of these suppression devices under two degree of freedom oscillations.

6.3 Force Measurements

Since the cylinder in these experiments undergoes a forced vibration as opposed to a self-excited vibration, it is necessary to consider contours of force coefficients over the tested parameter space. In a one degree of freedom oscillation, a free vibration must meet a condition such that the lift coefficient in phase with velocity, C_{Lv}, is zero if the structural damping is zero. This must occur in a free vibration under resonance or lock-in, since inertial forces will balance with spring forces under this condition. The zero contour of C_{Lv} is easily determined from forced vibrations over a range of reduced velocities and amplitudes. As in chapter 5, the average power over one cycle of motion is used to determine the equivalent zero damping free vibration condition for the cylinder oscillating in two degrees of freedom.

In order to determine the effectiveness of a particular suppression device, bare cylinder magnitudes of C_{Lv}, mean drag, and third harmonic lift force (for two degree of freedom motions) are compared to the strake cylinder and cylinder with holes. Since these parameters change as a function of reduced velocity, comparisons are presented graphically, rather than giving a single percentage increase or decrease in amplitudes.

6.3.1 Forced Cross-flow Motion

Inferred Oscillation Amplitude Reduction

Contours of $C_{Lv} = 0$ are shown for the bare cylinder, cylinders with holes, and strake cylinder in Fig. 6-3. The contour indicates a predicted free vibration of the bare cylinder to be on the order of A_y/D 0.6. This value is slightly low compared to

observed free vibrations of a cylinder's motion in one degree of freedom (see chapter 3), however this value is comparable to values obtained by Gopalkrishnan [18] in this reduced velocity range. The narrow $A_y/D = 0.8$ peak seen in Gopalkrishnan's data is not observed in the present study, likely due to the sparseness of test matrix points. The general trend of Gopalkrishnan's zero contour is captured in the present study.

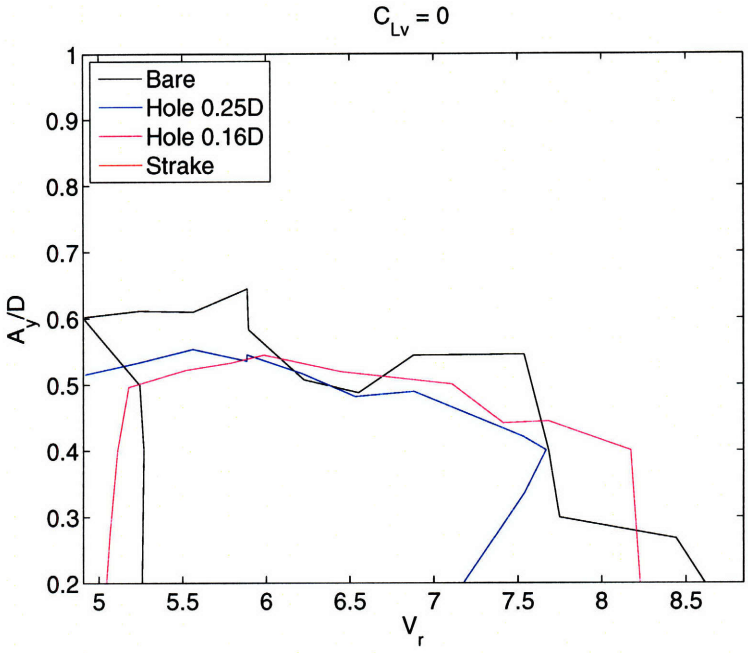

Figure 6-3: Comparison of vortex suppression devices oscillation amplitude reduction effectiveness for one degree of freedom motions. Figure shows contours of $C_{Lv} = 0$ for different suppression devices and the bare cylinder. Contour lines indicate the theoretical amplitude at which a structure with zero structural damping would oscillate.

Immediately apparent in Fig. 6-3 is the absence of a strake contour. The strake cylinder was observed to have negative C_{Lv} over the entire range of motions, indicating that the cylinder with strakes will likely not be excited with amplitudes larger than $A_y/D = 0.2$. Brankovic and Bearman [5] showed that a freely vibrating cylinder with strakes at very low mass ratio ($m^* = 0.82$) can still have excitations as large as $A_y/D = 0.5$, although the strake height was only 10 percent of the diameter in this case. The larger strake height of the present study may further disturb the unstable formation of regular vortices in the wake of the cylinder. In essence, strakes on the

cylinder are very effective at reducing the inferred transverse oscillation of the cylinder in one degree of freedom motions.

The cylinders with holes do not produce a similar effect on the measurement of C_{Lv} as the cylinder with strakes, as seen in Fig. 6-3. Neither the 16 percent nor the 25 percent diameter holes produce much reduction in inferred oscillation amplitude. The zero contour curves are nearly identical to the bare cylinder. One issue with the cylinder with holes is that the holes are aligned with the mean incoming flow velocity, not the true incident velocity seen by the cylinder, i.e. the cylinder does not rotate to ensure that the hole is parallel to the incident flow velocity. As the cylinder is forced with large amplitudes of motion, it becomes difficult for fluid to be forced through the cylinder hole and ejected into the wake. The fluid may become largely stagnant in the hole in this case, with insufficient flow velocities exiting the hole to affect the wake, causing the cylinder with holes to appear much like a bare cylinder.

Mean Drag

Mean drag coefficients for one degree of freedom oscillations are compared in the contour plots shown in Fig. 6-4. The drag coefficient associated with cylinder vibrations typically is a function of the amplitude of vibrations, hence, when comparing the drag coefficient for a certain VIV suppression device, one must consider drag coefficient at the amplitude which the cylinder is oscillating. For example, a non-oscillating bare cylinder at Reynolds numbers near 10,000 should exhibit a drag coefficient near 1.2. The bare cylinder, according to the previous free vibration amplitude estimation, will oscillate with amplitudes in excess of $A_y/D = 0.6$. The drag coefficient for reduced velocities near 6, in this case, will be between 2 and 2.3, much larger than for a stationary cylinder.

Since the strake was shown to have an oscillation amplitude less than A_y/D, the appropriate drag coefficient value will lie along the lower amplitude contours of Fig. 6-4b. One may expect an operational drag coefficient for this strake configuration to be around 2.6. This is actually larger than the drag coefficient of the bare cylinder in this particular case, although much larger amplitude motions are known to exist for

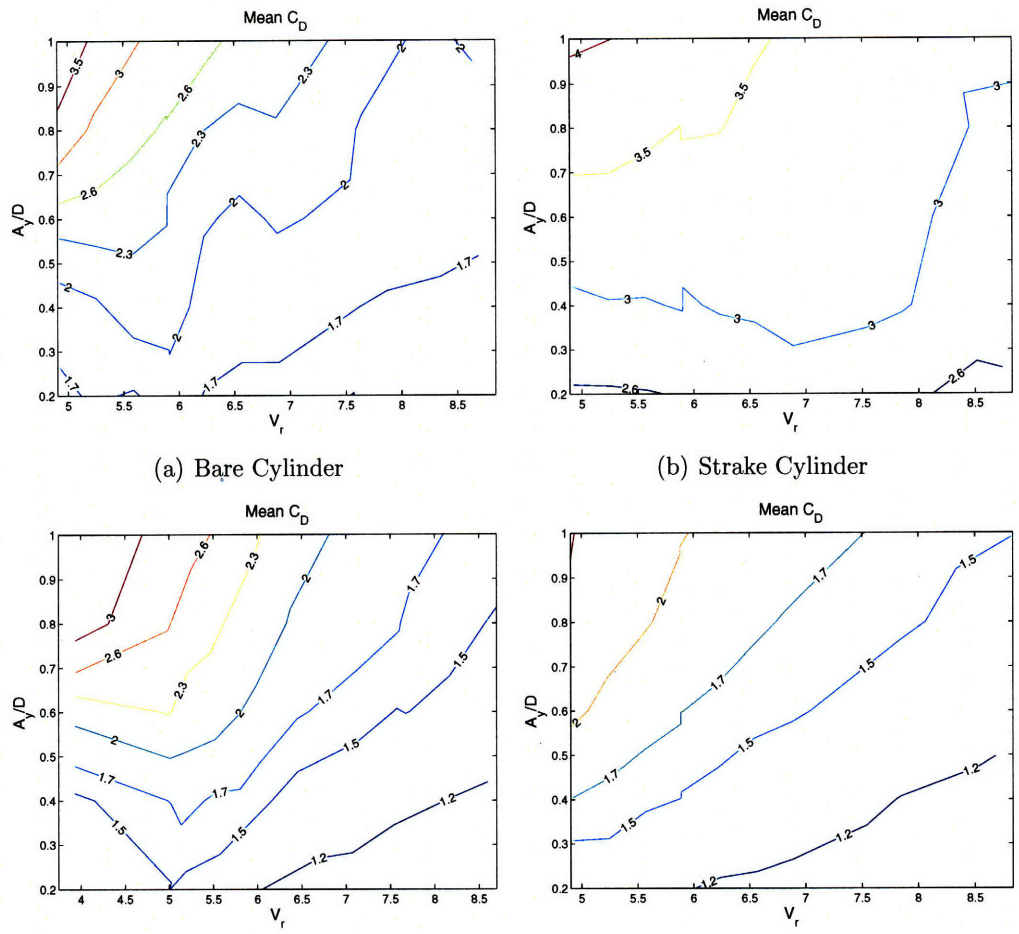

(a) Bare Cylinder

(b) Strake Cylinder

(c) Hole Cylinder 0.16D

(d) Hole Cylinder 0.25D

Figure 6-4: Contours of mean drag coefficient as a function of transverse amplitude and reduced velocity for various vortex suppression devices and the bare cylinder. Forced motion of the cylinder is in the cross-flow direction only.

bare cylinders under free vibrations, which may lead to larger drag coefficients.

The two cylinders with holes exhibit slightly different characteristics in mean drag. Each cylinder with holes will have an inferred oscillation amplitude near $A_y/D = 0.5$. For 16 percent diameter holes, the cylinder displays a drag coefficient near 1.7 for a reduced velocity of 6, a 23 percent reduction in drag from the bare cylinder. The 25 percent diameter holes result in a drag coefficient near 1.5 for a reduced velocity of 6, a 32 percent reduction in drag from the bare cylinder. Reduction in drag is expected in each case since the projected frontal area of the cylinder is effectively reduced by drilling holes through the cylinder. Fluid passing directly through the holes no longer

contributes to form drag on the cylinder. It is interesting to note that although the passive jet velocity was not large enough to reduced inferred transverse oscillation of the cylinder, fluid still passed through the holes, significantly reducing drag on the cylinder.

6.3.2 Cross-flow and in-line motion

Inferred Oscillation Amplitude Reduction

In two degree of freedom forced motions, the average power over one cycle of motion is used to infer oscillations of the cylinder. Contours of zero average power are shown in Fig. 6-5. In this case, the bare cylinder displays transverse amplitudes as large as 0.8 diameters for the highest reduced velocity. The contour is not completely contained by the parameter space of the experiments. It is important to note again that in-line motions are fixed as one-half the transverse motion, such that fairly large in-line amplitudes near 0.4 diameters are inferred from this contour as well.

Again, the cylinder with strakes performs well at reducing inferred oscillations of the cylinder. The zero power contour for the cylinder with strakes does not appear in Fig. 6-5, again inferring that amplitudes will be less than 0.2 diameters of motion in the transverse direction and less than 0.1 diameters of motion in the in-line direction. Again, it is important to note that these oscillations occur for a fixed phase between in-line and transverse motions. Without additional experimentation, it is not possible to say whether different phases will result in oscillations of the cylinder with strakes. If one considers the parameter C_{Lv} as opposed to average power, one can see that a small region of positive C_{Lv} exists for the strake at reduced velocities near 8 and 8.5 (see Fig. 6-6). This indicates a possibility for excitation of the cylinder, however large, negative C_{Dv} in the in-line direction effectively dissipates energy such that the total average power remains negative over this region (requiring external energy such as that supplied from the linear motors for an oscillation to occur).

The cylinders with holes exhibit a slight reduction in the inferred amplitude of motion when in-line motions are included. Fig. 6-5 shows that the cylinder with 16

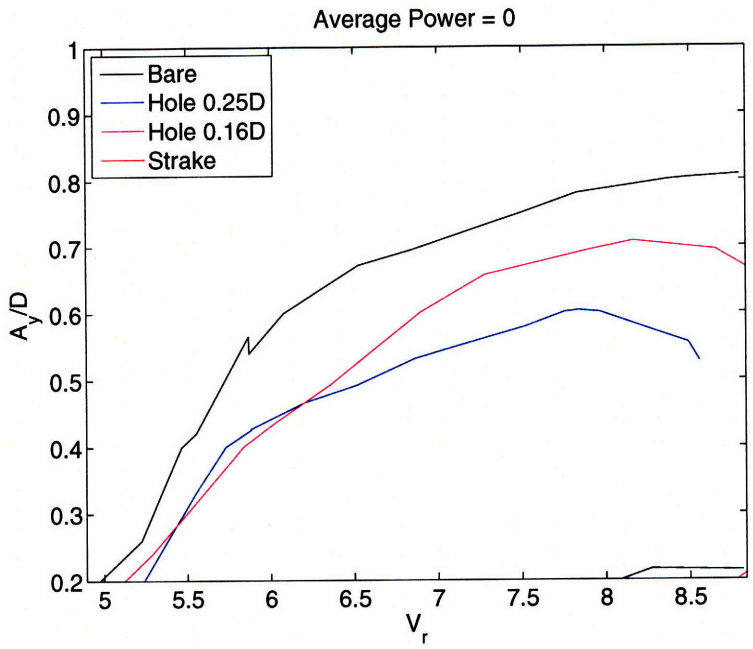

Figure 6-5: Comparison of vortex suppression devices oscillation amplitude reduction effectiveness for two degree of freedom motions. Figure shows contours of $C_p = 0$ (average power) for different suppression devices and the bare cylinder. Contour lines indicate the theoretical amplitude at which a structure with zero structural damping would oscillate. In-line amplitude is exactly half of the transverse amplitude and phase between in-line and transverse motions is 0 degrees.

percent diameter holes reduces the maximum transverse oscillation amplitude from 0.8 to 0.68. The larger holes at 25 percent of the diameter reduce the maximum transverse amplitude of motion to less than 0.6 diameters. The improved performance of the cylinder with holes is likely due to in-line oscillations of the cylinder. Since the cylinder surges forward due to the in-line oscillations, the incident velocity seen by the cylinder becomes more aligned with the direction of the holes. This allows a jet to properly form in the wake behind the cylinder. The jet, however is not steady since the cylinder is being forced to oscillate, thus the wake still has the opportunity to form unsteady vortices that affect the calculation of C_{Lv} and C_{Dv}.

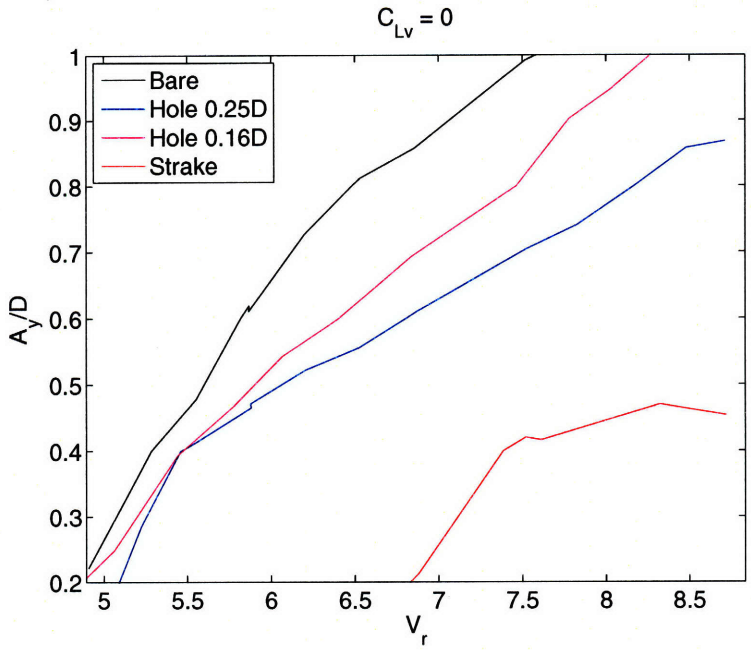

Figure 6-6: Comparison of contours of $C_{Lv} = 0$ for different suppression devices and the bare cylinder. In-line amplitude is exactly half of the transverse amplitude and phase between in-line and transverse motions is 0 degrees.

Mean Drag

Mean drag on the bare cylinder is enhanced by in-line motions, consistent with the observations from free vibrations. Fig. 6-7 shows mean drag contours for each test set. The mean drag coefficient on the bare cylinder at a reduced velocity of 8.5 with $A_y/D = 0.8$ and $A_x/D = 0.4$ is about 3.7, much larger than the value with only transverse motions. As was seen in chapter 5, the mean drag increases largely as a function of transverse and in-line motion of the cylinder, and can take on very large values.

Since the cylinder with strakes effectively reduces amplitudes below those observed in these forced experiments, the operational drag coefficient of the cylinder with strakes is similar to that observed for the cylinder with only transverse motion. In this case, the drag coefficient is less than a value of 3. Contours of mean drag are slightly larger at a transverse amplitude of 0.2 since there is slight in-line motion at an amplitude of 0.1, thus drag coefficient is slightly larger than in the one degree of

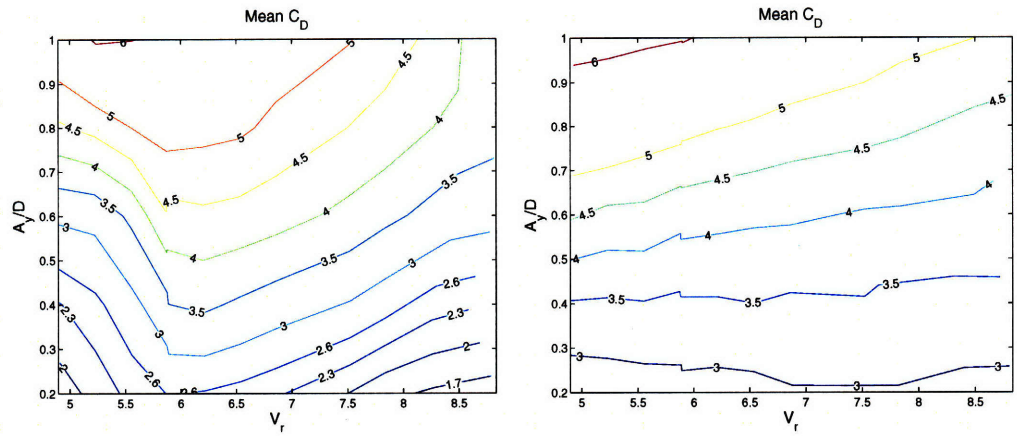

(a) Bare Cylinder

(b) Strake Cylinder

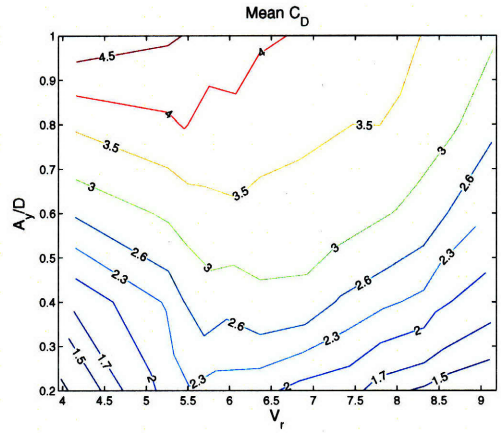

(c) Hole Cylinder 0.16D

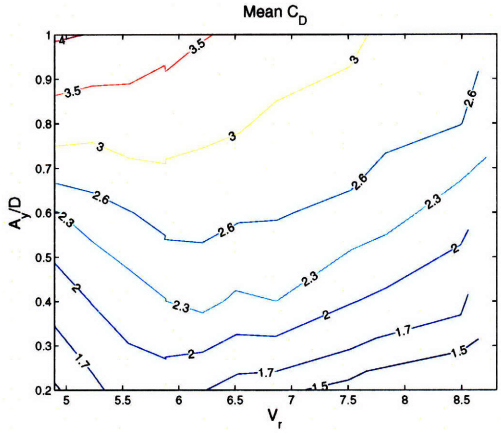

(d) Hole Cylinder 0.25D

Figure 6-7: Contours of mean drag coefficient as a function of oscillation amplitude and reduced velocity for various vortex suppression devices and the bare cylinder. Forced motion of the cylinder is in both in-line and cross-flow directions.In-line amplitude is exactly half of the transverse amplitude and phase between in-line and transverse motions is 0 degrees.

freedom case.

The cylinders with holes are again effective at reducing operational drag coefficient on the cylinder. The 16 percent diameter holes reduce the maximum operational drag coefficient to a value near 2.8, while the 25 percent diameter holes reduce the drag coefficient to a value near 2.3. The 25 percent diameter hole has effectively reduced the bare cylinder drag coefficient by 38 percent, while reducing oscillation amplitudes by 20 percent.

Third Harmonic Lift Coefficient

The third harmonic component of lift is a force unique to two degree of freedom motions of the cylinder. The third harmonic component of lift will largely cause problems in the fatigue life of a structure, hence ocean structures would benefit from VIV suppression devices that inhibit the third harmonic lift forces on the structure. In the particular set of experiments shown, the bare cylinder essentially exhibits third harmonic forces that increase almost linearly as a function of transverse and in-line amplitude (see Fig. 6-8). Third harmonic forces were previously shown to be almost exclusively a function of in-line motion. Since in-line motion increases as a function of transverse motion in these experiments, the third harmonic increases with transverse amplitude as well. The inferred free vibration of the bare cylinder follows motions such that the third harmonic portion of lift coefficient takes on values as large as 2. This is a fairly significant portion of the lift coefficient.

The cylinder with strakes is very effective at reducing third harmonic force magnitudes. One can see that the cylinder with strakes reduces the third harmonic lift coefficient to a value of 0.2 over almost the entire range of forced motions. Since the actual oscillation amplitude of the strake will be much lower than these values, the third harmonic force will be virtually non-existent.

The cylinder with holes is also partially effective at reducing third harmonic lift magnitudes. For both sized holes, the third harmonic lift coefficient is reduced for reduced velocities between 6 and 7. The larger sized holes with 25 percent cylinder diameter are slightly more effective at reducing the third harmonic magnitude, such that third harmonic lift coefficient magnitudes are less than 0.8 for almost the entire range of tested motions. It is difficult to determine exactly how strakes and holes change the wake such that third harmonic forces are reduced without visualizing the wake behind the cylinder. This issue is addressed in the next section.

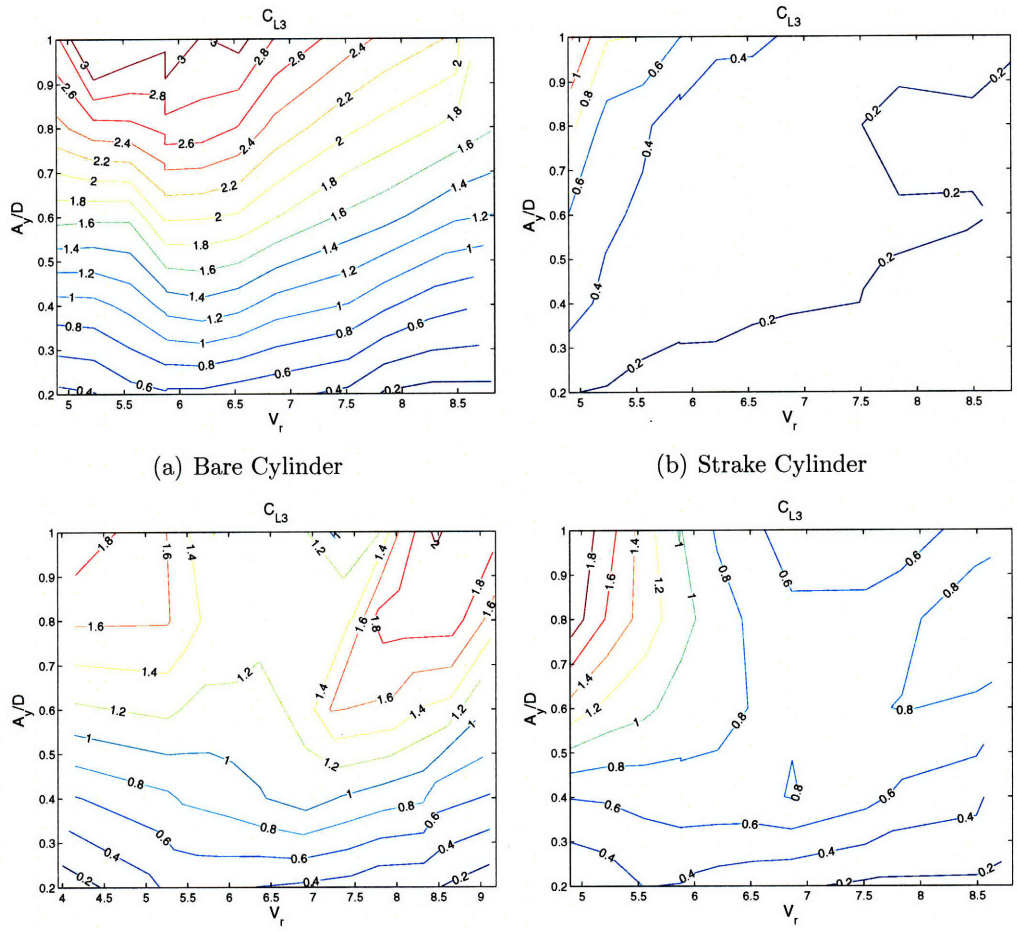

(a) Bare Cylinder

(b) Strake Cylinder

(c) Hole Cylinder 0.16D

(d) Hole Cylinder 0.25D

Figure 6-8: Contours of third harmonic lift coefficient as a function of oscillation amplitude and reduced velocity for various vortex suppression devices and the bare cylinder. Forced motion of the cylinder is in both in-line and cross-flow directions.In-line amplitude is exactly half of the transverse amplitude and phase between in-line and transverse motions is 0 degrees.

6.4 Flow Visualization of Suppression Devices

Fluid flow in the wake of each VIV suppression device is visualized using the same PIV system and methods from Chapter 4. The wake of each suppression device is compared with the wake behind a bare cylinder oscillating with equivalent motions at equivalent reduced velocity. Comparisons are made for a virtually stationary cylinder ($A_y/D = 0.1$), a cylinder oscillating with only transverse motion at an amplitude of $A_y/D = 0.6$, and a cylinder oscillating with transverse and in-line motions with

$A_y/D = 0.8$, $A_x/D = 0.3$, and $\theta = 0$. Reduced velocity is 6 in all cases. All figures show instantaneous fields of vorticity. Since the phase betweens motions is fixed, it is important to note that the observed wakes behind each cylinder in two degree of freedom motions may not be universal. Chapter 4 showed that the wake is highly sensitive to changes in the phase between in-line and transverse motions.

6.4.1 Virtually Stationary Cylinder

A virtually stationary cylinder is used for these visualizations as opposed to a stationary cylinder due to limitations of the field of view with the PIV system. When vortices form in the wake of a non-oscillating cylinder, the vortices require some formation time and the vortex structures typically do not appear to be coherent directly behind the cylinder. The vortices become more well formed several diameters behind the cylinder in the wake. By forcing the cylinder at a small amplitude, the shedding process is slightly enhanced, such that vortex shedding will occur closer to the cylinder, in the field of view of the PIV camera.

Fig. 6-9 shows the wake behind the bare cylinder at several points throughout one cycle of vortex shedding. The typical '2S' shedding pattern of two single vortices shedding per cycle is observed for the bare cylinder in this case. As strakes are applied to the cylinder in Fig. 6-10, the '2S' shedding pattern is no longer well defined in the wake. Instead, small vortices with weaker magnitude of vorticity shed from the strakes at a higher frequency than the Strouhal frequency. In this particular image, the strakes are aligned in such a way that vorticity sheds almost evenly to each side of the cylinder due to the hard edges of the strakes, similar to the sharp edges of a flat plate. An instability still exists in the wake since vorticity still tends to curl around the cylinder slightly, although it is not possible to tell if coherent vortex structures form further downstream in the wake.

The cylinders with holes are shown in Figs. 6-11 and 6-12. For the cylinder with holes 16 percent of the diameter, the wake still exhibits a '2S' shedding pattern, however the formation length of vortex shedding has been pushed further downstream from the cylinder. In the bare cylinder case, coherent vortices form approximately

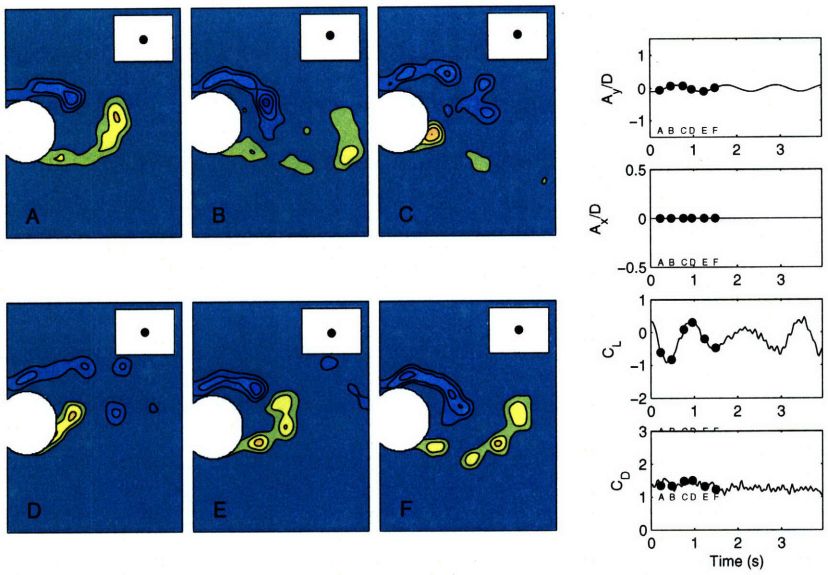

Figure 6-9: Wake behind bare cylinder with $A_y/D = 0.1$ (virtually stationary), $V_r = 6$. Vorticity contours show non-dimensional vorticity, $\frac{\omega D}{U} = \pm 3, \pm 5, \pm 7, \ldots$.

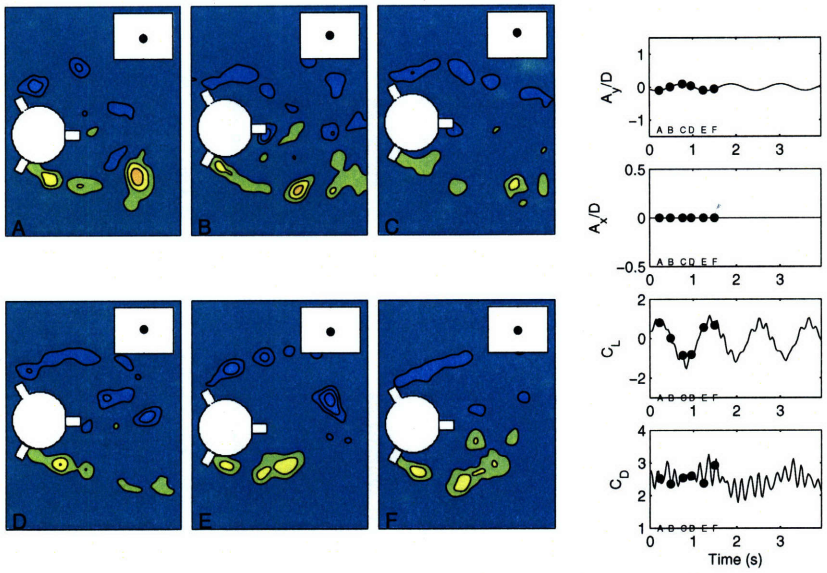

Figure 6-10: Wake behind strake cylinder with $A_y/D = 0.1$ (virtually stationary), $V_r = 6$. Vorticity contours show non-dimensional vorticity, $\frac{\omega D}{U} = \pm 3, \pm 5, \pm 7, \ldots$.

one diameter downstream from the cylinder. With 16 percent diameter holes through the cylinder, coherent vortices form nearly two diameters downstream from the cylinder. Formation of vortices further downstream from the cylinder will likely reduce

lift forces on the cylinder since the angle formed between the horizontal(drag) axis through the cylinder and a line through the center of the cylinder and the center of the vortex will be much shallower with a vortex further downstream.

The cylinder with larger holes exhibits a different wake phenomenon than that with smaller holes. Fig. 6-12 indicates that the wake behind the cylinder with larger holes does not clearly form a '2S' shedding pattern. Instead, the wake is nearly steady, with almost constant vorticity shedding from each side of the cylinder. Again, it is not possible to tell whether an unsteady vortex pattern forms further downstream than the three diameters shown in the figure. In this case, the jet formation from the holes effectively cancels the unsteady instability of vortex formation directly behind the cylinder. Slight wavering occurs in the wake due to the slight forced oscillation of the cylinder in the transverse direction.

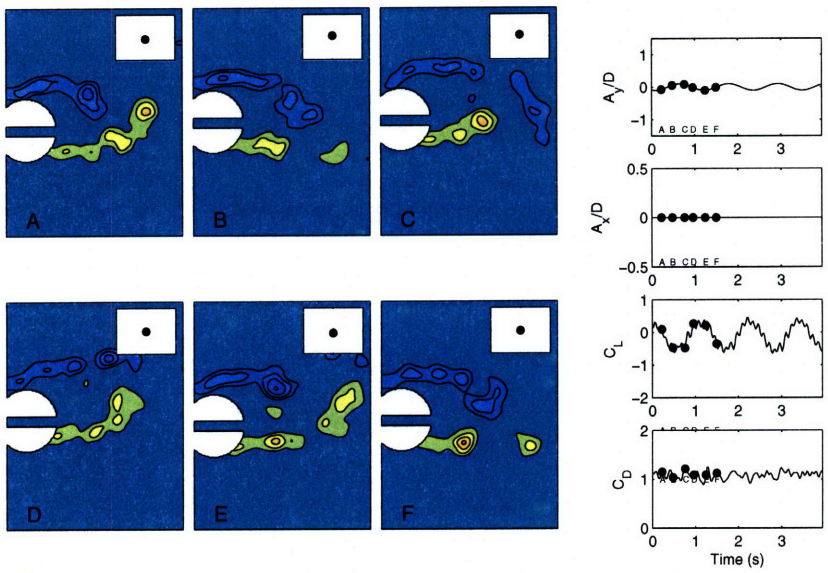

Figure 6-11: Wake behind hole cylinder (0.16D size holes) with $A_y/D = 0.1$ (virtually stationary), $V_r = 6$. Vorticity contours show non-dimensional vorticity, $\frac{\omega D}{U} = \pm 3, \pm 5, \pm 7, \ldots$.

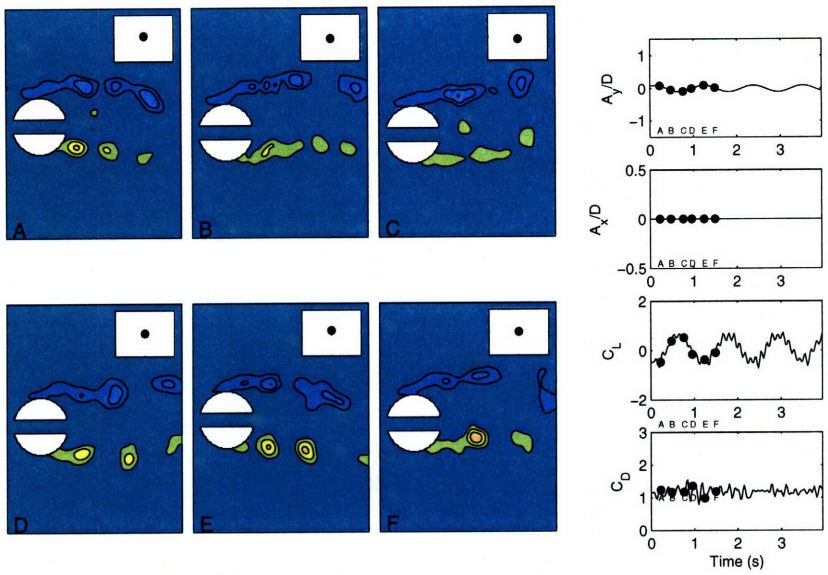

Figure 6-12: Wake behind hole cylinder (0.25D size holes) with $A_y/D = 0.1$ (virtually stationary), $V_r = 6$. Vorticity contours show non-dimensional vorticity, $\frac{\omega D}{U} = \pm 3, \pm 5, \pm 7, \ldots$.

6.4.2 Forced Cross-flow motion

When the cylinder is forced at a larger transverse amplitude, vortex formation becomes more well defined as cylinder motions enhance changes in the pressure gradient near the cylinder. The bare cylinder, in this case, displays large, strong vortices that trail the cylinder and shed alternately in the wake, as seen in Fig. 6-13. At this reduced velocity and amplitude of motion, the wake forms a '2P' pattern, as two pairs of counter-rotating vortices shed over one cycle of transverse motion. The paired vortices are most easily seen in the bottom right portion of frame A.

Applying strakes to the cylinder at this amplitude of oscillation creates a very messy wake (see Fig. 6-14). In the virtually stationary cylinder case, the incoming flow velocity dominated the direction of fluid motion such that shedding of vorticity primarily occurred at the two strakes located 60 degrees and -60 degrees from the forward stagnation point. When the cylinder is forced in transverse oscillations, the strake located at the aft stagnation point sheds vorticity caused by the strake dragging through the fluid in transverse motions. This creates a messy wake where

any clear patterns are difficult to distinguish. This case is shown in comparison, however it does not really represent a meaningful oscillation of the cylinder, since it was deduced earlier that a cylinder with these strakes will not likely oscillate with an amplitude this large.

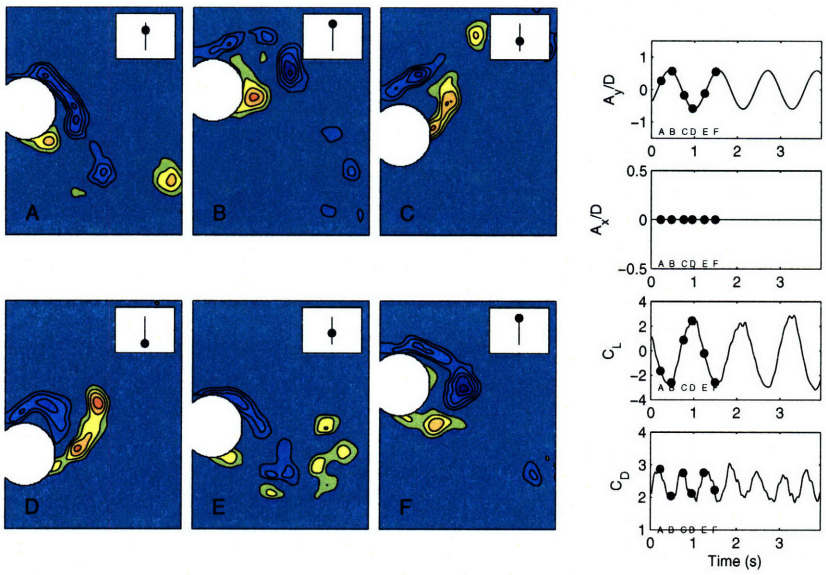

Figure 6-13: Wake behind bare cylinder with forced $A_y/D = 0.6$, $V_r = 6$. Vorticity contours show non-dimensional vorticity, $\frac{\omega D}{U} = \pm 3, \pm 5, \pm 7, \ldots$.

The wake behind the cylinders with holes were very similar regardless of hole size. In Figs. 6-15 and 6-16, one can see that the wake has been slightly altered from the bare cylinder wake. Again, it appears that vortex shedding occurs further downstream from the cylinder as the passive jet formed by the holes in the cylinder decreases the pressure deficit directly behind the cylinder. In both cases, the formation of a '2P' wake is not apparent although this pattern may become more well defined downstream from the cylinder since the holes tend to push the formation of vortices further downstream.

One can see from the wake images, that vorticity from vortex shedding is much larger in magnitude than vorticity caused by jet formation behind the hole since vorticity from the jets does not even appear on the scale used in the images. Additionally, one can see that as the cylinder moves with larger transverse motion, the vorticity

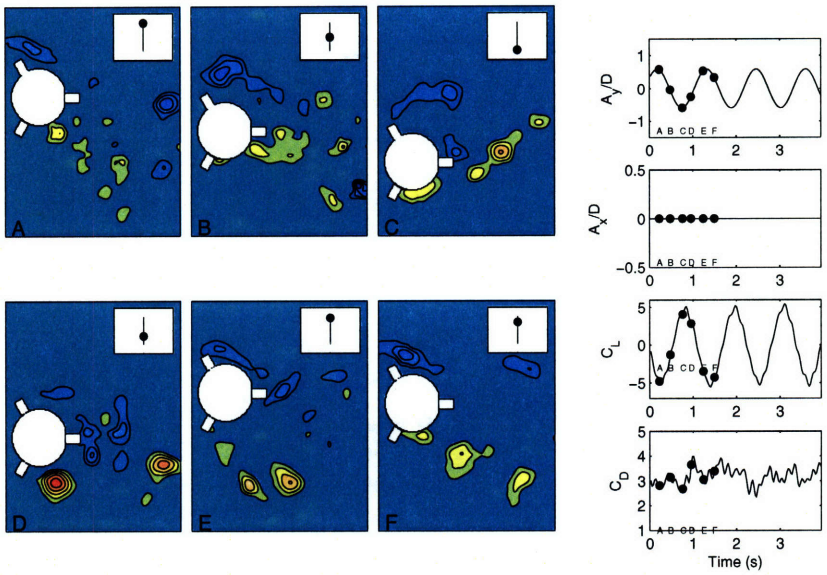

Figure 6-14: Wake behind strake cylinder with forced $A_y/D = 0.6$, $V_r = 6$. Vorticity contours show non-dimensional vorticity, $\frac{\omega D}{U} = \pm 3, \pm 5, \pm 7, \ldots$.

curls around the hole and is largely unaffected by the presence of the hole. This indicates that there is not a high flow rate through the holes and the jet formation in the wake is very weak when the cylinder is forced with large transverse oscillations. Again, this may be remedied by aligning the hole in the direction of the incident velocity or more simply by widening the hole entrance to allow the flow to be directed into the hole as the cylinder oscillates.

6.4.3 Forced In-line and Cross-flow Motion

In two degrees of freedom, the wake of the cylinder becomes more complicated and third harmonic forces in lift appear as the in-line motion of the cylinder interacts with large vortices shed in the wake. The bare cylinder in Fig. 6-17 displays a typical wake for a cylinder oscillating with $\theta = 0$. The bare cylinder sheds either two or 3 like-signed vortices per half cycle as the cylinder sweeps through its figure eight motion (the true motion through the fluid is not a figure eight since the cylinder has a forward velocity). Three red-yellow vortices are easily distinguished in Frame D, while the third of three blue vortices are forming in Frame F. This pattern is

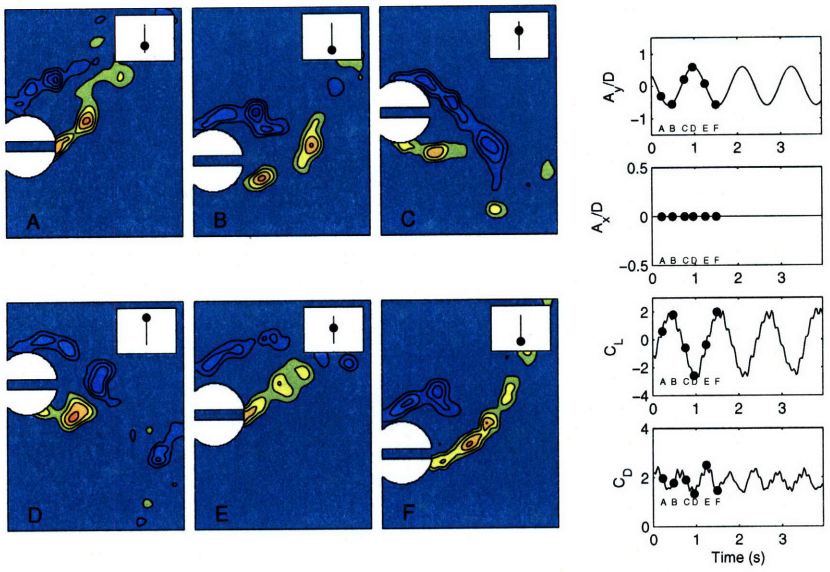

Figure 6-15: Wake behind hole cylinder (0.16D size holes) with $A_y/D = 0.6$, $V_r = 6$. Vorticity contours show non-dimensional vorticity, $\frac{\omega D}{U} = \pm 3, \pm 5, \pm 7, \ldots$.

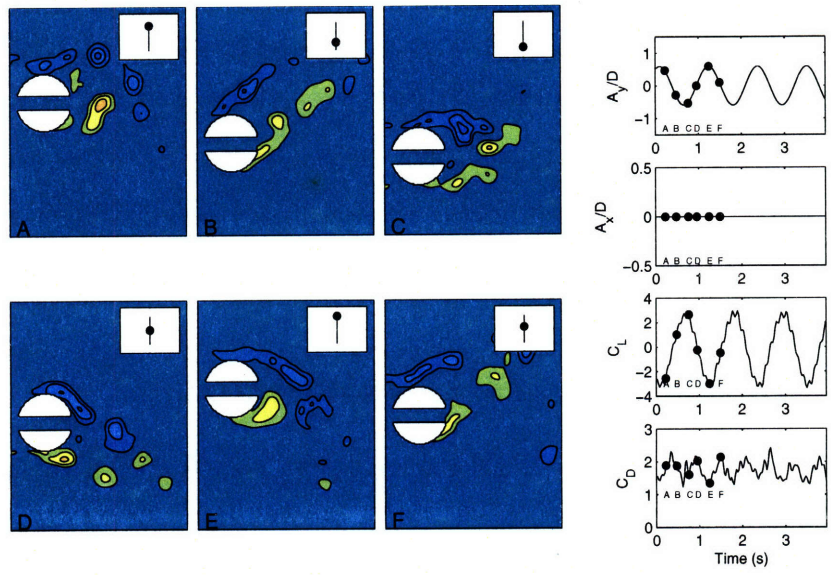

Figure 6-16: Wake behind hole cylinder (0.25D size holes) with $A_y/D = 0.6$, $V_r = 6$. Vorticity contours show non-dimensional vorticity, $\frac{\omega D}{U} = \pm 3, \pm 5, \pm 7, \ldots$.

comparable to the '2T' pattern of Jauvtis and Williamson [30], which is similar to a '2P' pattern, except an additional vortex forms due to additional accelerations of the cylinder. In this pattern, one large vortex forms and wraps around the cylinder as it

moves in the figure eight motion. The blue vortex in Frame A most clearly shows this phenomenon. The relative motion of this vortex with respect to the cylinder motions results in a large third harmonic force, as seen in the instantaneous lift coefficient, C_L.

In the case of a cylinder with strakes (Fig. 6-18), the strakes prohibit the ability of vortices to wrap around the cylinder as it moves through a figure eight motion. The strakes prevent vortices from moving with a relative velocity back towards the cylinder, hence when vortices shed, they tend to travel downstream in the relative carriage reference frame. As seen in Fig. 6-18, this results in largely clockwise (blue) vorticity shed to the upper side of the cylinder and largely counter-clockwise (red-yellow) vorticity shed to the lower side of the cylinder. In contrast, the bare cylinder allows vortices to move left in the carriage reference frame of the images. This results in large third harmonic forces. The particular pattern of shedding shown by the strake is not entirely meaningful without additional two dimensional slices of the wake at various other span points. Vortices tend to form at the strakes due to the forced motion of the cylinder.

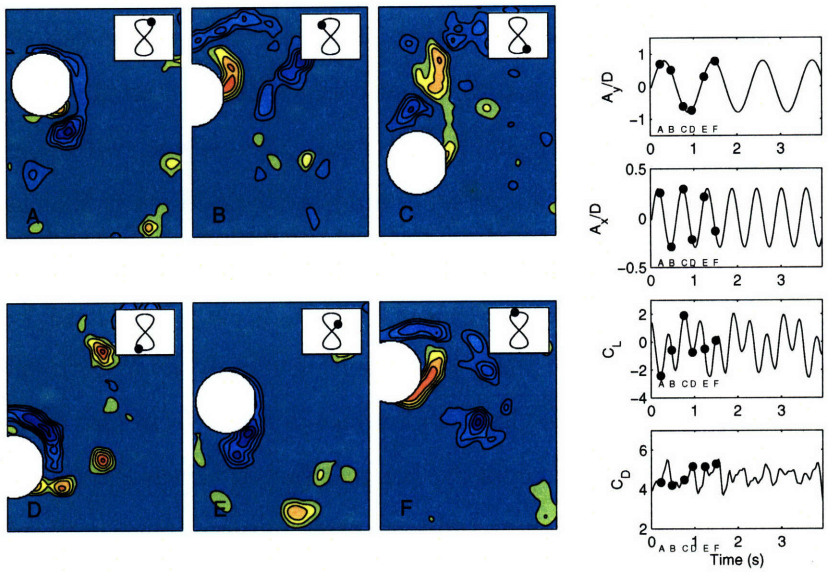

Figure 6-17: Wake behind bare cylinder with forced $A_y/D = 0.8$, $A_x/D = 0.3$, $V_r = 6$. Vorticity contours show non-dimensional vorticity, $\frac{\omega D}{U} = \pm 3, \pm 5, \pm 7, \ldots$.

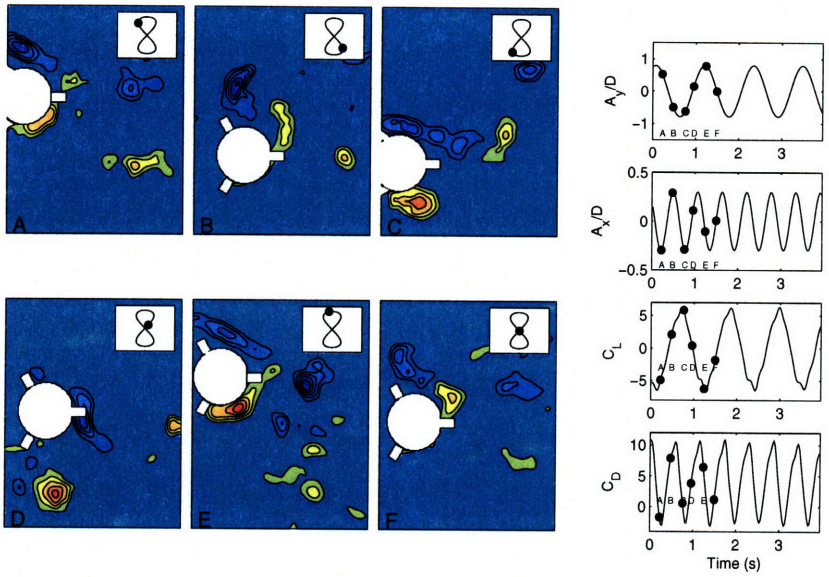

Figure 6-18: Wake behind strake cylinder with forced $A_y/D = 0.8$, $A_x/D = 0.3$, $V_r = 6$. Vorticity contours show non-dimensional vorticity, $\frac{\omega D}{U} = \pm 3, \pm 5, \pm 7, \ldots$.

Under these forced motions, the cylinders with holes are both effective at reducing the magnitude of third harmonic lift force on the cylinder. The mechanism for delaying third harmonic forces, however is different than in the case of the cylinder with strakes and the third harmonic is not completely eliminated as seen by the force contours in the previous section. In the case of the cylinder with holes (Figs. 6-19 and 6-20), a strong vortex still wraps around the cylinder as in the case of the bare cylinder. The presence of the hole, however, causes a jet to form when the cylinder surges forward at the top and bottom of its motion. This jet delays the vortex from traveling to the other side of the cylinder and essentially changes the phase at which this vortex sheds behind the cylinder. Consider Frame B from Fig. 6-17 and Frame D from 6-19. In both cases, the cylinder has just surged forward in the reference frame and is beginning to turn back as the transverse motion moves downward. The red-yellow vortex wrapping around the bare cylinder is unimpeded, while the red-yellow vortex wrapping around the cylinder with holes is slightly delayed in the cycle such that it moves around the cylinder at a slightly later time in the cycle. The result of this delay is a slight decrease in the magnitude of the third harmonic force and a

phase shift in the third harmonic force. The slight decrease in magnitude occurs since the vortex is further away from the cylinder as the cylinder moves in the transverse direction.

The phase shift in the third harmonic force is clearly visible in the time traces of C_L for the bare cylinder and the cylinder with holes. In the case of the bare cylinder, the third harmonic force is dominant and very large in amplitude. The third harmonic portion of lift is out in phase with the first harmonic portion of lift, such that a trough in the third harmonic occurs at a peak in the first harmonic. For the hole cylinders, the instantaneous lift coefficient shows a curve that looks dominated by the first harmonic portion of lift. Certainly a larger first harmonic portion of lift may exist due to a negative C_{Lv} or change in added mass at this amplitude with the presence of holes, but the phase of the third harmonic portion of lift has also changed such that the peak of third harmonic forces nearly aligns with the peak of first harmonic forces. This results in a very large magnitude total lift coefficient.

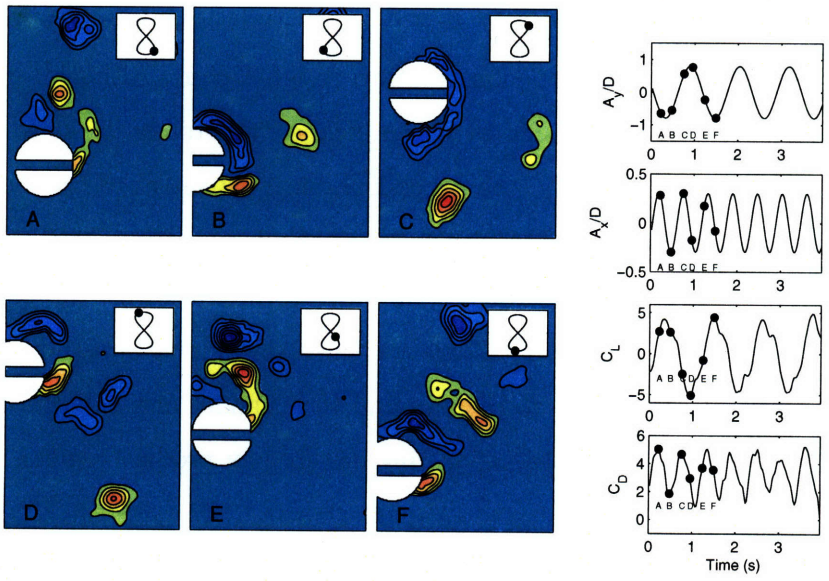

Figure 6-19: Wake behind hole cylinder (0.16D size holes) with $A_y/D = 0.8$, $A_x/D = 0.3$, $V_r = 6$. Vorticity contours show non-dimensional vorticity, $\frac{\omega D}{U} = \pm 3, \pm 5, \pm 7, \ldots$.

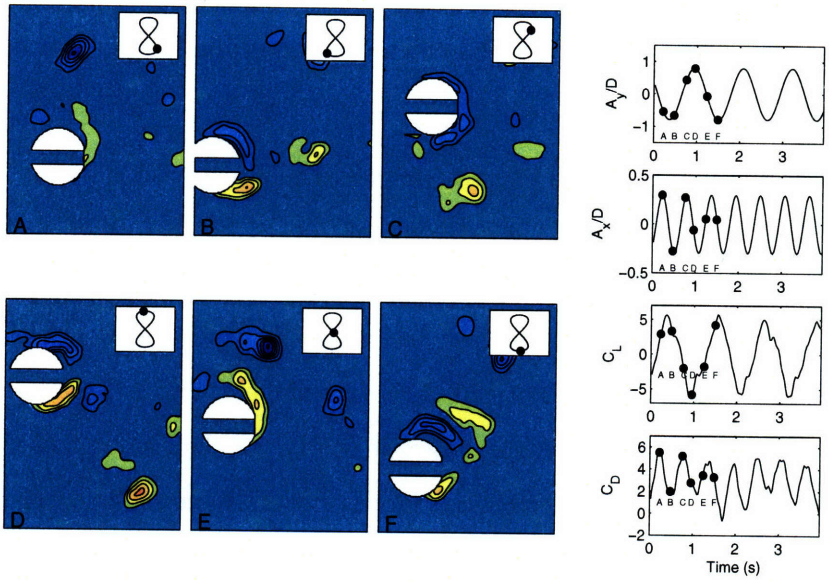

Figure 6-20: Wake behind hole cylinder (0.25D size holes) with $A_y/D = 0.8$, $A_x/D = 0.3$, $V_r = 6$. Vorticity contours show non-dimensional vorticity, $\frac{\omega D}{U} = \pm 3, \pm 5, \pm 7, \ldots$.

6.5 Discussion on vortex suppression methods

Each VIV suppression method discussed in this study has advantages and disadvantages depending on the particular limiting design factor. Although cylinders with holes are not a practical design by ocean engineering standards, since typical risers must be continuous conduits, the general physical principles of the idea can be engineered into a working device. For instance, the main feature of the cylinder with holes is passively generating a jet in the wake to interact with the unstable vortex street. A similar jet may be obtained by using a shroud with holes in it, housing the cylinder, and allowing fluid to pass around the cylinder and exit through a hole in the wake. This more feasible engineering design may produce similar results to the cylinder with holes.

The cylinder with holes did not work quite as expected, although it was very effective at reducing the operational drag of the cylinder at the inferred vibration amplitude. One issue with the cylinder with holes occurs due to the forced oscillation of the cylinder. The purpose of the hole through the cylinder was to create a symmetric unstable jet that interacts with the asymmetric unstable vortex street behind

the cylinder, resulting in a cancelation of the vortex street. When the cylinder is stationary in the fluid flow, the method appeared to work, as the formation of the vortex street was not apparent. When the cylinder was forced to vibrate, however, the flow conditions through the hole are forced to change, such that exit velocities from the holes now fluctuate with the cylinder motions.

It would be interesting to test the same device configuration on a flexibly mounted cylinder. If the cylinder starts from rest, the steady jet in the wake may inhibit any motions from occurring since the system may remain in a canceled vortex street state. If perturbed, however the system may oscillate as indicated by the forced vibration measurements. Perturbations may cause the hole exit velocity to fluctuate such that a steady wake condition cannot be achieved. The cylinder with holes may require that the hole be aligned in the direction of incident flow velocity in order to properly inhibit vortex formation.

The hole cylinder was also shown to be effective at decreasing the magnitude of the third harmonic lift coefficient, however this result must be carefully considered with the phase of force components. As shown by the flow visualization analysis, although the third harmonic component of force is slightly reduced due to the proximity of vortices to the cylinder, the change in phase of the third harmonic force does not aid in the reduction of forces. For the particular reduced velocity and motions shown, the total lift coefficient magnitude is actually increased by the presence of the hole in the cylinder. The change in phase will likely be consistent with other reduced velocities such that at some phases, a decrease in lift coefficient magnitude will occur, however changing the phase of forcing at specific reduced velocities is not a practical deterrent of large lift coefficients.

The cylinder with strakes performed very well at reducing inferred oscillation of the cylinder, however drag coefficients for the strake are still very large. In the two degree of freedom case, the drag coefficient of the strake is less than the drag coefficient of the oscillating cylinder while motions are virtually eliminated. This shows that the strake is still a useful tool for vortex suppression provided that relatively high drag coefficients are acceptable. The strake was extremely successful at eliminating third

harmonic forces as well by eliminating large relative motions of the vortices with respect to the in-line motion.

The flow visualization of the strakes in this study could be enhanced by additional plane images at different radial locations of the strakes. The strakes themselves do not inhibit vortex formation, but rather force fluid separation at the specific sharp edge of the strake. Since the strakes curve helically around the cylinder, the spanwise location of vortex shedding changes, resulting in poor correlation in the lift force caused by vortex shedding along the span. The three dimensionality of these vortex tubes can only be quantitatively observed through additional images at various span locations or through numerical simulation.

Chapter 7

Conclusions

7.1 Overview

The problems caused by vortex-induced vibrations are wide ranging as the phenomenon manifests in many different engineering applications. Many factors, whether they are economic, social, or political, drive energy consumption and viable solutions for obtaining natural resources. The search for natural resources in deep water requires a keen understanding of the physics involved with the ocean environment and the interaction of marine structures with this environment. The purpose of this study has been to focus primarily on ocean engineering applications of long risers in deep water, primarily how the ocean will interact with these structures.

The fundamental themes throughout this work have been the combined in-line and cross-flow excitation of a cylinder in a free stream and the appearance of large third harmonic forces in lift due to these combined motions. Understanding all forces acting on these structures in essential to avoiding catastrophic failures of marine risers. This study has attempted to shed light on characterizing why these forces exist and under what conditions these forces become large. Long risers with structural characteristics similar to strings will inevitably have the possibility of excitation of modes with a 2:1 ratio along the length. When the transverse mode of the cylinder corresponds to the Strouhal frequency of vortex shedding, the resonant behavior of the structure will lead to large third harmonic forces and dual resonance in both in-line and cross-flow

directions.

The following section outlines the most important contributions of this thesis from each chapter. A wide variety of experiments have been performed, resulting in a large number of observations concerned with vortex-induced vibrations. Analyzing forces from vortex-induced vibrations in two degrees of freedom is a fairly new approach to marine riser design. This study, by no means, offers a complete solution to the problem. Recommendations for future work are made in the following sections, primarily concerned with relevant continuation of the studies presented in this thesis or concerned with improvements upon the presented studies.

7.2 Principal Contributions of the thesis

7.2.1 Free vibrations of a cylinder in cross-flow and in-line motion

Analysis of the free vibrations of a cylinder in cross-flow and in-line motion was not a new type of experiment in itself, as Sarpkaya [53] showed results for a cylinder oscillating with 1:1 and 2:1 nominal natural frequency ratios and Jauvtis and Williamson [30] also performed a detailed study of the motions for a cylinder with 1:1 nominal natural frequency ratio. The major difference in this study was showing the transition from 1:1 to 2:1 through various intermediate frequency ratios while noting some previously unseen aspects the lift force due to the cylinder's motions. The low mass ratio and low damping coefficient contributed to observations not noted before in experimentation.

Large amplitude motions and reduced velocity shift in peak amplitudes

Very large amplitudes of transverse motion were observed for these free vibration experiments. The observed motions were limited to $A_y/D = 1.35$ due to the constraints of the experimental apparatus, however these large motions were consistent with those observed by Jauvtis and Williamson [30]. The peak magnitude in ampli-

tude was shown to shift to higher reduced velocities as the nominal natural frequency ratio of the system increased. At a natural frequency ratio of $f_{nx}/f_{ny} = 1.9$, two peaks in transverse amplitude of oscillation occur as a function of reduced velocity, consistent with the observations of Sarpkaya [53]. The shift of peak amplitudes to higher reduced velocities occurs in conjunction with a shift in the transition point for the phase between lift and transverse motion. This transition points shifts to higher reduced velocities as well, as nominal frequency ratio increases.

Large fluctuating drag coefficient

Very large fluctuating drag coefficients were observed along with an amplification of the mean drag behind the cylinder in two degree of freedom motions. The amplification of mean drag is larger than that from one degree of freedom motions due to the additional disturbance of the flow caused by in-line motion. The mean drag coefficient due to cylinder motions is shown to be as large as 4.5, with fluctuating drag driving the peak amplitudes as high as 6.5. These large drag coefficients are a major concern for marine riser design and operation.

Large third harmonic force in lift

An important aspect of two degree of freedom cylinder motions is the appearance of very large third harmonic forces in the direction of lift. Previously, forces in lift direction were thought to occur primarily at the fundamental frequency of vortex shedding, yet these experiments show that the third harmonic forces can dominate, being larger in magnitude than forcing at the first harmonic. The appearance of large magnitude third harmonic forces introduces a large concern for the reduction of fatigue life of marine risers. A simple estimate of fatigue life based on the observed combined first and third harmonic forces shows that fatigue life may be significantly reduced, however additional studies are necessary to solidify the effect of third harmonic forces on fatigue life.

Periodic orbital motion of the cylinder

The periodic orbit of the cylinder is shown to be closely related to the appearance of large third harmonic forces. In the carriage reference frame, the cylinder typically moves in a figure eight shape with upstream motion at the top and bottom of the figure eight. This particular motion is associated with large third harmonic forces at a nominal natural frequency ratio of 1.9. Reduced velocity is shown to alter this motion by changing the phase between in-line and transverse motions, θ. Typical values of θ are between -45 degrees and 45 degrees for a cylinder with nominal frequency ratio near 2.

Condition of dual lock-in for natural frequency ratios near 2

A condition of dual lock-in, where the oscillation frequency of the cylinder is equal to the equivalent natural frequency of the structure when corrected for added mass, is shown to exist for nominal frequency ratios near 2. Resonance in the in-line direction is not required, however, and it is shown that in-line motion will not oscillate at the equivalent natural frequency if the nominal natural frequency ratio is too low. Transverse oscillations are shown to always undergo a condition of lock-in. Additionally, regardless of the nominal natural frequency ratio, effective added mass is shown to drive the system towards an effective natural frequency ratio of 2 in all cases.

7.2.2 Flow visualization of cylinder wake

Flow visualizations behind a low mode number flexible cylinder, a flexible cylinder with tuned natural frequency ratio, and a rigid cylinder forced with free vibration motions were performed. The flow visualizations with the flexible cylinders were performed at very high velocities (between 1 and 2 m/s) using a high speed visualization system. A rigid cylinder was forced with kinematically equivalent motions to free vibrations in order to estimate the wake seen by a cylinder under free vibration. Additional visualizations of the wake behind a rigid cylinder were performed to indicate how perturbations on individual parameters affect wake formations.

Irregularity of flexible cylinder wake, multiple vortices

The wake behind a flexible cylinder at a fixed point along the span of the cylinder was shown to be very irregular due to irregularities in the oscillation of the cylinder. The wake was shown to exhibit a wide variety of wake mode formations such as '2S','2P','2T',and '2C', while also displaying groups of multiple vortices such as quadruplets or quintuplets. Over a small sample of oscillations, triplets were shown to form more often than any other pattern of vortex shedding. The cylinder had a tendency to try to oscillate with the same figure eight shape observed in free vibrations of a rigid cylinder, however the asymmetric second mode shape caused irregular motions to occur with no sustainable periodic motion.

Regular '2P' wake of 'tuned' flexible cylinder wake

By tuning the in-line natural frequency of the flexible cylinder to occur with an odd mode shape similar to the transverse mode shape, regular periodic motions of the flexible cylinder were obtained. The oscillations of the 'tuned' flexible cylinder were very similar to those observed for the free vibrations of a rigid cylinder. The wake behind the tuned flexible cylinder was shown to be very regular and the phase averaged wake appears to form '2S' or '2P' shedding patterns, depending on reduced velocity.

'2P' or '2T' shedding patterns associated with third harmonic forcing

Forcing a rigid cylinder with kinematically equivalent motions to observed free vibration motions results in the formation of '2P' or '2T' shedding patterns depending on the particular amplitude and phasing of the motions. The formation of '2T' wake modes occurs at a lower amplitude than those observed by Jauvtis and Williamson [30], however in-line motion of the cylinder was larger and the phasing between motions was different. The phasing between motions causes the phasing of vortex shedding to appear different as well in the formation of the wake mode. In both cases of '2P' or '2T' vortex shedding, the wake is characterized by one large vortex form-

ing per half cycle that is much stronger than other vorticity observed in the wake. This same observation is made in numerical simulations made by Dong and Karniadakis, reported in Dahl et al [11]. These particular shedding patterns lead to large magnitude third harmonic forces in lift.

Explanation of the third harmonic force in lift

A simple approach is taken for explaining the appearance of the third harmonic portion of the lift force. By only considering the two strong vortices that form in the wake of the cylinder, the wake is treated with a potential flow approximation by placing point vortices in the wake of a cylinder that propagate through the wake in time. This allows the forces on the cylinder to be written as a combination of forces caused by ideal added mass (acceleration of the fluid around the cylinder) and forces caused by the relative motion of vortices in the wake with respect to the cylinder. It is shown that third harmonic forces exist due to additional changes in the relative velocity of vortices with respect to the cylinder cause by in-line motion of the cylinder. The proximity of vortices with respect to the cylinder affect the magnitude of the third harmonic force. Additionally, a condition is shown to be possible where both lift in phase with velocity is equal to zero and effective added mass is equal to zero. The potential flow representation shows that this condition occurs when ideal added mass forces cancel completely with first harmonic forces caused by vortex shedding. This condition results in a dominant third harmonic force in lift. Combined with the observations of Jauvtis and Williamson [30], large magnitude third harmonic forces can exist due to both the presence of vortex triplets in the wake and due to the relative motion of the cylinder with respect to a '2P' shedding mode.

Effect of motion parameters (phase, amplitude, reduced velocity) on cylinder wake

The wake of the cylinder is shown to be largely affected by the phasing between in-line and transverse motions of the cylinder, while amplitude changes and reduced velocity changes have less dramatic effects of the wake. The '2P' or '2T' patterns

observed for the equivalent freely vibrating phase of $\theta = 0$ degrees is shown to change dramatically as phase increases or decreases. At $\theta = 180$ degrees, large co-rotating vortices form in the wake and lift force magnitudes become very large due to a very large amount of vorticity in the wake. The wake pattern is shown to change for a phase of $\theta = -135deg$, where the wake exhibits a '2S' shedding mode. The change in shedding mode also includes a reduction in the width of the wake, resulting in smaller mean drag forces on the cylinder.

7.2.3 Forced vibration database

A large matrix of two degree of freedom forced motions of a cylinder were performed to identify force coefficients associated with the different motions of the cylinder. The purpose of these experiments was to generate a force coefficient database to be used in helping predict forces on a riser, particulary third harmonic forces, since previous forced motion studies in one degree of freedom do not include third harmonic force coefficients.

The database of measured force coefficients

The database itself acts as a major contribution to the field of ocean engineering. The database consists of 2304 test runs performed with varied A_x/D between 0 and 0.75, A_y/D between 0.25 and 1.5, θ between -180 degrees and 180 degrees, and V_r between 4.5 and 8. The database provides force coefficient measurements for all combinations of these motions to be used as an initial predictive tool for studying vortex induced vibrations in both cross-flow and in-line motions.

Characterization of the third harmonic lift force over two degree of freedom motions

The forced vibration database is particularly useful in characterizing the third harmonic portion of lift since these forces only exist for a cylinder excited in both in-line and cross-flow motion. The database shows that in the region for which free vibra-

tions may occur, third harmonic forces increase almost linearly as a function of in-line motion. For very extreme in-line motions, which may occur on a long riser, the third harmonic lift coefficient can become very large, with values near 3.

Prediction of rigid cylinder motions using lock-in assumption

Using the simple observation that lock-in occurs in both the in-line and transverse directions in a free vibration with $f_{nx}/f_{ny} \approx 2$, this simple assumption is used to predict the free vibration of a rigid cylinder. By assuming lock-in one can calculate the appropriate in-line and transverse added masses required for the structure to resonate under lock-in. Using a third requirement that the average power over one cycle of oscillation must equal zero, the intersection of the in-line added mass, transverse added mass, and zero average power in the parameter space defined by the force coefficient database results in a very good prediction of the free vibration of the cylinder, particularly for $f_{nx}/f_{ny} = 1.9$. The lock-in assumption is not required for predicting free vibrations and it is shown that other vibrations without lock-in in the in-line direction can be predicted by assuming a different in-line oscillation frequency. Predictions capture trends and magnitudes remarkably well considering the sparseness of the test matrix.

Estimating third harmonic force distribution on a flexible riser

The distribution of force coefficient magnitudes along the length of a flexible riser are estimated using a quasi-steady assumption of fluid flow across the flexible riser. The distribution of the third harmonic force is shown to occur with roughly the same distribution as the first harmonic portion of lift force. This is expected due to the known mechanism for why third harmonic forces exist. The distribution along a riser in sheared flow with varied reduced velocity along the length bears a similarity to the forces observed in free vibrations for varied reduced velocity when the nominal natural frequency ratio is near 2.

7.2.4 VIV Suppression devices

Two VIV suppression devices were tested to observe their effectiveness at suppressing vortex induced vibrations of a cylinder in two degree of freedom motions while reducing third harmonic forces in lift. A traditional strake device was tested as a standard suppression device and a cylinder outfitted with holes, creating a passive wake jet, was tested as a new suppression device. Both cases were compared with a bare cylinder through force measurements and flow visualization.

Effectiveness of passive holes in a cylinder

Placing holes along the length of the cylinder was effective at reducing the operational mean drag on the cylinder, however the method did not effectively reduce inferred oscillations of the cylinder. A cylinder with holes that were 25 percent of the diameter performed better at VIV reduction than a cylinder with holes 16 percent of the diameter due to the increased flow rate through the holes. Third harmonic forces magnitudes were shown to decrease for a cylinder with holes, however flow visualization indicates that the primary mechanism for this reduction occurs due to a phase shift in vortex shedding. Although this phase shift reduces third harmonic magnitudes, it leads to a summation of third harmonic and first harmonic magnitude forces that are very large, a condition undesirable for a VIV suppression device.

Effectiveness of classic strakes in two degree of freedom oscillations

The classic strakes perform very well at eliminating vortex-induced vibrations in the two degree of freedom motions analyzed. Although this study showed that classic strakes would not be excited under any of the forced motions tested, it is important to note that other phases between motions may cause vibrations of the cylinder. Flow visualization showed that strakes were effective at completely eliminating third harmonic forces by not allowing vortices to cross the centerline of the cylinder and move with relative motion back towards the cylinder. Since this relative motion of these vortices was eliminated by the presence of strakes, third harmonic forces caused

by the relative motion of these vortices were non-existent.

7.3 Recommendations for future work

Certainly any piece of experimentation could have been improved by better equipment or better experimental conditions, however several aspects of this study have raised more questions important to the topic of vortex-induced vibrations in two degrees of freedom. The appearance of new forces previously unseen in experimentation offers new questions as to how to deal with these forces in ocean engineering applications.

7.3.1 Rigorous evaluation of effect of third harmonic force on fatigue life

A short estimation of the fatigue life reduction caused by the presence of large amplitude third harmonic forces indicates that fatigue life may be reduced by two orders of magnitude. This is an alarming number since structures expected to last 200 years may only last 2 years under these forcing conditions. A rigorous study needs to be performed to analyze how these third harmonic forces truly affect the fatigue life of structures. A rigorous study may require statistical analysis of the appearance of third harmonic forces on flexible risers. Since it has been shown that third harmonic forces are primarily a function in-line motions, it may be relevant to consider systems that suffer from large in-line motions combined with transverse motion. The initial steps of this study have begun based on the measurements in this thesis [41].

7.3.2 Mapping the wake modes for two degree of freedom motions

The mapping of wake modes by Williamson and Roshko [76] is an oft cited work in the academic community concerned with vortex induced vibrations. Vortex shedding in the wake ultimately drives the forces seen by an oscillating cylinder, thus understanding the formation of vortices in the wake under certain oscillations helps

to understand the particular forces observed. Mapping the wake behind a cylinder oscillating in two degrees of freedom poses a monumental task of experimental and computational time due to the large number of parameters to vary. The Williamson and Roshko [76] mapping is based on the forced variation of two motion parameters. Extending the same study to two degrees of freedom requires four varied parameters. This study has only attempted to visualize a few small slices of the parameter domain.

7.3.3 Finer grid for database test matrix, improved frequency resolution

Forces associated with the two degree of freedom oscillations of a cylinder are very non-linear, thus linearly interpolating the sparse force coefficient database is a poor way of estimating intermediate values of force coefficients. A finer grid resolution of force coefficient database will give much better estimates of forces on the cylinder. Similarly, this particular study suffered from a short towing tank with time traces limited to only a few cycles of motion. Ideally this experiment would benefit from a water tunnel or continuously flowing water channel where a statistically large number of cylinder oscillations may be recorded.

7.3.4 Achieving higher Reynolds number

The ultimate scaling issue for any fluid experimentalist testing at small scales is matching Reynolds number. Any of the experiments performed in this thesis would benefit from testing at higher Reynolds numbers in order to more accurately predict flow conditions that occur in the field. In particular, some questions exist, pertaining to third harmonic forces. Do third harmonic forces exist with large magnitudes at higher Reynolds numbers? Does the wake exhibit similar vortex formations in the post-boundary layer transition region? Testing at higher Reynolds number may be able to answer some of these questions.

7.3.5 Experimental verification of the distributed third harmonic lift force

The distribution of the third harmonic lift force estimated in Chapter 5 is based on a quasi-steady assumption that may not always be valid for an excited flexible cylinder. It would be advantageous to perform experiments on a flexible cylinder with devices capable of deducing the distributed third harmonic force along the length of the cylinder. This may be accomplished by outfitting a flexible cylinder with a very large number of strain gages, or could be accomplished with a sensor of continuous measurement capabilities. Recent studies have shown that third harmonic forces may even travel along the length of the riser, a condition that cannot be estimated by quasi-steady flow derived third harmonic coefficient magnitudes.

Bibliography

[1] Jamie Anderson. *Vorticity Control for Efficient Propulsion.* Doctor of philosophy in ocean engineering, Massachusetts Institute of Technology, 1996.

[2] K.H. Aronsen. *An experimental investigation of in-line and combined in-line and cross-flow vortex induced vibrations.* PhD thesis, NTNU, 2007.

[3] P.W. Bearman. Vortex shedding from oscillating bluff bodies. *Annual Review of Fluid Mechanics*, 16:195–222, 1984.

[4] R.D. Blevins. *Flow Induced Vibration.* Van Nostrand Reinhold Company, New York, NY, 1990.

[5] M. Brankovic and P.W. Bearman. Measurements of transverse forces on circular cylinders undergoing vortex-induced vibration. *Journal of Fluids and Structures*, 22:829–836, 2006.

[6] D. Brika and A Laneville. Vortex-induced vibrations of a long flexible circular cylinder. *Journal of Fluid Mechanics*, 250:481–508, 1993.

[7] J. Carberry, R. Govardhan, J. Sheridan, D. Rockwell, and C.H.K. Williamson. Wake states and response branches of forced and freely oscillating cylinders. *European Journal of Mechanics B/Fluids*, 23:89–97, 2004.

[8] J. Carberry, J. Sheridan, and D. Rockwell. Controlled oscillations of a cylinder: A new wake state. *Journal of Fluids and Structures*, 17:337–343, 2003.

[9] J. Carberry, J. Sheridan, and D. Rockwell. Controlled oscillations of a cylinder: Forces and wake modes. *Journal of Fluid Mechanics*, 538:31–69, 2005.

[10] J.M. Dahl, F.S. Hover, and M.S. Triantafyllou. Two-degree-of-freedom vortex-induced vibrations using a force assisted apparatus. *Journal of Fluids and Structures*, 22:807–818, 2006.

[11] J.M. Dahl, F.S. Hover, M.S. Triantafyllou, S. Dong, and G.E. Karniadakis. Resonant vibrations of bluff bodies cause multi-vortex shedding. *Physical Review Letters*, 99(144503), oct 2007.

[12] S. Dong and G.E. Karniadakis. Dns of flow past a stationary and oscillating cylinder at re = 10,000. *Journal of Fluids and Structures*, 20:519–531, 2005.

[13] S. Dong and G.E. Karniadakis. Suppressing the fluctuating lift on a circular cylinder. *Journal of Fluid Mechanics*, page Under Review, Received 2006.

[14] M. Van Dyke. *An Album of Fluid Motions.* Parabolic Press, Inc., Stanford, CA, 1982.

[15] C.C. Feng. The measurements of vortex-induced effects on flow past stationary and oscillating circular and d-section cylinders. Master thesis, University of British Columbia.

[16] F. Flemming and C.H.K. Williamson. Vortex-induced vibrations of a pivoted cylinder. *Journal of Fluid Mechanics*, 522:215–252, 2005.

[17] A.L.C. Fujarra, C.P. Pesce, F. Flemming, and C.H.K. Williamson. Vortex-induced vibration of a flexible cantilever. *Journal of Fluids and Structures*, 15:651–658, 2001.

[18] Ramnarayan Gopalkrishnan. *Vortex-Induced Forces on Oscillating Bluff Cylinders.* Doctor of science in oceanographic engineering, Massachusetts Institute of Technology and Woods Hole Oceanographic Institution, February 1993.

[19] R. Govardhan and C.H.K. Williamson. Modes of vortex formation and frequency response of a freely vibrating cylinder. *Journal of Fluid Mechanics*, 420:85–129, 2000.

[20] R.N. Govardhan and C.H.K. Williamson. Defining the 'modified griffin plot' in vortex-induced vibration: Revealing the effect of reynolds number using controlled damping. *Journal of Fluid Mechanics*, 561:147–180, 2006.

[21] J.M.R. Graham. The forces on sharp-edged cylinders in oscillatory flow at low keulegan-carpenter numbers. *Journal of Fluid Mechanics*, 97:331–346, 1980.

[22] O.M. Griffin and G.H. Koopman. The vortex-excited lift and reaction forces on resonantly vibrating cylinders. *Journal of Sound and Vibration*, 53:435–448, 1977.

[23] L. Gui and J.M. Seiner. An improvement in the nine-point central difference image correction method for digital particle image velocimetry recording evaluation. *Measurement Science and Technology*, 15(10):1958–1964, 2004.

[24] H. Honji, S. Taneda, and M. Tatsuno. Some practical details of the electrolytic precipitation method of flow visualization. *Reports of Research Inst. for Applied Math*, 28:83–89, 1980.

[25] M. Horowitz and C.H.K. Williamson. Dynamics of a rising and falling cylinder. *Journal of Fluids and Structures*, 22:837–843, 2006.

[26] F.S. Hover, A.H. Techet, and M.S. Triantafyllou. Forces on oscillating uniform and tapered cylinders in crossflow. *Journal of Fluid Mechanics*, 363:97–114, 1998.

[27] P. Huerre and P.A. Monkewitz. Local and global instabilities in spatially developing flows. *Annual Review of Fluid Mechanics*, 22:473–537, 1990.

[28] American Petroleum Institute. Design of risers for floating production systems (fsps) and tension-leg platforms (tlps). Technical Report RP 2RD, Washington, D.C., June 1998.

[29] N. Jauvtis and C.H.K. Williamson. Vortex-induced vibration of a cylinder with two degrees of freedom. *Journal of Fluids and Structures*, 17:1035–1042, 2003.

[30] N. Jauvtis and C.H.K. Williamson. The effect of two degrees of freedom on vortex-induced vibration at low mass and damping. *Journal of Fluid Mechanics*, 509:23–62, 2004.

[31] D. Jeon and M. Gharib. On circular cylinders undergoing two-degree-of-freedom forced motions. *Journal of Fluids and Structures*, 15:533–541, 2001.

[32] V. Jhingran. *Drag Amplification and Fatigue Damage due to Vortex-Induced Vibration.* PhD thesis, Massachusetts Institute of Technology, April 2008.

[33] G. Karniadakis and S. Sherwin. *Spectral/hp Element Methods for CFD.* Oxford Univ. Press, 2 edition, 1990.

[34] A. Khalak and C.H.K. Williamson. Dynamics of a hydroelastic cylinder with very low mass and damping. *Journal of Fluids and Structures*, 10:455–472, 1996.

[35] A. Khalak and C.H.K. Williamson. Motions, forces and mode transitions in vortex-induced vibrations at low mass-damping. *Journal of Fluids and Structures*, 13:813–851, 1999.

[36] LaVision. *DaVis 7.1 - Perspective Calibration Wizard.* LaVision GmbH, Gottingen, Germany, 2005.

[37] LaVision. *DaVis Flowmaster Software Manual.* LaVision GmbH, Gottingen, Germany, 2005.

[38] LaVision. *DaVis 7.1 Software Manual.* LaVision GmbH, Gottingen, Germany, 2006.

[39] D.J. Maull and M.G. Milliner. Sinusoidal flow past a circular cylinder. *Coastal Engineering*, 2:149–168, 1978.

[40] L.M. Milne-Thompson. *Theoretical Hydrodynamics.* The McMillan Company, New York, 1960.

[41] Y. Modarres-Sadeghi, M.S. Triantafyllou, and F.S. Hover. Fatigue life calculations of risers by taking into account the higher harmonic force components. In *Proceedings of the International Society of Offshore and Polar Engineering - ISOPE 2008*, Vancouver, July 2008. Under Review.

[42] G. Moe and Z.-J. Wu. The lift force on a cylinder vibrating in a current. *Journal of Offshore Mechanics and Arctic Engineering*, 112:297–303, nov 1990.

[43] T.L Morse and C.H.K. Williamson. Employing controlled vibrations to predict fluid forces on a cylinder undergoing vortex-induced vibration. *Journal of Fluids and Structures*, 22(6-7):877–884, 2006.

[44] H. Mukundan. *Vortex-Induced Vibration of Marine Risers: Motion and Force Reconstruction from Field and Experimental Data.* PhD thesis, Massachusetts Institute of Technology, April 2008.

[45] J.N. Newman. *Marine Hydrodynamics.* The MIT Press, Cambridge, MA, 1977.

[46] F. Noca, D. Shiels, and D. Jeon. A comparison of method for evaluating time-dependent fluid dynamic forces on bodies, using only velocity fields and their derivatives. *Journal of Fluids and Structures*, 13:551–578, 1999.

[47] C. Norberg. Fluctuating lift on a circular cylinder: Review and new measurements. *Journal of Fluids and Structures*, 17:57–96, 2003.

[48] J.F. Olsen and S. Rajagopalan. Vortex shedding behind modified circular cylinders. *Journal of Wind Engineering and Industrial Aerodynamics*, 86:55–63, 2000.

[49] J.P. Pontaza, H.C. Chen, and J.N. Reddy. A local-analytic based discretization procedure. *International Journal of Numerical Methods in Fluids*, 49:657–699, 2005.

[50] S. Rao. *Mechanical Vibrations.* Prentice Hall, New York, 2003.

[51] T. Sarpkaya. Transverse oscillations of a circular cylinder in uniform flow. Technical Report NPS-69SL77071, Naval Postgraduate School, Mechanical Engineering, Monterey, California, July 1977.

[52] T. Sarpkaya. Vortex induced oscillations. *Journal of Applied Mechanics*, 46:241–258, 1979.

[53] T. Sarpkaya. Hydrodynamic damping, flow-induced oscillations, and biharmonic response. *ASME Journal of Offshore Mechanics and Arctic Engineering*, 117:232–238, 1995.

[54] T. Sarpkaya. A critical review of the intrinsic nature of vortex-induced vibrations. *Journal of Fluids and Structures*, 19:389–447, 2004.

[55] K.B. Skaugset and C.M. Larsen. Drag force reduction and viv suppression of circular cylinders using radial water jets. In *Proceedings of the International Conference on Offshore Mechanics and Arctic Engineering - OMAE*, volume 1, pages 157–168, 2003.

[56] A. Slaouti and J.H. Gerrard. An experimental investigation of the end effects on the wake of a circular cylinder towed through water at low reynolds numbers. *Journal of Fluid Mechanics*, 74:641–655, 1981.

[57] Oyvind Smogeli. Design and evaluation of a force-feedback control system for viv experiments. Sivilingenior, NTNU and MIT, July 2002.

[58] P.K. Stansby. The effects of end plates on the base pressure coefficient of a circular cylinder. *Aeronautical Journal*, 78:36–37, 1974.

[59] T. Staubli. Calculation of the vibration of an elastically mounted cylinder using experimental data from forced oscillation. *Journal of Fluids Engineering, ASME*, 105:225–229, 1983.

[60] B. Mutlu Sumer and Jorgen Fredsoe. *Hydrodynamics Around Cylindrical Structures*, volume 26 of *Advanced Series on Ocean Engineering*. World Scientific, Singapore, revised edition, 2006.

[61] Susan B. Swithenbank. *Dynamics of Long Flexible Cylinders at High-Mode Number in Uniform and Sheared Flows.* Doctor of philosophy in mechanical engineering, Massachusetts Institute of Technology, 2007.

[62] B.T. Tan, M.C. Thompson, and K. Hourigan. Evaluating fluid forces on bluff bodies using partial velocity data. *Journal of Fluids and Structures*, 20:5–24, 2005.

[63] Alexandra Techet. Vortical patterns behind a tapered cylinder. Master of science in oceanographic engineering, MIT and Woods Hole Oceanographic Institution, June 1998.

[64] G. Triantafyllou, M. Triantafyllou, and C. Chryssostomidis. On the formation of vortex street behind stationary cylinders. *Journal of Fluid Mechanics*, 170:461–477, 1986.

[65] G. Triantafyllou, M. Triantafyllou, and C. Chryssostomidis. Stability analysis to predict vortex street characteristics and forces on circular cylinders. *Journal of Offshore Mechanics and Arctic Engineering*, 109:148–154, 1987.

[66] M.F. Unal, J.-C. Lin, and D. Rockwell. Force prediction by piv imaging: A momentum-based approach. *Journal of Fluids and Structures*, 11:965–971, 1997.

[67] J.K. Vandiver and T.Y. Chung. Hydrodynamic damping on flexible cylinders in sheared flow. *Journal of Waterway, Port, Coastal, and Ocean Engineering*, 115(2):154–171, 1989.

[68] J.K. Vandiver and J.-Y. Jong. The relationship between in-line and cross-flow vortex-induced vibration of cylinders. *Journal of Fluids and Structures*, 1:381–399, 1987.

[69] J.K. Vandiver, S. Swithenbank, V. Jaiswal, and V. Jhingran. Fatigue damage from high mode number vortex-induced vibration. In *25th International Conference on Offshore Mechanics and Arctic Engineering*, Hamburg, June 2006.

[70] K. Vikestad, J.K. Vandiver, and C.M. Larsen. Added mass and oscillation frequency for a circular cylinder subjected to vortex-induced vibrations and external disturbance. *Journal of Fluids and Structures*, 14:1071–1088, 2000.

[71] Kyrre Vikestad. *Multi-frequency Response of a Cylinder Subjected Vortex Shedding and Support Motions.* Doktor ingenioravhandling, NTNU, Institutt for Marine Konstruksjoner, April 1998.

[72] C.E. Willert and M. Gharib. Digital particle image velocimetry. *Experiments in Fluids*, 10:181–193, 1991.

[73] C.H.K. Williamson. Sinusoidal flow relative to circular cylinders. *Journal of Fluid Mechanics*, 155:141–174, 1985.

[74] C.H.K. Williamson and R. Govardhan. Vortex-induced vibrations. *Annual Review of Fluid Mechanics*, 36:413–455, 2004.

[75] C.H.K. Williamson and N. Jauvtis. A high-amplitude 2t mode of vortex-induced vibration for a light body in xy motion. *European Journal of Mechanics B/Fluids*, 23:107–114, 2004.

[76] C.H.K. Williamson and A. Roshko. Vortex formation in the wake of an oscillating cylinder. *Journal of Fluids and Structures*, 2:355–381, 1988.

[77] M.M. Zdravkovich. Review and classification of various aerodynamic and hydrodynamic means for suppressing vortex shedding. *Journal of Wind Engineering and Industrial Aerodynamics*, 7:145–189, 1981.

[78] M.M. Zdravkovich. *Flow Around Circular Cylinders Vol.1: Fundamentals.* Oxford University Press, New York, 1997.

[79] M.M. Zdravkovich. *Flow Around Circular Cylinders Vol.2: Applications.* Oxford University Press, New York, 1997.

Appendix A

Additional Selected Time Traces from Free Vibrations

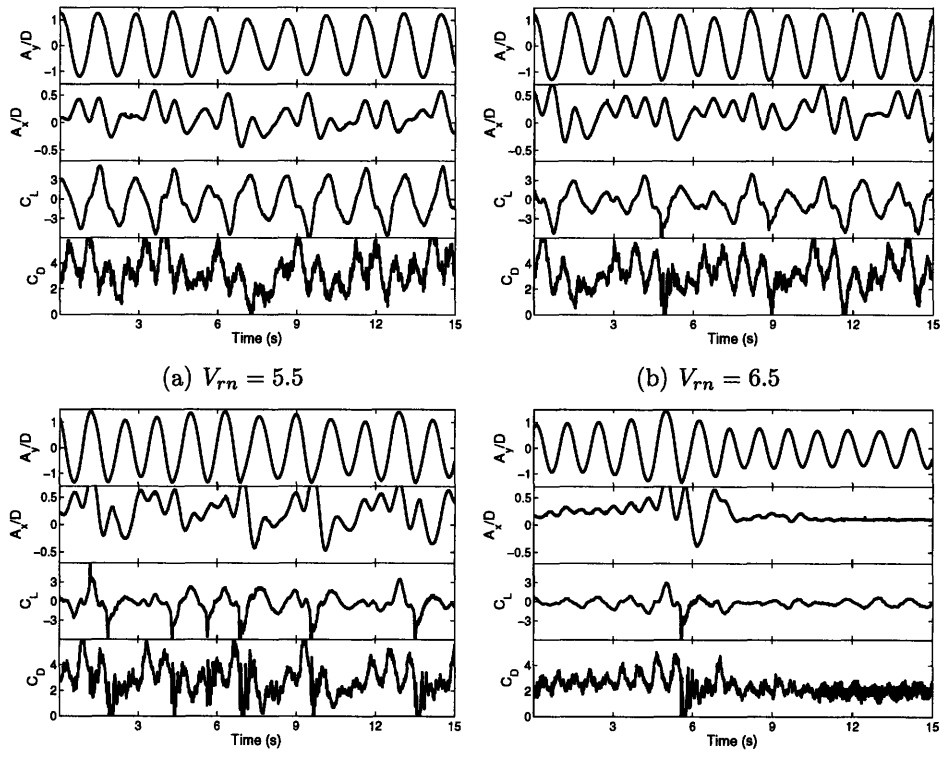

(a) $V_{rn} = 5.5$ (b) $V_{rn} = 6.5$

(c) $V_{rn} = 7.5$ (d) $V_{rn} = 8.0$

Figure A-1: Selected time traces from free vibration experiments showing transverse motion, in-line motion, lift coefficient, and drag coefficient, $f_{nx}/f_{ny} = 1.0$.

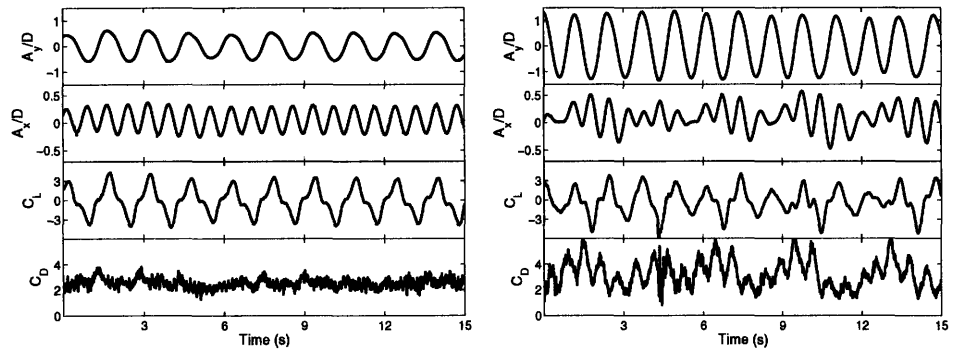

(a) $V_{rn} = 5.5$ (b) $V_{rn} = 6.5$

(c) $V_{rn} = 7.5$ (d) $V_{rn} = 8.0$

Figure A-2: Selected time traces from free vibration experiments showing transverse motion, in-line motion, lift coefficient, and drag coefficient, $f_{nx}/f_{ny} = 1.22$.

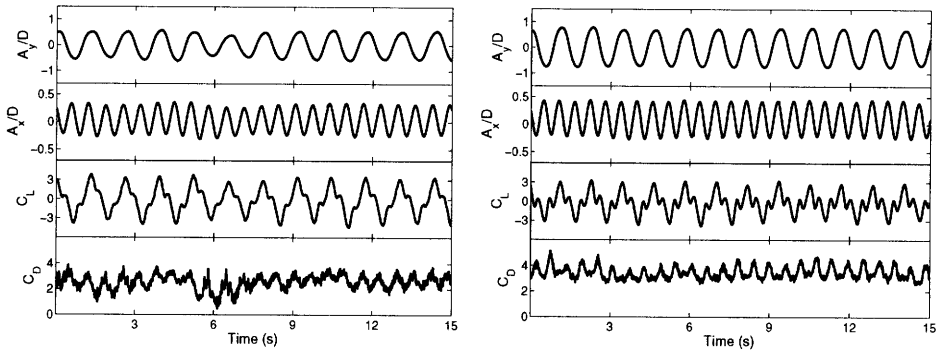

(a) $V_{rn} = 5.5$ (b) $V_{rn} = 6.5$

(c) $V_{rn} = 7.5$ (d) $V_{rn} = 8.0$

Figure A-3: Selected time traces from free vibration experiments showing transverse motion, in-line motion, lift coefficient, and drag coefficient, $f_{nx}/f_{ny} = 1.37$.

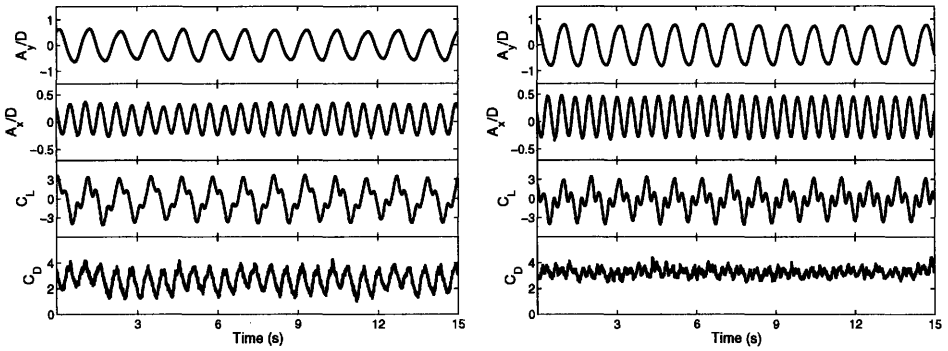

(a) $V_{rn} = 5.5$

(b) $V_{rn} = 6.5$

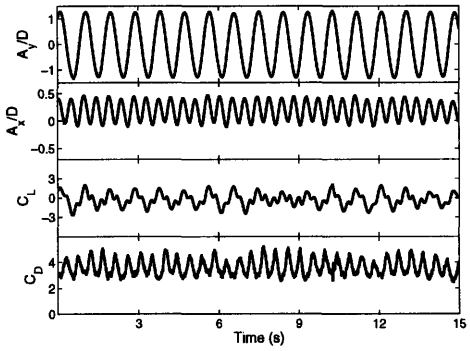

(c) $V_{rn} = 7.5$

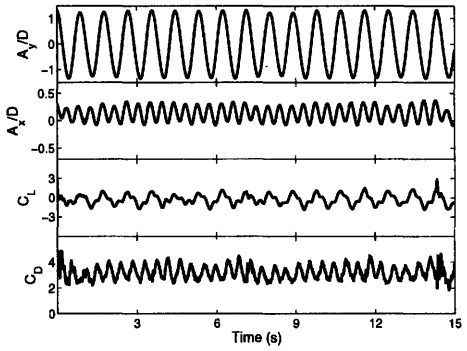

(d) $V_{rn} = 8.0$

Figure A-4: Selected time traces from free vibration experiments showing transverse motion, in-line motion, lift coefficient, and drag coefficient, $f_{nx}/f_{ny} = 1.52$.

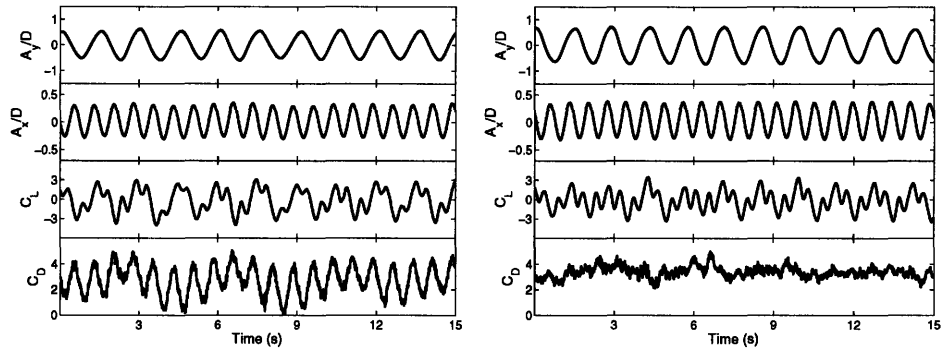

(a) $V_{rn} = 5.5$

(b) $V_{rn} = 6.5$

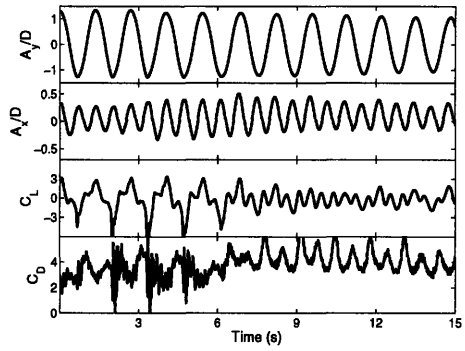

(c) $V_{rn} = 7.5$

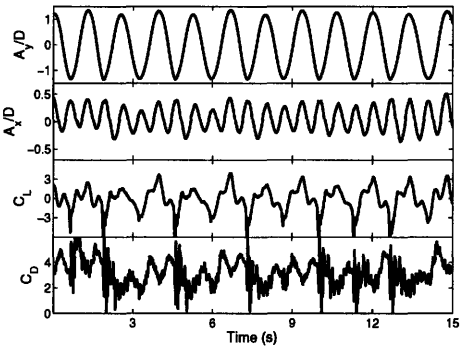

(d) $V_{rn} = 8.0$

Figure A-5: Selected time traces from free vibration experiments showing transverse motion, in-line motion, lift coefficient, and drag coefficient, $f_{nx}/f_{ny} = 1.67$.

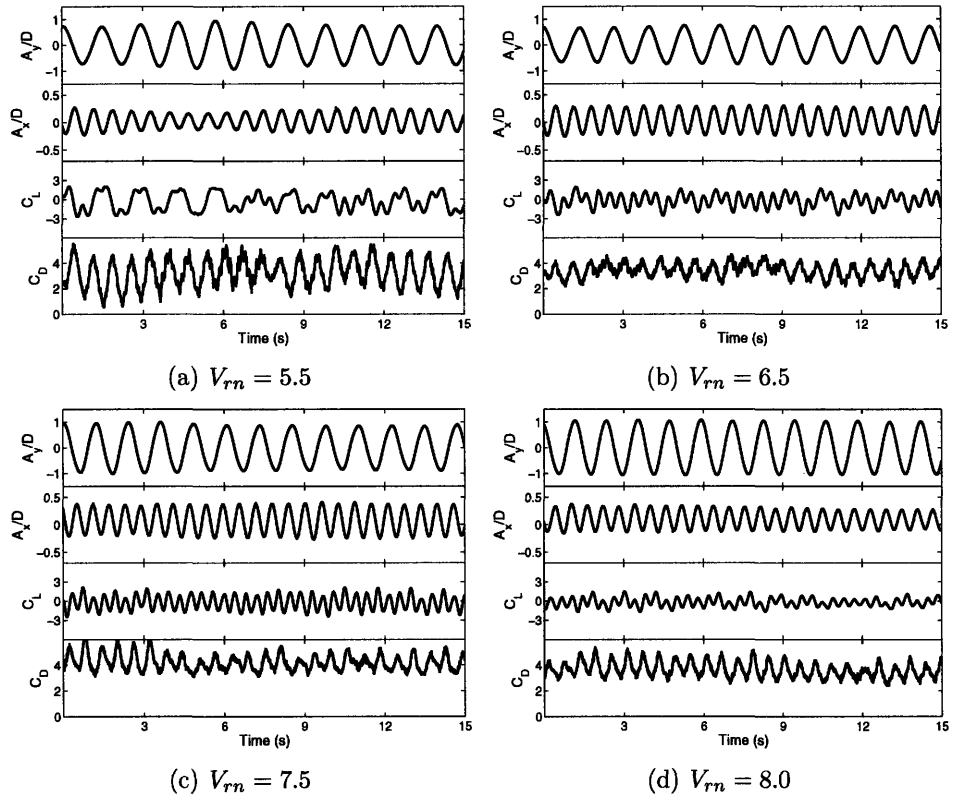

(a) $V_{rn} = 5.5$ (b) $V_{rn} = 6.5$

(c) $V_{rn} = 7.5$ (d) $V_{rn} = 8.0$

Figure A-6: Selected time traces from free vibration experiments showing transverse motion, in-line motion, lift coefficient, and drag coefficient, $f_{nx}/f_{ny} = 1.9$.

Appendix B

Derivation of vortex force on cylinder in potential flow

This derivation is based on potential flow assumptions and formulas found in Milne-Thompson [40] and compared with the formulas given by Triantafyllou et al [65].

B.1 Explanation of derivation

The purpose of this derivation is to find the force exerted on a cylinder due to the presence of a vortex in the wake of the cylinder. The derivation assumes that the fluid is inviscid and incompressible. For simplicity, we assume that the flow is two dimensional, hence we only consider a plane where a vortex will impose a force on a circle.

We consider the reference frame for this problem to be fixed to the cylinder. Therefore all vortex velocities will be relative to the cylinder's actual velocity.

B.2 Variable Definitions

F	Total complex force on the cylinder, $F = F_x - iF_y$
F_x	Drag force on the cylinder
F_Y	Lift force on the cylinder
ρ	Density of fluid
w	Complex potential describing the flow
z	Complex position in the flow field, $z = x + iy$
x	Position along the real axis in the flow field
y	Position along the imaginary axis in the flow field
Z_n	Complex position of vortex n in the flow field, $Z_n = X_n + iY_n$
a	Radius of the cylinder
$\dot{Z}_n$	Complex relative velocity of vortex n with respect to cylinder's velocity, $\dot{Z}_n = u_n - iv_n$
u	Vortex velocity in the x-direction
v	Vortex velocity in the y-direction
K_n	Strength of vortex n, $K_n = \frac{\Gamma_n}{2\pi}$
Γ	Circulation of vortex

B.3 Blausius Theorem

Milne-Thompson derives the Blausius theorem which calculates the force on a cylinder due to the flow described by the complex potential w. The complex potential in this case must satisfy the boundary conditions for a cylinder. The integral is then a line integral taken around the boundary of the cylinder. This is important to note because in the case of a cylinder formed by point vortex images, the vortex in the flow lies outside of this boundary and thus does not contribute to the integral, while the image vortex lies inside the boundary and does have a non-zero integral. The Blausius theorem is given in Equation B.1, the over bar denotes the complex conjugate.

$$F = F_x - iF_y = i\rho \oint \frac{\partial \bar{w}}{\partial t} d\bar{z} + i\frac{\rho}{2} \oint \left(\frac{\partial w}{\partial z}\right)^2 dz \tag{B.1}$$

In our case, the complex potential for a cylinder with one vortex in the wake can

be described by a set of image vortices and one vortex located at the center of the circle, all with equal strength. This potential is given in Equation B.2.

$$w = -iK_n ln(z - Z_n) + iK_n ln(z - \frac{a^2}{\bar{Z}_n}) - iK_n ln(z) \tag{B.2}$$

B.4 Derivatives

By the chain rule, we have Equation B.3.

$$\frac{\partial w}{\partial t} = \frac{\partial w}{\partial Z_n} * \frac{\partial Z_n}{\partial t} \tag{B.3}$$

$$\frac{\partial w}{\partial Z_n} = \frac{iK_n}{z - Z_n} + \frac{iK_n a^2}{\bar{Z}_n^2(z - \frac{a^2}{Z_n})} \tag{B.4}$$

$$\frac{\partial Z_n}{\partial t} = \dot{Z}_n \tag{B.5}$$

Plugging equations B.4 and B.5 into equation B.3, we get:

$$\frac{\partial w}{\partial t} = \frac{iK_n \dot{Z}_n}{z - Z_n} + \frac{iK_n a^2 \dot{Z}_n}{\bar{Z}_n^2(z - \frac{a^2}{Z_n})} \tag{B.6}$$

B.5 Evaluating the Integral

We will ignore the second term on the right hand side in Equation B.1, since this term goes by Γ^2 and is not a significant contribution to the force. Using the derivative in Equation B.6, we can now write the line integral:

$$\oint \frac{\partial w}{\partial t} dz = \oint \frac{iK_n \dot{Z}_n}{z - Z_n} + \frac{iK_n a^2 \dot{Z}_n}{\bar{Z}_n^2(z - \frac{a^2}{Z_n})} dz \tag{B.7}$$

Putting the integral into the Cauchy integral form:

$$\oint \frac{\partial w}{\partial t} dz = \oint \frac{iK_n \dot{Z}_n}{z - Z_n} + \frac{\frac{iK_n a^2 \dot{Z}_n}{\bar{Z}_n^2}}{z - \frac{a^2}{Z_n}} dz \tag{B.8}$$

By the Cauchy integral theorem, the first term on the right hand side of Equation B.8 is zero, since Z_n lies outside of the integral contour. Therefore we are left with only a term from the mirrored vortex inside the contour:

$$\oint \frac{\partial w}{\partial t} dz = 2\pi i \left(\frac{iK_n a^2 \dot{Z}_n}{\bar{Z}_n^2} \right) \tag{B.9}$$

Taking the complex conjugate of the integral and simplifying, we obtain an expression for the complex force:

$$F = F_x - iF_y = -2\pi K_n \rho i \left(\frac{a^2 \dot{\bar{Z}}_n}{Z_n^2} \right) \tag{B.10}$$

B.6 Expanded force relation

If we substitute for Z_n and $\dot{Z}_n$, we obtain explicit expressions for F_x and F_y.

$$F_x = \rho \Gamma_n a^2 \left(\frac{v_n(x_n^2 - y_n^2) - 2u_n x_n y_n}{(x_n^2 + y_n^2)^2} \right) \tag{B.11}$$

$$F_y = \rho \Gamma_n a^2 \left(\frac{u_n(x_n^2 - y_n^2) + 2v_n x_n y_n}{(x_n^2 + y_n^2)^2} \right) \tag{B.12}$$

This solution matches the solution presented in Triantafyllou et al [65]. To include multiple vortices in the wake, one can simply sum the force over a number of n vortices.

Appendix C

Additional Selected Flow Visualization

C.1 Equivalent Free Vibration

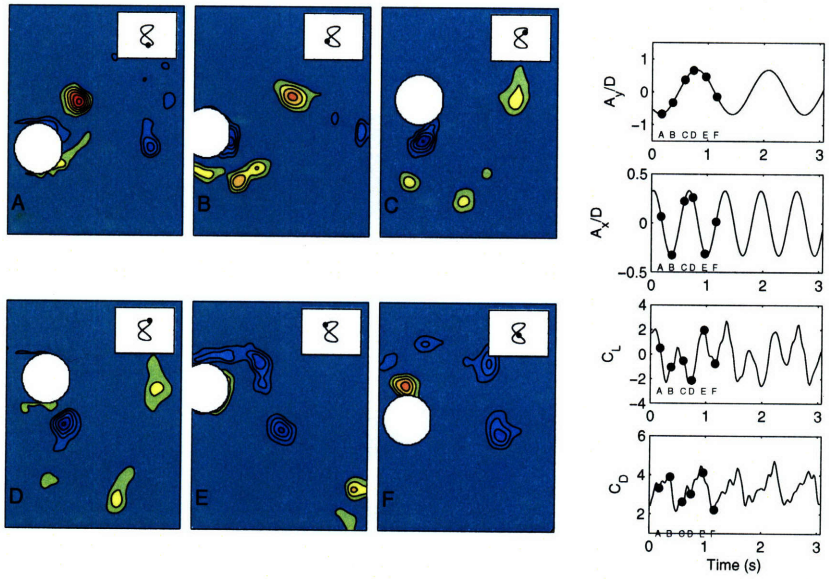

Figure C-1: Flow Visualization of equivalent motions for $f_{nx}/f_{ny} = 1.37$, $V_{rn} = 6.25$, $V_r = 6.80$. Vorticity contours show non-dimensional vorticity, $\frac{\omega D}{U} = \pm 3, \pm 5, \pm 7, \ldots$. Wake shows '2T' pattern of vortex shedding.

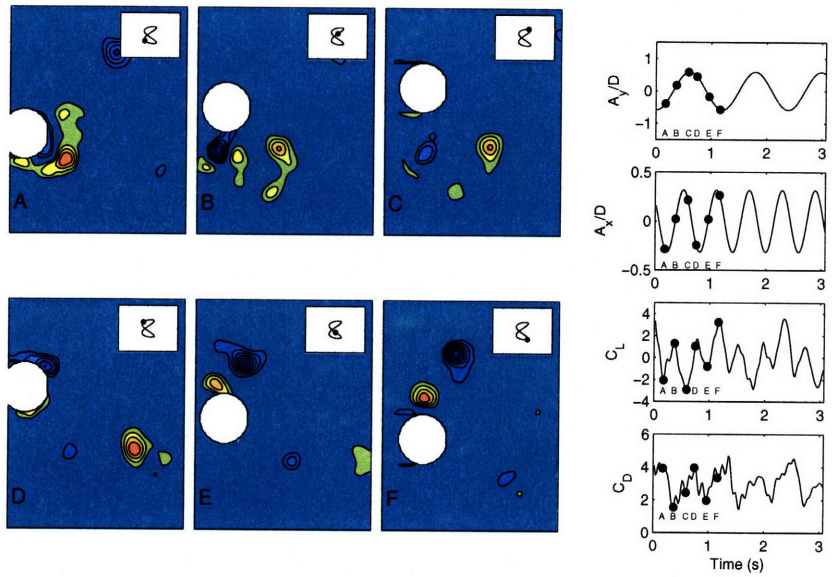

Figure C-2: Flow Visualization of equivalent motions for $f_{nx}/f_{ny} = 1.37$, $V_{rn} = 5.50$, $V_r = 6.39$. Vorticity contours show non-dimensional vorticity, $\frac{\omega D}{U} = \pm 3, \pm 5, \pm 7, \ldots$. Wake shows '2P' pattern of vortex shedding.

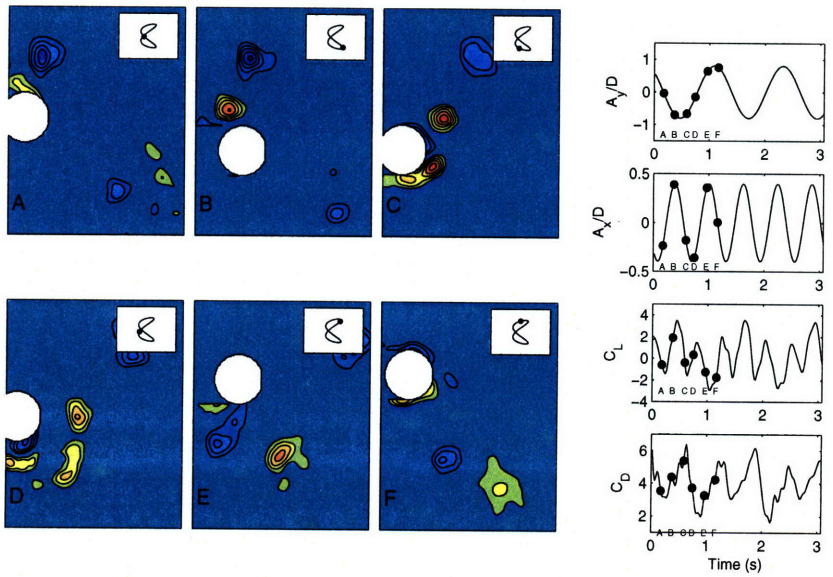

Figure C-3: Flow Visualization of equivalent motions for $f_{nx}/f_{ny} = 1.52$, $V_{rn} = 6.50$, $V_r = 6.69$. Vorticity contours show non-dimensional vorticity, $\frac{\omega D}{U} = \pm 3, \pm 5, \pm 7, \ldots$. Wake shows '2P' pattern of vortex shedding.

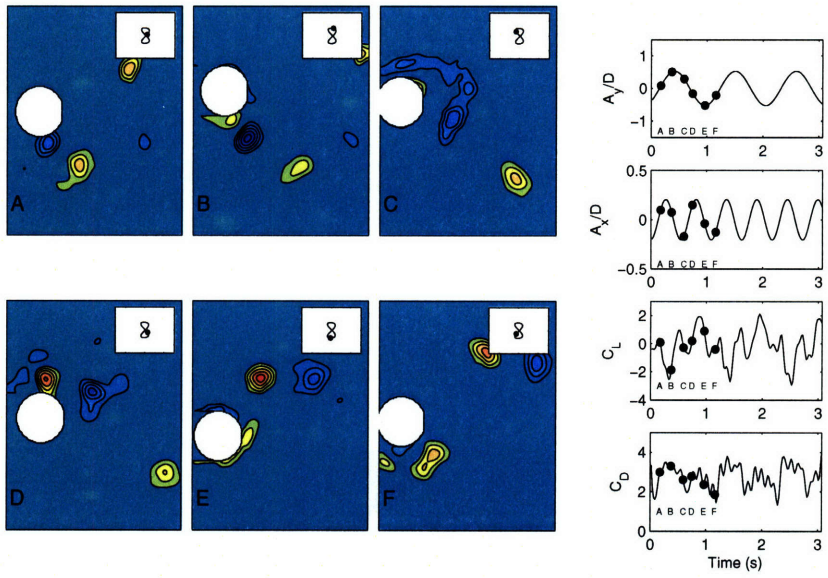

Figure C-4: Flow Visualization of equivalent motions for $f_{nx}/f_{ny} = 1.52$, $V_{rn} = 5.00$, $V_r = 5.85$. Vorticity contours show non-dimensional vorticity, $\frac{\omega D}{U} = \pm 3, \pm 5, \pm 7, \ldots$. Wake shows '2P' pattern of vortex shedding.

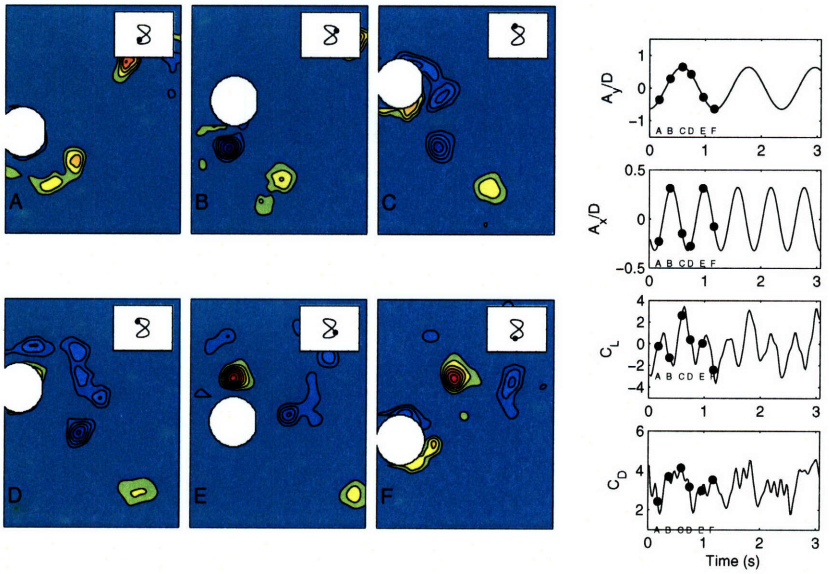

Figure C-5: Flow Visualization of equivalent motions for $f_{nx}/f_{ny} = 1.67$, $V_{rn} = 6.00$, $V_r = 6.17$. Vorticity contours show non-dimensional vorticity, $\frac{\omega D}{U} = \pm 3, \pm 5, \pm 7, \ldots$. Wake shows '2P' pattern of vortex shedding.

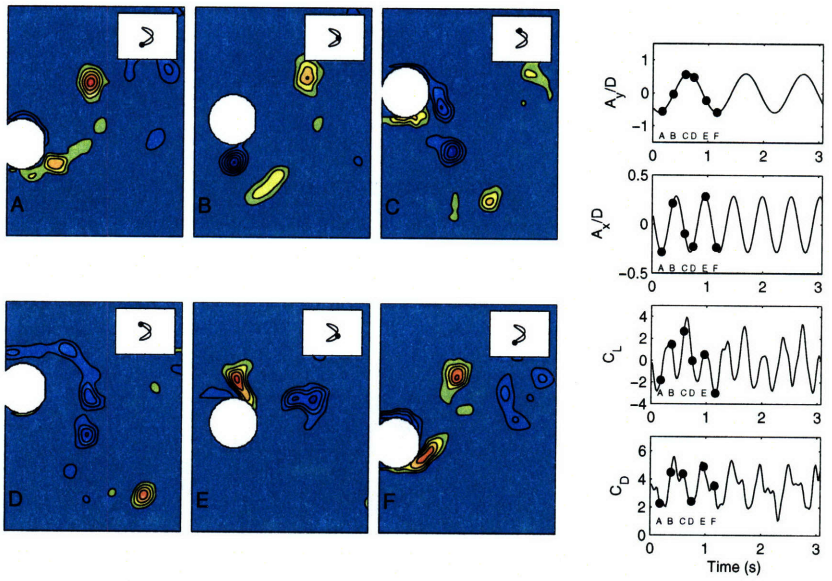

Figure C-6: Flow Visualization of equivalent motions for $f_{nx}/f_{ny} = 1.67$, $V_{rn} = 5.00$, $V_r = 5.38$. Vorticity contours show non-dimensional vorticity, $\frac{\omega D}{U} = \pm 3, \pm 5, \pm 7, \ldots$. Wake shows '2P' pattern of vortex shedding.

C.2 Forced Phase Variation

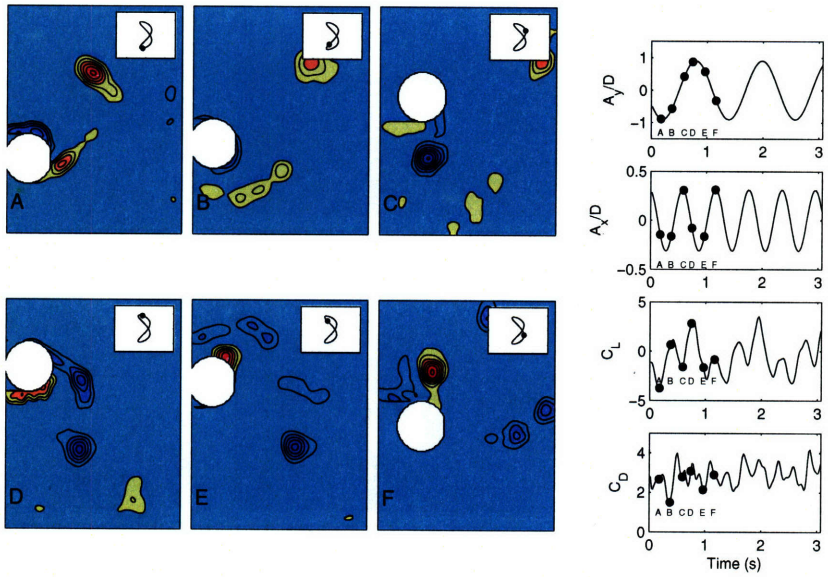

Figure C-7: Flow Visualization of forced motions, $V_r = 6.38$, $A_y/D = 0.91$, $A_x/D = 0.31$, $\theta = 45$ degrees. Vorticity contours show non-dimensional vorticity, $\frac{\omega D}{U} = \pm 3, \pm 5, \pm 7, \ldots$. Wake shows weak '2T' pattern of vortex shedding.

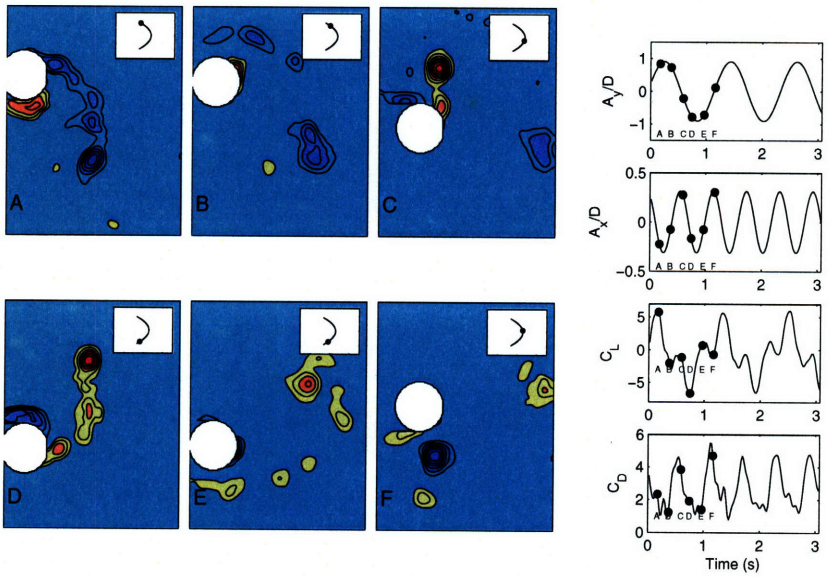

Figure C-8: Flow Visualization of forced motions, $V_r = 6.38$, $A_y/D = 0.91$, $A_x/D = 0.31$, $\theta = 90$ degrees. Vorticity contours show non-dimensional vorticity, $\frac{\omega D}{U} = \pm 3, \pm 5, \pm 7, \ldots$. Wake shows streaking '2T' pattern of vortex shedding.

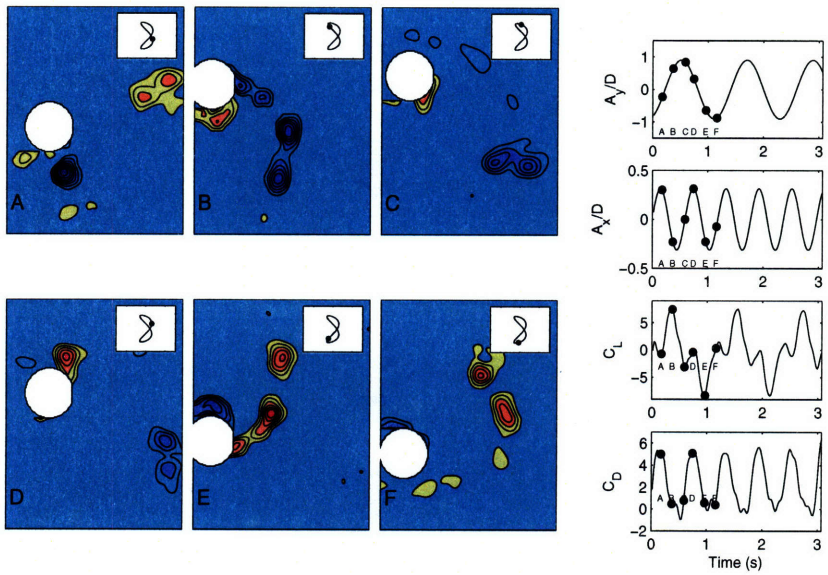

Figure C-9: Flow Visualization of forced motions, $V_r = 6.38$, $A_y/D = 0.91$, $A_x/D = 0.31$, $\theta = 135$ degrees. Vorticity contours show non-dimensional vorticity, $\frac{\omega D}{U} = \pm 3, \pm 5, \pm 7, \ldots$. Wake shows strong coupled vortices shedding in wake.

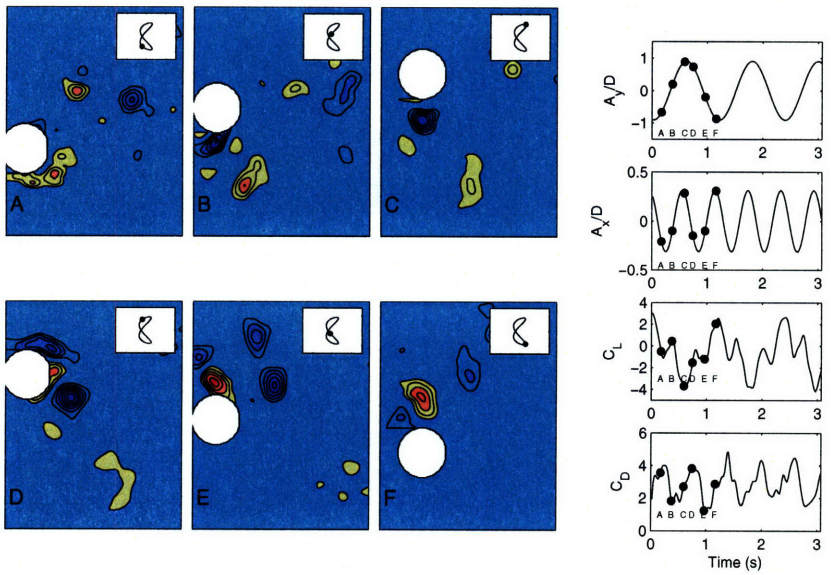

Figure C-10: Flow Visualization of forced motions, $V_r = 6.38$, $A_y/D = 0.91$, $A_x/D = 0.31$, $\theta = -45$ degrees. Vorticity contours show non-dimensional vorticity, $\frac{\omega D}{U} = \pm 3, \pm 5, \pm 7, \ldots$. Wake shows '2P' pattern of vortex shedding.

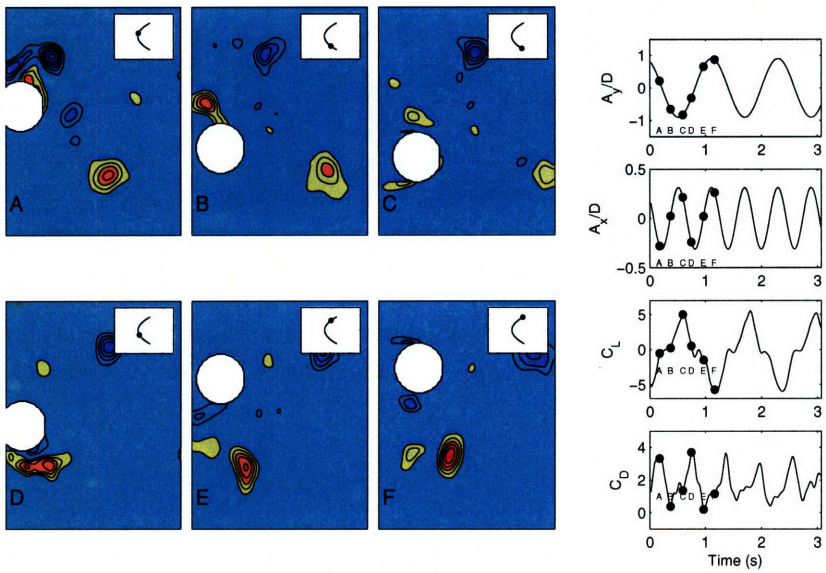

Figure C-11: Flow Visualization of forced motions, $V_r = 6.38$, $A_y/D = 0.91$, $A_x/D = 0.31$, $\theta = -90$ degrees. Vorticity contours show non-dimensional vorticity, $\frac{\omega D}{U} = \pm 3, \pm 5, \pm 7, \ldots$. Wake shows '2S' pattern of vortex shedding.

C.3 Forced Amplitude Variation

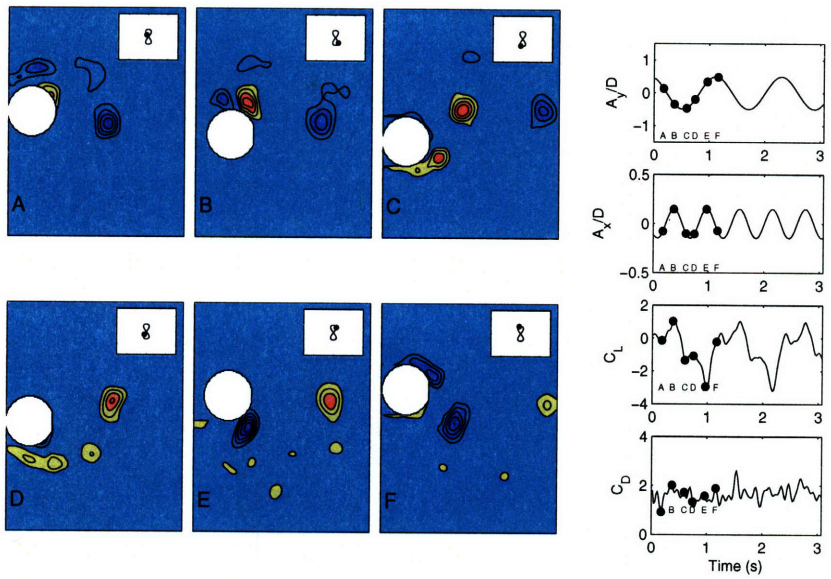

Figure C-12: Flow Visualization of forced motions, $V_r = 6.38$, $A_y/D = 0.5$, $A_x/D = 0.15$, $\theta = 0$ degrees. Vorticity contours show non-dimensional vorticity, $\frac{\omega D}{U} = \pm 3, \pm 5, \pm 7, \ldots$. Wake shows weak formation of '2P' pattern of vortex shedding.

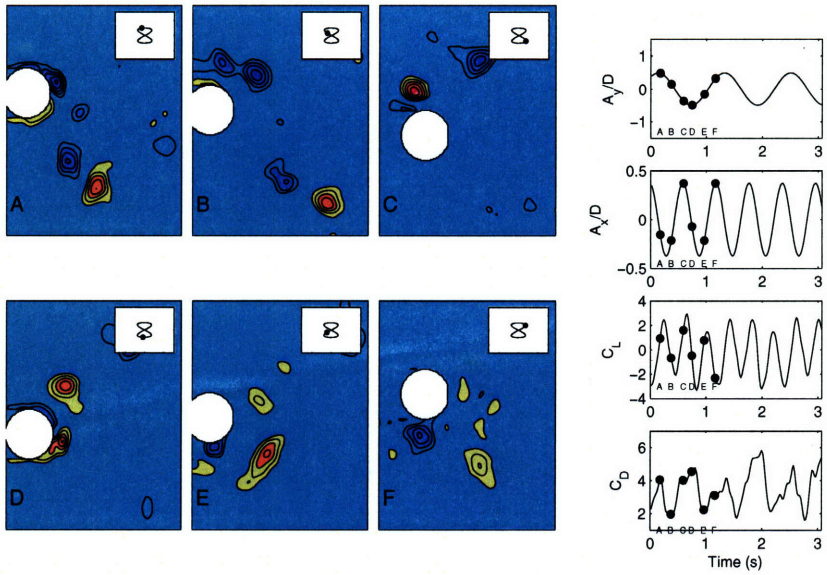

Figure C-13: Flow Visualization of forced motions, $V_r = 6.38$, $A_y/D = 0.5$, $A_x/D = 0.375$, $\theta = 0$ degrees. Vorticity contours show non-dimensional vorticity, $\frac{\omega D}{U} = \pm 3, \pm 5, \pm 7, \ldots$. Wake shows weak formation of '2T' pattern of vortex shedding.

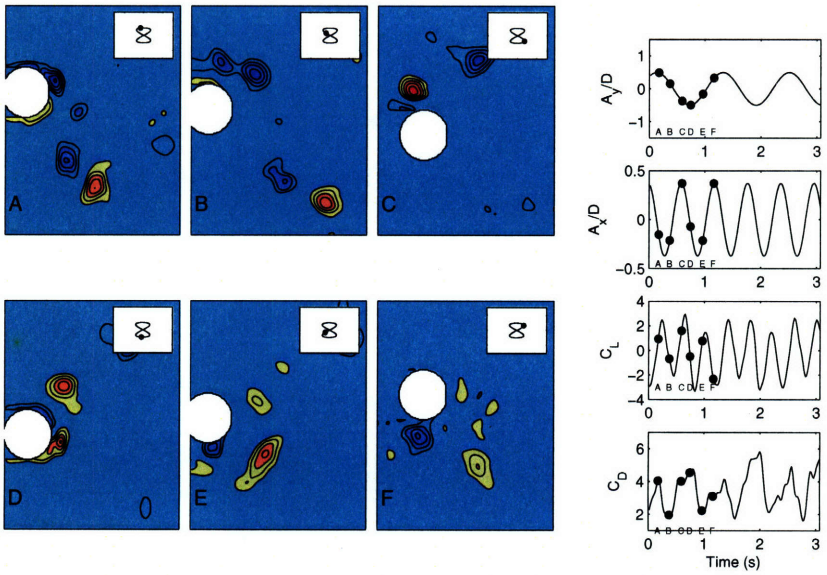

Figure C-14: Flow Visualization of forced motions, $V_r = 6.38$, $A_y/D = 0.5$, $A_x/D = 0.375$, $\theta = 0$ degrees. Vorticity contours show non-dimensional vorticity, $\frac{\omega D}{U} = \pm 3, \pm 5, \pm 7, \ldots$. Wake shows weak formation of '2T' pattern of vortex shedding.

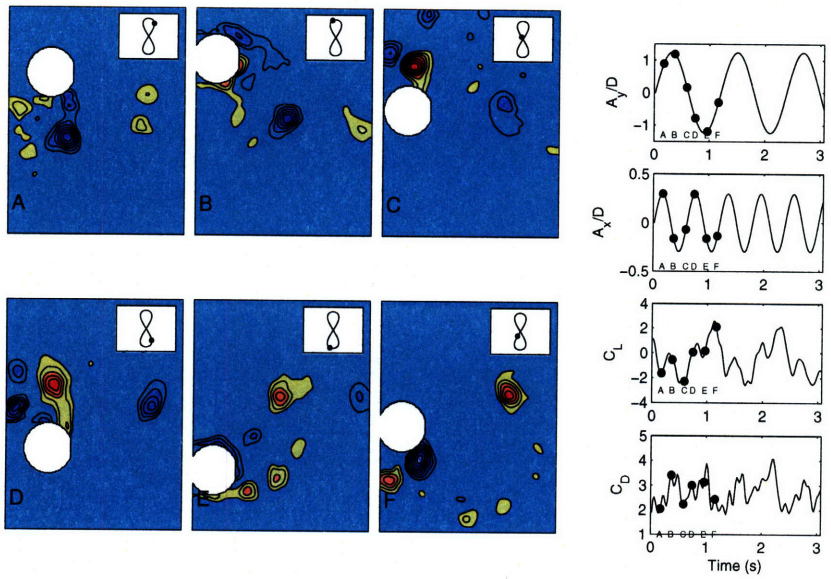

Figure C-15: Flow Visualization of forced motions, $V_r = 6.38$, $A_y/D = 1.25$, $A_x/D = 0.3$, $\theta = 0$ degrees. Vorticity contours show non-dimensional vorticity, $\frac{\omega D}{U} = \pm 3, \pm 5, \pm 7, \ldots$. Wake shows messy, streaking vortex shedding.

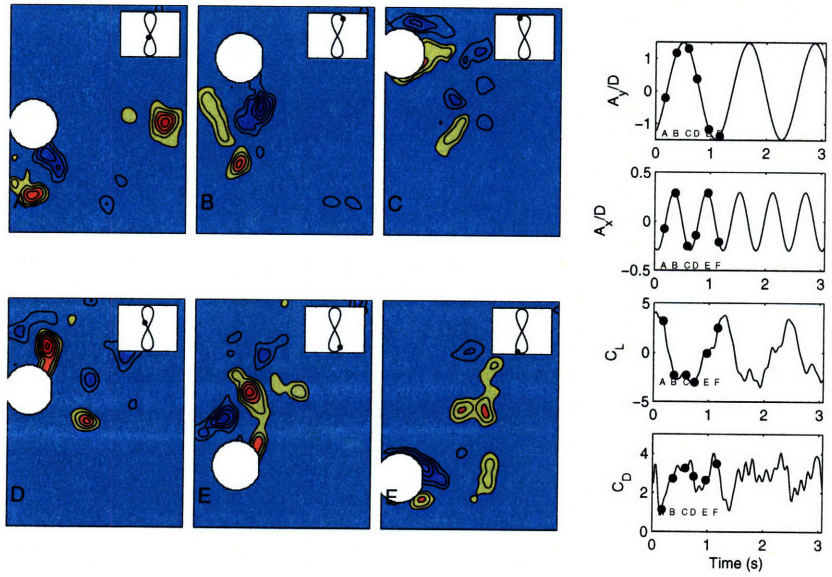

Figure C-16: Flow Visualization of forced motions, $V_r = 6.38$, $A_y/D = 1.5$, $A_x/D = 0.3$, $\theta = 0$ degrees. Vorticity contours show non-dimensional vorticity, $\frac{\omega D}{U} = \pm 3, \pm 5, \pm 7, \ldots$. Wake shows messy vortex shedding, almost forming a '2T' mode.

C.4 Forced Reduced Velocity Variation

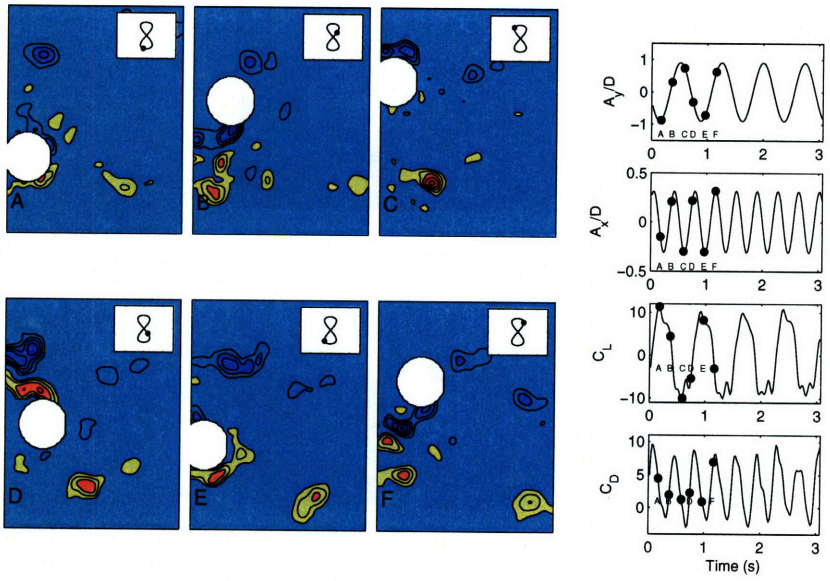

Figure C-17: Flow Visualization of forced motions, $V_r = 4$, $A_y/D = 0.91$, $A_x/D = 0.31$, $\theta = 0$ degrees. Vorticity contours show non-dimensional vorticity, $\frac{\omega D}{U} = \pm 3, \pm 5, \pm 7, \ldots$. Wake shows weak '2P' pattern of vortex shedding.

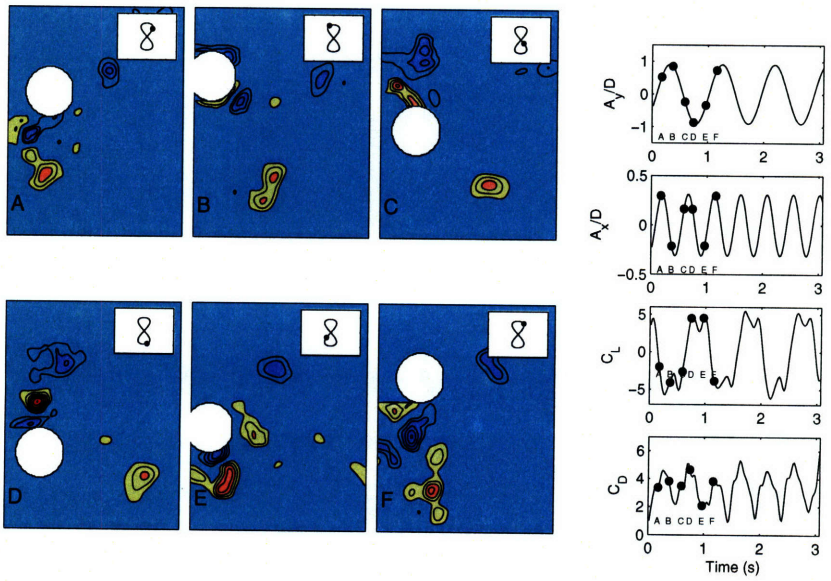

Figure C-18: Flow Visualization of forced motions, $V_r = 5$, $A_y/D = 0.91$, $A_x/D = 0.31$, $\theta = 0$ degrees. Vorticity contours show non-dimensional vorticity, $\frac{\omega D}{U} = \pm 3, \pm 5, \pm 7, \ldots$. Wake shows weak '2P' pattern of vortex shedding.

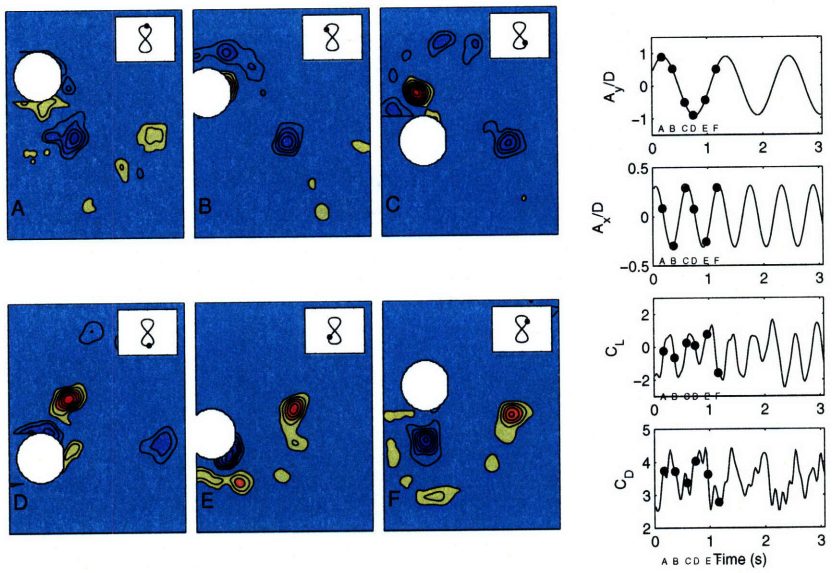

Figure C-19: Flow Visualization of forced motions, $V_r = 6$, $A_y/D = 0.91$, $A_x/D = 0.31$, $\theta = 0$ degrees. Vorticity contours show non-dimensional vorticity, $\frac{\omega D}{U} = \pm 3, \pm 5, \pm 7, \ldots$. Wake shows weak '2P' pattern of vortex shedding.

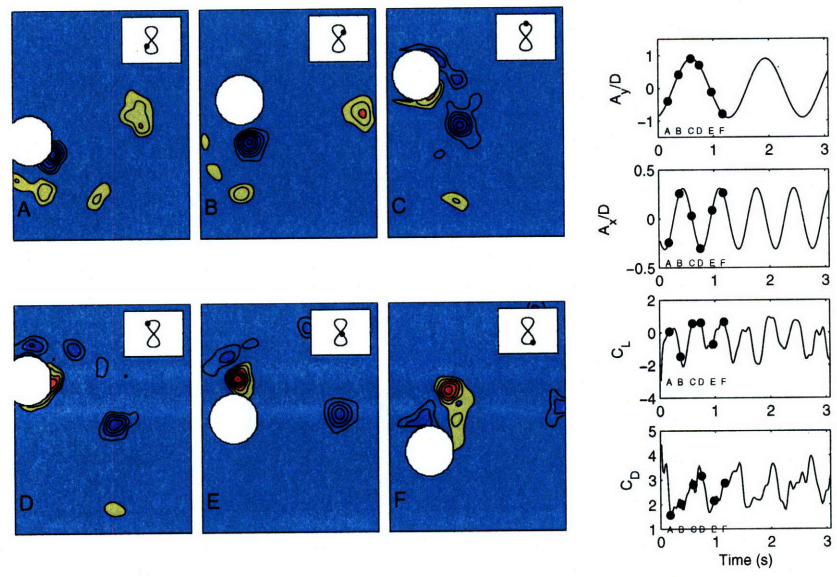

Figure C-20: Flow Visualization of forced motions, $V_r = 7$, $A_y/D = 0.91$, $A_x/D = 0.31$, $\theta = 0$ degrees. Vorticity contours show non-dimensional vorticity, $\frac{\omega D}{U} = \pm 3, \pm 5, \pm 7, \ldots$. Wake shows weak '2P' pattern of vortex shedding.

Appendix D

Forced Motion Database Force Contours

D.1 Third Harmonic Lift Coefficient, C_{L3}

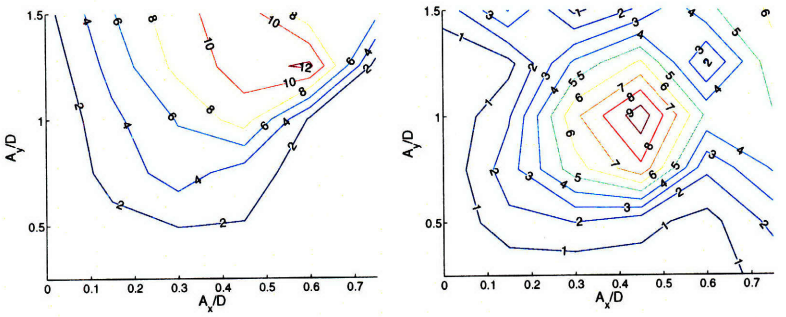

(a) $\theta = -180$ deg

(b) $\theta = -135$ deg

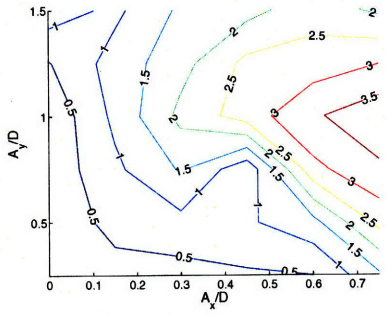

(c) $\theta = -90$ deg

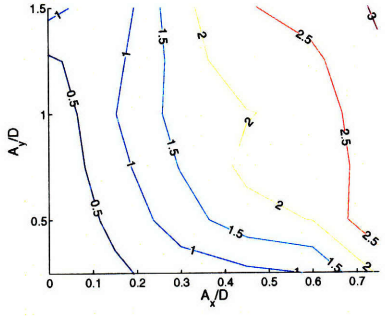

(d) $\theta = -45$ deg

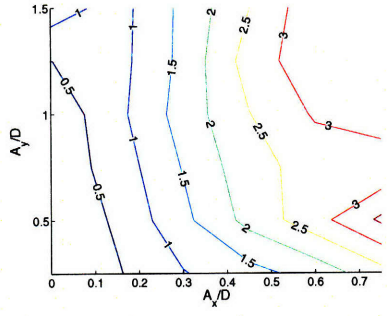

(e) $\theta = 0$ deg

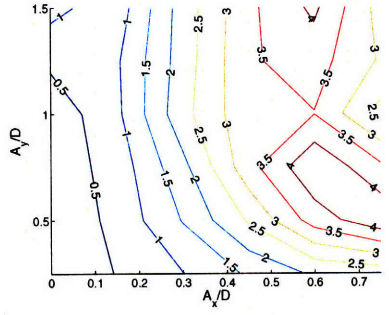

(f) $\theta = 45$ deg

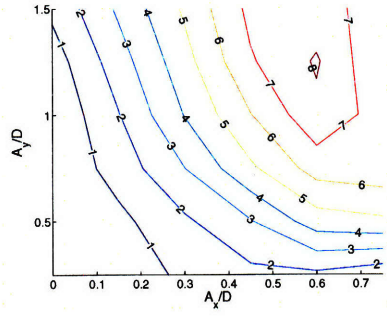

(g) $\theta = 90$ deg

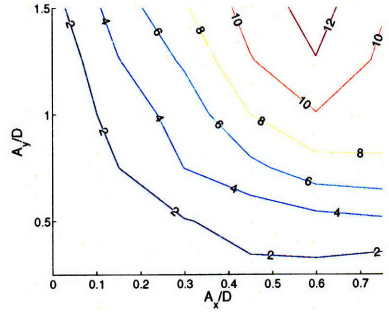

(h) $\theta = 135$ deg

Figure D-1: Third harmonic lift coefficient contours for $V_r = 4.5$.

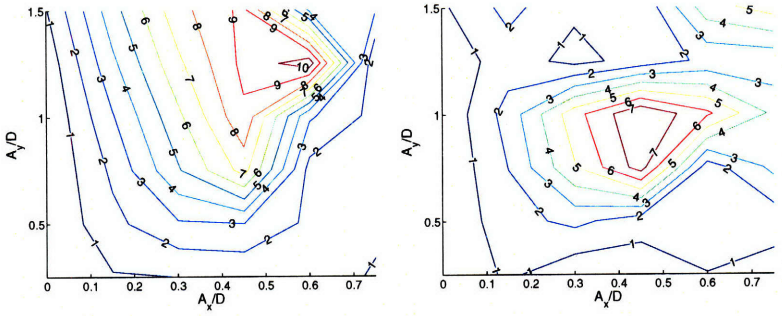

(a) $\theta = -180$ deg

(b) $\theta = -135$ deg

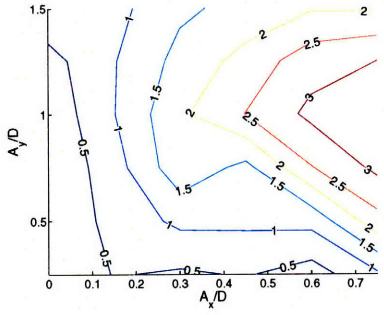

(c) $\theta = -90$ deg

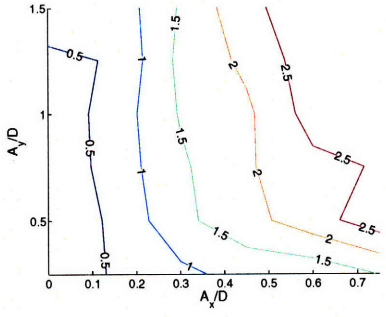

(d) $\theta = -45$ deg

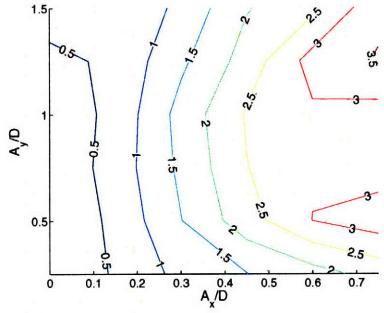

(e) $\theta = 0$ deg

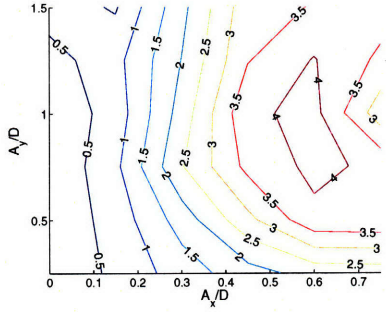

(f) $\theta = 45$ deg

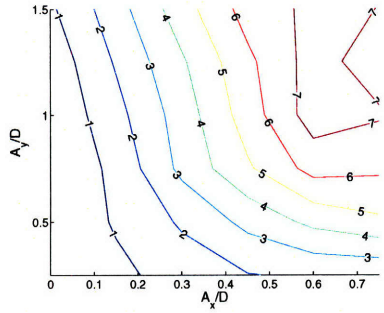

(g) $\theta = 90$ deg

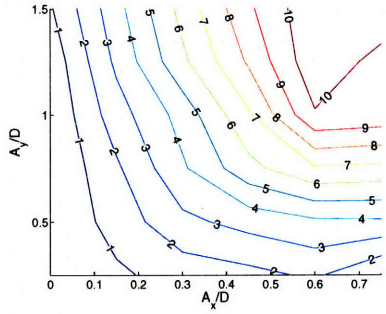

(h) $\theta = 135$ deg

Figure D-2: Third harmonic lift coefficient contours for $V_r = 5$.

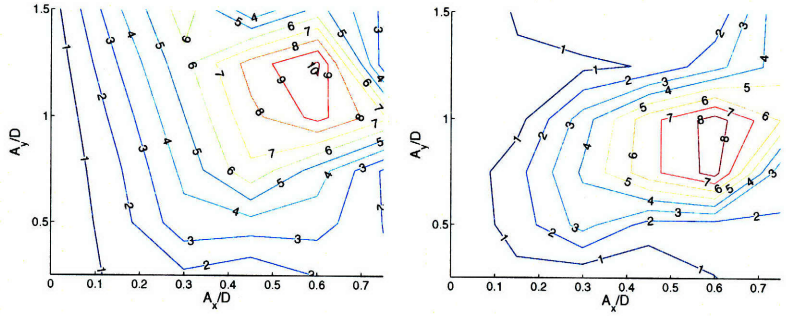

(a) $\theta = -180$ deg

(b) $\theta = -135$ deg

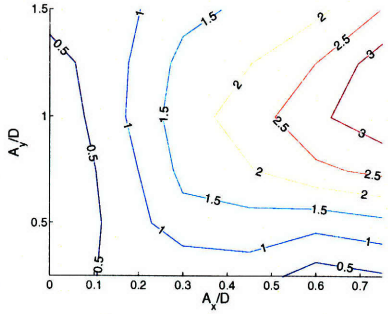

(c) $\theta = -90$ deg

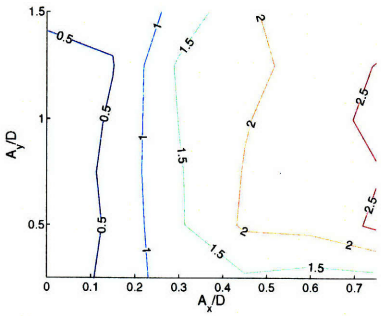

(d) $\theta = -45$ deg

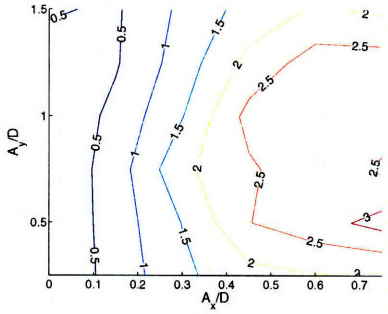

(e) $\theta = 0$ deg

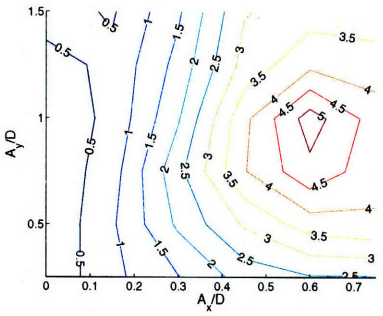

(f) $\theta = 45$ deg

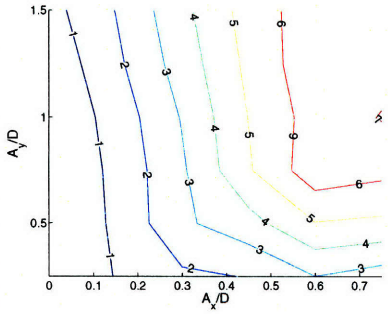

(g) $\theta = 90$ deg

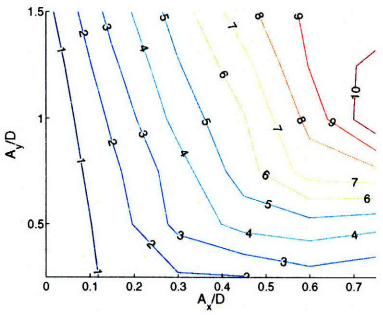

(h) $\theta = 135$ deg

Figure D-3: Third harmonic lift coefficient contours for $V_r = 5.5$.

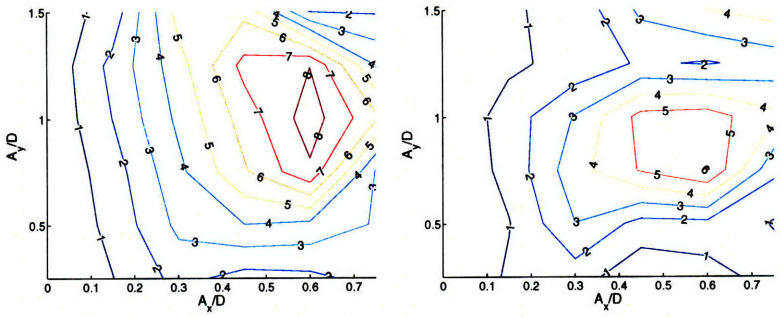

(a) $\theta = -180$ deg

(b) $\theta = -135$ deg

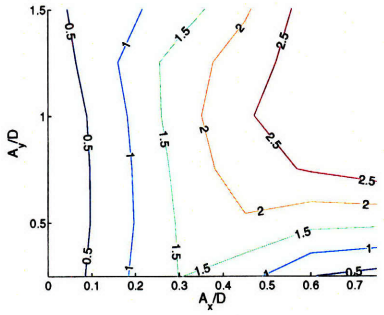

(c) $\theta = -90$ deg

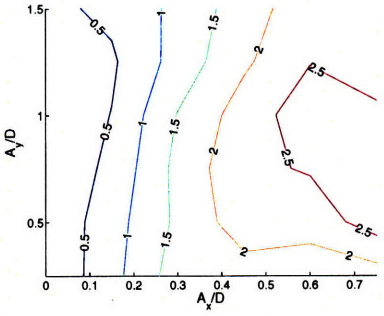

(d) $\theta = -45$ deg

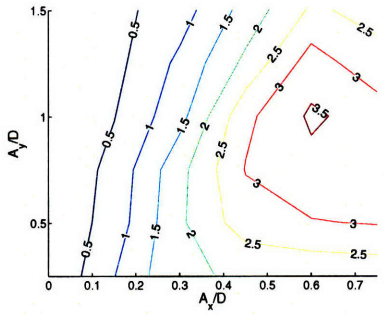

(e) $\theta = 0$ deg

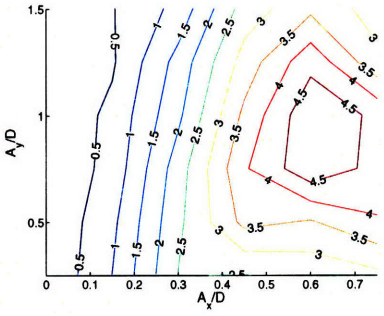

(f) $\theta = 45$ deg

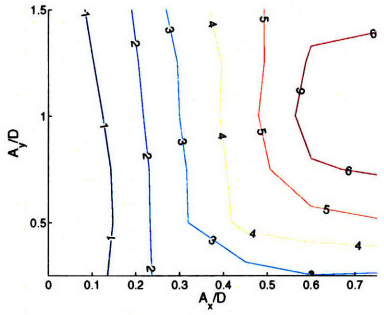

(g) $\theta = 90$ deg

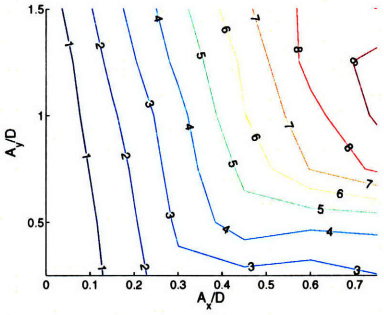

(h) $\theta = 135$ deg

Figure D-4: Third harmonic lift coefficient contours for $V_r = 6$.

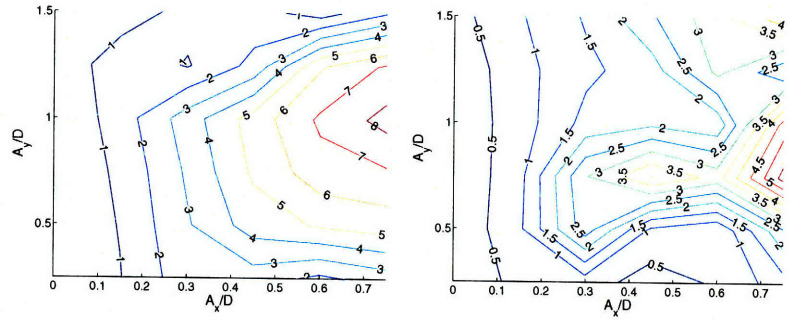

(a) $\theta = -180$ deg

(b) $\theta = -135$ deg

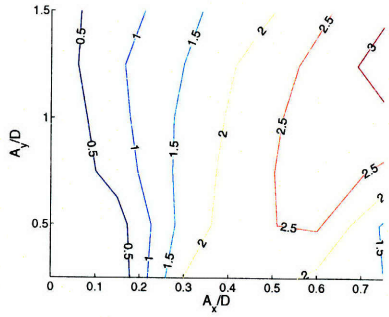

(c) $\theta = -90$ deg

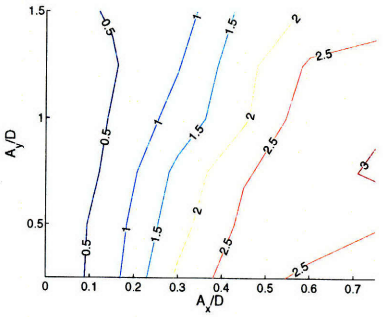

(d) $\theta = -45$ deg

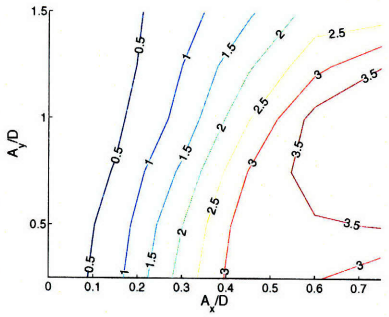

(e) $\theta = 0$ deg

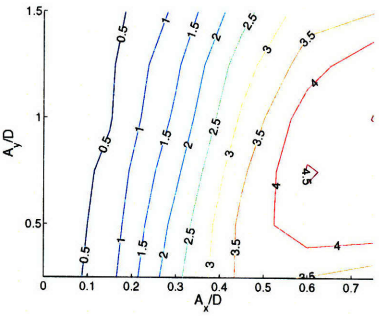

(f) $\theta = 45$ deg

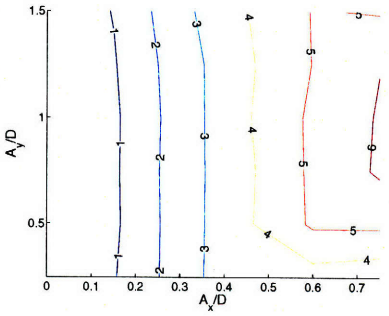

(g) $\theta = 90$ deg

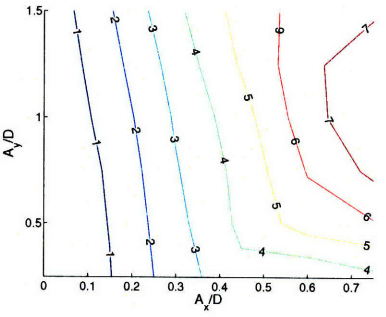

(h) $\theta = 135$ deg

Figure D-5: Third harmonic lift coefficient contours for $V_r = 6.5$.

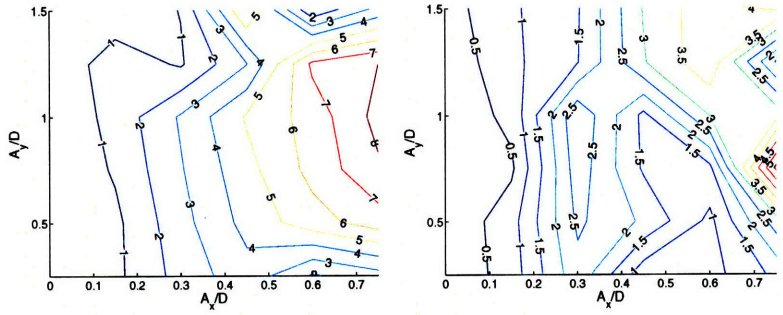

(a) $\theta = -180$ deg

(b) $\theta = -135$ deg

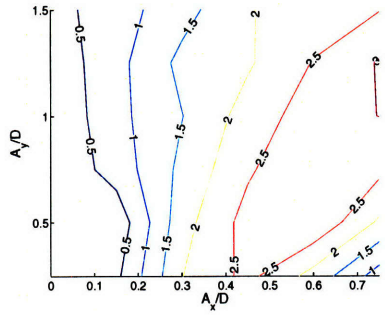

(c) $\theta = -90$ deg

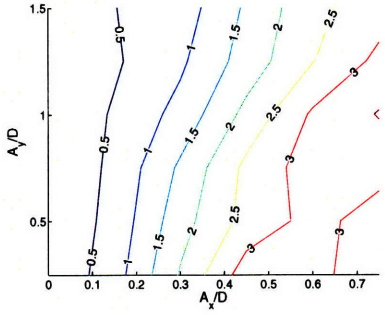

(d) $\theta = -45$ deg

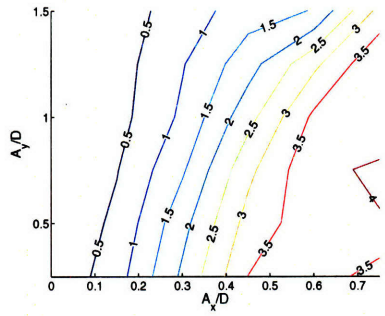

(e) $\theta = 0$ deg

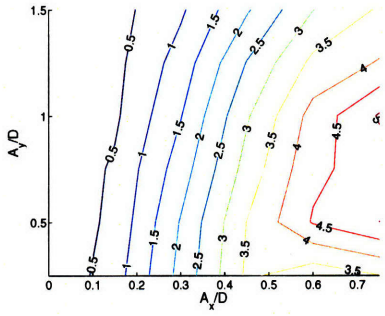

(f) $\theta = 45$ deg

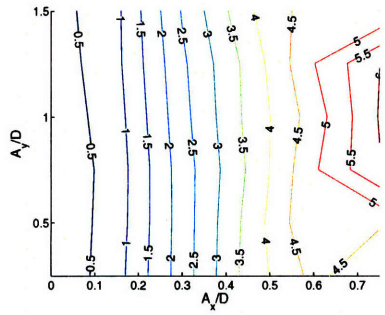

(g) $\theta = 90$ deg

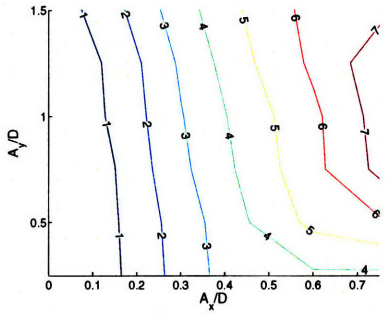

(h) $\theta = 135$ deg

Figure D-6: Third harmonic lift coefficient contours for $V_r = 7$.

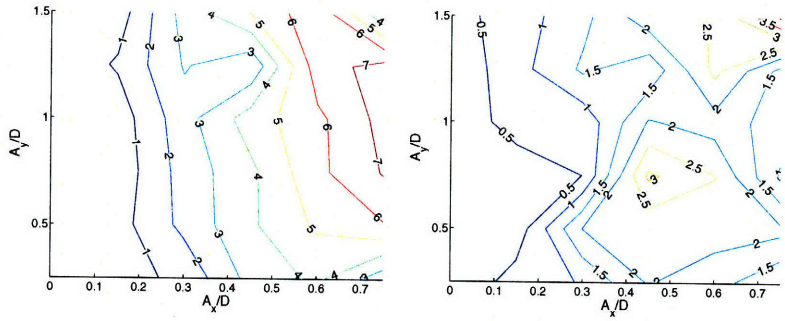

(a) $\theta = -180$ deg

(b) $\theta = -135$ deg

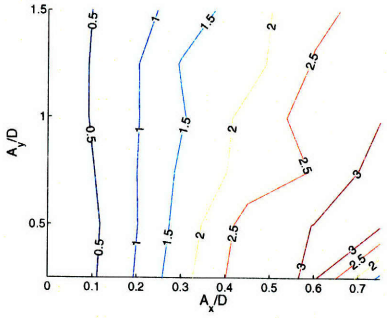

(c) $\theta = -90$ deg

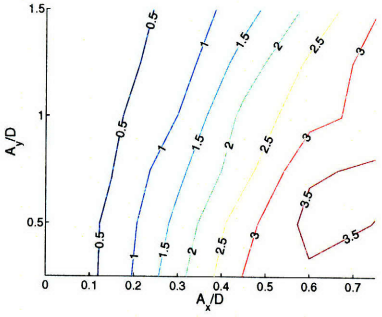

(d) $\theta = -45$ deg

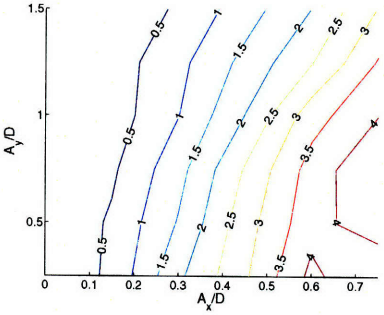

(e) $\theta = 0$ deg

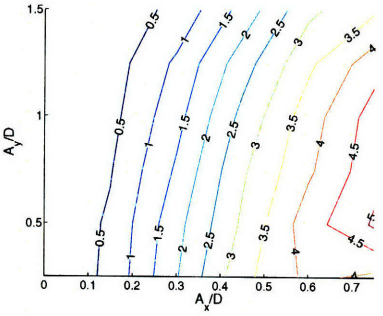

(f) $\theta = 45$ deg

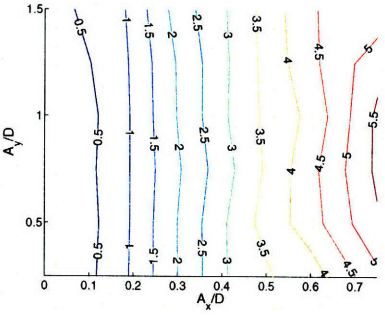

(g) $\theta = 90$ deg

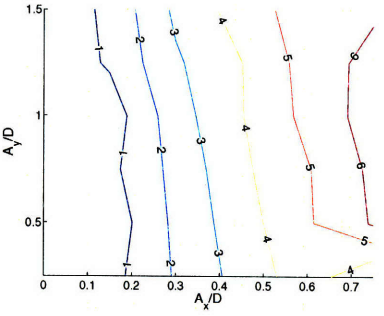

(h) $\theta = 135$ deg

Figure D-7: Third harmonic lift coefficient contours for $V_r = 7.5$.

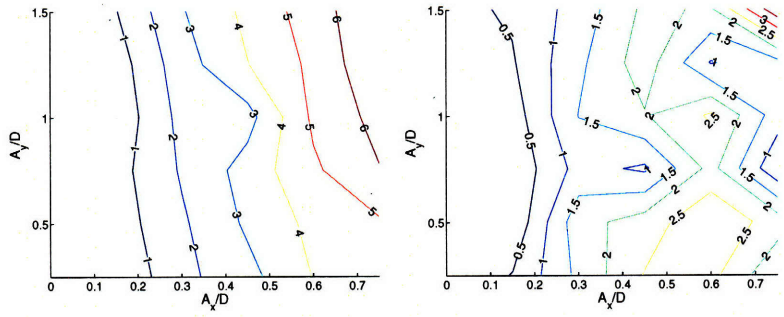

(a) $\theta = -180$ deg

(b) $\theta = -135$ deg

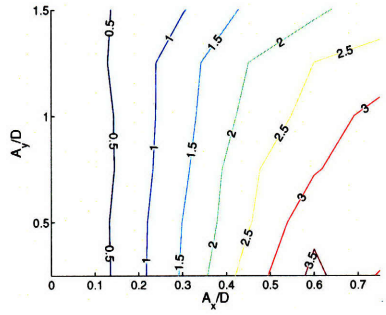

(c) $\theta = -90$ deg

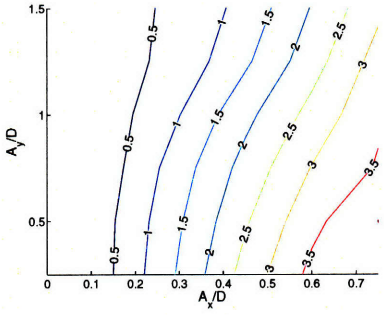

(d) $\theta = -45$ deg

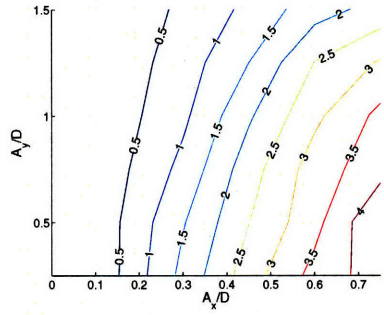

(e) $\theta = 0$ deg

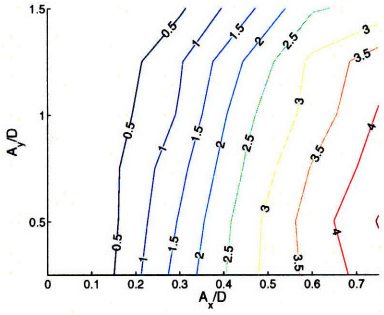

(f) $\theta = 45$ deg

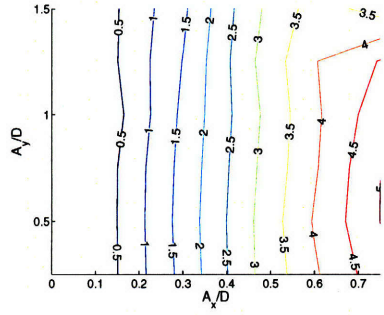

(g) $\theta = 90$ deg

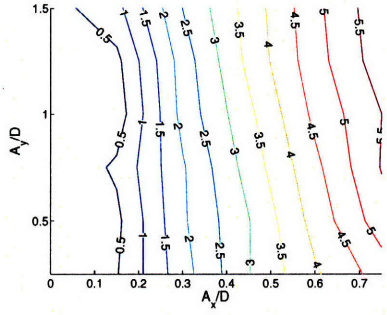

(h) $\theta = 135$ deg

Figure D-8: Third harmonic lift coefficient contours for $V_r = 8$.

D.2 Total Average Power Coefficient, C_{ap}

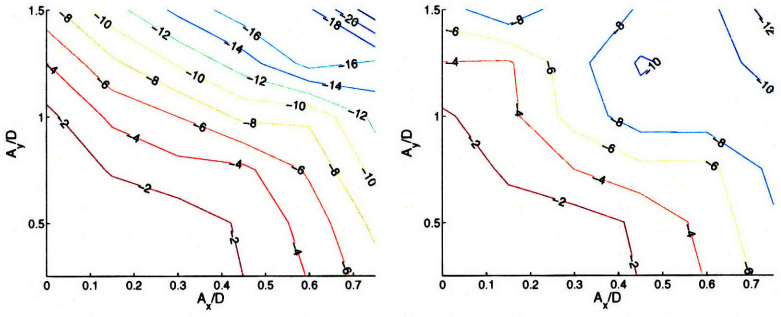

(a) $\theta = -180$ deg

(b) $\theta = -135$ deg

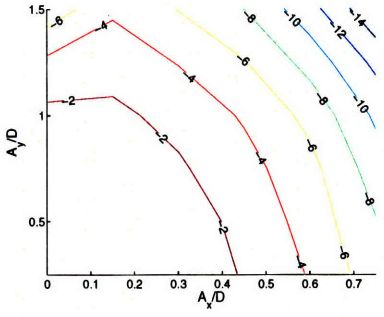

(c) $\theta = -90$ deg

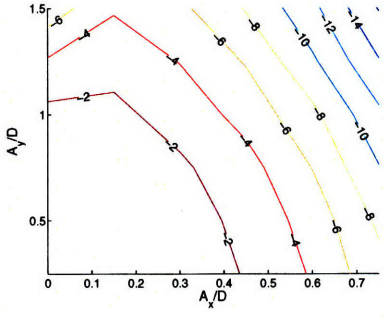

(d) $\theta = -45$ deg

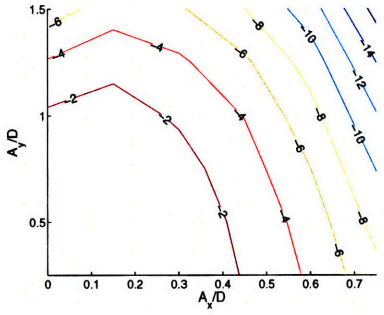

(e) $\theta = 0$ deg

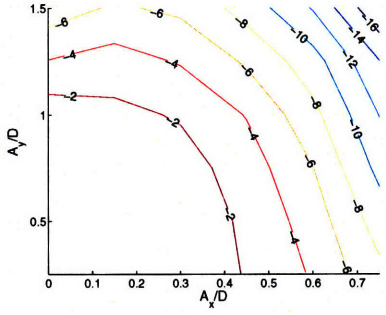

(f) $\theta = 45$ deg

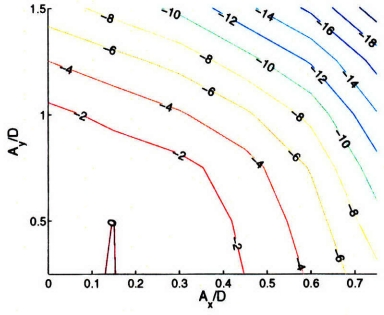

(g) $\theta = 90$ deg

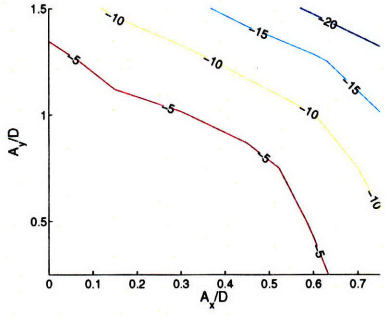

(h) $\theta = 135$ deg

Figure D-9: Total average power coefficient contours for $V_r = 4.5$.

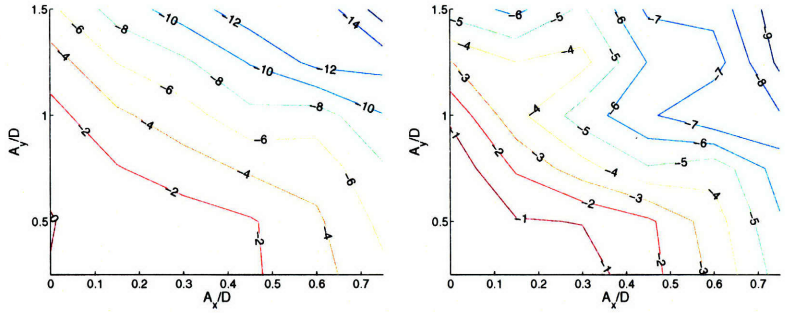

(a) $\theta = -180$ deg

(b) $\theta = -135$ deg

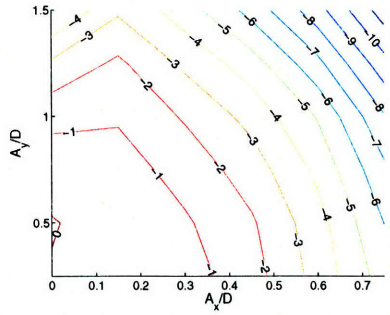

(c) $\theta = -90$ deg

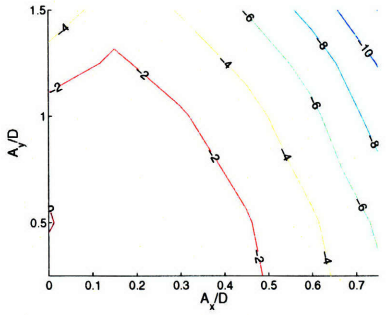

(d) $\theta = -45$ deg

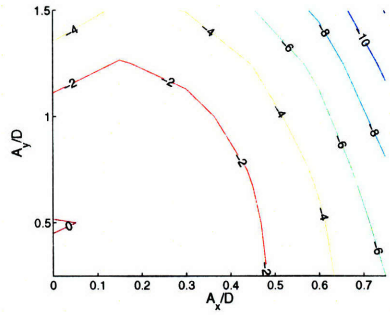

(e) $\theta = 0$ deg

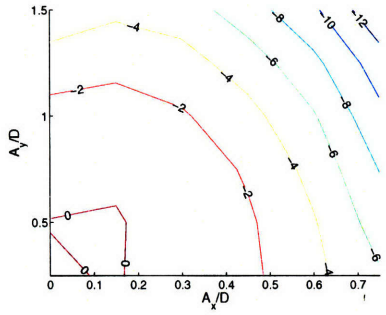

(f) $\theta = 45$ deg

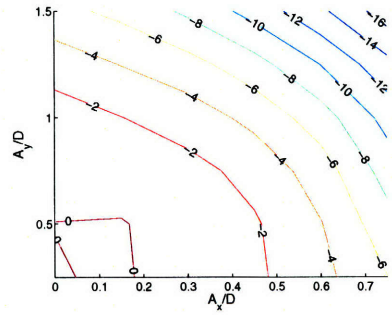

(g) $\theta = 90$ deg

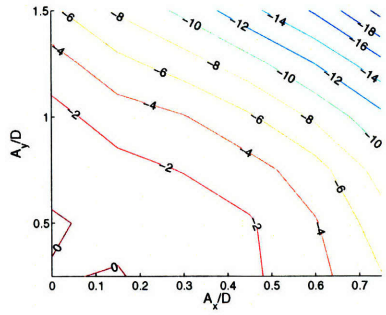

(h) $\theta = 135$ deg

Figure D-10: Total average power coefficient contours for $V_r = 5$.

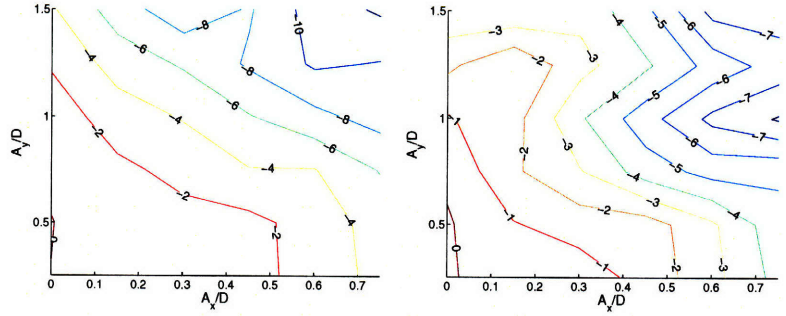

(a) $\theta = -180$ deg

(b) $\theta = -135$ deg

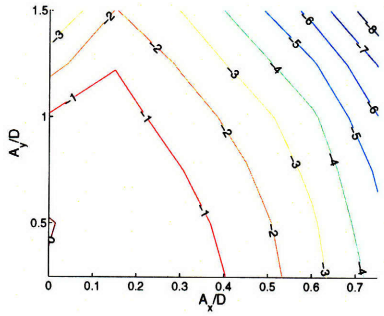

(c) $\theta = -90$ deg

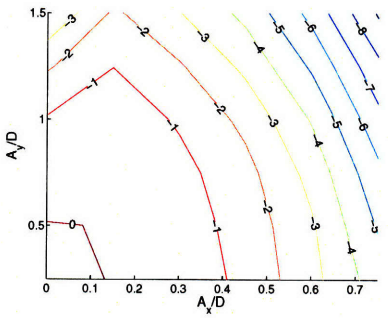

(d) $\theta = -45$ deg

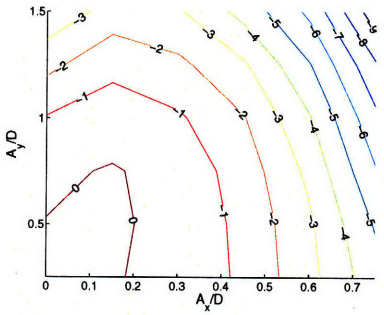

(e) $\theta = 0$ deg

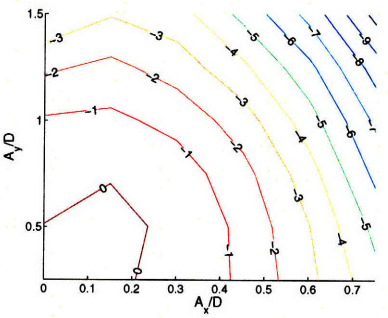

(f) $\theta = 45$ deg

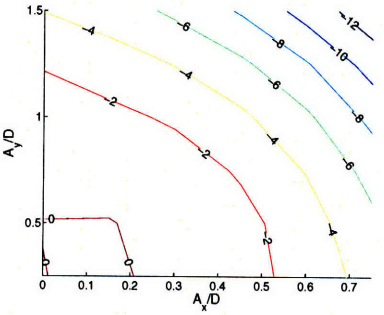

(g) $\theta = 90$ deg

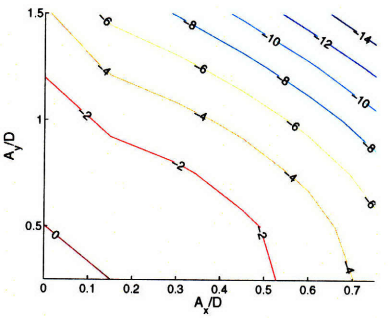

(h) $\theta = 135$ deg

Figure D-11: Total average power coefficient contours for $V_r = 5.5$.

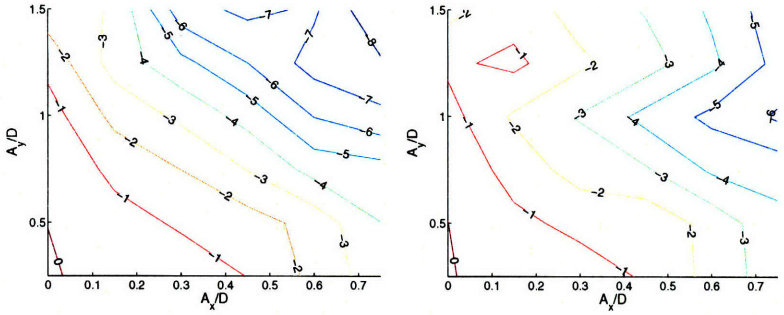

(a) $\theta = -180$ deg

(b) $\theta = -135$ deg

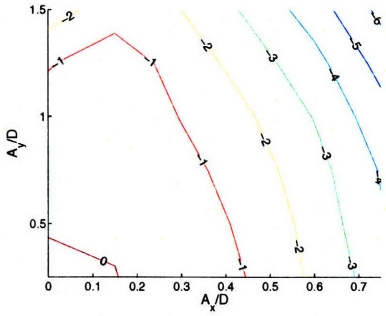

(c) $\theta = -90$ deg

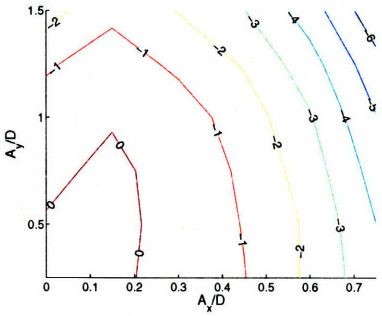

(d) $\theta = -45$ deg

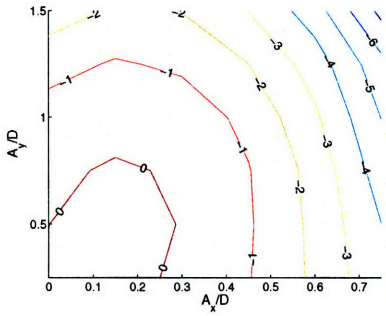

(e) $\theta = 0$ deg

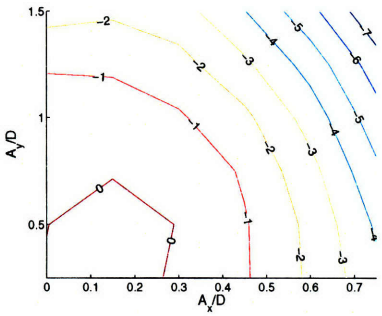

(f) $\theta = 45$ deg

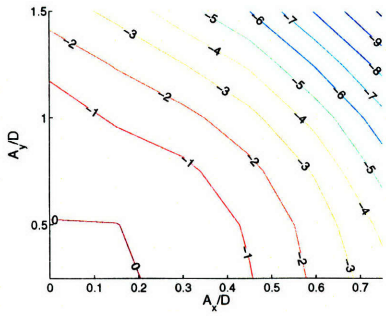

(g) $\theta = 90$ deg

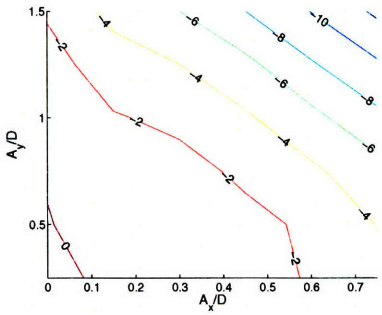

(h) $\theta = 135$ deg

Figure D-12: Total average power coefficient contours for $V_r = 6$.

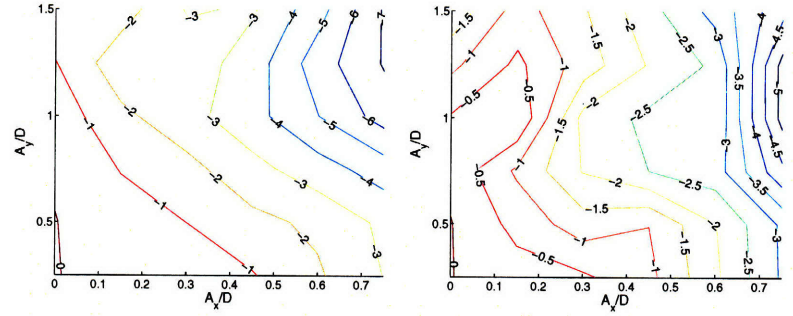

(a) $\theta = -180$ deg

(b) $\theta = -135$ deg

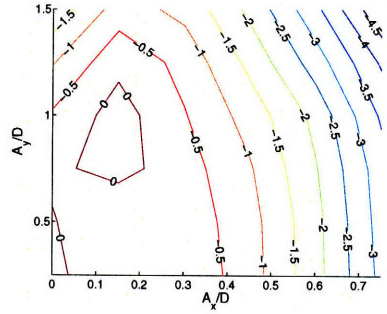

(c) $\theta = -90$ deg

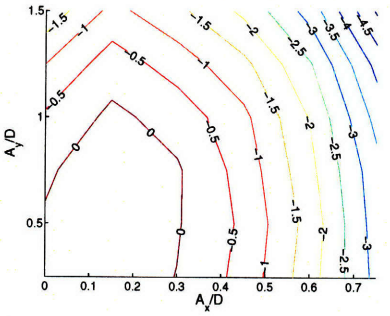

(d) $\theta = -45$ deg

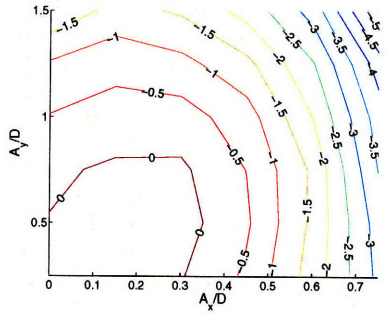

(e) $\theta = 0$ deg

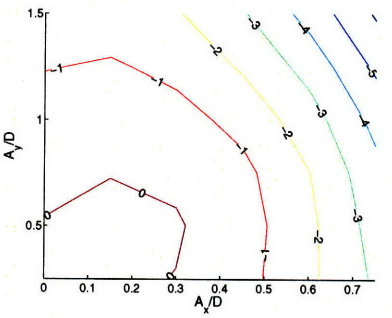

(f) $\theta = 45$ deg

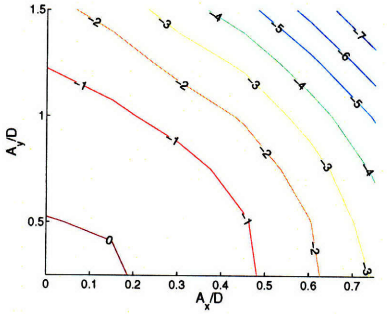

(g) $\theta = 90$ deg

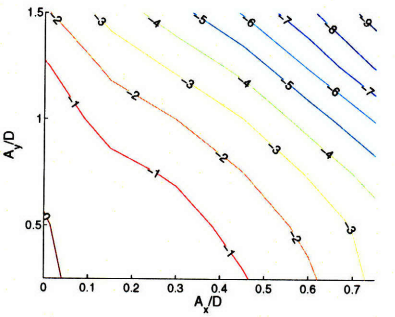

(h) $\theta = 135$ deg

Figure D-13: Total average power coefficient contours for $V_r = 6.5$.

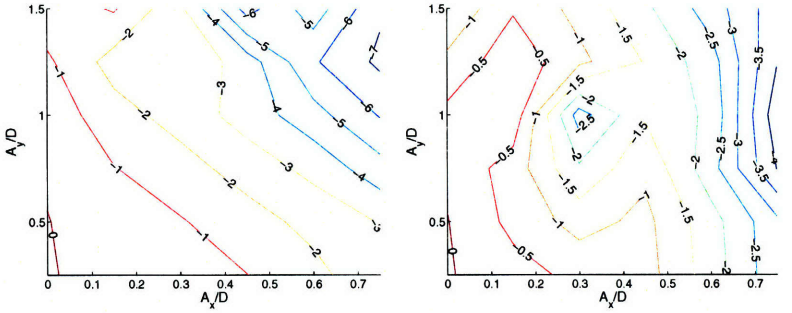

(a) $\theta = -180$ deg

(b) $\theta = -135$ deg

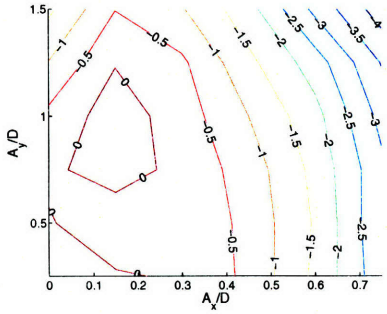

(c) $\theta = -90$ deg

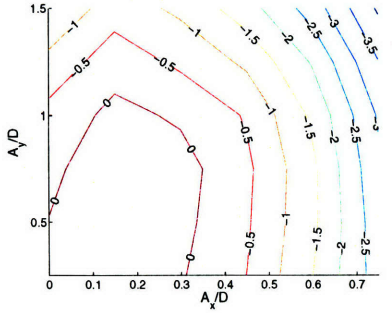

(d) $\theta = -45$ deg

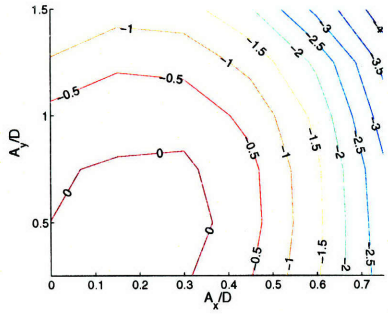

(e) $\theta = 0$ deg

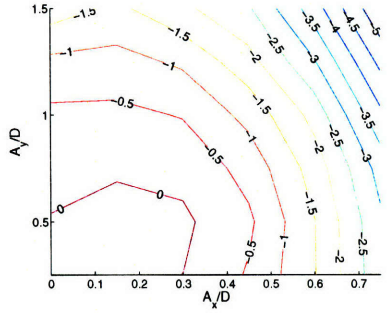

(f) $\theta = 45$ deg

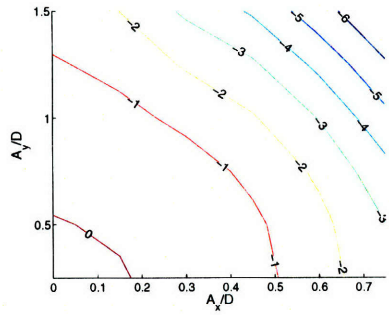

(g) $\theta = 90$ deg

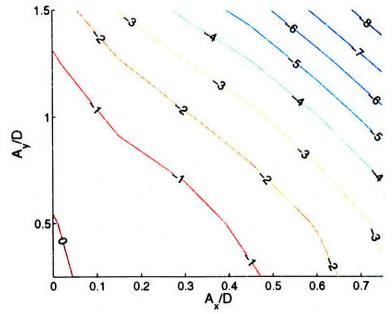

(h) $\theta = 135$ deg

Figure D-14: Total average power coefficient contours for $V_r = 7$.

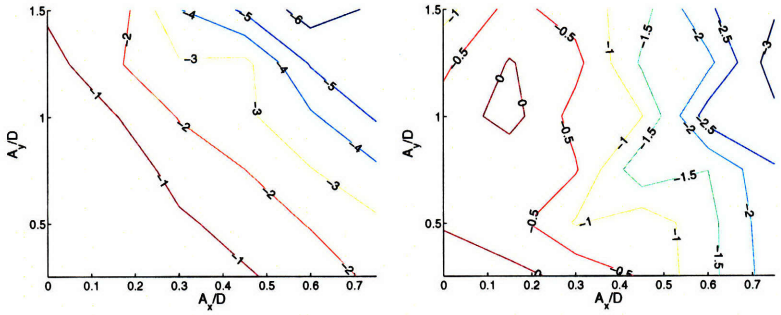

(a) $\theta = -180$ deg

(b) $\theta = -135$ deg

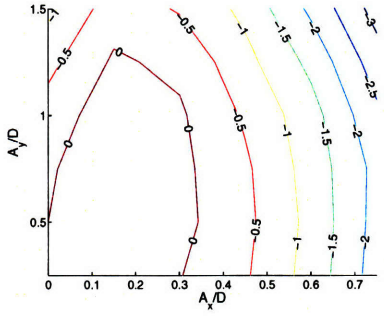

(c) $\theta = -90$ deg

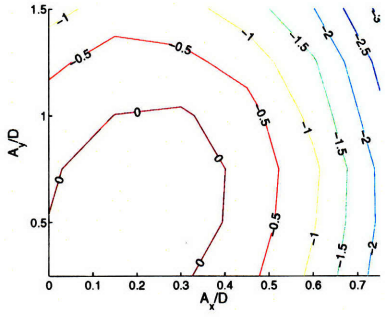

(d) $\theta = -45$ deg

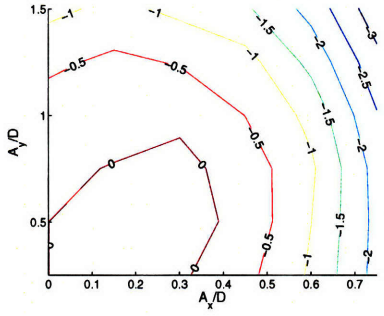

(e) $\theta = 0$ deg

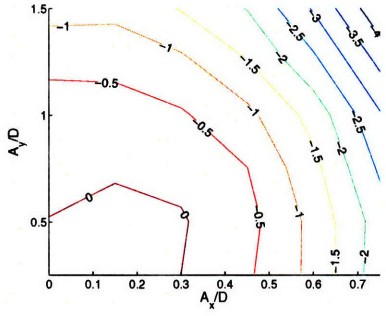

(f) $\theta = 45$ deg

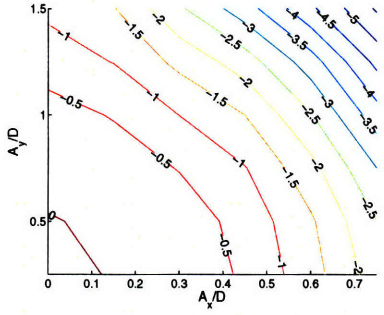

(g) $\theta = 90$ deg

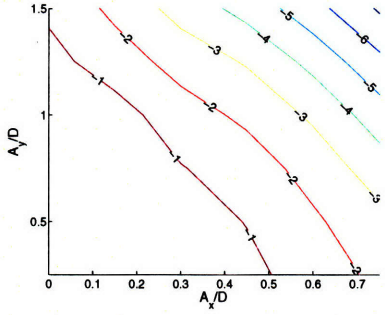

(h) $\theta = 135$ deg

Figure D-15: Total average power coefficient contours for $V_r = 7.5$.

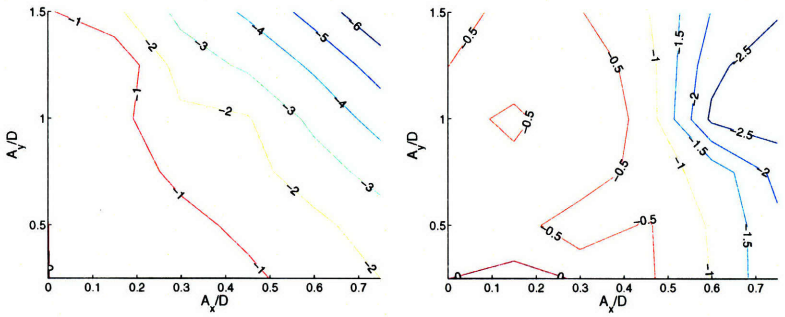

(a) $\theta = -180$ deg

(b) $\theta = -135$ deg

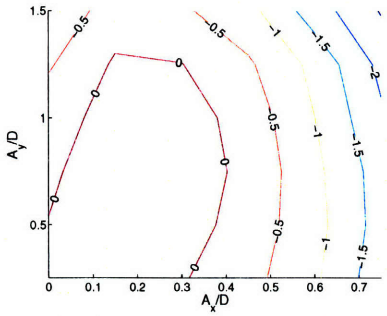

(c) $\theta = -90$ deg

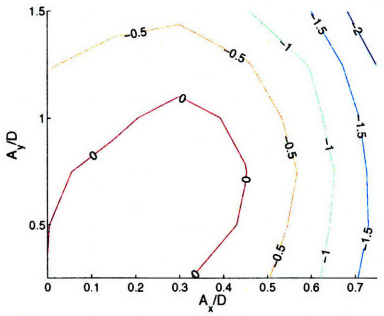

(d) $\theta = -45$ deg

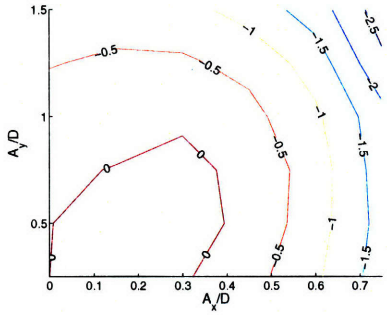

(e) $\theta = 0$ deg

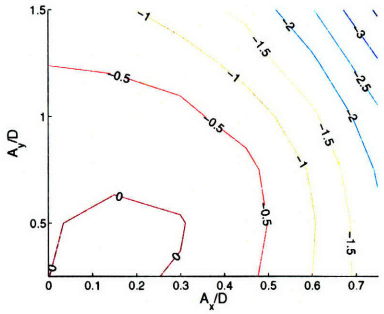

(f) $\theta = 45$ deg

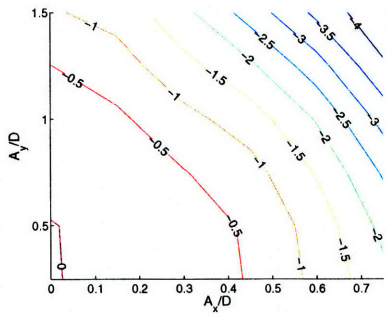

(g) $\theta = 90$ deg

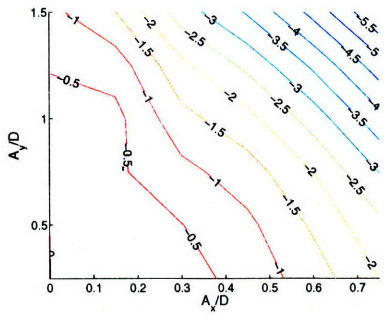

(h) $\theta = 135$ deg

Figure D-16: Total average power coefficient contours for $V_r = 8$.

D.3 Cross-flow Added Mass Coefficient, C_{my}

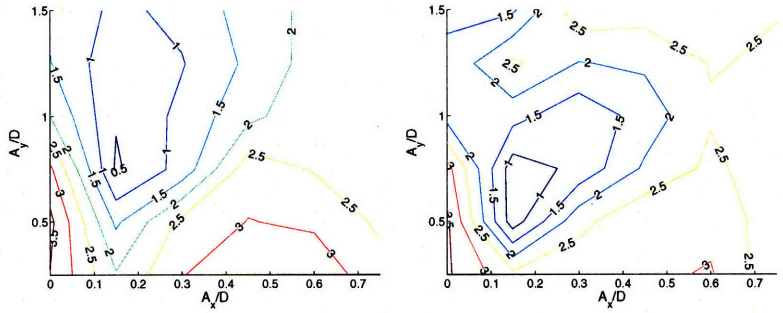

(a) $\theta = -180$ deg

(b) $\theta = -135$ deg

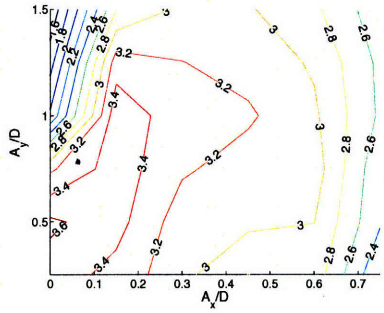

(c) $\theta = -90$ deg

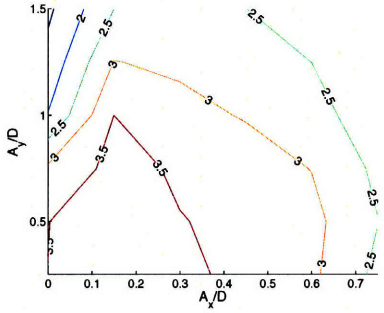

(d) $\theta = -45$ deg

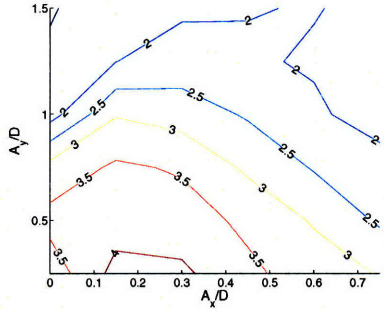

(e) $\theta = 0$ deg

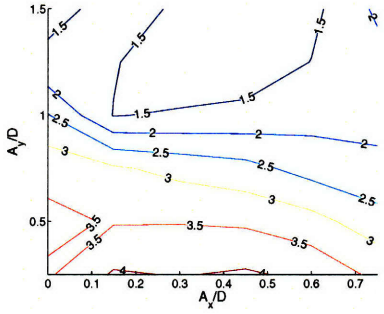

(f) $\theta = 45$ deg

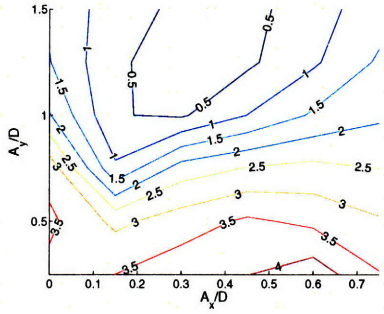

(g) $\theta = 90$ deg

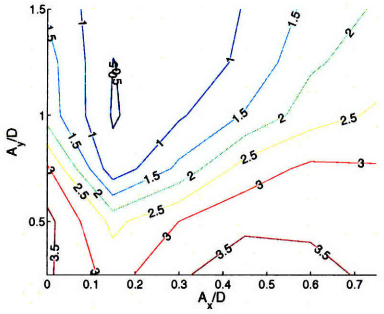

(h) $\theta = 135$ deg

Figure D-17: Cross-flow added mass coefficient contours for $V_r = 4.5$.

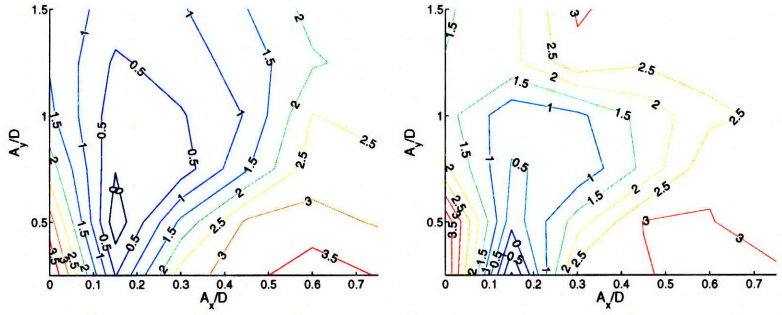

(a) $\theta = -180$ deg

(b) $\theta = -135$ deg

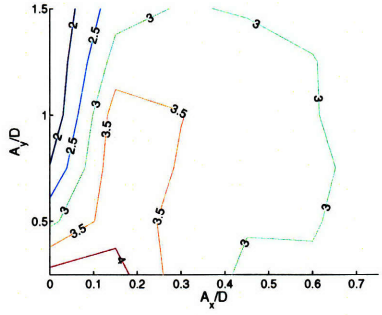

(c) $\theta = -90$ deg

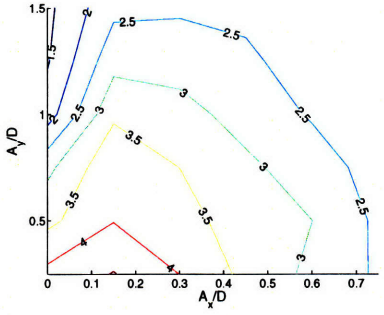

(d) $\theta = -45$ deg

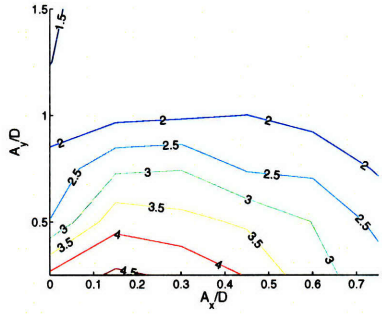

(e) $\theta = 0$ deg

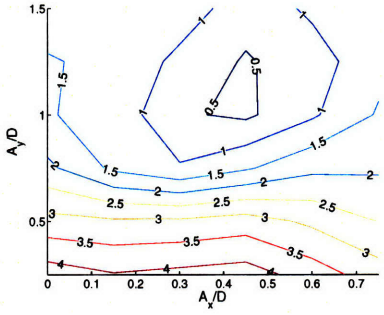

(f) $\theta = 45$ deg

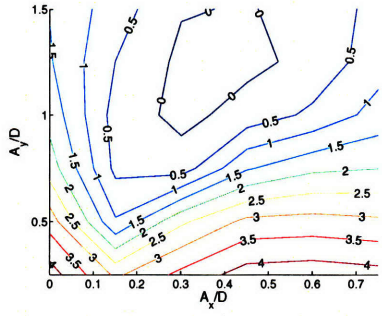

(g) $\theta = 90$ deg

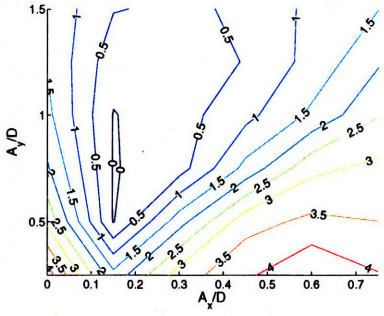

(h) $\theta = 135$ deg

Figure D-18: Cross-flow added mass coefficient contours for $V_r = 5$.

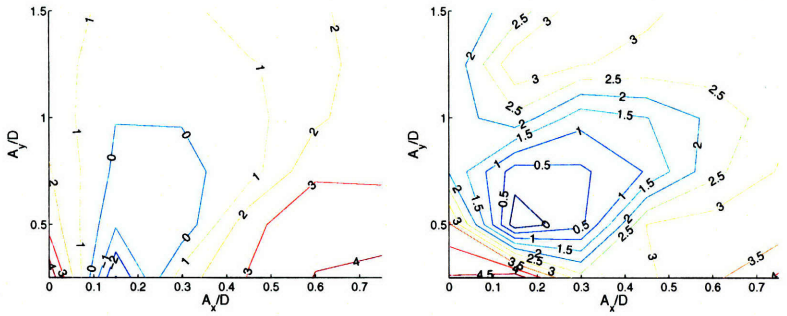

(a) $\theta = -180$ deg

(b) $\theta = -135$ deg

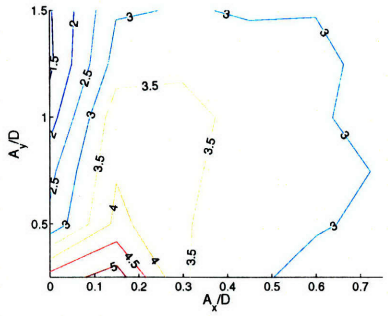

(c) $\theta = -90$ deg

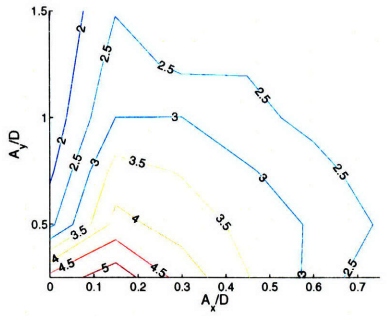

(d) $\theta = -45$ deg

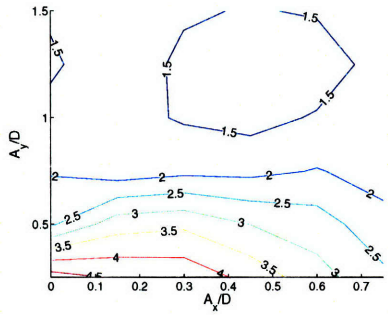

(e) $\theta = 0$ deg

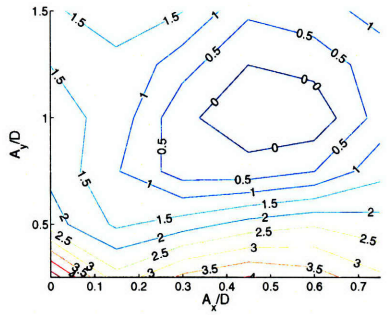

(f) $\theta = 45$ deg

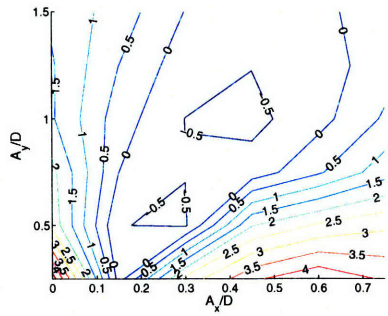

(g) $\theta = 90$ deg

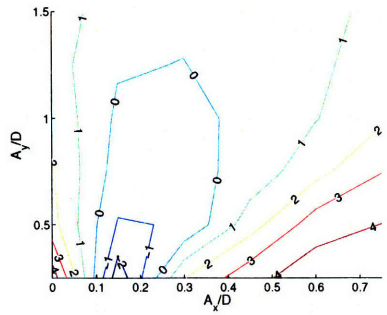

(h) $\theta = 135$ deg

Figure D-19: Cross-flow added mass coefficient contours for $V_r = 5.5$.

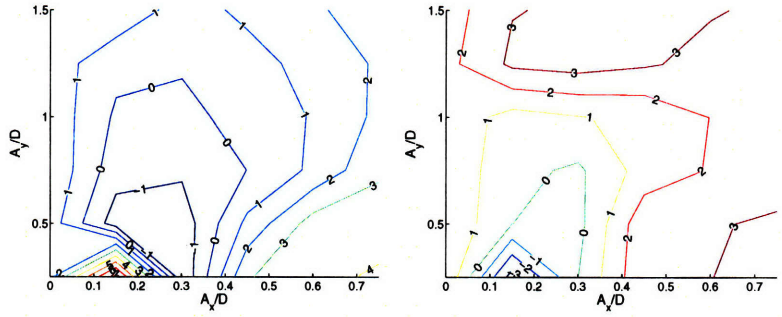

(a) $\theta = -180$ deg

(b) $\theta = -135$ deg

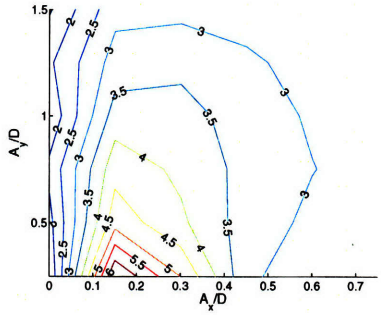

(c) $\theta = -90$ deg

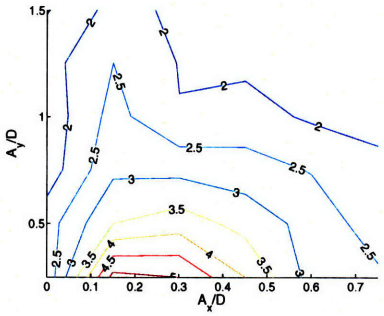

(d) $\theta = -45$ deg

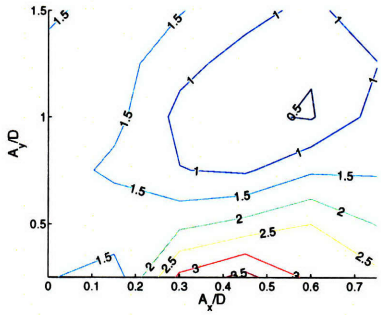

(e) $\theta = 0$ deg

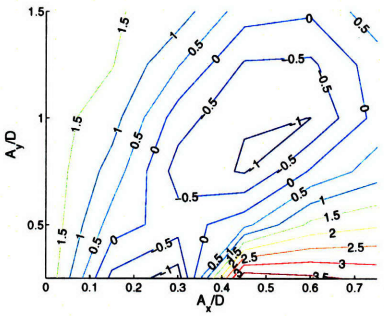

(f) $\theta = 45$ deg

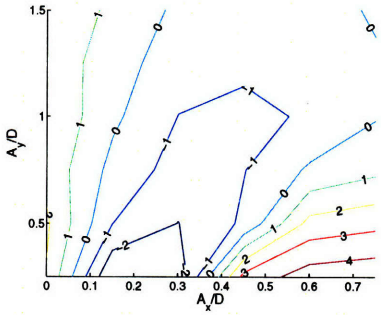

(g) $\theta = 90$ deg

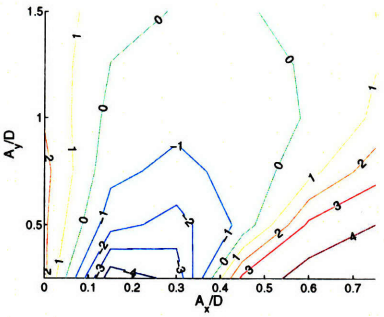

(h) $\theta = 135$ deg

Figure D-20: Cross-flow added mass coefficient contours for $V_r = 6$.

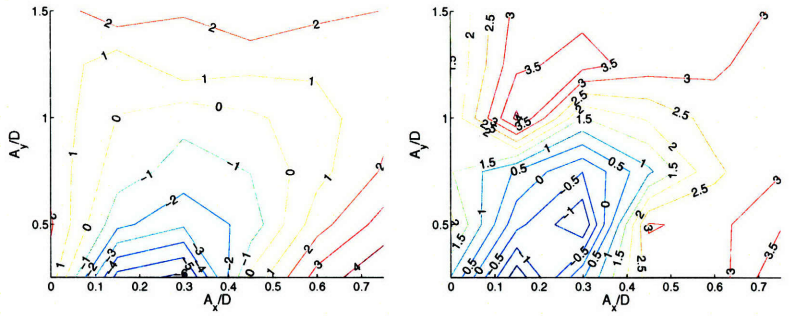

(a) $\theta = -180$ deg

(b) $\theta = -135$ deg

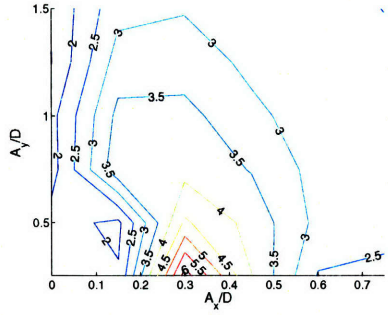

(c) $\theta = -90$ deg

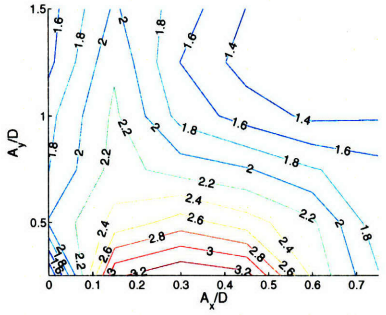

(d) $\theta = -45$ deg

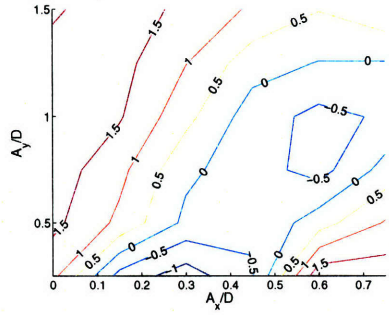

(e) $\theta = 0$ deg

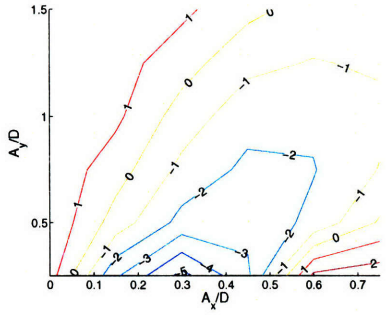

(f) $\theta = 45$ deg

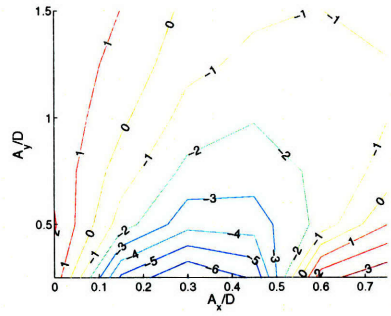

(g) $\theta = 90$ deg

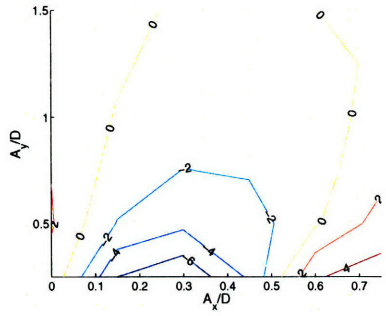

(h) $\theta = 135$ deg

Figure D-21: Cross-flow added mass coefficient contours for $V_r = 6.5$.

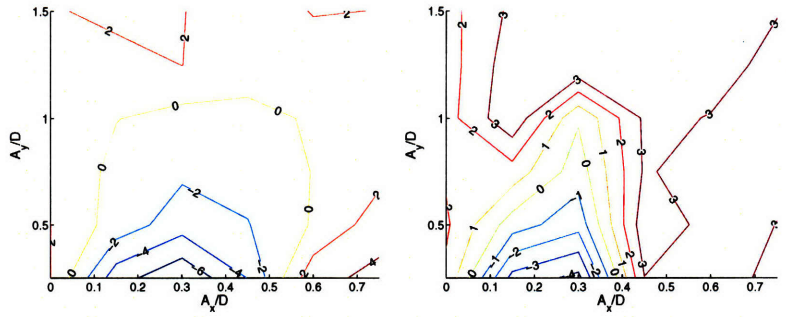

(a) $\theta = -180$ deg

(b) $\theta = -135$ deg

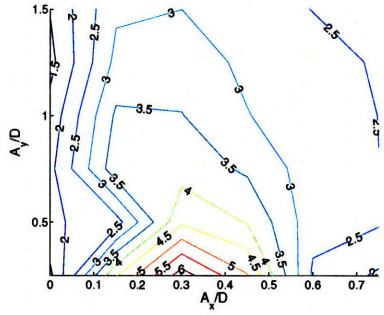

(c) $\theta = -90$ deg

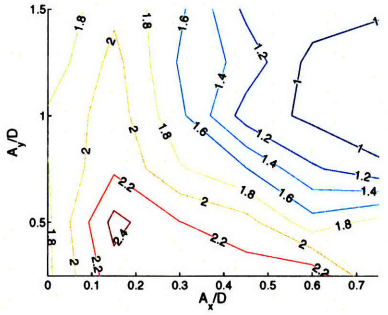

(d) $\theta = -45$ deg

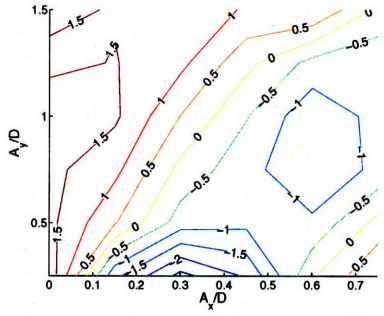

(e) $\theta = 0$ deg

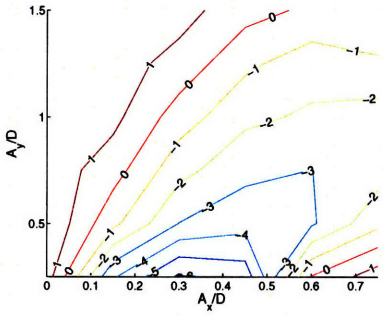

(f) $\theta = 45$ deg

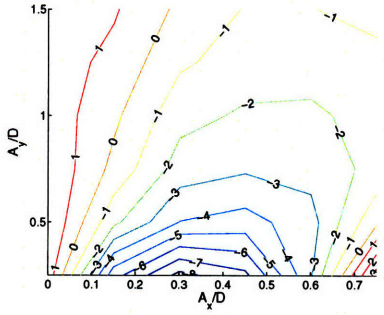

(g) $\theta = 90$ deg

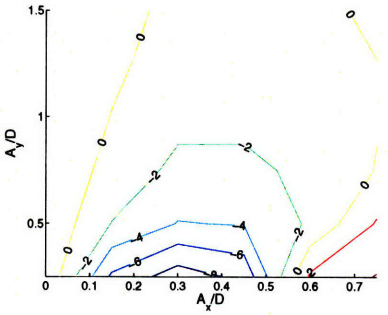

(h) $\theta = 135$ deg

Figure D-22: Cross-flow added mass coefficient contours for $V_r = 7$.

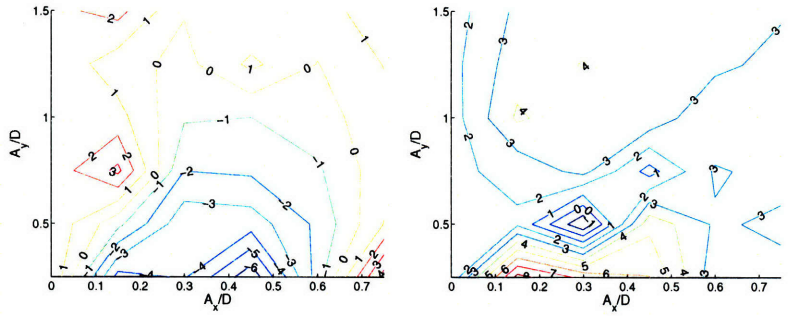

(a) $\theta = -180$ deg

(b) $\theta = -135$ deg

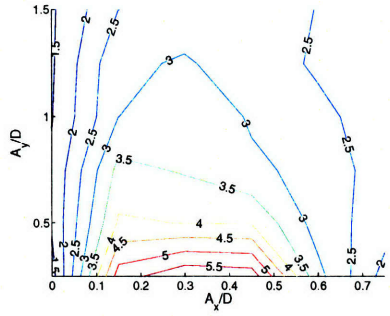

(c) $\theta = -90$ deg

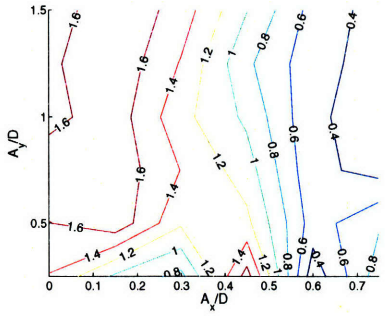

(d) $\theta = -45$ deg

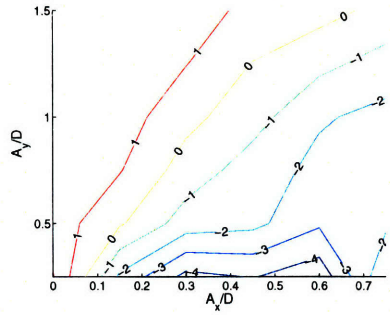

(e) $\theta = 0$ deg

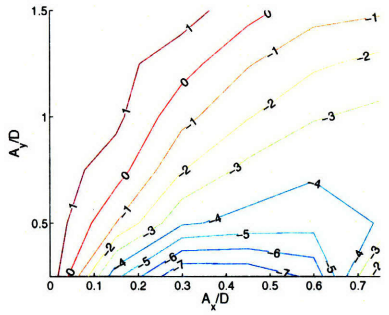

(f) $\theta = 45$ deg

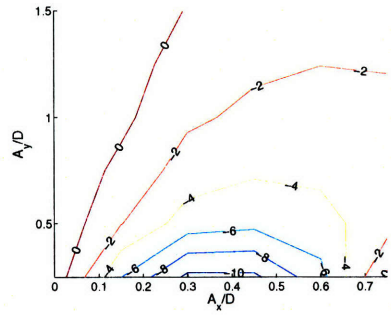

(g) $\theta = 90$ deg

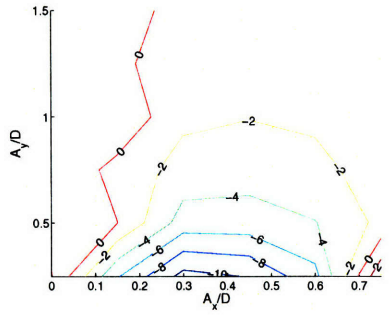

(h) $\theta = 135$ deg

Figure D-23: Cross-flow added mass coefficient contours for $V_r = 7.5$.

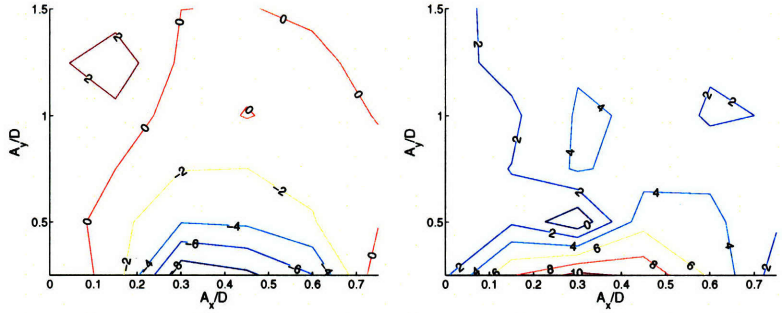

(a) $\theta = -180$ deg

(b) $\theta = -135$ deg

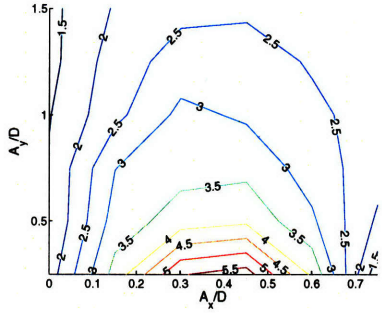

(c) $\theta = -90$ deg

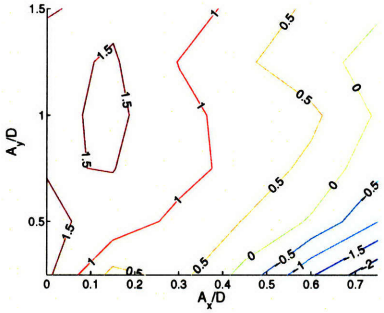

(d) $\theta = -45$ deg

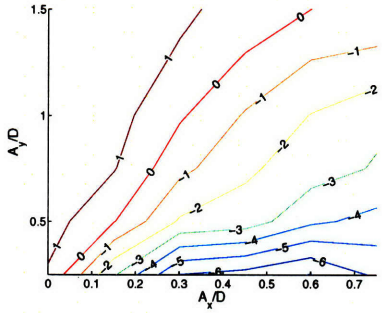

(e) $\theta = 0$ deg

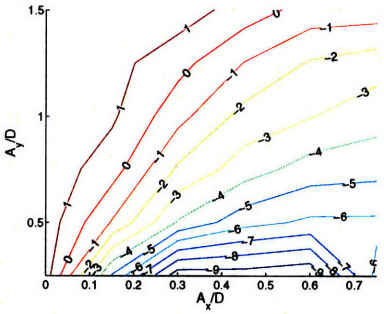

(f) $\theta = 45$ deg

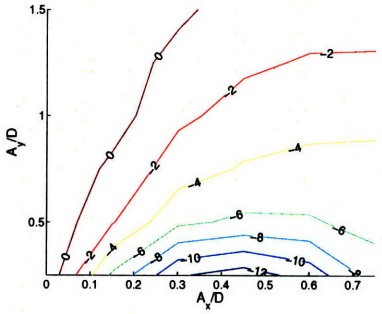

(g) $\theta = 90$ deg

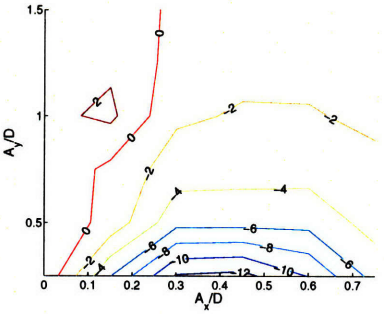

(h) $\theta = 135$ deg

Figure D-24: Cross-flow added mass coefficient contours for $V_r = 8$.

D.4 In-line Added Mass Coefficient, C_{mx}

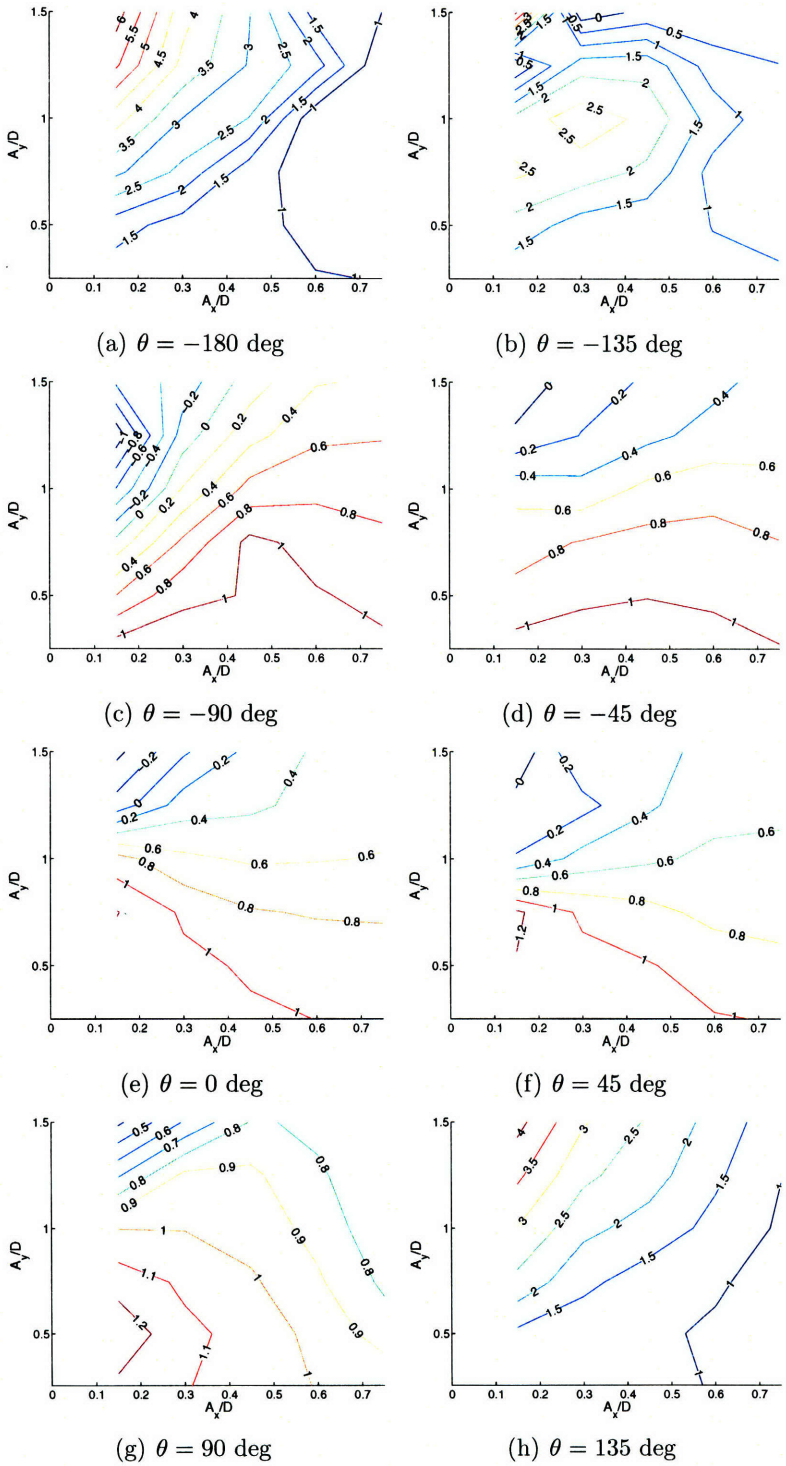

(a) $\theta = -180$ deg (b) $\theta = -135$ deg

(c) $\theta = -90$ deg (d) $\theta = -45$ deg

(e) $\theta = 0$ deg (f) $\theta = 45$ deg

(g) $\theta = 90$ deg (h) $\theta = 135$ deg

Figure D-25: In-line added mass coefficient contours for $V_r = 4.5$.

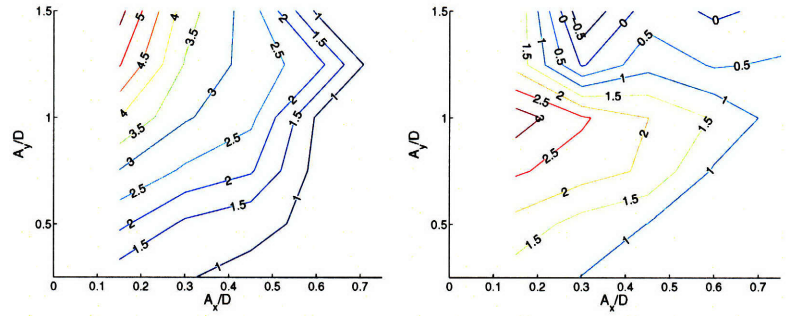

(a) $\theta = -180$ deg

(b) $\theta = -135$ deg

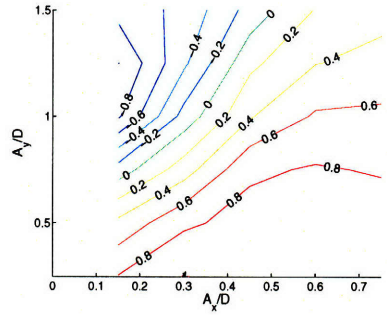

(c) $\theta = -90$ deg

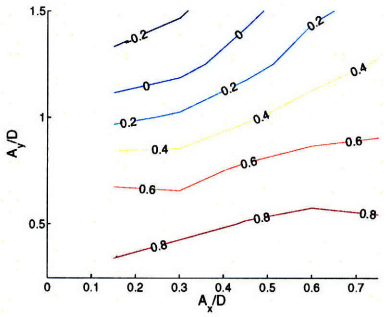

(d) $\theta = -45$ deg

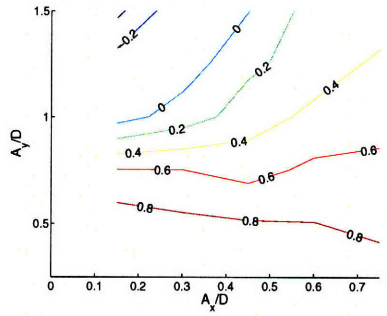

(e) $\theta = 0$ deg

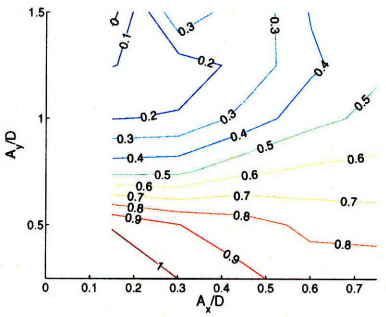

(f) $\theta = 45$ deg

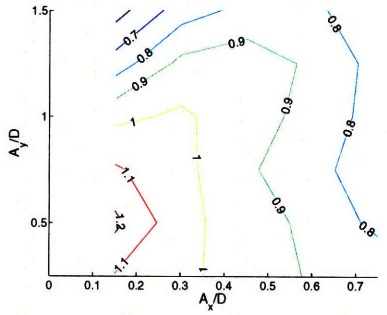

(g) $\theta = 90$ deg

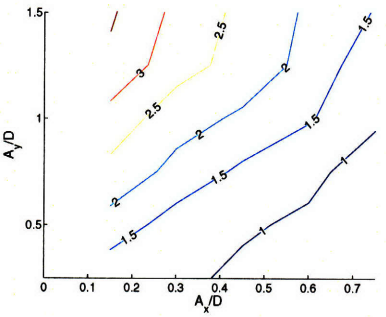

(h) $\theta = 135$ deg

Figure D-26: In-line added mass coefficient contours for $V_r = 5$.

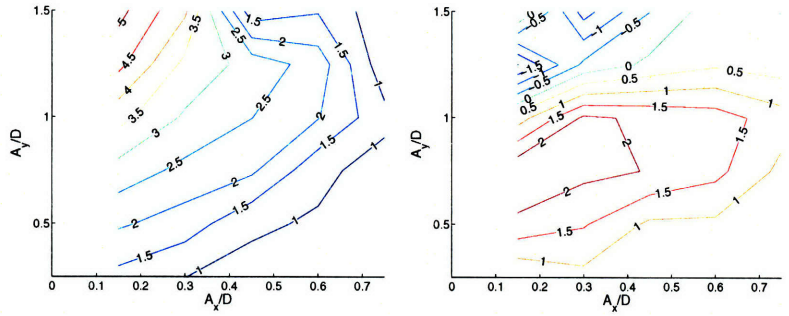

(a) $\theta = -180$ deg (b) $\theta = -135$ deg

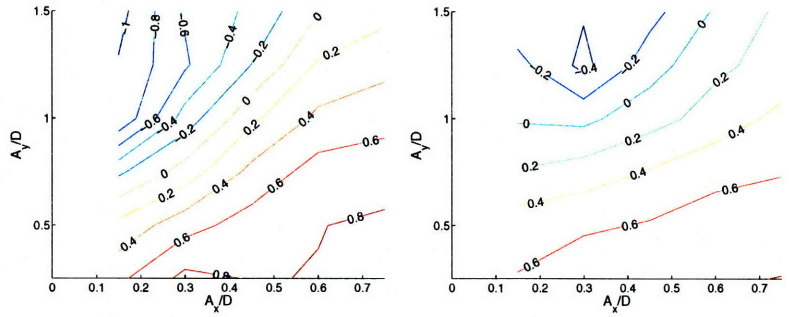

(c) $\theta = -90$ deg (d) $\theta = -45$ deg

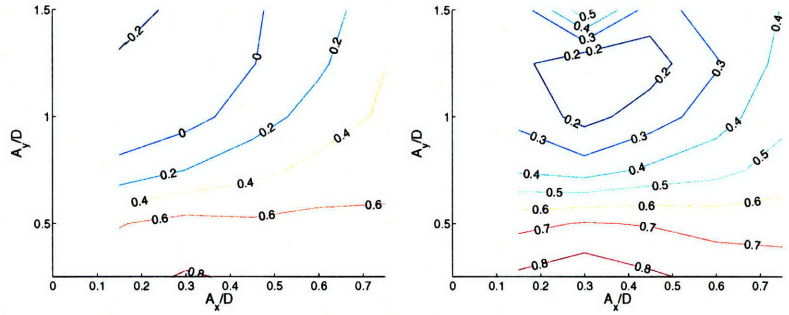

(e) $\theta = 0$ deg (f) $\theta = 45$ deg

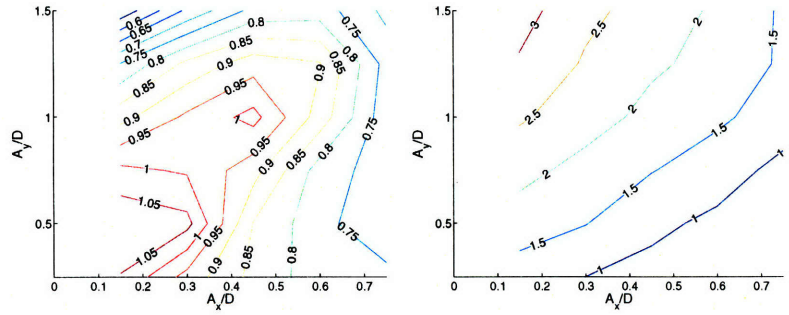

(g) $\theta = 90$ deg (h) $\theta = 135$ deg

Figure D-27: In-line added mass coefficient contours for $V_r = 5.5$.

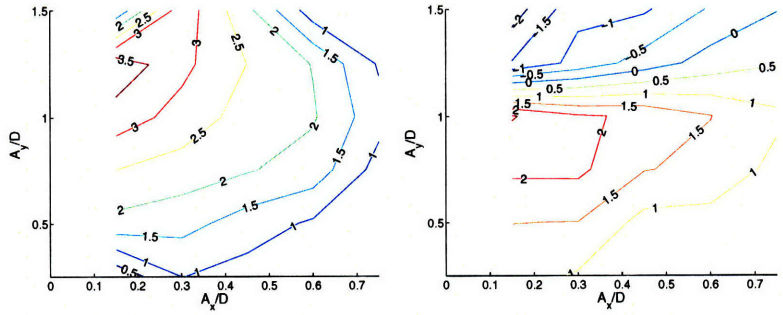

(a) $\theta = -180$ deg

(b) $\theta = -135$ deg

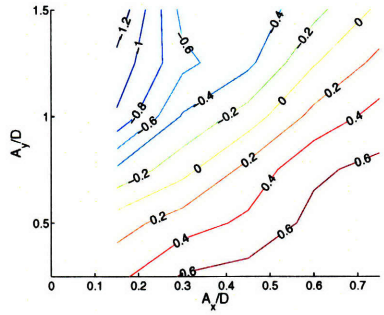

(c) $\theta = -90$ deg

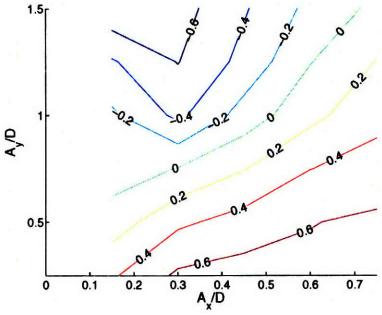

(d) $\theta = -45$ deg

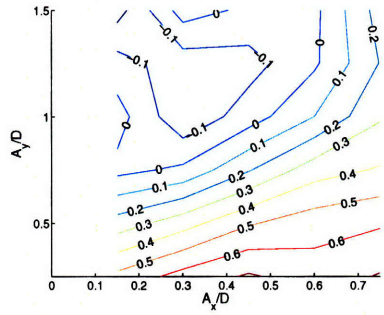

(e) $\theta = 0$ deg

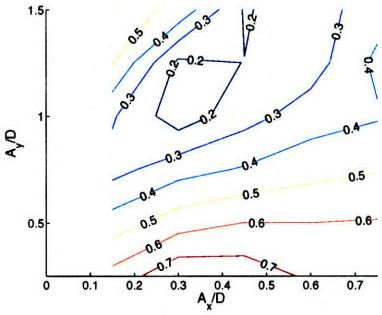

(f) $\theta = 45$ deg

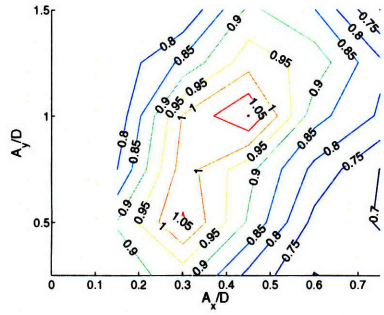

(g) $\theta = 90$ deg

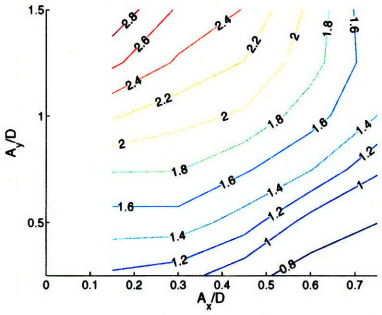

(h) $\theta = 135$ deg

Figure D-28: In-line added mass coefficient contours for $V_r = 6$.

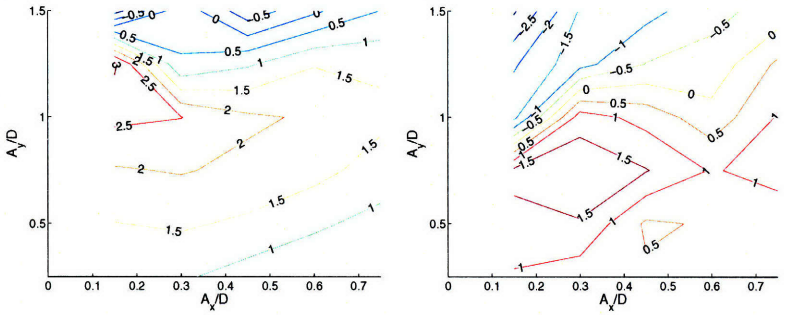

(a) $\theta = -180$ deg

(b) $\theta = -135$ deg

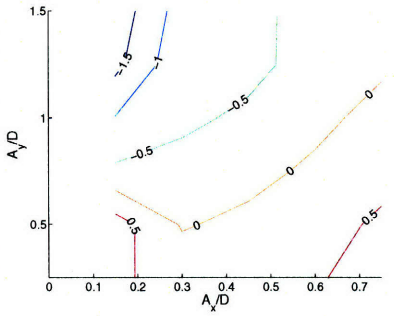

(c) $\theta = -90$ deg

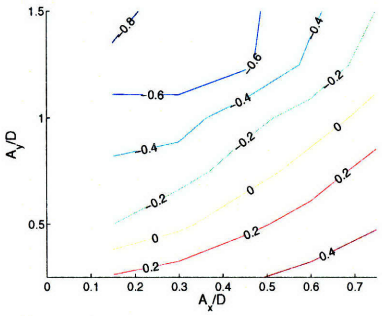

(d) $\theta = -45$ deg

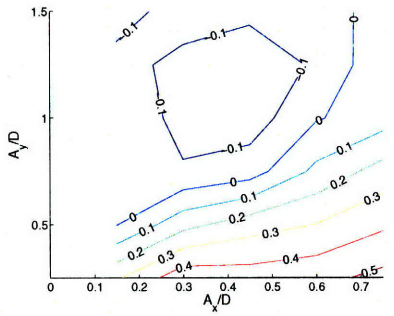

(e) $\theta = 0$ deg

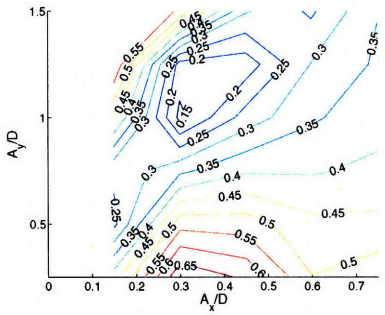

(f) $\theta = 45$ deg

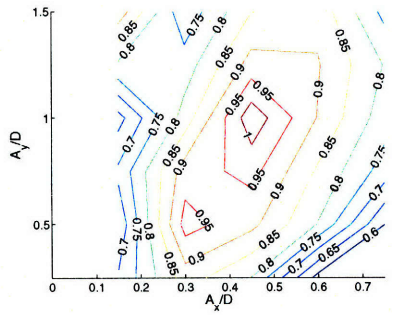

(g) $\theta = 90$ deg

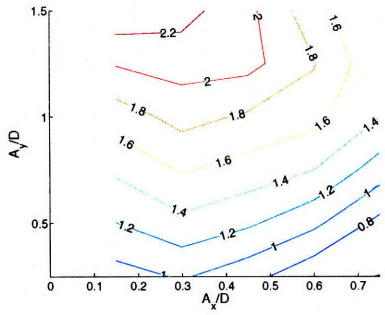

(h) $\theta = 135$ deg

Figure D-29: In-line added mass coefficient contours for $V_r = 6.5$.

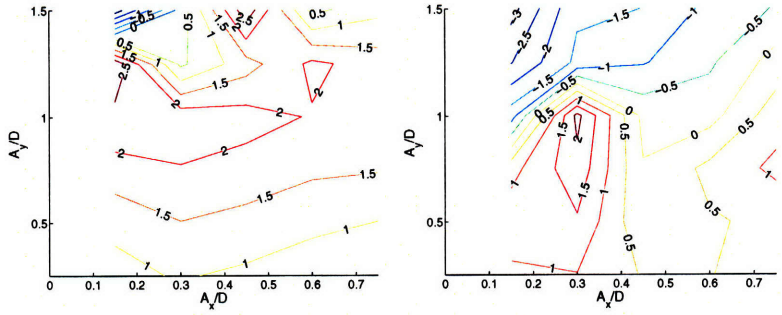

(a) $\theta = -180$ deg

(b) $\theta = -135$ deg

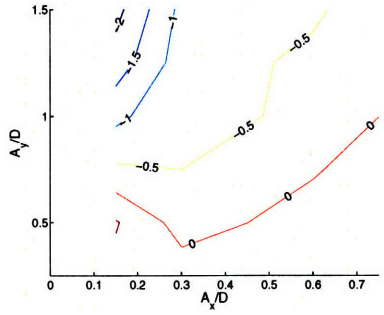

(c) $\theta = -90$ deg

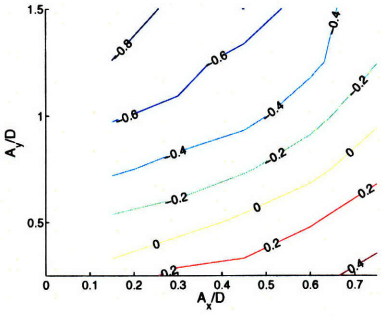

(d) $\theta = -45$ deg

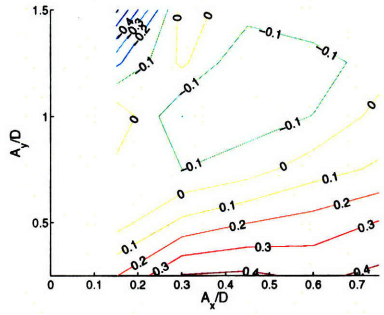

(e) $\theta = 0$ deg

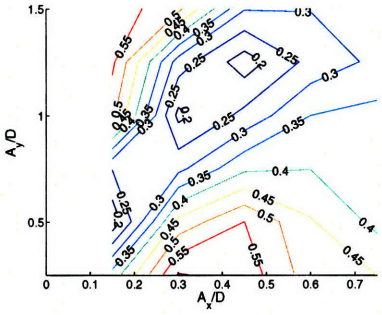

(f) $\theta = 45$ deg

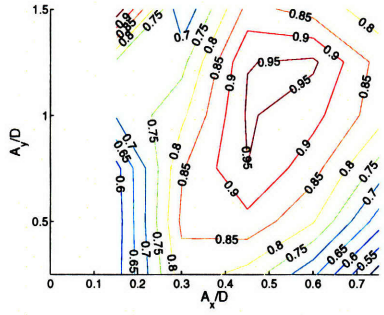

(g) $\theta = 90$ deg

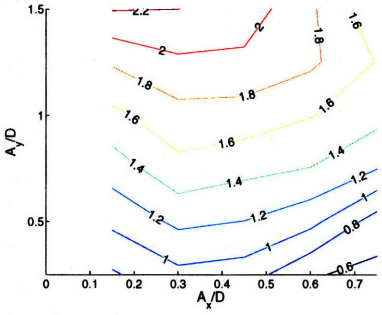

(h) $\theta = 135$ deg

Figure D-30: In-line added mass coefficient contours for $V_r = 7$.

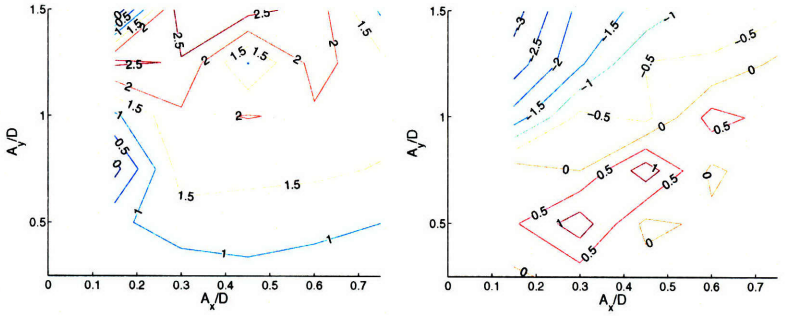

(a) $\theta = -180$ deg

(b) $\theta = -135$ deg

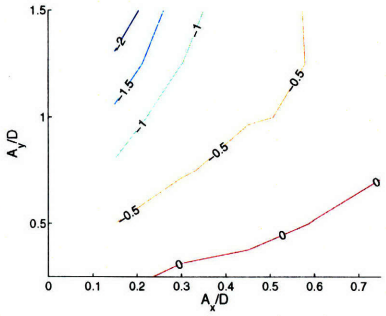

(c) $\theta = -90$ deg

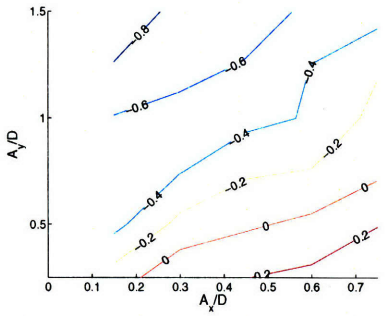

(d) $\theta = -45$ deg

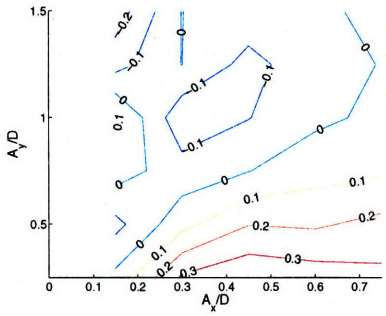

(e) $\theta = 0$ deg

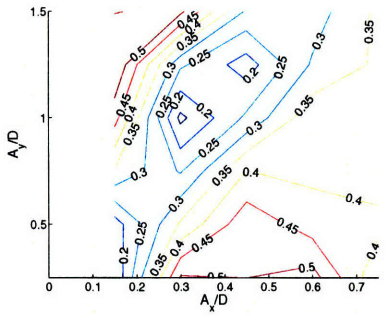

(f) $\theta = 45$ deg

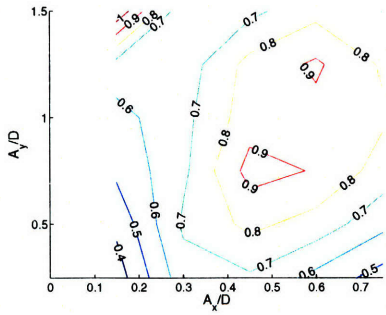

(g) $\theta = 90$ deg

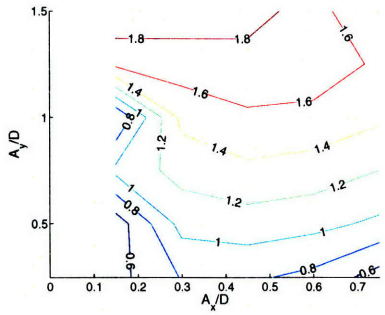

(h) $\theta = 135$ deg

Figure D-31: In-line added mass coefficient contours for $V_r = 7.5$.

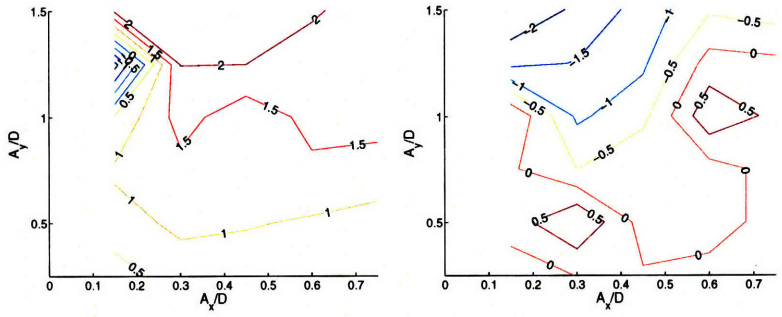

(a) $\theta = -180$ deg

(b) $\theta = -135$ deg

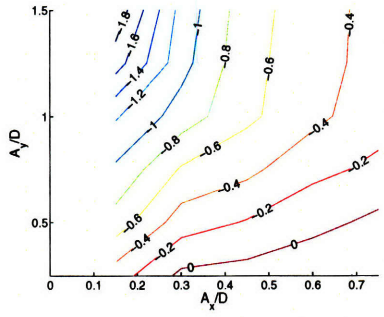

(c) $\theta = -90$ deg

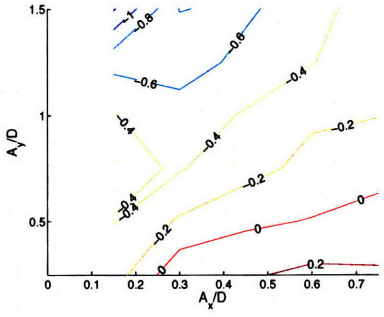

(d) $\theta = -45$ deg

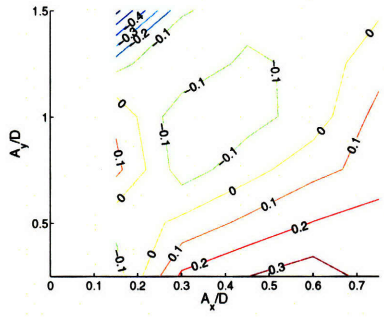

(e) $\theta = 0$ deg

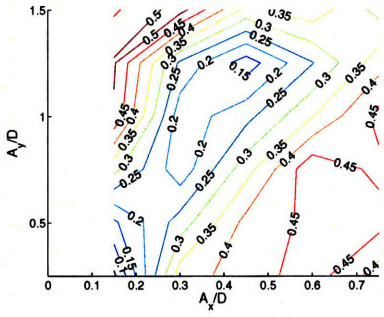

(f) $\theta = 45$ deg

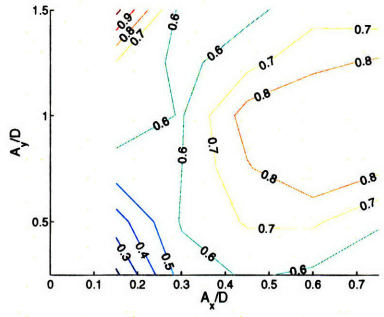

(g) $\theta = 90$ deg

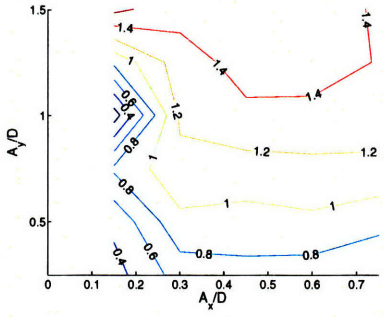

(h) $\theta = 135$ deg

Figure D-32: In-line added mass coefficient contours for $V_r = 8$.